Interactions between whistler waves and solar wind suprathermal electrons : Solar Orbiter and Parker Solar Probe observations

Lucas Colomban

UNIVERSITÉ D'ORLÉANS

ÉCOLE DOCTORALE Énergie Matériaux Sciences de la Terre et de l'Univers

Laboratoire de Physique et Chimie de l'Environnement et de l'Espace

THÈSE présentée par :

Lucas COLOMBAN

soutenue le : 30 novembre 2023

pour obtenir le grade de : Docteur de l'Université d'Orléans

Discipline/ Spécialité : Sciences de l'Univers

Interactions between whistler waves and solar wind suprathermal electrons: Solar Orbiter and Parker Solar Probe observations

THÈSE dirigée par :

KRETZSCHMAR Matthieu	Maître de conférences, Université d'Orléans (LPC2E, Orléans)
KRASNOSELSKIKH Vladimir	Directeur de recherche émérite, CNRS (LPC2E, Orléans)

RAPPORTEURS :

LE CONTEL Olivier	Directeur de recherche, CNRS (LPP, Paris)
PIERRARD Viviane	Professeur, Royal Belgian Institute for Space Aeronomy (IASB, Bruxelles) & Université catholique de Louvain (UCLouvain, Ottignies-Louvain-la-Neuve)

JURY :

ALEXANDROVA Olga	Astronome, Observatoire de Paris (LESIA, Meudon)
DUDOK DE WIT Thierry	Professeur, Université d'Orléans (LPC2E, Orléans), Président du jury
VERSCHAREN Daniel	Professeur, University College London (MSSL, London)

MEMBRE INVITE :

LAVRAUD Benoit	Directeur de recherche, CNRS (LAB, Bordeaux)
MAKSIMOVIC Milan	Directeur de recherche, Observatoire de Paris (LESIA, Meudon)

À Grand-mamie

Résumé

L'évolution de la fonction de distribution des électrons du vent solaire avec la distance héliocentrique présente des caractéristiques encore inexpliquées. Nous pouvons citer l'augmentation de la largeur angulaire du faisceau d'électrons suprathermiques aligné avec le champ magnétique (Strahl). Cette augmentation est associée à une augmentation de la densité relative des électrons suprathermiques plus isotrope du halo, à une diminution de la densité relative du Strahl et à la diminution rapide du flux de chaleur. Dans cette thèse, nous cherchons à préciser le rôle des interactions ondes-particules dans cette dynamique et en particulier à déterminer si les ondes de sifflement peuvent expliquer l'augmentation observée de la largeur angulaire du Strahl.

Pour ce faire, nous effectuons d'abord une analyse statistique de ces ondes avec Solar Orbiter et Parker Solar Probe (PSP), entre 0,2 et 1 UA. 110 000 paquets d'ondes sont détectés et caractérisés dans le référentiel du plasma. L'écrasante majorité des ondes ont un angle de propagation (θ) quasi-aligné avec le champ magnétique. Au-delà de 0,3 UA, les ondes se propagent dans la même direction radiale que le Strahl (y compris lors des "switchbacks"), et il n'y a pratiquement pas d'ondes fortement obliques ($\theta \sim 70°$). Ces dernières ont pourtant été prédites par de nombreuses études et sont théoriquement très efficaces pour diffuser les électrons du Strahl. À 0,2 UA, environ la moitié des ondes sont "counter-streaming" (se propagent dans la direction radiale opposé à celle du Strahl) et la proportion d'ondes obliques reste très faible. Les caractéristiques des ondes sont ensuite utilisées pour calculer les coefficients de diffusion dans le cadre de la théorie quasi-linéaire. Ces coefficients sont intégrés, en utilisant l'occurrence des ondes et le temps de propagation des électrons, afin de déduire l'effet global des ondes de sifflement sur les électrons suprathermiques. Au-delà de 0,3 UA, les ondes de sifflement peuvent expliquer l'augmentation observée de la largeur angulaire du Strahl et sont efficaces pour isotropiser le halo. Nous montrons que la diffusion du Strahl est due à des ondes légèrement obliques, $\theta \in [15, 45]°$. Près de 0,2 UA, les ondes counter-streaming diffusent les électrons de Strahl plus efficacement que les ondes alignées avec le Strahl de deux ordres de grandeur.

Par ailleurs, un problème technique (du a un fort gradient thermique) avec une bobine du fluxmètre tri-axial (SCM) de PSP à la fin de l'orbite 1 nous a empêché de déduire directement les propriétés de polarisation des ondes de sifflement pour les orbites suivantes. Nous proposons une technique utilisant les champs électromagnétiques disponibles pour reconstruire les composantes manquantes (et donc les propriétés de polarisation des ondes) en négligeant le champ électrique parallèle au champ magnétique. Cette technique est applicable avec les hypothèses suivantes : (i) la fréquence de l'onde dans le repère du plasma est petite par rapport à la fréquence cyclotronique électronique ; (ii) un petit angle de propagation par rapport au champ magnétique ; et (iii) une grande vitesse de phase par rapport à la vitesse du vent solaire perpendiculaire au champ magnétique. La méthode ne peut pas être appliquée si le champ magnétique est aligné avec la bobine du SCM concernée. Nous validons notre méthode en utilisant les mesures en mode rafale effectuées lors de l'orbite 1. Les conditions

de reconstruction sont satisfaites pour 80% des ondes de sifflement détectées. Cette méthode devrait permettre de révéler pour la première fois les propriétés de polarisation des ondes de sifflement jusqu'à 10 rayons solaires ($\simeq$ 0,05 UA).

Ce travail est une étape importante pour la prise en compte des interactions ondes-particules dans les modèles cinétiques et pour améliorer notre description du vent solaire.

Abstract

The evolution of the solar wind electron distribution function with heliocentric distance exhibits features that are still unexplained. We can mention the increase in the angular width of the beam of suprathermal electrons aligned with the magnetic field (Strahl). This increase is associated with an increase in the relative density of the more isotropic halo electrons, a decrease in the relative density of Strahl electrons, and a rapid decrease in the heat flux. In this thesis, we investigate the role of wave-particle interactions in these dynamics, and in particular whether whistler waves can explain the observed increase in the Strahl angular width.

To achieve this, we first perform a statistical analysis of these waves with Solar Orbiter and Parker Solar Probe (PSP), between 0.2 and 1 AU. 110,000 wave packets are detected and characterized in the plasma frame. The overwhelming majority of waves have an angle of propagation (θ) quasi-aligned with the magnetic field. Beyond 0.3 AU, the waves propagate in the same radial direction as the Strahl (including during switchbacks), and there are virtually no strongly oblique ($\theta \sim 70°$) waves. The latter were predicated by many studies and are theoretically very efficient in diffusing Strahl electrons. At 0.2 AU, about half of the waves are counter-streaming (propagate in the opposite radial direction to the Strahl), and the proportion of oblique waves remains very low. The wave characteristics are then used to compute the diffusion coefficients in the framework of quasi-linear theory. These coefficients are integrated, using the occurrence of the waves, in order to deduce the overall effect of whistlers on suprathermal electrons. Beyond 0.3 AU, whistler waves can explain the observed increase in Strahl angular width and are effective in isotropizing the halo. Strahl diffusion is due to slightly oblique ($\theta \in [15, 45]°$) waves. Near 0.2 AU, counter-streaming waves diffuse Strahl electrons more efficiently than Strahl-aligned waves by two orders of magnitude.

However, a technical issue with one coil of the Search-Coil Magnetometer (SCM) of PSP (due to a strong thermal gradient) at the end of Encounter 1 prevented us from directly deducing the polarization properties of whistler waves for the subsequent encounters. We propose a technique using the available electromagnetic fields to reconstruct the missing components (and therefore the polarization properties of the waves) by neglecting the electric field parallel to the background magnetic field. This technique is applicable with the assumptions of (i) a small wave frequency in the plasma frame with respect to the electron cyclotron frequency; (ii) a small propagation angle with respect to the background magnetic field; and (iii) a large wave phase speed relative to the cross-field solar wind velocity. Critically, the method cannot be applied if the background magnetic field is aligned with the affected SCM coil. We validate our method using burst mode measurements made during Encounter 1. The reconstruction conditions are satisfied for 80% of the whistlers detected. This method should reveal the polarization properties of whistler waves down to 10 solar radii ($\simeq 0.05$ AU) for the first time.

This work is an important step in order to include wave-particle interactions in kinetic

models and to improve our description of the solar wind.

Remerciements

En premier lieu, je voudrais remercier mes deux directeurs de thèse, Matthieu et Volodya. J'ai énormément appris à vos côtés et je suis très reconnaissant pour votre encadrement. Votre bienveillance et votre compréhension, notamment face à mon organisation souvent approximative, furent remarquables et très appréciées. Je suis heureux de maintenant vous compter parmi mes amis. Je voudrais particulièrement remercier Matthieu pour sa très grande disponibilité et pour m'avoir poussé à améliorer ma communication orale et écrite jusqu'à ce que j'en aie marre. Merci pour ton soutien. Je remercie également Volodya pour m'avoir partagé une petite partie de sa très grande connaissance, son humour et ses anecdotes à rallonge. Même si je n'arrive toujours pas très bien à suivre quand tu calcules à l'oral. Je veux par ailleurs remercier Oleksiy pour son aide très précieuse lors de cette dernière année de thèse. Merci pour tes conseils et pour tout ce que tu m'as appris. Merci pour les invitations à Berkeley et de me faire confiance pour la suite. I'm looking forward to working with you.

Merci de plus à Loïc pour ton aide et pour la façon dont tu m'as guidé à l'IUT. Merci pour ta bienveillance. Merci pareillement aux membres de l'IUT que j'ai pu rencontrer, votre gentillesse m'a beaucoup marquée et ce fut un plaisir de venir enseigner.

Je souhaite également remercier tous les membres du jury : Olivier, Viviane, Olga, Thierry, Daniel, Benoit et Milan. Merci pour le temps que vous m'avez accordé, pour votre lecture détaillée du manuscrit et pour la riche discussion de la soutenance. Je suis extrêmement reconnaissant pour tous vos commentaires très positifs.

Merci pour toutes les riches discussions que j'ai pu avoir lors de conférences et de réunions d'équipe. Je suis conscient de la chance que j'ai eue de pouvoir évoluer dans un environnement de travail si remarquable. Merci tout particulièrement à Milan pour la promotion du travail de la commutée RPW et pour avoir toujours soutenu mon travail. Merci aussi à Matthieu Berthomier et à Laura Berčič.

Merci à tous les membres du laboratoire (personnel administratif, ingénieurs, doctorants, post-docs, chercheurs...) pour leur aide et pour avoir rendu mon séjour au LPC2E très agréable. Merci notamment à Clara, Nina, Andrea et Thierry pour les discussions scientifiques. Merci à ce groupe de doctorants et d'ingénieurs si spécial : Jérémie, Matthieu, Melody, Gaëtane, Pietro, Andrea, Nina, Pierre, Yanis, Hakim et Anna avec qui j'ai énormément ri et passé de super soirées. Merci d'avoir pris en compte mon esprit de compétition et de m'avoir parfois laissé gagner (on pourra citer le laser game et le lancer de haches, j'ai des preuves). Je n'étais pas toujours au laboratoire, mais ça a toujours été un plaisir de venir vous retrouver.

Merci pour les très chères amitiés que j'ai pu forger pendant mes études (Julien J, Thomas R, Julien R, Franck, Tom, Remi, Thomas B, Lucas, Yassine, Maurice et Stéphane) et qui m'ont permis d'apprécier chaque étape.

Merci à toute ma famille et notamment à mes oncles, tantes, cousins (il me semble nécessaire de faire apparaitre ici le terme “Col team”), cousines, grands-parents et à ma belle famille (Emmanuel, Sylvie, Sam et Evan) pour leur soutien sans faille. Aujourd'hui, je pense particulièrement à ma grand-mamie qui venait m'attendre à la sortie de l'école. Maintenant que mon parcours scolaire se termine, je sais que de là où tu me regardes, tu es infiniment fière. Merci à Jacqueline (meilleure marraine du monde) et à Philippe d'avoir toujours été présents pour moi. Merci à ma Camille pour son soutien sans limite depuis des années. Souvent, je me demande comment tu me supportes. Je suis très impatient que tu aies encore à me supporter dans nos prochaines aventures. Mon petit frère (Sacha) voulait absolument que je le mentionne, je n'ai pas vraiment compris pourquoi. Voilà qui est fait.

Papa, Maman, Sacha, Camille, il m'est difficile de trouver les mots justes. Vous me guidez et m'inspirez chaque jour. J'essaie de faire de mon mieux pour vous rendre fiers.

Contents

Chapter 1

Necessity for wave-particle interactions in solar wind models

1.1 The solar wind

The idea that the Sun emits a continuous flow of particles and that the interplanetary medium is therefore not empty was put forward at the end of the 19th century by the Norwegian physicist Kristian Birkeland (Meyer-Vernet, 2007). The presence of a "solar corpuscular flux" was definitely revealed in 1951 by Ludwig Biermann through the study of comet tails (Biermann, 1951; Mendis, 2006). Indeed, comets have two tails. One is composed of gas and has a straight shape always pointing away from the Sun. The other is composed of dust and has a rounded shape. The rounded shape is simply explained by the action of gravity and radiative pressure on the dust grains. On the other hand, to explain the straight shape of the first tail one must invoke the presence of a continuous outflow of plasma coming from the Sun. It is only after the work of Eugene Parker (Parker, 1958) that the term Solar wind was used to designate this plasma flow.
We know today that the solar wind is a permanent and turbulent flow of charged particles. The plasma comes from the expansion of the hot solar corona (1 to 2 MK) and is accelerated to supersonic velocities. This flow consists mainly of electrons and protons. There are also alpha particles (He^{++}) whose relative density with respect to protons is of the order of $\sim 4\%$, and much smaller amounts of heavy ions ($\sim 0.1\%$) (Schwenn and Marsch, 1990; Wimmer-Schweingruber, 2002; Meyer-Vernet, 2007). The solar wind was first measured by the Luna 1 spacecraft in 1959 and was then studied *in situ* by many missions (among others and with their launch dates: Helios 1974, Voyager 1977, Ulysses 1990, Wind 1994, SOHO 1995, ACE 1997, Cluster II 2000, STEREO 2006, Artemis 2006, DSCOVR 2015, MMS 2015, Parker Solar Probe 2018, Solar Orbiter 2020).
Ulysses' measurements have notably revealed the existence of two solar wind regimes. The fast wind ($V_{\mathrm{SW}} \geq 500$ km/s) is generally tenuous, relatively homogeneous and Alfvénic (V_{SW} being the solar wind speed). The slow wind ($V_{\mathrm{SW}} \leq 400$ km/s) is denser and highly variable. Figure 1.1 shows plots of the solar wind speed versus heliospheric latitude observed by Ulysses during three of its orbits, corresponding to three periods of solar activity (Figures 1.1a to

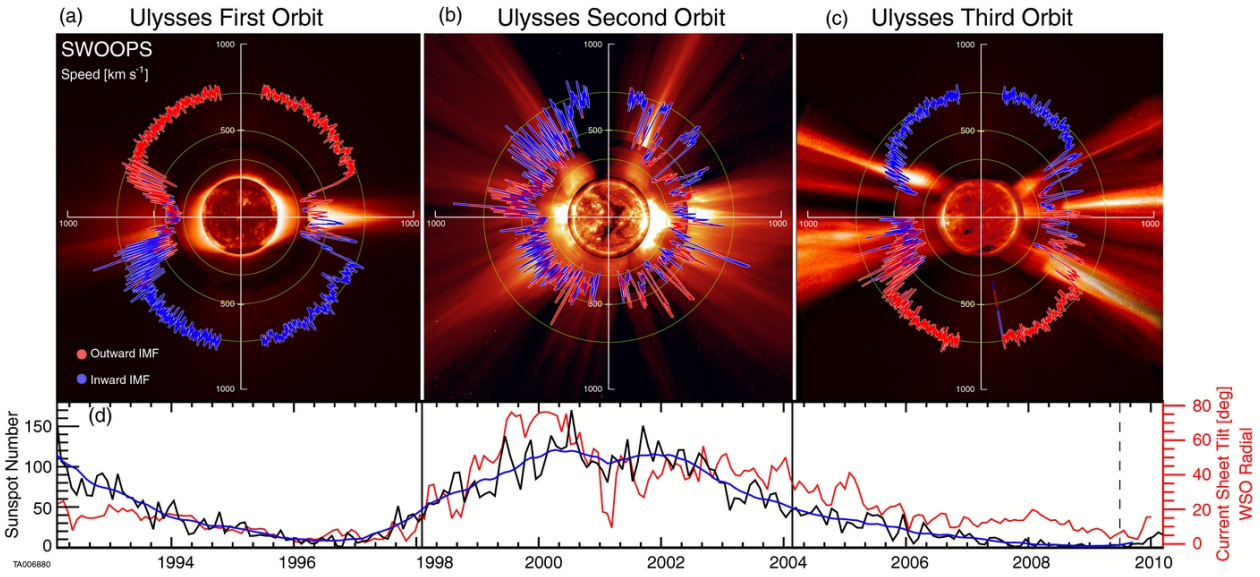

Figure 1.1: *Panels a),b) and c):* Dependence of the solar wind speed upon heliospheric latitude measured by the Ulysses probe during three orbits. The polarization of the background magnetic field is indicated in blue (resp., red) for the field lines pointing toward (resp., away from) the Sun. *Panel d):* Sunspot number (black), smoothed sunspot number (blue), and current sheet tilt (red) as a function of time. Figure taken from McComas et al. (2013).

1.1c). The activity of the Sun is measured here by the sunspot number and the current sheet tilt (Figure 1.1d). During the periods of low activity (Figures 1.1a and 1.1c) the solar wind is mainly slow at the equator (where the plasma temperature is high) and fast near the poles where it takes its origin in coronal holes (where the plasma temperature is lower). In periods of intense activity (Figure 1.1b) the distribution of speeds is more complex and there are fast and slow winds at all latitudes (McComas et al., 2008, 2013).

As will be detailed later, a better understanding of the evolution of electrons in the solar wind is the main objective of this thesis. In this first chapter, we first briefly describe the main observed characteristics of these electrons (Section 1.2). Next, we present the theoretical models used to describe the evolution of the solar wind (Section 1.3). Finally, we highlight the limitations of these models (Section 1.4).

1.2 Solar wind electron populations

1.2.1 Electron velocity distribution functions

The solar wind plasma can be described at the macroscopic level by using standard statistical approaches. These statistical approaches involve the loss of particle discernibility. The aim is to find the distribution function of each species (s) of the system $f_s(\vec{r}, \vec{v}, t)$. This distribution represents the number of particles at a time t, at the point $\vec{r}$ and $\vec{v}$ ($\vec{r}, \vec{v}$ being the position

and velocity variables, respectively) within a volume $d^3\vec{r}d^3\vec{v}$ of the phase space (Stix, 1992). In the following, we are mainly interested in electrons, therefore unless otherwise specified the distribution functions detailed below correspond to this species. Moreover, we will in general deal with the velocity distribution function (i.e., at a given position and time: $f(\vec{v})$).

In the solar wind, it is common to classify the electron populations into three categories, based on their observed velocity distribution functions (Feldman et al., 1975; Pilipp et al., 1987a; Hammond et al., 1996; Marsch, 2006). The thermal electrons of the core are present at low energies, are affected by Coulomb collisions, and thus have close to Maxwellian distributions. On average the core population represents 95% of the total electron density (Pilipp et al., 1987a; Maksimovic et al., 2005a; Štverák et al., 2009). The suprathermal electrons of the halo have higher energies (Feldman et al., 1975, 1978; Lazar et al., 2020) and are often represented by Kappa distributions (Scudder, 1992a,b; Maksimovic, Pierrard, and Lemaire, 1997; Pierrard and Lazar, 2010; Lazar et al., 2015; Pierrard, Lazar, and Stverak, 2022). The Strahl is a beam of high-energy electrons that follows the magnetic field lines, propagating away from the Sun (Rosenbauer et al., 1976, 1977; Pilipp et al., 1987a; Hammond et al., 1996). The pitch angle is the angle between the background magnetic field and the velocity of a particle. The Strahl pitch angle width (PAW) is defined as a full-width half maximum of the pitch-angle distribution of Strahl electrons at a given energy. The suprathermal populations (halo and Strahl) have energies between about 100 and 1000 eV which evolve with distance (Pierrard, Maksimovic, and Lemaire, 2001; Štverák et al., 2008; Pierrard, Lazar, and Stverak, 2022). Although they account for only a small percentage of electrons, suprathermal populations have a kinetic energy density comparable to that of the core (Maksimovic, Gary, and Skoug, 2000; Lazar, Poedts, and Fichtner, 2015). As we will see in Section 1.4.1, the relative density of suprathermal populations and the Strahl PAW evolve with distance. Understanding this evolution is one of the two main open questions about electrons in the solar wind.

In the solar wind frame, the core has a sunward drift velocity ($v_{\mathrm{c}||}$) while the halo and the Strahl have an anti-sunward drift velocity ($v_{\mathrm{H}||}$, $v_{\mathrm{S}||}$ (Feldman et al., 1975; Scime et al., 1994)). These drift speeds satisfy the zero current condition:

$$n_{\mathrm{c}}v_{\mathrm{c}||} + n_{\mathrm{H}}v_{\mathrm{H}||} + n_{\mathrm{S}}v_{\mathrm{S}||} = 0 \tag{1.1}$$

where $n_{\mathrm{c}}, n_{\mathrm{H}}$ and n_{S} correspond to core, halo, and Strahl density, respectively. Here and in the following, unless otherwise specified, the parallel and the perpendicular directions are defined with respect to the background magnetic field. The velocity distribution functions (VDFs) of these populations are represented schematically in the solar wind reference frame in Figure 1.2.

To take into account these drift velocities and the possible anisotropies, drifting bi-Maxwellian or bi-Kappa VDFs are often used to fit these different populations. Therefore, for the core electrons, the VDFs can be expressed as (Štverák et al., 2008; Tong et al., 2019b; Berčič, 2020):

$$f_{\mathrm{c}}(v_\perp, v_{||}) = A_{\mathrm{c}} \exp\Big(-\frac{v_\perp^2}{v_{\mathrm{thc}\perp}^2} - \frac{(v_{||} - v_{\mathrm{c}||})^2}{v_{\mathrm{thc}||}^2}\Big) \tag{1.2}$$

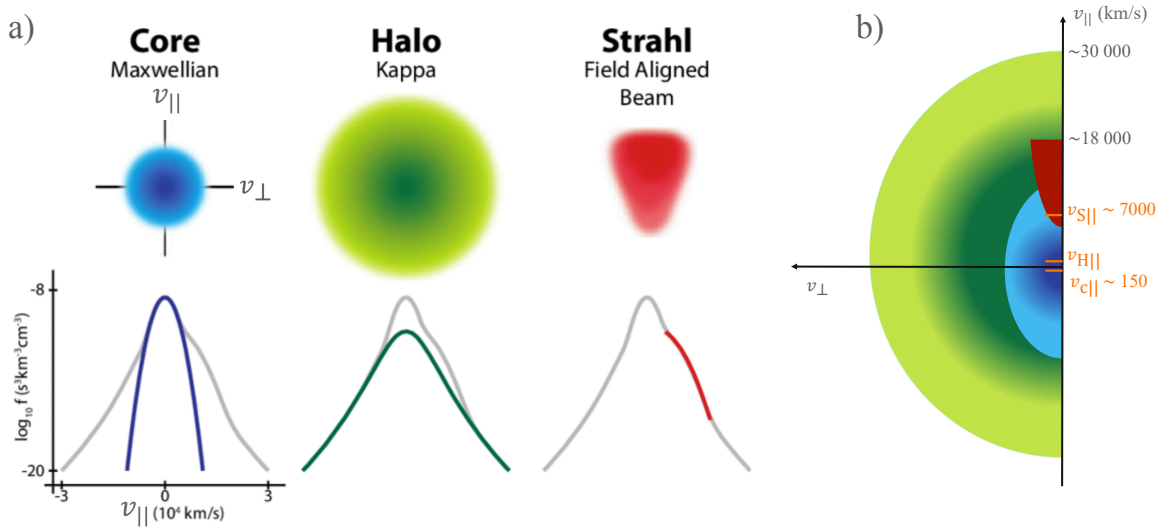

Figure 1.2: Representation of the velocity distribution functions of the three electron populations in the solar wind, the core is in blue, the halo is in green and the Strahl is in red. *Panel a):* Electron velocity distribution functions in the plane $(v_\perp, v_{||})$ (top) and with a cut in the parallel ($||$) direction (bottom). This panel is adapted from Salem et al. (2021). *Panel b):* Electron velocity distribution function in the plane $(v_\perp, v_{||})$ showing approximately which populations dominate at which energies as well as the orders of magnitude of the drifts of the different populations around 20 $R_\odot$ (solar radii). These values were obtained by Halekas et al. (2021a, 2022) using Parker Solar Probe data.

where $v_{\mathrm{thc}\perp}$ and $v_{\mathrm{thc}||}$ are the core perpendicular and parallel thermal speeds, respectively. The thermal speed is expressed as $v_{\mathrm{th}} = \sqrt{2k_{\mathrm{B}}T/m_{\mathrm{e}}}$ where T is the temperature (K), k_{B} is the Boltzmann's constant and m_{e} is the electron mass. The total core temperature T_{c} is $T_{\mathrm{c}} = \frac{2}{3}T_{\mathrm{c}\perp} + \frac{1}{3}T_{\mathrm{c}||}$. Finally, A_{c} is defined as:

$$A_{\mathrm{c}} = \frac{n_{\mathrm{c}}}{\pi^{3/2} v_{\mathrm{thc}\perp}^2 v_{\mathrm{thc}||}} \tag{1.3}$$

For halo electrons, depending on the shape of the distribution, one can use a drifting bi-Maxwellian (equation 1.2) or a bi-Kappa VDF (Tsallis, 1988; Maksimovic, Pierrard, and Lemaire, 1997; Pierrard, Maksimovic, and Lemaire, 1999; Pierrard and Lazar, 2010; Pierrard, Lazar, and Stverak, 2022):

$$f_{\mathrm{H}}(v_\perp, v_{||}) = \frac{n_{\mathrm{H}}}{\pi^{3/2} v_{\kappa \mathrm{H}\perp}^2 v_{\kappa \mathrm{H}||} \kappa^{3/2}} \frac{\Gamma(\kappa+1)}{\Gamma(\kappa-1/2)} \Big(1 + \frac{v_\perp^2}{\kappa v_{\kappa \mathrm{H}\perp}^2} + \frac{(v_{||} - v_{\mathrm{H}||})^2}{\kappa v_{\kappa \mathrm{H}||}^2}\Big)^{-\kappa-1} \tag{1.4}$$

where Γ is the Reimann Γ function (Abramowitz and Stegun, 1972) and

$$v_\kappa = \sqrt{\frac{\kappa - 3/2}{\kappa} \frac{2k_{\mathrm{B}}T}{m_{\mathrm{e}}}} \tag{1.5}$$

κ is a parameter that determines the amount of suprathermal particles. The Kappa distribution tends toward a Maxwellian when $\kappa \to \infty$.

Electrons are the lightest particles in the solar wind and the electron populations have drift velocities along the background magnetic field lines. Electrons therefore carry most of the solar wind heat flux, which is directed parallel to the field lines. The heat flux is an important quantity in the solar wind as it contributes to the energy balance between the solar wind and the corona. We describe this quantity in more detail below.

1.2.2 Electron heat flux

The heat flux (Wm^{-2}) is the third moment of the distribution function. The parallel component of the electron heat flux is defined as follows:

$$\vec{q}_{\mathrm{e}||} = \frac{1}{2} m_{\mathrm{e}} \int (v_{||} - < v_{||} >)(\vec{v} - < \vec{v} >)^2 f_{\mathrm{e}} d\vec{v} \tag{1.6}$$

where $< \vec{v} >$ represents the bulk velocity. The heat flux is carried by the two suprathermal components of the electron distribution function, the Strahl and the halo, because of their high energies and drifts in the proton reference frame (Scime et al., 1994). When the Strahl is clearly present in the observed distribution function the heat flux is dominated by its contribution (Pilipp et al., 1987a). The Strahl is strongly present close to the Sun (Halekas et al., 2020, 2021a) and in the fast solar wind (Fitzenreiter et al., 1998; Štverák et al., 2009), its contribution to heat flux is, therefore, generally significant in these conditions. On the

other hand, around 1 AU and beyond, the Strahl is not always observed, especially in the slow solar wind (Graham et al., 2017; Gurgiolo and Goldstein, 2017).

Feldman et al. (1975) used Ulysses measurements to show that the electron heat flux at 1 AU and beyond verifies the following empirical equation (Scime et al., 1994):

$$q_{e||} = \frac{1}{2} m_e k_b n_H v_{H||} (3(T_{H||} - T_{C||}) + 2(T_{H\perp} - T_{C\perp})) \tag{1.7}$$

We must note that the Ulysses measurements used by Feldman et al. (1975) didn't resolve the Strahl. This population is therefore included in the halo component. Equation 1.7 shows that the heat flux is indeed dominated by the drift of the suprathermal populations. The core population contributes negatively to the heat flux, while the suprathermal populations contribute positively. As the temperature of the suprathermal populations is higher, an anti-sunward heat flux is present. We can note that using a kinetic exospheric model (these models are described in Section 1.3.2) Pierrard and Lemaire (1998) calculated the electron heat flux using kappa VDFs. They showed that the heat flux increases when κ decreases because the number of suprathermal particles increases.

The electron heat flux has been observed to decrease with distance (Feldman et al., 1978; Scime et al., 1994; Štverák, Trávníček, and Hellinger, 2015; Halekas et al., 2021a; Pierrard, Lazar, and Stverak, 2022). As we will see in Section 1.4.2, the understanding of this decrease constitutes an open question regarding the solar wind electrons.

Several physical descriptions of the solar wind have been undertaken to model its evolution and to understand the evolution and the origins of these populations. The main goal of these models was initially to understand the mechanisms responsible for the acceleration of the solar wind. We can distinguish two categories of models, kinetic and fluid, whose main assumptions and results are briefly described in the next section.

1.3 Fluid and kinetic models

The kinetic models aim to solve the Boltzmann's equation to infer the distribution function of each species (s) of the system $f_s(\vec{r}, \vec{v}, t)$ (Marsch, 2006; Echim, Lemaire, and Lie-Svendsen, 2011; Pierrard, 2011). This equation is as follows:

$$\frac{\partial f_s}{\partial t} + \vec{v} \cdot \frac{\partial f_s}{\partial \vec{r}} + \frac{Z_s e}{m_s} (\vec{E}(\vec{r}, t) + \vec{v} \wedge \vec{B}(\vec{r}, t)) \frac{\partial f_s}{\partial \vec{v}} = (\frac{\partial f_s}{\partial t})_{cc} \tag{1.8}$$

where the term on the right-hand side represents the Coulomb collisions, $\vec{E}$ is the electric field, $\vec{B}$ is the magnetic field, e is the elementary charge and Z_s is the charge of the species s.
The solution of this equation being difficult to obtain, some models make the hypothesis of local thermodynamic equilibrium and thus assume that the distribution functions are Maxwellian. These multi-fluid or fluid theories (at very low frequencies) allow one to access

"only" averaged macroscopic quantities, which are the moments of the distribution functions. On the other hand, kinetic exospheric models neglect collisions. Since the solar wind is weakly collisional (and the presence of collisions depends strongly on the considered particle energy), neither model is perfectly suited. In the following, we briefly present these two types of models and their main results.

1.3.1 Fluid models

The fluid, hydrodynamic, thermally driven model of Parker (Parker, 1965), is the first to predict a supersonic, accelerated wind. This was not the case with the first exospheric kinetic models, which were initially set aside (Chamberlain, 1960). The hydrodynamic model of Parker is an improvement of the hydrostatic model of Chapman (Chapman and Zirin, 1957). Indeed, the latter predicts a finite pressure at infinity much larger than what was expected. On the other hand, the Parker model does not predict solar wind speeds as fast as the ones observed in the fast wind, for reasonable coronal temperatures. Fluid models are extremely useful, thanks to their predictive power and relative simplicity. However, in this thesis, we will be focusing on distribution functions, and in particular on their suprathermal parts, which fluid models cannot describe.

1.3.2 Kinetic exospheric models

The kinetic exospheric models (Chamberlain, 1960; Lemaire and Scherer, 1970, 1971; Echim, Lemaire, and Lie-Svendsen, 2011) aim to describe in a more complete way the solar wind above a certain altitude: the exobase. This limit represents the transition from a collisional plasma (as in the low corona) to a non-collisional plasma. This transition is generally considered to take place when the Knudsen number becomes greater than 1. The Knudsen number (K_n) is the ratio between the mean free path (L_fp) and the scale of the temperature gradient (L_T), and becomes greater than 1 between typically 2.5 and 10 $R_\odot$ (Maksimovic, Pierrard, and Lemaire, 1997; Echim, Lemaire, and Lie-Svendsen, 2011; Boldyrev, Forest, and Egedal, 2020). We can note that, in these models, one has to choose the distribution function at the exobase. Maxwellian functions were used in early models (Chamberlain, 1960; Lemaire and Scherer, 1970, 1971).

Above the exobase, the collision term of Boltzmann's equation can be neglected (Vlasov's equation), which greatly simplifies the calculations. Indeed, in this case, there is an adiabatic expansion that conserves the first adiabatic invariant and the energy. The conservation of these two quantities can be applied with Liouville's theorem to solve Vlasov's equation for a time-stationary wind. The first adiabatic invariant is defined as: $\mu = \frac{m_\mathrm{e} v_\perp^2}{2B_0}$, where $v_\perp$ is the perpendicular velocity of the particle and B_0 is the norm of the background magnetic field. The energy of an electron is expressed as $E = \frac{m_\mathrm{e}}{2}(v_{||}^2 + v_\perp^2) - e\Phi$, where Φ is the electrostatic potential of the electric field. Before the work of Lemaire and Scherer (1970, 1971), the Pannekoek-Rosseland electrostatic field was used (Pannekoek, 1922; Rosseland, 1924). This field is due to the fact that the ions are heavier than the electrons and are therefore subject to a stronger gravitational force. To ensure the quasi-neutrality an electric field that accelerates

protons and holds back electrons must exist. Considering that the protons and the electrons are in hydrostatic equilibrium and that their temperatures are equal and independent of the altitude, the Pannekoek-Rosseland electrostatic field can be expressed as:

$$\vec{E}_{\mathrm{PR}} = -\nabla\Phi_{\mathrm{PR}} = \frac{-\nabla P_{\mathrm{e}}}{e n_{\mathrm{e}}} = \nabla(\frac{(m_{\mathrm{p}} - m_{\mathrm{e}})\Phi_g}{2e}) \tag{1.9}$$

where Φ_{PR} and Φ_g are respectively the Pannekoek-Rosseland and gravity potentials and depend on the heliocentric distance. P_{e} is the electron pressure, n_{e} is the electron density and m_{p} is the proton mass (Pannekoek, 1922; Rosseland, 1924; Echim, Lemaire, and Lie-Svendsen, 2011). As mentioned in Section 1.3.1, these first models lead to too low solar wind speeds ($\sim$ 20km/s), they were named Solar breeze models and set aside.

In reality, the corona is not in hydrostatic equilibrium and a permanent evaporation of electrons and protons takes place. The $\vec{E}_{\mathrm{PR}}$ electric field is therefore inadequate and predicts a large electric current leaving the corona due to the faster electron evaporation, and therefore an unphysical charging of the Sun. Lemaire and Scherer (1970, 1971) showed that a stronger electric field is, therefore, necessary to balance the flux of evaporating electrons and protons. They calculated the so-called ambipolar electric field by ensuring quasi-neutrality and zero current condition at each distance r.The potential difference between the exobase and infinity obtained in this way is more than twice that obtained using the Pannekoek-Rosseland potential. Lemaire and Scherer (1971) have shown that this potential difference must be of the order of 410 V to ensure quasi-neutrality and zero current conditions. With this correction, radial profiles of bulk velocity, total temperature, and radial density consistent with the slow solar wind have been obtained. Moreover, the increase in bulk velocity with radial distance obtained is similar to that obtained with Parker's model (Lemaire and Pierrard, 2001; Pierrard, 2011). As will be detailed later, the predictions of these models depend on the chosen exobase distribution function. These models have revealed the importance of the ambipolar electric field in solar wind acceleration.

One can show that the electric field potential energy evolves at large distances as (Boldyrev, Forest, and Egedal, 2020):

$$e\phi = e\phi_\infty - C/r^{\alpha_T} \tag{1.10}$$

where C is a constant and $e\phi_\infty$ is the electric field potential energy at infinity. α_T corresponds to the exponent of the decrease law of the electronic temperature with the heliocentric distance, $T_{\mathrm{e}} \propto r^{-\alpha_T}$. The potential is measured with respect to its value at the exobase r_0 and therefore $\phi(r_0) = 0$.

Exospheric models predict the existence of 4 categories of particles depending on their energies and angular momentum (Echim, Lemaire, and Lie-Svendsen, 2011; Berčič, 2020). For electrons, the effect of gravity is negligible, so they are only slowed down by the ambipolar electric field.

Figure 1.3 represents electrons in these categories as a function of energy and distance (Figure 1.3a) and in the $(v_{||}, v_\perp)$ plane (Figure 1.3b).

- Particles that have a sufficient speed to escape the potential (gravitational for protons and ambipolar for electrons) are called escaping or runaway particles. For electrons these particles must verify $\frac{1}{2}m_e v^2 > e(\phi_\infty - \phi(r))$ and are identified as the Strahl population;
- Particles that have a speed lower than the escape speed will fall on the Sun and are called ballistic or returning particles. For electrons, these particles form part of the core population;
- Particles that are trapped between a magnetic mirror point and a gravitational or ambipolar return point are called trapped particles. In particular, it is possible if weak Coulomb collisions, wave-particle interactions, or other diffusion mechanisms are considered as they cause a pitch-angle diffusion that can slightly increase the perpendicular velocity. For electrons, these particles form the most important part of the core population;
- Particles coming from outside the solar system are called incoming particles and their effect is often neglected.

At each distance r, all electrons propagating anti-sunward, with energy verifying $\frac{1}{2}m_e v^2 < e\phi_\infty - e\phi(r)$, will not have sufficient speed to escape the Sun's gravitational potential and will form the sunward part of the distribution function. The velocity $v(r)_* = \sqrt{\frac{2(e\phi_\infty - e\phi(r))}{m_e}}$ constitutes therefore a cutoff (Figure 1.3b). This cutoff separates the core and Strahl electrons in the anti-sunward direction. In the sunward direction, it represents the maximum achievable speed for electrons (Boldyrev, Forest, and Egedal, 2020; Berčič, Landi, and Maksimović, 2021). In Section 2.3.1.2, we explain that this cutoff is the source of an instability that can generate whistler waves.

We now compare the predictions of exospheric models with observations of electron velocity distributions in the solar wind. In this thesis, we will be mainly interested in the heliospheric distance between 10 $R_\odot$ ($\simeq 0.047$ AU) and 1 AU.

1.4 Comparison with observations and limits of current theoretical models

Purely exospheric models neglect collisions in the solar wind (Lemaire and Scherer, 1970, 1971; Maksimovic, Pierrard, and Lemaire, 1997). As it is detailed in Section 1.4.1, it is clear that kinetic models, taking into account the collision term $((\frac{\partial f_s}{\partial t})_{cc})$ of Equation 1.8, using, for example, the Fokker-Planck equation are more suitable (Lie-Svendsen, Hansteen, and Leer, 1997; Pierrard, Maksimovic, and Lemaire, 1999; Pierrard, Maksimovic, and Lemaire, 2001). Furthermore, the adiabatic expansion, assumed in exospheric models, predicts an electron temperature decay law in $r^{-4/3}$, whereas observations show that this decrease is rather between $r^{-0.3}$ and $r^{-0.7}$ (Štverák, Trávníček, and Hellinger, 2015). Boldyrev, Forest, and Egedal

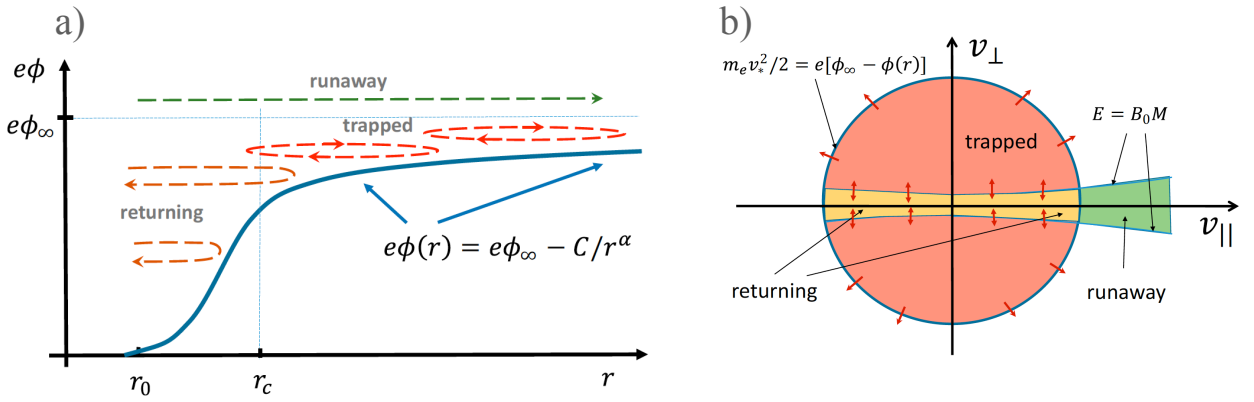

Figure 1.3: *Panel a):* Sketch of the evolution of the ambipolar electric field potential energy $e\phi$ as a function of the heliocentric distance (r). The trajectories of runaway, trapped, and returning electrons are shown. r_c is the value at which the electric field potential energy nearly reaches its asymptotic value, $r_c \simeq r_0(\frac{m_i}{m_e})^{1/4}$. *Panel b):* Representation of runaway, trapped and returning electrons in the $(v_{||}, v_\perp)$ plane, in the solar wind reference frame. Both panels are taken from Boldyrev, Forest, and Egedal (2020).

(2020) have recently shown, by taking collisions into account while remaining in an almost collision-free regime $K_n >> 1$ that a decay law in $r^{-2/5}$, close to what is observed, can be retrieved. In this study, the heating is provided by an exchange of energy between the Strahl and the background plasma.

Moreover, exospheric models using Maxwellian velocity distribution functions at the exobase don't predict velocities sufficient to explain the presence of the fast solar wind (Lemaire and Scherer, 1970, 1971; Echim, Lemaire, and Lie-Svendsen, 2011). However, the use of kappa distribution, assuming the presence of suprathermal particles at the exobase (Scudder, 1992a,b), has allowed to obtain such velocities (Pierrard and Lemaire, 1996; Maksimovic, Pierrard, and Lemaire, 1997). These studies underline the importance of suprathermal electrons in the solar wind acceleration process (Pierrard, 2011). Pierrard, Maksimovic, and Lemaire, 1999; Pierrard, Maksimovic, and Lemaire, 2001 used observed VDFs by the WIND spacecraft around 1 AU and the Fokker-Planck equation to determine the VDFs at 4 $R_\odot$. The observed distributions were used as a boundary condition at 1 AU to deduce the distributions at 4 $R_\odot$. They confirmed that in order to obtain a fast solar wind it is necessary to have suprathermal tails in the VDFs used at the exobase. However, we note that distributions having substantial suprathermal tails were not observed by the recent measurements of Paker Solar Probe (up to 12 $R_\odot$) (Halekas et al., 2020, 2021a, 2022). The mechanism allowing the acceleration of the fast solar wind is therefore still not clearly identified. The possible presence and origin of significant suprathermal tails in the corona is still under debate and will be discussed in greater detail in Section 2.3.2.

In the next two sections, we address two open questions on the solar wind that will be our

main interest in this thesis, the Strahl broadening (Section 1.4.1) and the heat flux regulation (Section 1.4.2).

1.4.1 The Strahl broadening and the origin of halo electrons

Exospheric models predict a focusing of electrons along the background magnetic field. This is easily understood by considering the conservation of energy and of the first adiabatic invariant with a background magnetic field that decreases with distance (as r^{-2} at our distances of interest, (Scime et al., 1994)). For core electrons, exospheric models predict greater $\frac{T_{||}}{T_{\perp}}$ than what is observed, this feature can however be corrected by introducing collisions (Phillips et al., 1989; Salem et al., 2003; Štverák et al., 2008; Boldyrev, Forest, and Egedal, 2020; Berčič, Landi, and Maksimović, 2021). Simulations of Berčič, Landi, and Maksimović (2021) (that take collisions into account in a statistical way) calculate the ambipolar electric field in a self-consistent way and model a continuous transition between regions with and without collisions. In their most collisional simulation run, the electron isotropization was effective up to 250 eV. Moreover, calculations of Boldyrev and Horaites (2019) have suggested that this limit is about 200 eV at 1 AU. Above this limit, even when collisions are taken into account, kinetic models predict a focusing of electrons along the background magnetic field. These models therefore predict an increase in relative density and a focusing along the field lines of the Strahl with distance. Thus, beyond a certain energy, since collisions are not efficient enough to isotropize the distribution to counter the effect of electron focusing, only the Strahl population is predicted. These models therefore do not predict the presence of the halo (if not assumed at the exobase).

Observations, on the other hand, clearly show the presence of a halo and that the relative density of halo electrons increases with distance while the fraction of Strahl electrons decreases (Maksimovic et al., 2005a; Štverák et al., 2009). The Strahl population even disappears completely beyond 5.5 AU (Graham et al., 2017). These observations suggest the existence of a transfer mechanism from the Strahl to the halo, not present in classical kinetic models. The evolution of the relative density of the different electron populations as a function of the heliocentric distance between 0.3 and $\sim$ 3 AU is shown in Figure 1.4. This figure was produced by Štverák et al. (2009) using data from Helios, Cluster II, and Ulysses at low ecliptic latitudes covering distances between 0.3 and 4 AU and in the slow solar wind ($\leq$ 500km/s). At 0.3 AU, the Strahl represents 6% of the density and the halo less than 1%, while at 3 AU the Strahl represents only 2% and the halo more than 3%. In the fast solar wind ($\geq$ 500km/s), this tendency is also present but the Strahl is generally stronger and the decrease of its relative density with distance is slower. Associated with this phenomenon, the Strahl PAW is observed to increase with distance (Hammond et al., 1996; Graham et al., 2017; Bercic et al., 2019), which is named Strahl broadening. It is therefore assumed that the Strahl electrons are diffused in pitch angle and become halo electrons.

Figure 1.5 shows the difference between the predictions of a simple exospheric model (in red) and observations (in blue and green). This figure was obtained by Bercic et al. (2019) using Helios data between 0.3 and 1 AU; the point at 0.16 AU is a linear extrapolation of the observations. The observations are classified according to the core electron $\beta_{\mathrm{ec}||}$ parallel

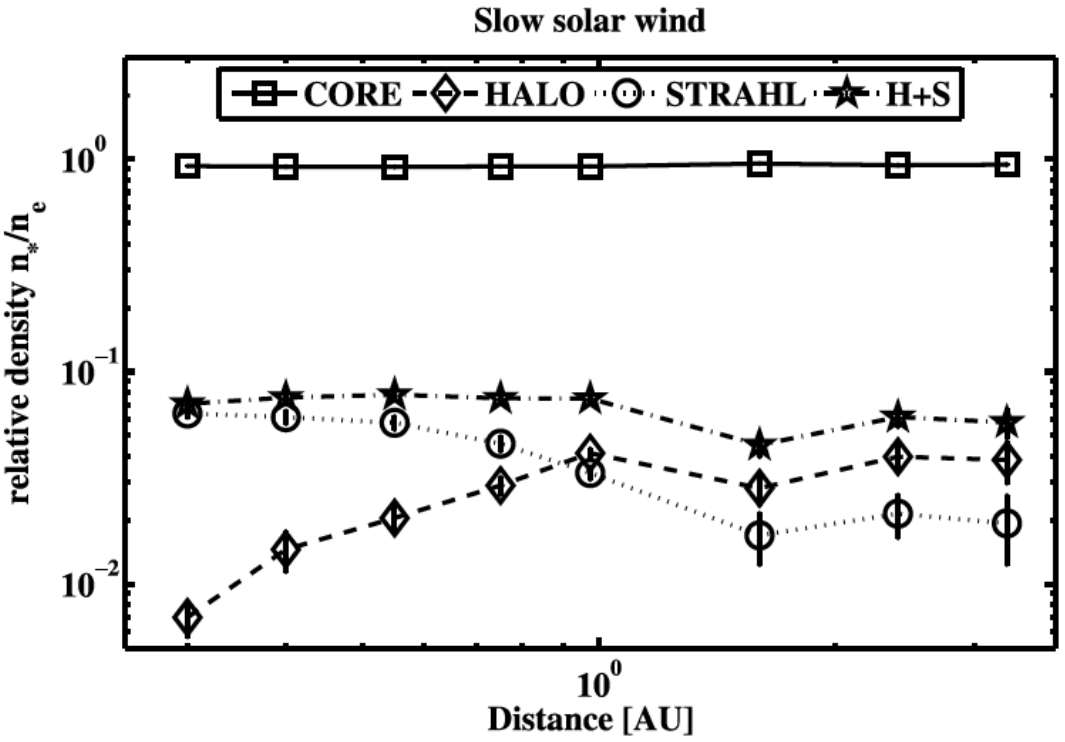

Figure 1.4: Evolution of the relative density of the different electron populations in the slow solar wind as a function of the heliocentric distance. Figure taken from Štverák et al. (2009).

value. The latter represents the ratio of the parallel thermal pressure of the core electrons to the magnetic pressure. The most notable feature is that for both $\beta_{ec||} < 0.2$ and $\beta_{ec||} > 0.4$, there is a very significant discrepancy between the simple exospheric model, which predicts a Strahl focus along field lines, and observations. We also notice that the observed PAW depends rather weakly on the energy for $\beta_{ec||} > 0.4$ (second line), while for $\beta_{ec||} < 0.2$ (first line) the PAW increases with energy. We can note that a correlation between PAW and energy was found by Pagel et al. (2007), while an anti-correlation was found by Feldman et al. (1978), Pilipp et al. (1987b), and Kajdič et al. (2016).

It is therefore necessary to call upon other mechanisms than the ones included in these models to explain the evolution of the distribution function at higher suprathermal energies. These mechanisms seem to be more efficient or more present in the slow solar wind and must explain the continuous diffusion in pitch angle of the Strahl and the increase of the halo relative density. Macneil et al. (2020) showed that the Strahl PAW is larger during measurements in which the Strahl is sunward directed. This configuration can appear in the case of switchbacks (with a change of sign of the radial component of the background magnetic) which are localized deflections of the background magnetic field (Bale et al., 2019; Kasper et al., 2019; Dudok De Wit et al., 2020; Krasnoselskikh et al., 2020; Agapitov et al., 2022). The sunward-directed Strahl electrons follow the magnetic field lines and thus

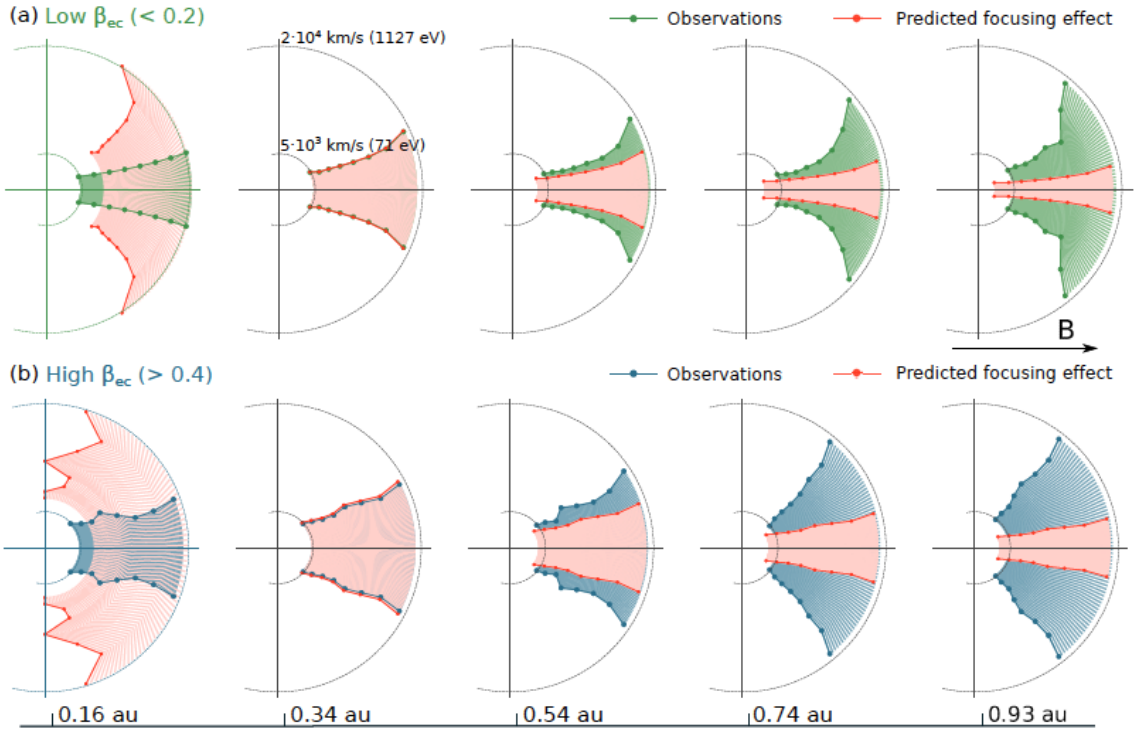

Figure 1.5: Comparison of the radial evolution of the Strahl PAW predicted by a simple exospheric model (in red), with that observed in a solar wind with $\beta_{ec||} < 0.2$ (first line in green) and with a $\beta_{ec||}$ (second line in green). Figure taken from Bercic et al. (2019).

travel more distance. This suggests that the mechanism responsible for diffusion is relatively constant along the propagation. Finally, as can be seen in Figure 1.5, the Strahl PAW is larger for high $\beta_{\mathrm{ec}||}$. The latter is an important parameter that favors instabilities in the solar wind. It is therefore an indication that wave-particle interactions (not taken into account in most current kinetic models) can explain the observations.

1.4.2 Heat flux regulation

As mentioned in Section 1.2.2, the solar wind heat flux decreases with the heliocentric distance (Feldman et al., 1978; Scime et al., 1994; Štverák, Trávníček, and Hellinger, 2015; Halekas et al., 2021a; Pierrard, Lazar, and Stverak, 2022). The observed decrease is in $r^{-\mathrm{a}}$ with a between 3 and 2.4 (Scime et al., 1994; Halekas et al., 2021a). Štverák, Trávníček, and Hellinger (2015), using Helios data between 0.3 and 1 AU, found that this coefficient is about 2.84 in the slow wind and 2.44 in the fast wind.
We first consider the case of a free expansion and then the fully collisional case and show that neither model succeeds in describing this decrease.

1.4.2.1 Free expansion

We first study the case of free expansion, which means that there is no collision or interaction between ions and electrons (the interplanetary electrostatic potential is therefore neglected). In this case, the heat flux decreases as r^{-2} near the Sun and as r^{-1} far from the Sun (Scime et al., 1994). Indeed, with a free expansion, there is a conservation of the total heat flux power emanating from the Sun: Q (W). By considering first a purely radial background magnetic field we have (Scime et al., 1994):

$$\iint_S \vec{q}_{\mathrm{e}||} d\vec{S} = 4\pi r^2 q_{\mathrm{e}||} = Q \tag{1.11}$$

where $q_{\mathrm{e}||}$ therefore decreases as r^{-2} with distance. Then, by considering the background magnetic field lines according to the Parker spiral model, one can show that (Scime et al., 1994):

$$q_{\mathrm{e}||}(r) = \frac{Q}{4\pi r^2}\sqrt{1 + (\frac{r\omega_{\mathrm{rot}}}{V_{\mathrm{SW}}})} \tag{1.12}$$

where ω_{rot} is the Sun's angular velocity. In that case, there is a decrease of $q_{\mathrm{e}||}$ as r^{-2} near the Sun and in r^{-1} far from the Sun, that is to say too slow with respect to the observations. It is therefore necessary to introduce a heat flux dissipation mechanism. This mechanism can be collisions or wave-particle interactions. In the following section, we address the collisional case.

1.4.2.2 Collision limited heat flux

A fully collisional closure relationship that keeps the total energy of the electron distribution function constant can be expressed as:

$$q_{\mathrm{eSH||}} = -\kappa_{\mathrm{SH||}} \nabla_{||} T_{\mathrm{e}} \tag{1.13}$$

where $\kappa_{\mathrm{SH||}}$ is the electron thermal conductivity. This conductivity is taken equal to the Spitzer and Harm conductivity $\kappa_{\mathrm{SH||}} = \frac{3.2 n_{\mathrm{e}} k_{\mathrm{B}}^2 T_{\mathrm{e}}}{m_{\mathrm{e}} \nu_{\mathrm{ee}}}$ for a hot plasma (Spitzer and Härm, 1953), with ν_{ee} the collisional frequency for transport phenomena. Equation 1.13 is valid if the electron distribution function is close to a Maxwellian, which is equivalent to assuming a low Knudsen number.
Since the temperature is observed to decrease with the distance as $T_{\mathrm{e}} \propto r^{-\alpha_T}$ (Scime et al., 1994; Štverák, Trávníček, and Hellinger, 2015), $\frac{\partial T_{\mathrm{e}}}{\partial r} \propto -\alpha_T T_{\mathrm{e}}/r$ and (Salem et al., 2003):

$$q_{\mathrm{eSH||}} = 3.2 \alpha_{\mathrm{T}} \frac{n_{\mathrm{e}} k_b^2 T_{\mathrm{e}}^2}{m_{\mathrm{e}} \nu_{\mathrm{ee}} r} \tag{1.14}$$

The heat flux can be normalized by the saturation heat flux, expressed as $q_0 = \frac{3}{2} n_{\mathrm{e}} k_b T_{\mathrm{e}} v_{\mathrm{the}}$. By using the definition of the mean free path $L_{\mathrm{fp}} = v_{\mathrm{the}}/\nu_{\mathrm{ee}}$ and of the temperature gradient $L_{\mathrm{T}} = T_{\mathrm{e}}/|\frac{\partial T_{\mathrm{e}}}{\partial r}| = r/\alpha_T$ one can deduce that the normalized heat flux q_{nSH} is expressed as (Salem et al., 2003; Bale et al., 2013):

$$q_{\mathrm{nSH}} = \frac{q_{\mathrm{eSH||}}}{q_0} \simeq 1.07 \frac{L_{\mathrm{fp}}}{L_{\mathrm{T}}} = 1.07 K_{\mathrm{n}} \tag{1.15}$$

The applicability of this approach can therefore be verified by choosing a coefficient α_T and by checking experimentally the validity of Equation 1.15. Bale et al. (2013) showed that for Knudsen numbers larger than 0.28 the normalized heat flux is no longer proportional to the Knudsen number as predicted by Equation 1.15. This was recently confirmed by Halekas et al. (2021a) by using Parker Solar Probe observations. Indeed, as can be seen in Figure 1.6, they showed by using a temperature law more consistent with the observed one ($\alpha_T = 0.5$, instead of $\alpha_T = 2/7$ for Bale et al. (2013)) that the observed normalized heat flux is always smaller than the one predicted by Equation 1.15. Measurements by Halekas et al. (2021a) are consistent with fully kinetic simulations including collisions by Landi, Matteini, and Pantellini (2014) and theoretical work by Shoub (1983) and Scudder and Karimabadi (2013) showing that Equation 1.13 is in fact invalid for Knudsen numbers larger than 0.01.
We can finally note that Scime et al. (1994) showed that the use of Equation 1.13 gives a too rapid decay (in $r^{-4.6}$) and heat flux values that are significantly larger than the observations for $r < 1\ AU$.

It is therefore clear that a purely collisional mechanism alone cannot explain the heat flux decay. Halekas et al. (2021a) showed that the dissipation of the heat flux is more important when β_e is large, which is an indication that a collisionless mechanism such as wave-particle interactions could be regulating the heat flux. On the other hand, fully kinetic simulations

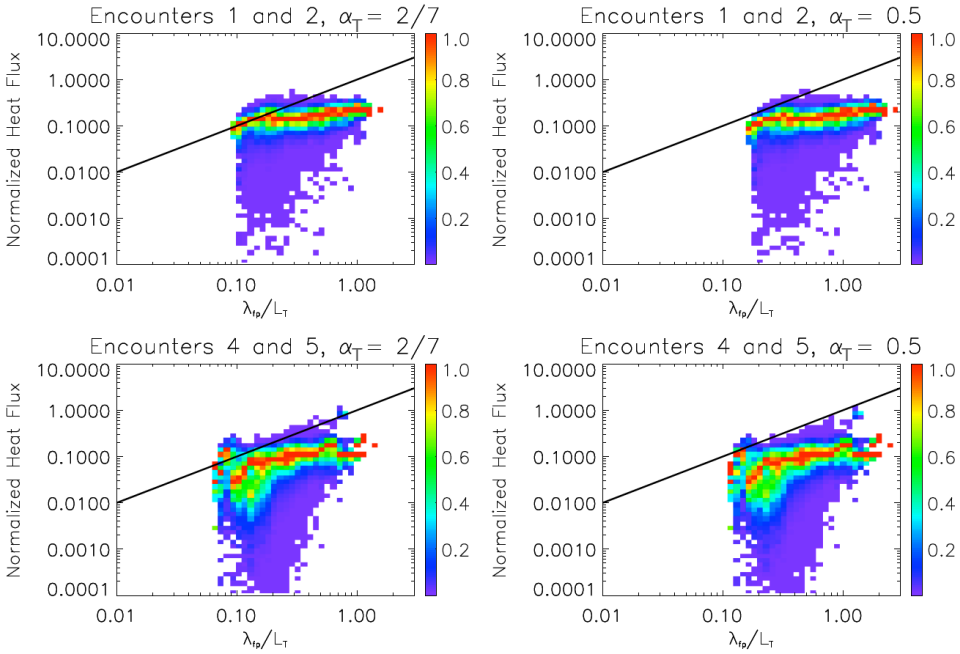

Figure 1.6: Comparison between the normalized heat flux predicted by Equation 1.15 (black lines) and the observations of Parker Solar probe during Encounters 1 and 2 (first line) and Encounters 3 and 4 (second line) using $\alpha_T = 2/7$ (first column) and $\alpha_T = 0.5$ (first column) (colorbars). Figure taken from Halekas et al. (2021a).

by Landi, Matteini, and Pantellini (2014), which take into account binary Coulomb collisions between particles and calculate the ambipolar electric field in a self-consistent manner, call into question the need to invoke wave-particle interactions to explain the evolution of the heat flux. Indeed, these simulations do not include particle-wave interactions but produce a heat flux in agreement with the observations of Bale et al. (2013) at 1 AU. This would indicate that taking into account binary Coulomb collisions between particles and the ambipolar electric field would be sufficient to explain the decrease in heat flux.
We can finally remark that the heat flux dissipation is a subject of interest in other astrophysical contexts such as hot gases in galaxy clusters, clouds within supernovas, and accretion flows (Cowie and McKee, 1977; Roberg-Clark et al., 2018).

1.5 Conclusions of Chapter 1

We have examined two major unsolved features concerning the evolution of electrons in the solar wind: the Strahl broadening (Section 1.4.1) and the heat flux regulation (Section 1.4.2). These problems are related since the Strahl carries a significant proportion of the heat flux. We have shown that current models based on adiabatic expansion or that take collisions into account are unable to reproduce the observations correctly. These models do not include the interaction of the waves that propagate in the solar wind with the particles. While, as will be detailed in the next chapters, it is clear that many waves are present in the solar wind and can interact effectively with electrons.
In particular, whistler waves have been commonly observed in the solar wind since their first measurements by the Helios spacecraft (Gurnett and Anderson, 1977; Neubauer, Musmann, and Dehmel, 1977). As detailed in the next chapter, these waves are a good candidate for answering, at least in part, the unsolved features mentioned in this chapter.

1.6 Résumé en français du chapitre 1

Dans ce premier chapitre, nous présentons tout d'abord brièvement les principales caractéristiques du vent solaire. Ce dernier est un flux permanent et turbulent de particules chargées constituant un plasma. Ce plasma provient de l'expansion de la couronne solaire, qui est une couche très chaude de l'atmosphère solaire (1 à 2 MK). On peut distinguer deux types de vent solaire. Le vent rapide (vitesse supérieure à 500 km/s) est généralement ténu, relativement homogène, Alfvénique et provient de trous coronaux. Le vent solaire lent est plus dense, très variable et son origine est encore débattue. Ce flux de particules accéléré à des vitesses supersoniques se compose principalement d'électrons, de protons, de quelque pour cent (en densité) de particules alpha et de très faible proportions d'ions lourds. Ce sont les électrons et notamment l'évolution de leurs fonctions de distribution avec la distance au Soleil qui constituent le point d'intérêt principal de cette thèse.

Il est courant de classer les populations d'électrons en trois catégories, sur la base des fonctions de distribution de vitesse observées. Les électrons thermiques du cœur sont présents à basses énergies, sont affectés par les collisions Coulombiennes et ont donc des distributions proches de fonctions Maxwelliennes. Les électrons suprathermiques du halo ont des énergies plus élevées et sont souvent modélisés par des distributions de type kappa. Le Strahl est un faisceau d'électrons de haute énergie qui suit les lignes de champ magnétique, en s'éloignant du Soleil. Dans le repère du vent solaire, ces populations ont des vitesses de dérive le long du champ magnétique. Le cœur a une vitesse de dérive vers le Soleil tandis que le halo et le Strahl ont une vitesse de dérive anti-solaire. Ces vitesses de dérive satisfont la condition de courant nul.

Les électrons étant les particules les plus légères du vent solaire, ils transportent donc la majeure partie du flux de chaleur. Le flux de chaleur est le troisième moment de la fonction de distribution, il est transporté par les électrons suprathermiques et il est dû aux vitesses de dérive. Le flux de chaleur est une quantité importante dans le vent solaire, car il contribue à l'équilibre énergétique entre le vent solaire et la couronne.

Plusieurs modèles théoriques ont permis de comprendre, au moins en partie, d'importants mécanismes du vent solaire, comme son processus d'accélération. On peut citer en particulier les modèles cinétiques exosphériques. Les protons sont plus lourds que les électrons et sont donc soumis à une force gravitationnelle plus importante. Dans les modèles cinétiques, pour assurer la quasi-neutralité, un champ électrique qui accélère les protons et ralentit les électrons doit donc exister. Ce champ électrique, appelé champ électrique ambipolaire est calculé en assurant la quasi-neutralité et un courant nul à chaque distance.

En revanche, ces modèles ne permettent pas d'expliquer deux phénomènes qui sont encore mal compris. Tout d'abord, les observations montrent que la largeur angulaire du Strahl augmente avec la distance au Soleil. Au contraire, les modèles exosphériques prédisent une focalisation des électrons le long des lignes de champ. Cette focalisation provient de la

conservation de l'énergie et du premier invariant adiabatique alors que la norme du champ magnétique diminue avec la distance. De plus, les modèles exosphériques ne permettent pas d'expliquer l'origine des électrons du halo. On observe pourtant que la densité relative de cette population augmente avec la distance, associée à une décroissance de la densité relative des électrons du Strahl. Cela suggère l'existence d'un mécanisme qui diffuse les électrons du Strahl en pitch angle et forme le halo. On peut noter qu'il a été montré que les collisions Coulombiennes (négligées dans les modèles exosphériques) ne permettent pas d'expliquer la diffusion du Strahl et du halo pour les électrons suffisamment énergétiques ($\gtrsim$ 250 eV). De plus, les mesures du flux de chaleur montrent qu'il décroît plus rapidement que ce que prédisent les modèles exosphériques et trop lentement par rapport aux prédictions des modèles purement collisionnels.

L'augmentation de la largeur angulaire du Strahl et la régulation du flux de chaleur constituent deux questions ouvertes. Il est très probable que la prise en compte des interactions ondes-particules soit nécessaire pour régler, au moins en partie, ces difficultés. En particulier, les ondes de sifflement (whistler waves) ont été couramment observées dans le vent depuis leurs premières mesures par la sonde Helios. Comme nous le verrons en détail dans le chapitre suivant, ces ondes sont un bon candidat pour répondre à ces deux questions.

Chapter 2

Interactions between whistlers and particles in the solar wind, theory and state of the art

In this chapter, we review the state of the art on the potential role of whistler waves in the two open questions raised in Chapter 1. As will be explained in detail, using cold plasma theory one can show that whistlers are right-hand polarized electromagnetic modes propagating between the lower hybrid frequency ($f_{\rm lh}$) and electron cyclotron frequency $f_{\rm ce}$. These waves are commonly observed in the solar wind (Gurnett and Anderson, 1977; Neubauer, Musmann, and Dehmel, 1977; Lacombe et al., 2014; Tong et al., 2019a; Cattell et al., 2020; Kretzschmar et al., 2021; Froment et al., 2023). We first present some theoretical frameworks for describing waves, especially whistler waves in a plasma (Section 2.1) and their interactions with particles (Section 2.2). We explain the choice of models made in this thesis. We then review the various instabilities that can generate whistler waves in the solar wind and their potential interactions with suprathermal electrons (Section 2.3). The role of these waves in diffusing suprathermal electrons, between 10 $R_\odot$ ($\simeq$ 0.047 AU) and 1 AU, is the main subject of study of this thesis. Finally, we present the problematic and the plan of this manuscript (Section 2.4).

2.1 Linear theory

In linear theory, perturbations are assumed to be small, so that the system is only slightly affected. Therefore, the perturbations $\vec{A_1}(\vec{r},t)$ of a quantity $\vec{A}(\vec{r},t)$ of the system will verify $A_1 \ll A$. $\vec{A}(\vec{r},t)$ is decomposed as $\vec{A}(\vec{r},t) = \vec{A_0} + \vec{A_1}(\vec{r},t)$, where $\vec{A_0} = <\vec{A}(\vec{r},t)>$ is averaged over time or space. Furthermore, if a perturbation is a solution of a dispersion equation (as will be detailed later) and if its amplitude is large compared to the thermal noise level of the plasma, it can be considered a wave perturbation. The low amplitude of the wave perturbation makes it possible to assume that the plasma response to the perturbation is linear. The wave perturbation can therefore be represented as a plane waves sum: $\vec{A_1}(\vec{r},t) = \sum_{\vec{k}} \vec{A}_{1\vec{k}}(\vec{k},\omega)\exp(i\vec{k}\cdot\vec{r} - i\omega t)$, $\vec{k}$ being the wavevector and ω the frequency (Stix, 1992; Gary,

1993). Thus, using Maxwell's equations one can show that there is a linear relation between the current $\vec{J}_{1\vec{k}}$ and the electric field $\vec{E}_{1\vec{k}}$ (linked by the conductivity tensor $\sigma_{ij}(\vec{k},\omega)$, Ohm's law) and can derive the general dispersion relation (Stix, 1992):

$$[k^2c^2\delta_{\rm ij} - c^2k_{\rm i}k_{\rm j} - \omega^2\varepsilon_{\rm ij}(\vec{k},\omega)]E_{1\vec{k}{\rm j}}(\vec{k},\omega) = 0 \tag{2.1}$$

where $\delta_{\rm ij}$ is the identity matrix and $\varepsilon_{\rm ij} = \bar{\bar{\varepsilon}}$ is the tensor of dielectric conductivity:

$$\varepsilon_{\rm i,j}(\vec{k},\omega) = \delta_{\rm i,j} + \frac{i}{\omega\varepsilon_0}\sigma_{i,j}(\vec{k},\omega) \tag{2.2}$$

with ε_0 the vacuum permittivity. Solutions of Equation 2.1 are the modes propagating in the plasma. To find these modes, it is necessary to know the $\varepsilon_{\rm ij}$ tensor, which depends on the model chosen for the plasma. This model can be: one-fluid magnetohydrodynamic, multi-fluid, or kinetic.

2.1.1 Cold electrons model

At low frequencies, verifying $\omega << (\omega_{\rm ci}, \omega_{\rm pi})$ where $\omega_{\rm ci} = \frac{eB_0}{m_{\rm i}}$ is the proton cyclotron frequency ($m_{\rm i}$ is the mass of a proton) and $\omega_{\rm pi} = \sqrt{\frac{n_{\rm i}e^2}{m_{\rm i}\varepsilon_0}}$ is the proton plasma frequency, the one-fluid magnetohydrodynamic theory is valid and electron inertia can safely be neglected. In the following, we are mainly interested in whistler waves, which are electronic waves and therefore can not be described by the magnetohydrodynamic.
To describe these waves, we first adopt a fluid model. Moreover, since whistlers verify $\omega >> (\omega_{\rm ci}, \omega_{\rm pi})$ (Lacombe et al., 2014; Tong et al., 2019a; Kretzschmar et al., 2021; Froment et al., 2023) the ions do not have the time to react to the perturbation and constitute only a neutralizing background. For a plasma composed solely of protons and electrons, to neglect the ion motion, it is also necessary that $\theta < \arccos f_{\rm lh}/f_{\rm ce} \sim 88.7°$, θ being the angle between the background magnetic field $\vec{B}_0$ and the wave vector $\vec{k}$ (or Wave Normal Angle: WNA) (Artemyev et al., 2016). As shown in Chapters 4 and 5, this condition is valid for the observed whistler waves. We can also note that in the oblique limit ($\cos\theta \lesssim \frac{m_{\rm e}}{m_{\rm p}}$), protons are not negligible and the waves propagate in the lower-hybrid regime (Verscharen et al., 2019).
Finally, we take a cold plasma model, which means that we neglect the electron pressure due to the electron temperature. This means neglecting the effect of thermal particle motion on wave propagation. Formally, for this approximation to be valid, the frequency of the wave must not be close to the electron cyclotron frequency and the phase velocity of the wave must be high compared to the thermal velocity of the particles. This last condition is not met in the solar wind. However, Akhiezer et al. (1975) and Artemyev et al. (2016) have shown that thermal corrections are negligible for whistler waves when the propagation angle is less than the resonance cone angle: $\cos^2\theta_{\rm r} = \frac{\omega}{\omega_{\rm ce}}^2\left(1 + \frac{\omega_{\rm ce}^2-\omega^2}{\omega_{\rm pe}^2}\right)$. Previous studies of these waves have shown that $\theta_{\rm r} \gtrsim 85°$ (Cattell et al., 2020; Kretzschmar et al., 2021; Froment et al., 2023), therefore thermal corrections are negligible for the observed whistler waves. The cold electron model is therefore applicable, and solar wind whistler waves are expected to have

right-hand circular polarization (Artemyev et al., 2016).
This cold electrons model allows us to easily obtain the dispersion relation of whistler waves.

According to the assumptions mentioned above, the conservation equations of mass and momentum are written, in the non-relativistic case as (Stix, 1992):

$$\frac{\partial n_{\mathrm{e}}}{\partial t} + \nabla \cdot (n_{\mathrm{e}} \vec{v_{\mathrm{e}}}) = 0 \tag{2.3}$$

$$\frac{\partial \vec{v_{\mathrm{e}}}}{\partial t} + (\vec{v_{\mathrm{e}}} \cdot \nabla)\vec{v_{\mathrm{e}}} = \frac{-e}{m_{\mathrm{e}}}(\vec{E} + \vec{v_{\mathrm{e}}} \wedge \vec{B}) \tag{2.4}$$

where v_{e} is the bulk velocity of the electrons. By linearizing these equations (with $\vec{E_0} = \vec{0}$ and $\vec{v_{\mathrm{e}0}} = \vec{0}$) and using Equation 2.1, we obtain the following dielectric tensor:

$$\varepsilon_{\mathrm{ij}} = \begin{pmatrix} \varepsilon_1 & i\varepsilon_2 & 0 \\ -i\varepsilon_2 & \varepsilon_1 & 0 \\ 0 & 0 & \varepsilon_3 \end{pmatrix} \tag{2.5}$$

where
$\varepsilon_1 = (1 - \frac{\omega_{\mathrm{pe}}^2}{\omega^2 - \omega_{\mathrm{ce}}^2}); \varepsilon_2 = \frac{\omega_{\mathrm{pe}}^2 \omega_{\mathrm{ce}}}{\omega(\omega^2 - \omega_{\mathrm{ce}}^2)}; \varepsilon_3 = 1 - \frac{\omega_{\mathrm{pe}}^2}{\omega^2}; \omega_{\mathrm{ce}} = \mid \frac{eB_0}{m_{\mathrm{e}}} \mid$
and $\varepsilon_{\mathrm{ij}}$ is expressed in the reference frame where $\vec{B_0}$ is directed along the $\vec{z}$ axis.
We can then make the high-density assumption: $\omega_{\mathrm{pe}}^2 \gg \omega_{\mathrm{ce}}^2 > \omega^2$. Indeed, extrapolation of Helios data (between 0.3 and 1 AU, Bale et al., 2016) shows that the expected $\omega_{\mathrm{pe}}^2/\omega_{\mathrm{ce}}^2$ is around 150 at 10 $R_\odot$ ($\simeq$ 0.05 AU). This ratio increases with distance, indicating that this assumption should be valid for all our measurements. Thus, these expressions may be simplified as follows:

$\varepsilon_1 = -\frac{\omega_{\mathrm{pe}}^2}{\omega^2 - \omega_{\mathrm{ce}}^2}; \varepsilon_2 = \frac{\omega_{\mathrm{pe}}^2 \omega_{\mathrm{ce}}}{\omega(\omega^2 - \omega_{\mathrm{ce}}^2)}; \varepsilon_3 = -\frac{\omega_{\mathrm{pe}}^2}{\omega^2}$
The solution of the system is well known and may be found in the following equation (Stix, 1992):

$$AN^4 + BN^2 + C = 0 \tag{2.6}$$

where $N^2 = (\frac{kc}{\omega})^2$ and:

$$A = \varepsilon_1 \sin^2\theta + \varepsilon_3 \cos^2\theta = -\frac{\omega_{\mathrm{pe}}^2 \sin^2\theta}{\omega^2 - \omega_{\mathrm{ce}}^2} - \frac{\omega_{\mathrm{pe}}^2 \cos^2\theta}{\omega^2} = -\frac{\omega_{\mathrm{pe}}^2(\omega^2 - \omega_{\mathrm{ce}}^2 \cos^2\theta)}{\omega^2(\omega^2 - \omega_{\mathrm{ce}}^2)}$$

$$B = -\varepsilon_1\varepsilon_3(1 + \cos^2\theta) - (\varepsilon_1^2 - \varepsilon_2^2)\sin^2\theta = -\frac{2\omega_{\mathrm{pe}}^4}{\omega^2(\omega^2 - \omega_{\mathrm{ce}}^2)}$$

$$C = \varepsilon_3(\varepsilon_1^2 - \varepsilon_2^2) = -\frac{\omega_{\mathrm{pe}}^6}{\omega^4(\omega^2 - \omega_{\mathrm{ce}}^2)}$$

One can find for whistler waves:

$$N^2 = \frac{\omega_{\rm pe}^2}{\omega(\omega_{\rm ce} \mid \cos\theta \mid -\omega)}$$

$$\omega = \omega_{\rm ce} \mid \cos\theta \mid \frac{\frac{k^2c^2}{\omega_{\rm pe}^2}}{(1+\frac{k^2c^2}{\omega_{\rm pe}^2})} \tag{2.7}$$

Equation 2.7 corresponds to the dispersion relation for whistler waves in the cold electron approximation. Taking ions into account, the cold plasma dispersion relation can be written as (Lyons, 1974b; Stix, 1992):

$$N^2 = \left(\frac{\omega_{\rm pe}}{\omega_{\rm ce}}\right)^2 \frac{1+M}{M}\Psi^{-1} \tag{2.8}$$

where $M = m_{\rm e}/m_{\rm i}$ and Ψ is given by the following equation :

$$\Psi = 1 - \frac{\omega^2}{\omega_{\rm ci}\omega_{\rm ce}} - \frac{\sin^2(\theta)}{2} + \sqrt{\frac{\sin^4(\theta)}{4} + \left(\frac{\omega}{\omega_{\rm ci}}(1-M)\cos(\theta)\right)^2} \tag{2.9}$$

The cold electron fluid model allows us to obtain a simple dispersion relation for whistler waves. However, it does not enable us to describe correctly the interactions between these waves and the electrons. Indeed, whistler waves are generated by instabilities, which are normal modes of the plasma that grow in space or in time. An instability implies a well-defined relation between ω and k and that the linear theory can be applied. There are macro-instabilities that affect the plasma as a whole that can be modeled with the fluid theory, however, micro-instabilities that affect the distribution function have to be modeled by the kinetic theory. When one is interested in the interactions of waves with suprathermal populations like the Strahl and the halo, one needs to use kinetic theory.

2.1.2 Kinetic theory

This section briefly describes how kinetic theory can be used to describe instabilities.
The kinetic model is based on Boltzmann's equation (1.8) and Maxwell's equations. In a collisionless plasma, a Fourier or Laplace transformation can be applied to Vlasov's equation. Then, using Maxwell's equations it is possible to obtain a dispersion relation. The dispersion equation is often solved using the initial value problem, that is, by taking $\vec{k}$ real and by solving for $\omega = \omega_r + i\gamma$ (where ω_r and γ are the complex and real parts of ω, respectively (Gary, 1993)). For waves propagating at an arbitrary angle θ with respect to the background magnetic field, this analytic procedure can be cumbersome.
Kennel and Wong (1967) have derived an expression for the linear wave growth rate (γ) of an arbitrary plasma wave having an arbitrary angle of propagation:

$$\frac{\gamma}{\omega} = \sum_n (\frac{\omega_{\rm pe}}{\omega})^2 \frac{\pi}{8n_{\rm e}} \int_0^\infty v_\perp^2 dv_\perp \int_{-\infty}^\infty dv_{||}\delta(v_{||} - \frac{\omega + n\omega_{\rm ce}}{k_{||}}) \frac{\Theta_{{\rm n}\vec{k}}}{W_{\vec{k}}} \hat{G} f_0 \tag{2.10}$$

where δ is the Dirac delta function and f_0 is the electron distribution function. In the following, unless otherwise stated, we are interested in the electron distribution function. $W_{\vec{k}}$ is the total energy of the wave and $\Theta_{\mathrm{n}\vec{k}}$ is the polarization of the electric field:

$$\Theta_{\mathrm{n}\vec{k}} = [\frac{E_{1\vec{k},\mathrm{L}} J_{\mathrm{n}-1} + E_{1\vec{k},\mathrm{R}} J_{\mathrm{n}+1}}{\sqrt{2}} - \frac{v_{||}}{v_{\perp}} E_{1\vec{k},||} J_{\mathrm{n}}]^2 \tag{2.11}$$

where $E_{1\vec{k},\mathrm{R}}$, $E_{1\vec{k},\mathrm{L}}$, $E_{1\vec{k},||}$ are the right-hand, the left-hand and the parallel polarized parts of the electric field, respectively. J_{n} is the Bessel function of argument $\frac{k_{\perp} v_{\perp}}{\omega_{\mathrm{ce}}}$ and

$$\hat{G} = \big((\frac{\omega}{k_{||}} - v_{||})\frac{\partial}{\partial v_{\perp}} + v_{\perp}\frac{\partial}{\partial v_{||}}\big) \tag{2.12}$$

This last term is discussed in detail in the next section. To obtain Equation 2.10, the plasma is supposed spatially homogeneous and the background magnetic field uniform. Moreover, as shown by the presence of the δ function, only resonant electrons, that is, those satisfying Equation 2.13, are taken into account:

$$\omega + n\omega_{\mathrm{ce}} = v_{||} k_{||} \tag{2.13}$$

where n is the order of resonance. For $n = 0$ (Landau resonance), Equation 2.13 corresponds to electrons having a resonance velocity $v_{\mathrm{res}||}$ equal to the wave's parallel phase velocity. For orders $n \neq 0$, this corresponds to electrons having a frequency in the wave reference frame that is a harmonic of the cyclotron frequency. It can be assumed that wave-particle interactions occur only at resonances when the wave is of low amplitude (as described above) and its growth rate verifies $\gamma \ll \omega$ (Lyons and Williams, 1984; Shprits et al., 2008; Shklyar and Matsumoto, 2009; Artemyev et al., 2016). This is equivalent to neglecting non-resonant and non-linear interactions. Furthermore, the effect of particles propagating perfectly perpendicular to the magnetic field ($k_{||} = 0$) is not properly described. Equation 2.10 is described further in Section 2.2.2.

In this section, we have shown how linear theory can be used to describe waves in the solar wind. We first used a cold electron model to derive the dispersion relation of whistler waves. Then we presented how growth rates of micro-instabilities can be calculated using the kinetic theory. As explained in Section 1.2 the electron distribution function in the solar wind has suprathermal populations. Moreover, electron populations can have drifts and anisotropies. All these elements constitute possible sources of free energy that can create instabilities. The different instabilities that can generate whistler waves in the solar wind are presented in Section 2.3.

On the other hand, the linear theory can not describe the process of saturation of the instability since if $\gamma \geq 0$ there is an exponential increase of the perturbations. This is due to the fact that linear theory does not take into account the effect of perturbations on the equilibrium distribution function f_0. Mathematically, this translates into a non-dependence of $f_0(\vec{v})$ on time. Indeed, using linear theory it is classical to write $f(\vec{r}, \vec{v}, t) =$

$f_0(\vec{r},\vec{v}) + f_1(\vec{v},\vec{r},t)$, with $|f_1| \ll f_0$ (meaning that the perturbations around the background distribution are small). In order to model the effect of the waves on the distribution function and the saturation of the instability we use the quasi-linear theory.

2.2 Quasi-linear theory

2.2.1 Hypothesis

The quasi-linear theory (QLT) can be used to describe wave-particle interactions if wave energy is both much lower than the thermal energy of the particles and much higher than the thermal noise energy (Vedenov, 1963; Yakimenko, 1963). Kennel and Engelmann (1966) used QLT to derive the diffusion equation of zeroth-order particle distribution function in the velocity space, in a magnetized plasma, for any oscillation branch propagating at an arbitrary angle θ. In their calculations, the plasma was considered non-relativistic, uniform, collisionless, and immersed in a constant, non-curved, and infinite background magnetic field. The amplitude of the waves that are supposed to be randomly self-excited (not correlated in phase) is assumed to be small. Specifically, the effect of waves on the distribution function is slow (slow variation with respect to the wave period) and their growth rates must verify $\gamma \ll \omega$. This small amplitude allows us once again to split the physical quantities into slow and fast varying parts. In particular, $f(\vec{v},\vec{r},t)$ is decomposed into $f(\vec{v},\vec{r},t) = f_0(\vec{v},t) + f_1(\vec{v},\vec{r},t)$, where $f_0(\vec{v},t)$ depends slowly on time (with respect to the wave frequency). Because $f_0(\vec{v},t)$ depends on time the saturation of the instability can be described. The saturation process is the evolution of the distribution function caused by the waves to eliminate the sources of free energy. Finally, $f_0(\vec{v},t)$ is assumed to depend weakly on the azimuth around $\vec{B}_0$ (Kennel and Engelmann, 1966) and the nonlinear coupling between modes is neglected. $f_0(\vec{v},t)$ is defined explicitly as $f_0(\vec{v},t) = \lim_{V\to\infty} \frac{1}{V} \int f(\vec{v},\vec{r},t) d^3\vec{r}$ (where V is the volume of integration).

2.2.2 Diffusion equation

The method (rather calculatory, described in detail in Kennel and Engelmann (1966)) to determine the temporal variations of $f_0(\vec{v},t)$ is the following. We take Vlasov's equation, at order 1 (in the wave amplitude), assuming that $f_0(\vec{v},t)$ does not depend on time in order to express $f_1(\vec{v},\vec{r},t)$ as a function of $f_0(\vec{v},t)$. Then the space averaged Vlasov's equation at order zero is used to derive the following equation (Kennel and Engelmann, 1966; Lyons and Williams, 1984):

$$\frac{\partial f_0}{\partial t} = \lim_{V\to\infty} \int \frac{d^3\vec{k}}{(2\pi)^3} \frac{\pi e^2}{V m_{\mathrm{e}}^2} \sum_{n=-\infty}^{\infty} [\frac{k_{||}}{\omega}\hat{G} + \frac{\omega - k_{||}v_{||}}{\omega v_\perp}] \delta(k_{||}v_{||} - n\omega_{\mathrm{ce}} - \omega) \Theta_{\mathrm{n}\vec{k}} \frac{k_{||}}{\omega} \hat{G} f_0 \qquad (2.14)$$

We can note that Equation 2.14 has similarities with Equation 2.10. First, they both contain the weighting function $\Theta_{\mathrm{n},\vec{k}}$, which is a coupling term of the wave-particle interactions in the different zones of the velocity space. Moreover, in both equations, we are in the limit

of resonant diffusion (described in Section 2.1.2), and a sum of the considered resonances is realized. It is worth noting that Kennel and Engelmann (1966) have shown using an H-like theorem that whether or not only resonant particles are considered, the waves will force the distribution function in a marginally stable state ($\gamma \to 0$). Finally, these equations both depend on the operator $\hat{G}$ that is applied to f_0, we explain this dependence in the following.

Kennel and Engelmann (1966) proposed a simple physical argument to interpret the expression of $\hat{G}$. By interacting with a particle, the wave loses energy: $\Delta E = -\hbar\omega_k$ (where $\hbar = h/(2\pi)$, with h the Planck constant). The parallel energy gain for the particle is $\Delta E_{||} = m_e v_{||} \Delta v_{||} = \hbar k_{||} v_{||}$, so the total energy gain can be written as: $\Delta E = m_e(v_{||}\Delta_{||} + v_\perp \Delta v_\perp) = \Delta E_{||}\omega_k/(k_{||}v_{||}) = m_e v_{||}\Delta v_{||} * \omega_k/(k_{||}v_{||})$. Therefore we have: $(v_{||} - \omega_k/k_{||})\Delta v_{||} + v_\perp \Delta v_\perp = 0$ (similar to $\hat{G}$) that we can integrate as:

$$(v_{||} - \frac{\omega}{k_{||}})^2 + v_\perp^2 = Cste \tag{2.15}$$

Equation 2.15 defines circles centered on the parallel phase speed $v_{\varphi||} = \frac{\omega}{k_{||}}$ which are called "single-wave characteristics". Particles are forced to move along these circles as they interact with the waves.

Since we are in the resonant limit, only particles with a resonant parallel speed (verifying Equation 2.13) are considered and their motion is equally likely to be in both directions along the single-wave characteristics. If each interaction with the waves causes a small increase in particle energy, their motion can be interpreted as a diffusion process along the single-wave characteristics. In that case, the net flux of particles will be in the direction of the less dense area of the phase space along these circles. One can show that $\hat{G}f_0$ is directly proportional to the gradient of the distribution function, along the single-wave characteristics in the direction of increasing energy in the reference frame $(v_\perp, v_{||})$. Therefore, for a resonant point of the phase space: If $\hat{G}f_0 \geq 0$ the gradient of particles in the direction of increasing energy is positive. In that case, the net particle diffusion will be toward the less dense zone by losing energy which will amplify the wave (and conversely if $\hat{G}f_0 \leq 0$).
To estimate the global amplification or damping of the waves it is necessary to integrate over the perpendicular velocity for each resonance, which explains the integration along $v_\perp$ and the sum over n in Equation 2.10. On the other hand, for Equation 2.14 the integration is over a set of $\vec{k}$ in order to determine the role of all considered waves on the distribution function (Lyons and Williams, 1984).

A schematic representing the particle diffusion in the framework of the QLT is presented in Figure 2.1. The interaction of a wave having a positive phase speed ($\frac{\omega}{k_{||}} > 0$) (with a distribution function described in the caption of Figure 2.1) is shown. The arrows (representing the net particle flux) point upwards, that is, toward the areas of lowest density of the phase space, along the single wave characteristics. Only the resonant electrons are taken into account because all arrows are located on resonant parallel velocities, corresponding

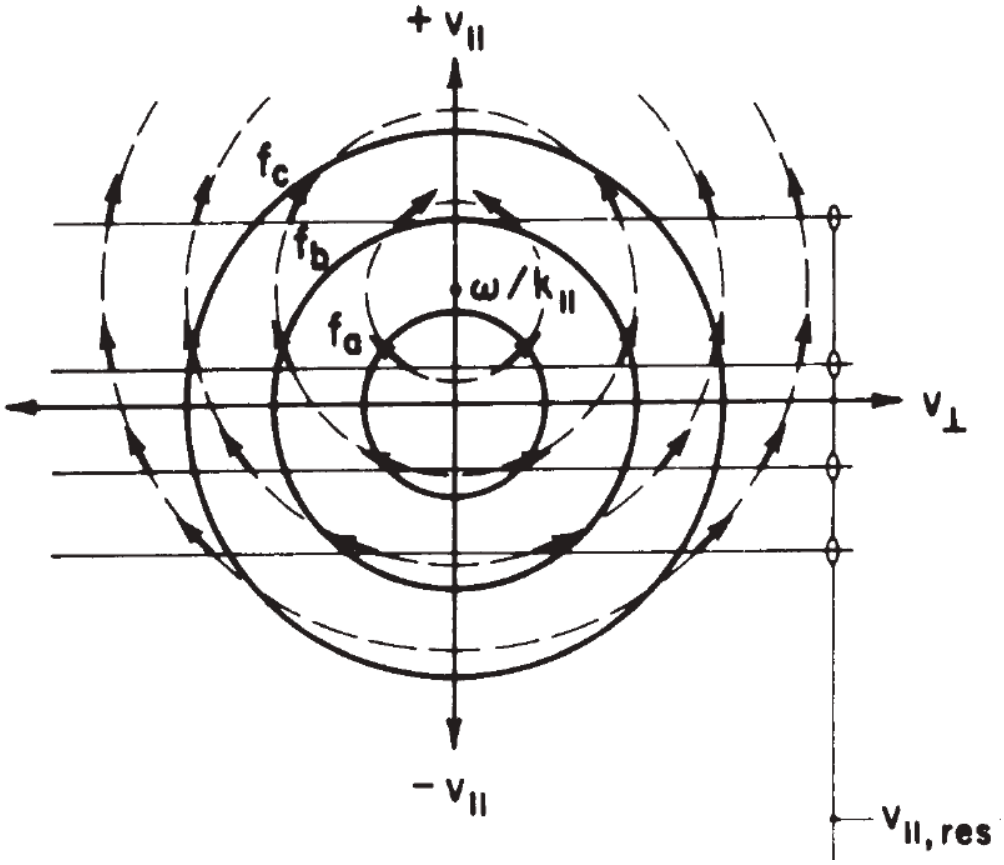

Figure 2.1: Diffusion schematic in the $(v_\perp, v_{||})$ space. Three levels of the distribution function are represented in solid lines, respecting $f_\mathrm{a} > f_\mathrm{b} > f_\mathrm{c}$. The single-wave characteristics are represented in dotted lines. The resonance speeds are represented by horizontal lines. The flux of diffusing particles is represented by arrows. Figure taken from Lyons and Williams (1984).

to different resonance orders. The net particle flux is for each resonance speed toward the direction of increasing energy in the reference frame $(v_\perp, v_{||})$, therefore $\gamma \leq 0$ and the wave is damped.

Finally, it is worth noting that, in the resonant and marginally stable case ($\gamma \to 0$), Kennel and Engelmann (1966) derived a necessary and sufficient condition for the existence of a plateau (in cases where the reconstruction of the distribution function requires finite energy). A plateau corresponds to the asymptotic case in which waves remain ($E_1(\vec{r}, t \to \infty) \neq 0$ and $B_1(\vec{r}, t \to \infty) \neq 0$) despite the fact that there is no more variation and free energy in the distribution function ($\frac{\partial f_0}{\partial t} = 0$). This necessary and sufficient condition is $\hat{G} f_0 = 0$, which means that the function f_0 must be constant (in the velocity space) along the contour defined by $\hat{G}$.

An efficient way to determine the time scale of the diffusion process is to calculate the diffusion coefficients. The work of Lyons, Thorne, and Kennel (1971, 1972) and Lyons (1973) led to the general expression of diffusion coefficients within the framework of linear theory, presented by Lyons (1974a). The derivation of these coefficients is presented in the next section.

2.2.3 Diffusion coefficients

We now express $\hat{G}$ using the variables (α,v) where α is the pitch angle (Lyons, 1974a).

We have $v_{||} = v\cos\alpha$ and $v_\perp = v\sin\alpha$, thus:
$\frac{\partial}{\partial v_\perp} = \sin\alpha\frac{\partial}{\partial v} + \frac{\cos\alpha}{v}\frac{\partial}{\partial\alpha}$
$\frac{\partial}{\partial v_{||}} = \cos\alpha\frac{\partial}{\partial v} - \frac{\sin\alpha}{v}\frac{\partial}{\partial\alpha}$
Therefore:

$$\frac{k_{||}}{\omega}\hat{G} = (1 - \frac{k_{||}v_{||}}{\omega})\frac{\partial}{\partial v_\perp} + \frac{k_{||}}{\omega}v_\perp\frac{\partial}{\partial v_{||}} \tag{2.16}$$

$$\frac{k_{||}}{\omega}\hat{G} = (1 - \frac{k_{||}v_{||}}{\omega})(\sin\alpha\frac{\partial}{\partial v} + \frac{\cos\alpha}{v}\frac{\partial}{\partial\alpha}) + \frac{k_{||}}{\omega}v_\perp(\cos\alpha\frac{\partial}{\partial v} - \frac{\sin\alpha}{v}\frac{\partial}{\partial\alpha}) \tag{2.17}$$

$$\frac{k_{||}}{\omega}\hat{G} = (\frac{\cos\alpha}{v} - \frac{k_{||}}{\omega})\frac{\partial}{\partial\alpha} + \sin\alpha\frac{\partial}{\partial v} \tag{2.18}$$

$$\frac{k_{||}}{\omega}\hat{G} + \frac{\omega - k_{||/}v_{||}}{\omega v_\perp} = \frac{1}{\sin\alpha}\frac{\partial}{\partial\alpha}\sin\alpha(\frac{\cos\alpha}{v} - \frac{k_{||}}{\omega}) + \frac{1}{v^2}\frac{\partial}{\partial v}v^2\sin\alpha \tag{2.19}$$

We can thus write Equation 2.14 as (Lyons, 1974a; Glauert and Horne, 2005):

$$\frac{\partial f_0}{\partial t} = \nabla\cdot(\hat{D}\cdot\nabla f_0) = \frac{1}{p\sin\alpha}\frac{\partial}{\partial\alpha}\sin\alpha(D_{\alpha\alpha}\frac{1}{p}\frac{\partial f_0}{\partial\alpha} + D_{\alpha p}\frac{\partial f_0}{\partial p}) + \frac{1}{p^2}\frac{\partial}{\partial p}p^2(D_{p\alpha}\frac{1}{p}\frac{\partial f_0}{\partial\alpha} + D_{pp}\frac{\partial f_0}{\partial p}) \tag{2.20}$$

with

$$D_{\alpha\alpha} = \sum_{n=-\infty}^{\infty}\int_0^\infty k_\perp dk_\perp D_{\alpha\alpha}^{nk_\perp} \tag{2.21}$$

$$D_{\alpha p} = D_{p\alpha} = \sum_{n=-\infty}^{\infty}\int_0^\infty k_\perp dk_\perp D_{\alpha p}^{nk_\perp} \tag{2.22}$$

$$D_{pp} = \sum_{n=-\infty}^{\infty}\int_0^\infty k_\perp dk_\perp D_{pp}^{nk_\perp} \tag{2.23}$$

To take into account the relativistic correction, here and in the following, we used $\vec{p}$ instead of $\vec{v}$ where $\vec{p} = \gamma_l m_e\vec{v}$ and γ_l is the Lorentz factor. This correction is minor in the case of the solar wind electron populations (presented in Section 1.2) but is necessary in

particular for the study of the electrons of the earth radiation belt. The resonance equation becomes:

$$\omega + \frac{n\omega_{ce}}{\gamma_l} = v_{||} k_{||} \tag{2.24}$$

and

$$D_{\alpha\alpha}^{\mathrm{n}k_\perp} = \lim_{V\to\infty} \frac{e^2}{4\pi V} \left[\frac{-n\omega_{\mathrm{ce}}/\gamma_l\omega - \sin\alpha^2}{\cos\alpha} \right]^2 \left[\frac{|\Theta_{\mathrm{n},\vec{k}}|}{|v_{||} - \frac{\partial\omega}{\partial k_{||}}|} \right]_{(k_{||\mathrm{i}})} \tag{2.25}$$

where $(k_{||\mathrm{i}})$ corresponds to the evaluation in $k_{||\mathrm{i}}$ verifying Equation (2.24). In the following we are interested mainly in $D_{\alpha\alpha}$, expressions for $D_{\alpha p}^{nk_\perp}$ and $D_{pp}^{nk_\perp}$ can be found in Lyons (1974a).

Using cold plasma theory and the Stix parameters (R, L, S, D, P, Stix, 1992), the study of Lyons (1974b) have allowed to calculate $D_{\alpha\alpha}$ (detailed in Appendix A.1) as:

$$D_{\alpha\alpha} = \sum_{\mathrm{n=nl}}^{\mathrm{nh}} \int_{X_{\min}}^{X_{\max}} X\, dX\ D_{\alpha\alpha}^{nX} \tag{2.26}$$

with nh and nl the maximum and minimum resonances taken into account in Equation 2.24. $X = \tan\theta$ and $D_{\alpha\alpha}^{nX}$ is given by Equation 2.27:

$$D_{\alpha\alpha}^{nX} = \sum_i \frac{(e\omega_i)^2}{4\pi(1+X^2)N(\omega_i)} \left(\frac{\frac{-n\omega_{\mathrm{ce}}}{\gamma_l\omega_i} - \sin\alpha^2}{\cos\alpha} \right)^2 B\mathrm{w}^2(\omega_i) g(X) \left[\frac{|\Phi_{\mathrm{n},\vec{k}}|^2}{|v_{||} - \frac{\partial\omega}{\partial k_{||}}|} \right]_{(k_{||\mathrm{i}})} \tag{2.27}$$

where the summation is performed on the resonant frequencies ω_i of Equation 2.24. $B\mathrm{w}^2(\omega_i)$ and $g(X)$ are the power spectral density of the perturbations and the distribution of wave normal angles, respectively. These distributions are supposed to be Gaussian. General expressions and in the special case of whistler waves of the normalization factor $N(\omega_i)$ and of $\Phi_{\mathrm{n},\vec{k}}$ are presented in Appendix A.1. Note that $\Phi_{\mathrm{n},\vec{k}}$, $N(\omega)$ and, $\frac{\partial\omega}{\partial k_{||}}$ depend on the dispersion relation of the considered mode and that $|\Phi_{\mathrm{n},\vec{k}}|^2$ is directly proportional to $|\Theta_{\mathrm{n},\vec{k}}|$.
Note that Jeong et al. (2020) have developed a quasi-linear resonant scattering model based on an arbitrary mode modeled as a Gaussian wave packet. This mode can propagate in an arbitrary direction relative to the background magnetic field.

We have presented some approaches to wave modeling in a plasma. We have concluded that quasi-linear theory is suitable for dealing with the interactions of whistler waves with suprathermal electrons in the solar wind. In particular, we derived the expression for the $D_{\alpha\alpha}$ coefficient, which will be used in the Chapter 4. But first, we devote the next section to a state-of-the-art review of whistler waves in the solar wind.

2.3 Whistler waves in the solar wind

Naturally, Equation 2.27 depends on the polarization properties of the waves (e.g., amplitude, planarity, ellipticity, angle, and radial direction of propagation). The radial direction of propagation can be sunward (propagating toward the Sun) or anti-sunward (propagating away from the Sun). Amplitude, angle of propagation, and especially the radial direction of propagation are the most important parameters to quantify wave-particle interactions.
In the literature, one can distinguish three categories of whistler waves depending on their direction of propagation with respect to the background magnetic field and their radial direction of propagation. These categories are: quasi-parallel anti-sunward whistler, sunward whistler, and anti-sunward oblique whistler waves and are presented in Sections 2.3.1, 2.3.2 and 2.3.3, respectively. Note that we use the terms parallel or aligned to designate both a parallel or anti-parallel propagation with respect to the background magnetic field.

Before detailing these three categories, let us explain qualitatively how the waves interact with suprathermal electrons (and especially Stralh electrons) depending on their polarization properties, to fully understand the next sections.
First of all, using cold plasma theory, one can calculate theoretically the electric field components with some wave polarization properties and plasma parameters. Using typical values in the solar wind: $\frac{\omega}{\omega_{\mathrm{ce}}} = 0.2$, $\frac{\omega_{\mathrm{pe}}}{\omega_{\mathrm{ce}}} = 200$, $B_{1\vec{k}} = 0.005$ nT/(Hz)$^{1/2}$ ($B_{1\vec{k}}$ being the Fourier transform of the magnetic field), one can determine the right-hand $E_{1\vec{k},\mathrm{R}}$, the left-hand $E_{1\vec{k},\mathrm{L}}$ and electrostatically $E_{1\vec{k},||}$ polarized electric field (see Appendix A.1). These components are shown in Figure 2.2a. The electric field is predominantly right-handed, but the left-hand and electrostatic components increase with θ.

In the following, we use an anti-sunward magnetic field convention, so that the electrons with a pitch angle between 0 and 90° (respectively, 90 and 180°) propagate anti-sunward (respectively, sunward) in the solar wind reference frame. Anti-sunward whistler waves ($k_{||} > 0$) can resonate with electrons verifying:

- $v_{||} < 0$ ($n \leq 0$ resonances, normal resonances), that is, halo electrons, mainly with the right-hand polarized part of the wave (for not too oblique whistlers). This interaction is highly efficient since the wave is mainly right-hand polarized (Figure 2.2a). $\Theta_{\mathrm{n},\vec{k}}$ is shown for the first normal resonance ($n = -1$), for a 700 eV electron with a pitch angle of 150° (corresponding to halo electrons) in Figure 2.2b. The properties of the whistler wave and of the plasma considered are those described above. The interactions between the whistler wave and the electron depend little on the angle of propagation;

- $v_{||} > 0$ ($n \geq 0$ resonances, anomalous resonances), that is halo or Strahl electrons depending on the pitch angle, mainly with the left-hand polarized part of the wave (for not too oblique whistlers). This interaction is slower (than for $n \leq 0$) since the left-hand polarized part of the wave is weaker (Figure 2.2a). $\Theta_{\mathrm{n},\vec{k}}$ is shown for the first anomalous resonance ($n = 1$), for a 700 eV electron with a pitch angle of 30° (corresponding potentially to Strahl electrons) in Figure 2.2b. The properties of the

whistler wave and of the plasma considered are again those described above. The interactions between the whistler wave and the electron increase rapidly with the angle of propagation.

Finally, for sunward-propagating waves, $k_{||} < 0$, therefore all the signs are reversed. These waves therefore resonate with Strahl electrons with $n \leq 0$ resonances and are very effective at diffusing these electrons. It is therefore well known that anti-sunward oblique and sunward waves are the most effective for scattering Strahl electrons. We can note that in all cases, resonances with a low $|n|$ are the most efficient (Lyons, Thorne, and Kennel, 1971) and that when the amplitude of the wave increases the interaction is more efficient (Equation 2.27).

2.3.1 Small-amplitude quasi-parallel anti-sunward whistler waves

Small-amplitude ($B\mathrm{w} << B_0$), quasi-parallel, anti-sunward whistler waves are commonly observed in the solar wind (Lacombe et al., 2014; Tong et al., 2019a; Jagarlamudi et al., 2020; Chust et al., 2021; Kretzschmar et al., 2021; Froment et al., 2023; Karbashewski et al., 2023). It is worth noting that it was the work of Lacombe et al. (2014) that first made it possible to clearly identify bursts of activity observed in the magnetic field of the solar wind as whistler waves. In this study, they showed that these waves are present in around 10% of observations. These waves can be generated by the Whistler Heat Flux Instability (WHFI), the Temperature Anisotropy Instability (TAI), or, the sunward suprathermal electron deficit. These instabilities are caused by halo electrons at the $n = -1$ resonance (first normal resonance) and have maximal growth rates at $\theta = 0°$. They are detailed in Sections 2.3.1.1 and 2.3.1.2.

2.3.1.1 Whistler Heat Flux and Temperature Anisotropy Instabilities

Many works have studied the WHFI and the TAI near 1 AU, in a slow solar wind, when the proportion of Strahl electrons is low (Gary et al., 1975; Lazar, Poedts, and Schlickeiser, 2011; Lazar, Poedts, and Michno, 2013; Lazar, Poedts, and Schlickeiser, 2014; Lazar et al., 2015, 2018, 2019; Kuzichev et al., 2019; Tong et al., 2019b; Vasko et al., 2020). Moreover since the Strahl does not usually play a major role in these instabilities, in this section the distribution functions considered are only composed of a core and a halo population with opposite drifts (core sunward and halo anti-sunward). Note that in some studies (Shaaban, Lazar, and Poedts, 2018; Shaaban et al., 2019; López et al., 2019), the term "beam" is used to designate the halo, the Strahl, or both, depending on the situation.

Choosing a Maxwellian velocity distribution function for the core and a kappa distribution for the halo, the growth rate of the WHFI and the TAI is written as (Gary and Feldman, 1977; Vasko et al., 2020):

$$\gamma(k) = -\frac{\pi sign(k)}{\frac{\partial \mathcal{D}}{\partial \omega}_{\omega=\omega_\mathrm{r}(\mathrm{k})}} \sum_{\alpha=\mathrm{c,H}} (\frac{\omega_{\mathrm{pe}}^2}{\omega_r})^2 \frac{n_\alpha}{n} z_\alpha(\xi_\alpha) \Big[A_\alpha \big(\frac{\omega_r - k v_{\alpha||}}{k v_{\mathrm{th}\alpha}} \big) + \frac{\omega_{\mathrm{ce}}}{k v_{\mathrm{th}\alpha}} \big(1 - A_\alpha\big) \Big] \tag{2.28}$$

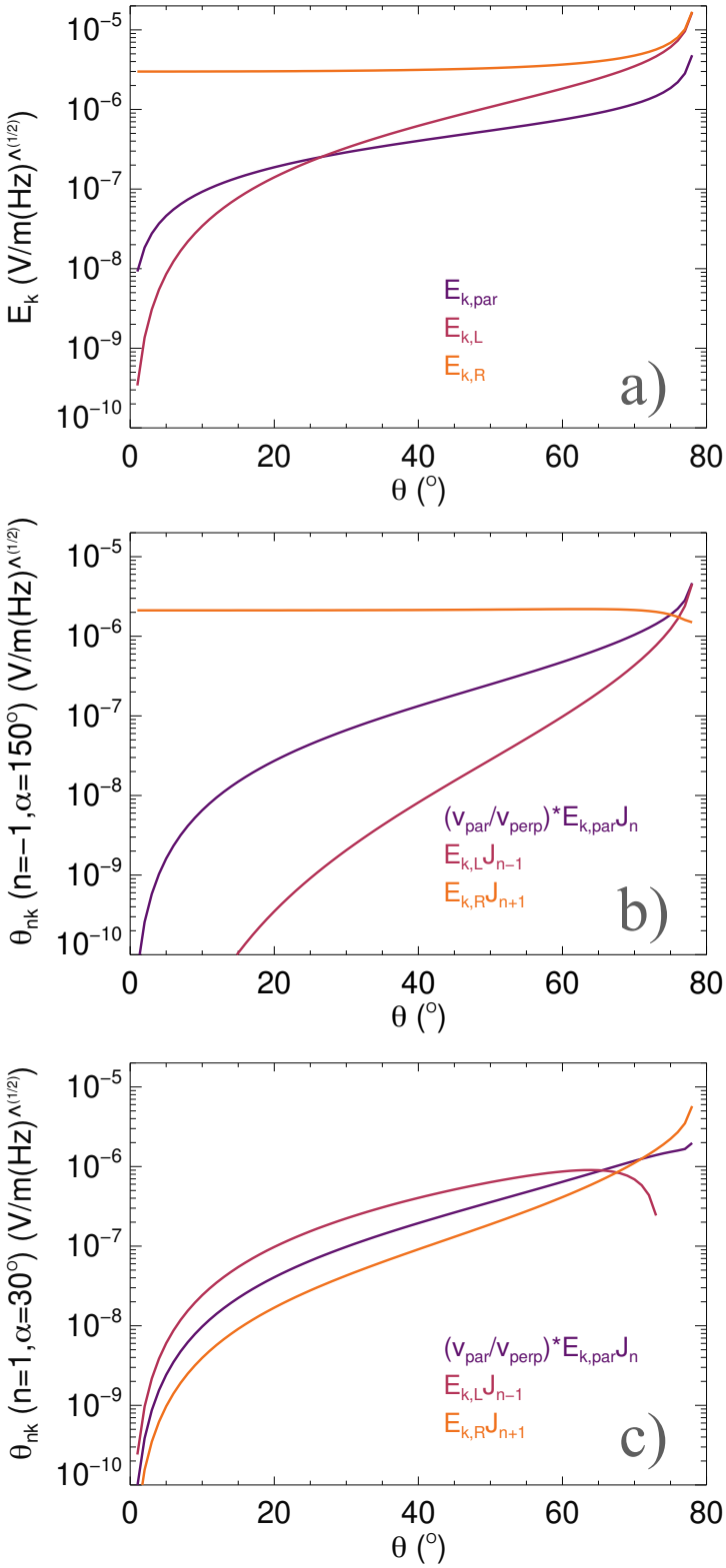

Figure 2.2: *Panel a):* Different terms of the electric field of whistler waves as a function of propagation angle (more details in the text). *Panel b):* Different terms of the whistler electron interactions coupling ($\Theta_{n,\vec{k}}$), as a function of propagation angle for $n = -1$ and $\alpha = 150°$ (more details in the text). *Panel c):* Same as *panel b)* for $n = 1$ and $\alpha = 30°$.

where $A_\alpha = \frac{T_{\alpha\perp}}{T_{\alpha||}}$, $\mathcal{D}$ is the dispersion relation,

$$\xi_\alpha = (\omega_\mathrm{r} - k v_{\alpha||} - \omega_\mathrm{ce})/v_{\mathrm{th}\alpha} k \tag{2.29}$$

$$z_c(x) = \exp\left(\frac{-x^2}{2}\right)/(2\pi)^{1/2} \tag{2.30}$$

and

$$z_\mathrm{H}(x) = \frac{\Gamma(k)}{(2\pi)^{1/2}(\kappa - 3/2)^{1/2}\Gamma(\kappa - 1/2)}\left[1 + \frac{x^2}{2\kappa - 3}\right]^{-\kappa} \tag{2.31}$$

The bracketed term of Equation 2.28 takes into account two possible free energy sources, the heat flux due to the drift of the halo population (left term) or the temperature anisotropy (right term).

Whistler Heat Flux instability

Using Maxwellian distribution functions for the core and the halo and solving numerically the electromagnetic linear dispersion relation for a collisionless plasma (Stix, 1992), Gary et al. (1975) first showed that the heat flux instability can generate aligned anti-sunward whistlers. Tong et al. (2019b) used distribution functions measured *in situ* by Artemis to show that the WHFI is at work in the solar wind. Indeed, they showed in several examples that the distribution functions (fitted by kappa functions for the halo) measured simultaneously with whistler waves were unstable for the WHFI. The representation of the quasi-linear resonant diffusion of the WHFI is presented in Figure 2.3. Halo electrons at the $n = -1$ resonance are diffused in pitch angle preferentially toward less dense areas of the phase space (black arrow). These electrons lose energy in the plasma frame which amplifies the wave. This phenomenon is in competition with the diffusion of core electrons which dampens the wave (grey arrow) (Verscharen et al., 2022).

Lacombe et al. (2014) analyzed Cluster data at 1 AU and proposed that quasi-parallel anti-sunward whistler waves could regulate the heat flux, as previously suggested by theoretical works (Gary et al., 1975; Gary and Feldman, 1977) and observations (Scime et al., 1994; Gary, Skoug, and Daughton, 1999). The first simulation of the WHFI with realistic parameters of the solar wind has been realized with a one-dimensional Particle-In-Cell (PIC) simulation by López et al. (2019). This study showed that whistler waves cause a perpendicular temperature increase for the core, a parallel one for the halo, and that they diffuse Strahl electrons in pitch angles. In particular, they showed a reduction of the drifts between populations and therefore a possible regulation of the heat flux. These evolutions of the VDF provoke a saturation of the instability at low amplitudes.
However, Tong et al. (2019a) using Artemis observations questioned the role of these waves on the heat flux regulation because of their small amplitudes and suggested that additional work was needed. Shaaban et al. (2019) performed quasi-linear calculations and found similar results to those of López et al. (2019). Nevertheless, we note that the effect of a single

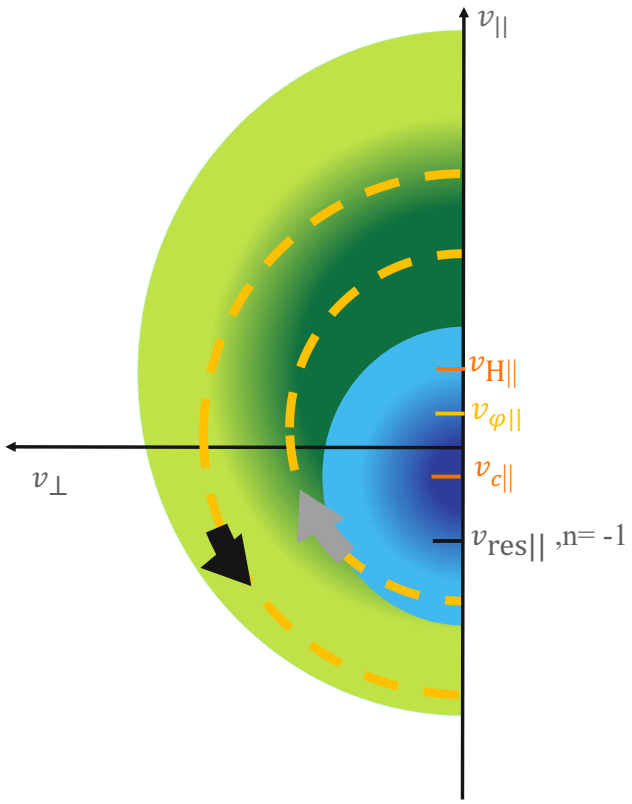

Figure 2.3: Schematic of the quasi-linear resonant diffusion of the WHFI. The core population is in blue and the halo is in green. The single-wave characteristics are represented by yellow dotted circles centered around the parallel phase velocity $v_{\varphi||}$. The resonance velocity ($v_{\text{res}||}$) associated with the $n = -1$ resonance is indicated in grey. Core and halo drift velocities ($v_{c||}$ and $v_{H||}$, respectively) are shown in orange). The black (resp., grey) arrow represents the electron diffusion which amplifies (resp., dampens) the waves.

mode calculated with the QLT indicates that saturation comes mainly from the increase in temperature anisotropy and that the drift relaxation (and therefore the heat flux regulation) is small. Finally, PIC simulations of Kuzichev et al. (2019) suggested that whistler waves do not significantly suppress the electron heat flux.
The role of this instability on heat flux regulation is therefore still under debate.

Since quasi-aligned whistlers interact only weakly with the Strahl, their possible role in the Strahl diffusion has been less studied. Nevertheless, we note that Kajdič et al. (2016) used cluster data to show that the presence of whistlers, which were in large majority quasi-aligned and anti-sunward, was linked to a higher Strahl PAW than without whistlers. The observation of increased Strahl PAW during broadband whistler fluctuations was also observed by Pagel et al. (2007) using ACE data. Pierrard, Lazar, and Schlickeiser (2011) have adopted a kinetic approach by solving the Fokker-Planck equation (thus taking into account the collision term) and adding a term taking into account a turbulent whistler wave spectrum. Quasi-linear scattering turbulence is due to interaction with aligned whistlers, whose intensity verifies $(B\mathrm{w}/B_0)^2 = 0.01$. This interaction is modeled by the formalism developed by Schlickeiser (1999) and Vainio (2000). The study by Pierrard, Lazar, and Schlickeiser (2011) indicates that assuming this turbulence spectrum, whistlers can determine halo formation.
Finally, the role of anti-sunward waves in explaining the possible presence of halo electrons in the corona was investigated (Vocks and Mann, 2003). Vocks and Mann (2003) proposed that anti-sunward waves, generated beneath the corona, with high phase velocity could accelerate electrons with low sunward velocity to high perpendicular velocity and thus create suprathermal electrons. The idea that whistler waves could accelerate electrons and create kappa-like distributions in space plasma was first proposed by Ma and Summers (1999).

Temperature Anisotropy Instabilitiy

Sufficiently large $\frac{T_{H\perp}}{T_{H||}}$ can produce quasi-aligned whistler waves by the TAI (which can also be called Electromagnetic Electron Cyclotron (EMEC) instability). Unlike the WHFI, the TAI can produce whistler waves propagating both sunward and anti-sunward. Qualitatively, this can be explained by the schematic of the quasi-linear resonant diffusion of this instability, shown in Figure 2.4a. Indeed, we note that electron diffusion at the $n = -1$ resonance amplifies whistlers that propagate anti-sunward ($v_{\varphi||} > 0$), whereas electron diffusion at the $n = 1$ resonance (first anomalous resonance) amplifies whistlers that propagate sunward ($v_{\varphi||} < 0$). The anisotropy of the distribution decreases until a plateau is reached at resonance speeds (Verscharen et al., 2022).
If there is a drift between the core and the halo (Figure 2.4b), as is generally the case in the solar wind (see Section 1.2.1), the generation of anti-sunward whistlers is favored. This is explained by the fact that the density gradient at the $n = -1$ resonance is greater. Vasko et al. (2020) have studied in detail the situations described in Figures 2.4a and 2.4b by performing linear stability analysis and using typical solar wind distribution functions at 1 AU. They showed that sunward whistlers can be generated, but at lower amplitudes, wave numbers, and, frequencies compared to anti-sunward waves.

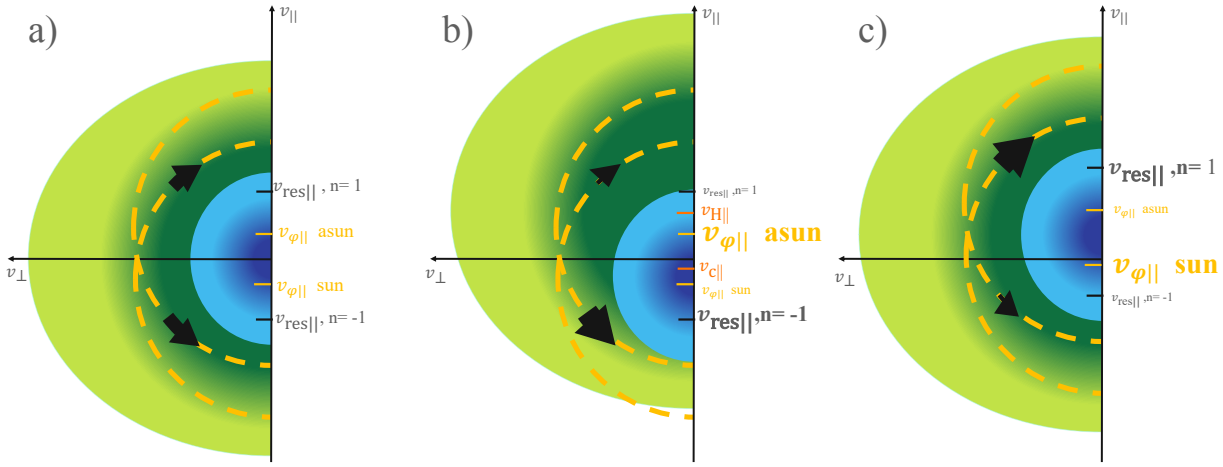

Figure 2.4: Representation of the quasi-linear resonant diffusion of the TAI. *Panel a):* no drift. *Panel b):* Sunward drift for the core and anti-sunward drift for the halo. *Panel c):* Anti-sunward drift for the core and the halo. For *Panels b) and c)*, the size of the arrows and the font size represent which generation process is favored. See more details in the text. The color code is the same as for Figure 2.3.

Lazar, Poedts, and Schlickeiser (2011) investigated the impact of using product-bi-Kappa distributions (allowing $\kappa_\perp \neq \kappa_{||}$) instead of bi-Kappa to fit the halo population. They showed that when product-bi-Kappa distributions are used, the instability threshold is very sensitive to the shape of the distributions. Lazar, Poedts, and Michno (2013) examined the effect of varying the κ index of bi-Kappa distributions. This index is related to the suprathermal particle density, as explained in Section 1.2.1 when κ decreases the number of suprathermal particles increases. They showed that the lowest thresholds, close to marginal stability, decrease when κ decreases. For higher thresholds, the κ value has the opposite effect. However, in the solar wind, κ does not play an important role since the density of suprathermal particles is often very low (Lazar et al., 2018). Finally, the anisotropy of the core, even if weak $\frac{T_{c\perp}}{T_{c||}} \in [1, 1.2]$, favors the TAI (Lazar, Poedts, and Schlickeiser, 2014) but high core thermal speed tends to inhibit the instability (Lazar et al., 2015).
Jagarlamudi et al. (2020) have shown, using the characteristics of whistlers observed by Helios and the thresholds of heat flux and temperature anisotropy instabilities, that these two instabilities are probably at work in the solar wind. Using quasi-linear theory, Sarfraz and Yoon (2020) studied the combined role of these two instabilities, and in particular which conditions were more favorable to one of the two instabilities.

2.3.1.2 Sunward suprathemal electron deficit instability

In Section 1.3.2 we explained that exospheric models predict the existence of an ambipolar potential that slows down the electrons and creates a cutoff velocity $v(r)_* = \sqrt{\frac{m_e(e\phi_\infty - e\phi(r))}{2}}$ at

every distance r. This cutoff corresponds to the separation between core and Strahl electrons in the anti-sunward direction and the maximum electron velocity in the sunward direction. A suprathermal electron deficit is therefore expected in the sunward direction.
This deficit was observed by Pilipp et al. (1987a) using the Helios plasma experiment at heliocentric distances between 0.3 and 1 AU. However, this deficit was not present in the majority of observations. This is probably due to the fact that for $r > 0.3$ AU the deficit is expected at low energies and can be erased by instabilities or collisions. Using data from Parker Solar Probe, at $r < 0.2$ AU Halekas et al. (2020), Berčič et al. (2020), and Halekas et al. (2021a,b, 2022) were able to clearly demonstrate the existence of this deficit in numerous observations. This deficit was found to have a shape consistent with that predicted by the simulations of Berčič, Landi, and Maksimović (2021). Halekas et al. (2021b) have shown that below 0.2 AU this deficit is present between 60% and 80% of observations, but disappears rapidly with distance.
Using Solar Orbiter's distribution function measurements, Berčič et al. (2021) associated the presence of anti-sunward quasi-aligned whistler waves with this deficit. This observation suggests that the sunward suprathermal electron deficit could generate this type of wave. The proposed mechanism, whose quasi-linear resonant diffusion schematic is shown in Figure 2.5a, can be described as follows. Halo electrons at the $n = -1$ resonance diffuse toward the less dense areas of the $(v_\perp, v_{||})$ space, created by the deficit. In so doing, electrons lose energy and amplify fluctuations (black arrow of Figure 2.5a). Note that the Strahl population is not represented for readability reasons. A distribution function measured by Berčič et al. (2021), associated with quasi-aligned anti-sunward whistler waves is shown in Figure 2.5b. The electron deficit at resonance velocity is not observed before or after whistler activity. Note the difference in color codes and notations between Figures 2.5a and 2.5b.

2.3.2 Sunward whistler waves

An interval containing sunward and anti-sunward whistler waves was observed in association with a magnetic flux rope by Lacombe et al. (2014) using Cluster data. In this study, they proposed that wave generation in these two directions is due to the presence of a bi-directional electron distribution associated with the flux rope. However, the absence of electron distribution function measurements during this interval makes it impossible to verify this hypothesis.
Sunward whistler waves were measured during Encounter 1 (37.5 $R_\odot \simeq 0.2$ AU) of PSP. Using waveforms data Agapitov et al. (2020) studied a sunward propagating whistler wave packet in association with a magnetic field dip at a switchback boundary. This wave packet contained subpackets with propagation angles varying from quasi-parallel to oblique, probably due to propagation in an inhomogeneous background magnetic field. Froment et al. (2023) also studied in detail some examples of sunward wave packets measured in burst waveforms. Using spectral matrices and band-pass filtered data, they showed that whistler waves (without making the distinction sunward /anti-sunward) are associated with magnetic field dips in 64% of the cases. Finally, Karbashewski et al. (2023) detected sunward, anti-sunward, and counter-propagating (propagating in both directions) whistlers in burst waveforms. In this

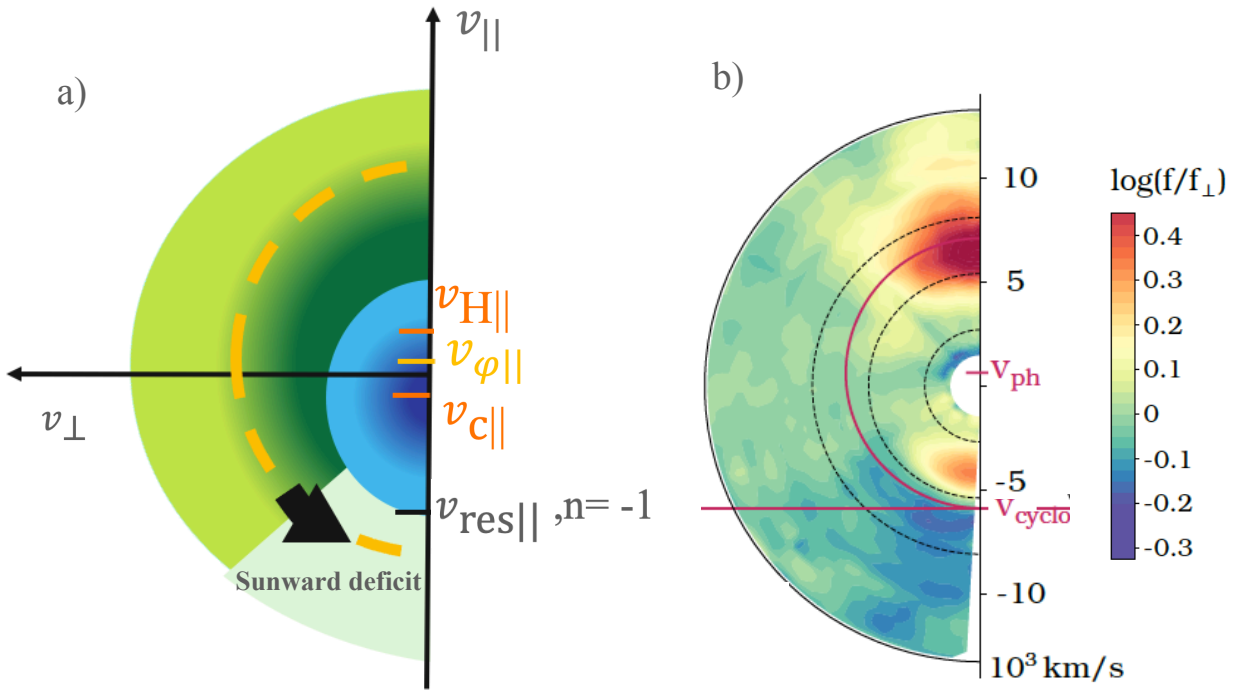

Figure 2.5: *Panel a):* Representation of the quasi-linear resonant diffusion of the sunward suprathemal electron deficit instability. The color code is the same as for Figures 2.3 and 2.4. *Panel b):* VDF normalized by the perpendicular cut measured by Solar Orbiter on June 24th, 2020 between 6:05:15 and 6:05:45. The whistler parallel phase ($v_{\rm ph}$) and resonance ($v_{\rm cyclo}$) velocities are shown in purple. A single-wave characteristic is represented by a purple circle centered around the parallel phase velocity. *Panel b)* is taken taken from Berčič et al. (2021).

last study, they proposed a mechanism for the generation of these waves that is based on the temperature anisotropy caused by electrons trapped in a magnetic dip. A shift in the distribution functions of the trapped electrons, caused by the propagation of the magnetic dip in the proton reference frame, would favor the generation of sunward waves. The latter are theoretically expected at higher frequencies than the anti-sunward waves. Depending on the shifts and drifts between populations, this mechanism could explain the observations of sunward, anti-sunward, and counter-propagating (sunward at low frequency and anti-sunward at high frequency) whistler waves. This mechanism is schematized in Figure 2.4c. In this panel, electrons have been shifted upward due to the supposed propagation of the magnetic dip. In this case, sunward propagation is privileged since electrons at $n = 1$ are at higher energies compared to the $n = -1$ resonance. It's important to note that the distribution functions considered by Karbashewski et al. (2023) are different from the typical 1 AU distribution functions used by Vasko et al. (2020). In particular, the supposed drift of trapped electrons due to magnetic dip motion explains the difference in predicted frequencies for sunward versus anti-sunward waves in these two studies. Note that Figure 2.4c is simplified for clarity, it should actually represent a trapped population using for example a loss cone distribution and only trapped electrons should be shifted. We can also note that Saito and Gary, 2007 proposed a wave/wave interaction mechanism to produce quasi-aligned sunward whistler waves. The origin of sunward waves in the solar wind will be discussed in detail in Chapters 4 and 6.

Sunward whistler waves are particularly interesting because they can interact very efficiently with the Strahl and therefore also potentially regulate the heat flux (Vocks et al., 2005; Saito and Gary, 2007; Sarfraz and Yoon, 2020; Cattell and Vo, 2021).
Observations of these waves during Parker Solar Probe Encounter 1 indicate that they may play an important role close to the Sun ($r < 0.2AU$). However, they were rarely observed far from the Sun ($r > 0.2$ AU).

2.3.3 High amplitude oblique whistler waves

Anti-sunward oblique whistler waves can be generated by the fan instability and have been proposed to regulate the heat flux, especially close to the Sun (Pistinner and Eichler, 1998; Komarov et al., 2018; Roberg-Clark et al., 2018; Verscharen et al., 2019; Vasko et al., 2019; Roberg-Clark et al., 2019; Micera et al., 2020, 2021; Cattell and Vo, 2021; Halekas et al., 2021a; Cattell et al., 2021b,a). This instability is driven by Strahl electrons (resonance $n = 1$) and is due to an important drift and density of this population (Verscharen et al., 2019; Vasko et al., 2019). A schematic of the quasi-linear diffusion of electrons due to this instability is available in Figure 10 of Verscharen et al. (2022).
Vasko et al. (2019) performed a stability analysis by considering a distribution function composed only of core and Strahl populations, modeled by Maxwellian distributions. They derived thresholds for this instability on the relative density and heat flux of the Strahl as a function of the plasma β_e. Their analysis shows that the growth rate is maximum for waves propagating with $\theta \in [70 - 80]^\circ$ and with $\omega \in [0.05, 0.25]\omega_{ce}$.
Using the cold electrons dispersion relation and arguing that to be unstable, the Strahl

electron resonance must not undergo core or cyclotron damping, Verscharen et al. (2019) also derived thresholds on this instability. In the low $\beta_{\rm ec}$ case the threshold is the following:

$$v_{\rm S||} \gtrsim 3v_{\rm thc||} \tag{2.32}$$

while in the $\beta_{\rm ec} \sim 1$ the instability criterion is:

$$v_{\rm S||} \gtrsim [2\frac{n_{\rm S}}{n_{\rm c}}\frac{T_{\rm S||}}{T_{\rm c||}}v_{\rm Ae}^2 v_{\rm thc||}^2 \frac{(1+\cos\theta)}{(1-\cos\theta)\cos\theta}]^{1/4} \tag{2.33}$$

where $v_{\rm Ae} = \frac{B_0}{\sqrt{4\pi n_{\rm e} m_{\rm e}}}$ is the electron Alfvén speed.

Comparing the thresholds obtained by Verscharen et al. (2019) with the Strahl properties measured by Parker Solar Probe and Helios, Jeong et al. (2022) showed that Strahl electrons are on average stable against the fan instability between 0.1 et 1 AU. These results suggest that this instability is probably very rare in the solar wind (in this heliocentric distance range) and if it exists it can only be exited sporadically. This is in line with the results of the kinetic stability analysis carried out by Schroeder, Boldyrev, and Astfalk (2021).

Anti-sunward oblique whistler waves have been observed at 1 AU by Cattell et al. (2020) using STEREO data and in association with stream interaction regions, coronal mass ejections, and interplanetary shocks. Using cross spectra of Parker Solar Probe's first encounter, Froment et al. (2023) showed that 3% of observed waves had oblique propagation angle ($\geq 45°$). To our knowledge, there are very few observations of oblique whistler waves in the free solar wind beyond 0.3 AU.

Studies have also investigated the interplay between this instability and other instabilities due to drifts between the different populations (Shaaban, Lazar, and Poedts, 2018; López et al., 2020b). López et al. (2020b) has shown that for low drifts of the suprathermal population (s): $v_{\rm s||} < v_{\rm ths}$ the WHFI dominates and when $v_{\rm s||}$ increases the fan instability dominates. Moreover, when $v_{\rm s||} > v_{\rm ths}$, other electrostatic instabilities can be exited.

Finally, we can note that Jagarlamudi et al. (2021) and Cattell et al. (2021b) used electromagnetic and particle data of Parker Solar Probe to show evidence of diffusion of the Strahl electrons by whistler waves. However, Cattell et al. (2022), using Parker Solar Probe data from Encounters 1 through 9, showed that whistler waves are rarely observed inside ~ 0.13 AU ($\simeq 28\ R_\odot$).

2.3.4 Role of other plasma modes

In sections 2.3.1, 2.3.2 and 2.3.3 we presented the categories of whistler waves that can propagate in the solar wind with respect to their polarization properties and discussed their potential roles in Strahl diffusion and heat flux regulation. Other instabilities and phenomena could also be mentioned, such as those below.

First, as explained in Section 2.1.1, when $\cos\theta \lesssim \frac{m_e}{m_p}$, ions are no longer negligible and under these conditions the oblique fast-magnetosonic whistler branch is known as the lower-hybrid branch. These waves can be generated by the fan instability and interact very effectively with Strahl electrons. However, their growth rate is lower than the one of the oblique fast-magnetosonic waves (Verscharen et al., 2019).
Secondly, ion-acoustic waves (Fried and Gould, 1961) are regularly observed in the solar wind (Gurnett and Anderson, 1977; Graham et al., 2021; Mozer et al., 2020, 2021; Mozer, Vasko, and Verniero, 2021). These electrostatic waves have a maximum growth rate at $k_\perp = 0$ and are not intensely damped when $T_e \gg T_p$. They can be generated when the core population has an important drift in the proton frame. However, these waves cannot interact effectively with Strahl electrons (Verscharen et al., 2019, 2022).
Langmuir waves are also commonly observed in the solar wind (Pulupa and Bale, 2008; Graham et al., 2021; Boldú et al., 2023). However, these electrostatic waves are generated around the electron plasma frequency and therefore interact with suprathermal electrons at high resonance orders that do not efficiently diffuse electrons. (Pavan et al., 2013) nevertheless suggested that these waves could have a significant impact on Strahl diffusion.
Magnetohydrodynamic waves have a phase velocity on the order of the Alfvén velocity, that is, ∼10 times smaller than the phase velocity of whistler waves. Therefore, they cannot interact as effectively as whistler waves with suprathermal electrons.
Finally, other instabilities observed or predicted in the solar wind include electron-acoustic instability, kinetic Alfvén heat-flux instability, electrostatic ion-cyclotron instability, and electron firehose instability. The latter is mentioned in particular for potentially limiting the $\frac{T_{e||}}{T_{e\perp}}$ ratio (López et al., 2020a; Lazar et al., 2022; Lazar et al., 2023). On the other hand, these modes cannot theoretically interact effectively with Strahl electrons (Verscharen et al., 2019, 2022).

To conclude, because of their phase velocities (of the order of hundreds of $\frac{\text{km}}{\text{s}}$) and their possible polarization characteristics (obliquity or sunward propagation) whistler waves are the most promising candidates for interacting effectively with the suprathermal populations of the solar wind. On the other hand, obviously, the modes presented in this section, as well as other phenomena, are likely to contribute to suprathermal electron diffusion even if less effectively.

2.4 Problematic and plan of the thesis

In Chapter 1 we described the two main open questions concerning the electron distribution function in the solar wind: the Strahl diffusion and the heat flux regulation. Indeed, these two phenomena are not correctly described by the current solar wind models. It is therefore necessary to invoke other mechanisms, such as wave-particle interactions. In this chapter, we explain that whistler waves are commonly observed and are the most interesting candidate to answer these questions. We review the different types of whistler waves observed in the Solar wind and we emphasize that knowing the polarization properties is necessary to describe

wave-particle interactions. Oblique and sunward waves seem to be the most promising for answering these questions since they interact very effectively with Strahl electrons. On the other hand, sunward waves have been little observed beyond 0.3 AU and oblique waves have been rarely observed in the free solar wind. Quasi-aligned anti-sunward waves are abundantly observed but interact inefficiently with Strahl electrons. Furthermore, recent numerical simulations suggest that they cannot explain the regulation of heat flux. We note that, despite the fact that whistlers have been abundantly studied in the solar wind, quantification of their role in the diffusion of suprathermal electrons is still missing. In this thesis, our aim is to finely characterize the properties and occurrence of whistler waves between 0.2 and 1 AU in order to achieve this quantification. In particular, we question whether the observed whistler waves can explain Strahl's pitch-angle diffusion, leaving their role in heat flux regulation for later study.

To this end, we use data from Solar Orbiter and Parker Solar Probe. Observation and characterization methods of whistler waves from these two satellites are presented in detail in Chapter 3. We emphasize the work done and the precautions to be taken in order to exploit at best these data.
In Chapter 4, we first carry out a study of plasma waves observed at frequencies between around 0.02 and $0.3f_{ce}$ (i.e., the expected frequency range of whistler waves in the Solar wind) and distances between 0.2 and 1 AU. We note that at these frequencies and distances, the vast majority of the waves observed are whistlers, and we produce a large statistic on the occurrence and characteristics of these waves. We then use the results of this statistic with quasi-linear theory to realize the quantification of the pitch angle diffusion of Strahl electrons by these waves for the first time.

However, as will be explained, this quantification can only be performed between 0.3 and 1 AU (using Solar Orbiter data). Closer to the Sun, with Parker Solar Probe, only particular cases will be presented. Indeed, since March 2019 (end of Encounter 1), a technical issue has affected one antenna of the tri-axial search-coil magnetometer of Parker Solar Probe. Without the data of this antenna, the determination of the polarization properties of whistler waves (obliquity, radial direction of propagation, ellipticity) is impossible directly.
We propose in Chapter 5 a technique for the reconstruction of polarization properties of whistlers under these conditions. Finally, in Chapter 6 we conclude and summarize the main findings of this thesis. We also present future prospects.

2.5 Résumé en français du chapitre 2

Dans ce chapitre, on présente brièvement certaines approches théoriques bien connues, permettant la description d'ondes se propageant dans un plasma. On s'intéresse principalement aux ondes de sifflement, qui sont des ondes électromagnétiques électroniques et à leur rôle potentiel dans les deux questions ouvertes exposées au chapitre 1. On présente le formalisme permettant de calculer théoriquement l'effet d'ondes électromagnétiques sur la fonction de distribution des électrons.

La théorie linéaire et le modèle "électrons froids" nous permettent tout d'abord d'obtenir simplement la relation de dispersion des ondes de sifflement. Dans ce modèle fluide, les ions n'ont pas le temps de réagir à la perturbation et ne constituent qu'un fond neutralisant. De plus, c'est un modèle "froid", c'est-à-dire que la pression due à la température et donc l'effet du mouvement thermique des particules sur la propagation des ondes est négligé. En effet, les corrections thermiques sont négligeables pour les ondes de sifflement lorsque l'angle de propagation est inférieur à l'angle du cône de résonance. En revanche, les modèles fluides ne permettent pas de traiter des fonctions de distribution complexes, avec des composantes suprathermiques, comme celles des électrons dans le vent solaire, exposées au chapitre 1. Pour comprendre la génération et l'interaction des ondes de sifflement dans le vent solaire, il est donc nécessaire d'utiliser la théorie cinétique.

On présente ensuite comment la théorie cinétique linéaire permet de calculer le taux de croissance d'un mode plasma. On note que pour avoir une instabilité, l'existence d'énergie libre dans la fonction de distribution est nécessaire. En revanche, la théorie linéaire ne permet pas de décrire la fin de l'instabilité, car elle prédit une croissance exponentielle des fluctuations. De plus, cette théorie ne permet pas de prendre en compte l'évolution de la fonction de distribution d'équilibre sous l'effet des ondes. Pour modéliser correctement l'effet des ondes sur la fonction de distribution et la saturation de l'instabilité, on utilise donc la théorie quasi-linéaire.

La théorie quasi-linéaire permet de quantifier les interactions ondes-particule si l'énergie de l'onde est à la fois beaucoup plus faible que l'énergie thermique des particules et beaucoup plus élevée que l'énergie du bruit thermique. Pour réaliser cette quantification, on utilise l'équation de diffusion dans l'espace des vitesses, valable pour un plasma uniforme, sans collision, immergé dans un champ magnétique constant non incurvé et infini. L'amplitude des ondes qui sont supposées être auto-excitées de manière aléatoire (non corrélées en phase) est supposée faible. Plus précisément, l'effet des ondes sur la fonction de distribution est lent (variation lente par rapport à la période de l'onde) et le taux de croissance des ondes est faible par rapport à leurs fréquences. On obtient ensuite l'expression des coefficients de diffusion qui permettent de calculer, en connaissant les propriétés de polarisation des ondes, l'échelle de temps de la diffusion des électrons dans l'espace des vitesses. Un état de l'art sur les ondes de sifflement dans le vent solaire en fonction de leurs propriétés de polarisation est ensuite effectué. Les ondes de sifflement sont des ondes électromagnétiques à polarisation circulaire

droite, dont la fréquence est inférieure à la fréquence cyclotronique électronique. Ces ondes peuvent se propager de façon parallèle ou oblique par rapport au champ magnétique, vers le Soleil ou en s'en éloignant. Des ondes de sifflement de faibles amplitudes, quasi-parallèles, s'éloignant du Soleil sont couramment observées dans le vent solaire. Ces ondes peuvent être générées par l'instabilité de flux de chaleur, d'anisotropie de température ou de déficit électronique suprathermique vers le Soleil. Ces instabilités sont causées par les électrons du halo à la première résonance normale. Ces ondes interagissent lentement avec les électrons du Strahl. Leur rôle dans la régulation du flux de chaleur est encore en débat.
Les ondes s'éloignant du Soleil, obliques et intenses peuvent être générées par l'instabilité de l'éventail et peuvent théoriquement diffuser les électrons de Strahl. Ces ondes ont été abondamment étudiées (théorie et simulation). En revanche, elles ont été très peu observées dans le vent solaire libre au-delà de 0,3 UA.
Finalement, les ondes en direction du Soleil sont particulièrement intéressantes, car elles peuvent interagir de manière très efficace avec le Strahl. En revanche, seulement quelques exemples ont été observés avec Parker Solar Probe (distance inférieure à 0,3 UA).
Nous notons que, malgré le fait que les ondes de sifflement ont été abondamment étudiées dans le vent solaire, une quantification de leur rôle sur la diffusion des électrons suprathermiques est toujours manquante. La réalisation de cette quantification est l'objectif principal de cette thèse.

À cette fin, nous utilisons les données de Solar Orbiter et de Parker Solar Probe. Les méthodes d'observation et de caractérisation des ondes de sifflement utilisées pour ces deux satellites sont présentées en détail dans le chapitre 3. Nous insistons sur le travail effectué et les précautions à prendre pour exploiter au mieux ces données.
Dans le chapitre 4, nous effectuons d'abord une étude des ondes plasma observées à des fréquences comprises entre environ 0,02 et 0,3 f_{ce} et à des distances comprises entre 0,2 et 1 UA. Nous constatons qu'à ces fréquences et distances, la grande majorité des ondes observées sont des ondes de sifflement, et nous produisons une importante statistique sur l'occurrence et les caractéristiques de ces ondes. Nous utilisons ensuite les résultats de cette statistique avec la théorie quasi-linéaire pour réaliser la quantification de la diffusion en largeur angulaire des électrons du Strahl par ces ondes.

Cependant, comme nous l'expliquerons, cette quantification ne peut être réalisée qu'entre 0,3 et 1 UA (en utilisant les données de Solar Orbiter). Plus près du Soleil, avec Parker Solar Probe, seuls des cas particuliers seront présentés. En effet, depuis mars 2019 (fin de l'orbite 1), un problème technique affecte une antenne du fluxmètre tri-axial à bobine de Parker Solar Probe. Sans les données de cette antenne, la détermination des propriétés de polarisation des ondes de sifflement (obliquité, direction radiale de propagation, ellipticité) est impossible directement.
Nous proposons au chapitre 5 une technique pour la reconstruction des propriétés de polarisation des ondes de sifflement dans ces conditions. Enfin, dans le chapitre 6, nous concluons et résumons les principaux résultats de cette thèse. Nous présentons également les travaux en cours et les perspectives.

Chapter 3

Data analysis

The first two Sections (3.1, 3.2) of this chapter briefly introduce the two satellites used in this thesis (Solar Obiter and Parker Solar Probe, respectively), with a focus on the instruments that we used.

3.1 Solar Orbiter

Solar Orbiter is an EAS/NASA M-class mission, the first mission of the Cosmic Vision 2015-2025 program. Launched in February 2020, it aims at answering the following four questions (taken from Mueller et al., 2013):

- What drives the solar wind and where does the coronal magnetic field originate?
- How do solar transients drive heliospheric variability?
- How do solar eruptions produce energetic particle radiation that fills the heliosphere?
- How does the solar dynamo work and drive connections between the Sun and the heliosphere?

To answer these questions Solar Orbiter has 10 experiments, 4 *in situ:* Energetic Particle Detector (EPD) (Rodríguez-Pacheco et al., 2020), Magnetometer (MAG) (Horbury et al., 2020), Radio and Plasma Wave (RPW) (Maksimovic et al., 2020), Solar Wind Analyzer (SWA) (Owen et al., 2020) and 6 remote sensings: Extreme Ultraviolet Imager (EUI) (Rochus et al., 2020), Visible light and UV Coronagraph (Metis) (Antonucci et al., 2020), Polarimetric and Helioseismic Imager (SO/PHI) (Solanki et al., 2020), Heliospheric Imager (SoloHI) (Howard et al., 2020), Extreme Ultraviolet Imaging Spectrograph (SPICE) (SPICE Consortium et al., 2020), X-ray Spectrometer/Telescope (STIX) (Krucker et al., 2020). These instruments are shown in Figure 3.1. The nominal phase of the mission should last 7 years with orbital periods between 150 and 180 days and with Gravity Assist Maneuvers (GAMs) around Earth and Venus. The closest perihelion is at 0.28 AU and the furthest aphelion is at 1.02 AU. Solar Orbiter will reach a heliospheric latitude up to 18° during the nominal

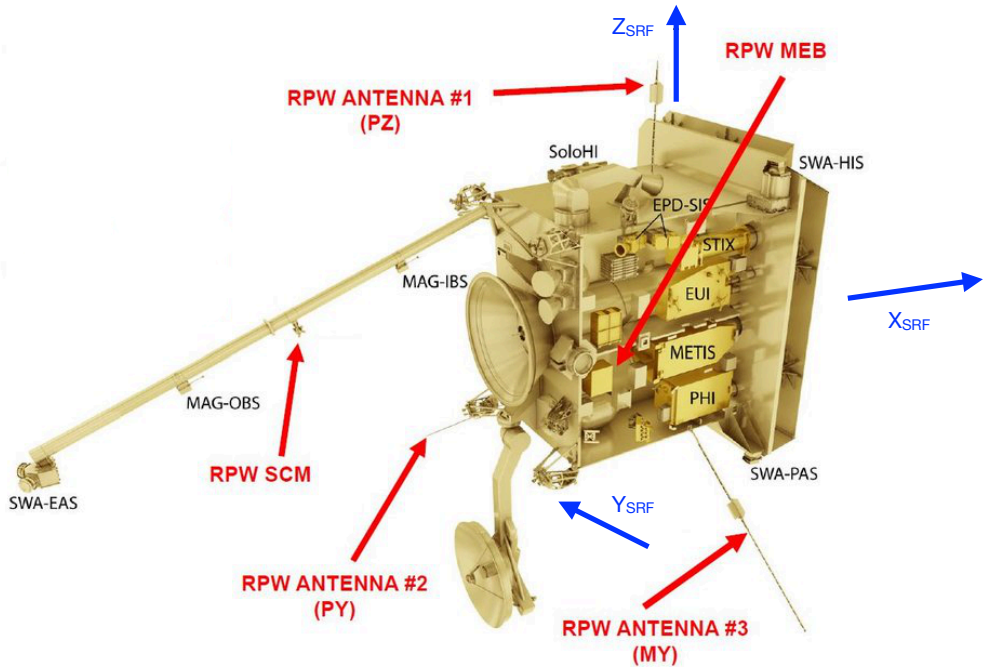

Figure 3.1: Representation of Solar Orbiter and its instruments. The instruments from the RPW experiment are indicated in red. Solar Orbiter Spacecraft Reference Frame (SRF) is represented by blue arrows. Adapted from Maksimovic et al. (2020).

phase and above 30° during the extended phase of the mission (3 years). The combination of its trajectory and its numerous *in situ* and remote sensing instruments represents a unique opportunity to improve our understanding of the heliosphere (Müller et al., 2020).

In this thesis, we use measurements from RPW, SWA, and MAG. We present briefly hereafter the main characteristics of these instrument suites in Sections 3.1.1, 3.1.2, and 3.1.3, respectively. Unless otherwise specified we are working in the Solar Orbiter Spacecraft Reference Frame (SRF) frame where $\vec{X}$ points to the sun, $\vec{Z}$ points to the north, and $\vec{Y}$ completes the direct reference frame. This reference frame is shown in Figure 3.1.

3.1.1 RPW

3.1.1.1 RPW science objectives and measurements

As mentioned in Section 1.1, the solar wind is turbulent, which means that there is a transfer of energy from large to small scales. It is likely that the energy dissipation is located at the kinetic scales (Alexandrova et al., 2013). The sensitivity of the RPW instruments allows us to measure this turbulence up to the electron scales both in the electric field and in the magnetic field during the perihelia (Maksimovic et al., 2020).
Moreover, as explained in Section 1.2.1, the electron distribution functions (and also those of other species) include non-equilibrium populations whose evolution and origins are not com-

pletely understood. Many instabilities such as ion cyclotron waves, magnetosonic-whistler waves, ion acoustic waves, or Langmuir waves can play a role in the evolution of these distributions. With the RPW experiment, it is possible to characterize these instabilities and their roles in the solar wind by measuring their electric and magnetic components (only electric for the highest frequency waves).
Finally, Langmuir waves (produced by an electron beam) can generate type III radio waves (Melrose, 1982) via non-linear interactions and the importance of density fluctuations in this phenomenon is known (Krafft and Savoini, 2022). Langmuir waves can also be produced at shocks by energetic electrons and produce type II radio waves. Radio waves are strongly scattered by density fluctuations during their propagation (Thejappa and MacDowall, 2008; Kontar et al., 2017). RPW measures radio emissions and density fluctuations precisely in order to better understand these phenomena.
To achieve these objectives RPW has a triaxial search-coil magnetometer (SCM), 3 electric antennas, and different analyzers at low and high frequency (LFR, TDS, TNR-HFR) (Maksimovic et al., 2020). The SCM and electrical antennas are presented hereafter (Sections 3.1.1.2 and 3.1.1.3).

3.1.1.2 SCM

The SCMs of the Solar Orbiter and Parker Solar Probe missions were built at LPC2E and are used to detect whistler waves in this thesis. The SCMs measure the fluctuations of the magnetic field between 3 Hz and 50 kHz in three directions and up to 1 MHz in one direction (Jannet et al., 2021). They are composed of 3 antennas, which measure the magnetic field aligned with their axes. The antennas are composed of a magnetic core with a coil wounds around it. The measurement of the magnetic field is based on the Faraday's law of induction:

$$V_{\text{ind}} = -N_1 \frac{d\phi}{dt} = -\mu_{\text{app}} N_1 S \frac{dB}{dt} \tag{3.1}$$

where V_{ind} is the voltage induced by the variation of the magnetic flux ϕ and N_1 is the number of turns of the coil. The flux variation is only caused by the variation of the component of the magnetic induction parallel to the core of the coil (B) since the cross section S and the apparent permeability μ_{app} do not vary. One of the antennas has a second winding, which allows to measure at higher frequencies in one direction. Since the induction is due to the variation of the magnetic field, the SCM is not adapted to measure low frequencies (lower than 3 Hz) (Jannet et al., 2021). For these frequencies, we use the fluxgate magnetometer (MAG, presented in Section 3.1.3).

3.1.1.3 Electric antennas

The three electrical antennas of RPW (6.5m stacer deployable monopole) visible in Figure 3.1 measure the electric field fluctuations from DC to 16 MHz. The electric antennas are in the plane $(\vec{Z}, \vec{Y})$, meaning the radial component of the electric field ($E\text{w}_\text{X}$) cannot be measured ($E\text{w}$ being the electric field waveform). The components $E\text{w}_\text{Y}$ and $E\text{w}_\text{Z}$ can be obtained as follows (Chust et al., 2021):

$$E\mathrm{w_Y} = -V_{2,3}/L_{\mathrm{effY}} \tag{3.2}$$
$$E\mathrm{w_Z} = -(V_{1,2} + V_{2,3}/2)/L_{\mathrm{effZ}} \tag{3.3}$$

where $V_{\mathrm{i,j}} = V_{\mathrm{i}} - V_{\mathrm{j}}$ with V_{i} the potential of the electric antenna i (Figure 3.1). We can note that $E\mathrm{w_Z}$ can also be expressed as: $E\mathrm{w_Z} = -(V_{1,2} + V_{1,3})/2L_{\mathrm{effZ}}$. The knowledge of the amplitude of $E\mathrm{w_Y}$ and $E\mathrm{w_Z}$ thus requires to know the effective lengths of the antennas (L_{effY} and L_{effZ}). The methods that we use for estimating these effective lengths are presented in Section 3.3.1.3.
Finally, the electron density and temperature are measured using the Quasi-Thermal Noise (QTN) technique. QTN is based on the measurement of the electrostatic spectrum produced by the thermal motion of ions and electrons in a stable plasma. This spectrum is measured by a passive electric antenna. This method is applicable if the length of the electrical antenna is larger than the Debye length and if the antenna radius is much smaller than the Debye length (Maksimovic et al., 1995, 1998; Meyer-Vernet, Issautier, and Moncuquet, 2017). This is the case in the majority of measurements in the dense solar wind at 1 AU (Maksimovic et al., 2005b, 2020).

3.1.1.4 Examples of studies realized with Solar Orbiter RPW

Numerous studies using RPW measurements have been performed and are reviewed in Maksimovic et al. (2021). We can mention, among others, the following works. Ion acoustic waves were observed by Graham et al. (2021), their occurrence is around 1% at 1 AU. These waves are probably produced by ion beams or by the current-driven instability and their occurrence decreases with increasing distances (Píša et al., 2021). Khotyaintsev et al. (2021) studied low-frequency waves ($\omega \in [\omega_{\mathrm{He^{++}}}, \omega_{ci}]$, in the plasma frame) and showed that magnetic field fluctuations (measured by MAG) were in phase with density fluctuations. They used a three-fluid model (electrons, protons, and alphas) to identify these waves (left-hand and right-hand circularly polarized) as proton-band electromagnetic ion cyclotron waves propagating (anti-sunward and sunward, respectively). Several type III wave measurements have been performed using simultaneous measurements from other satellites in order to triangulate the source of the emission (Musset et al., 2021; Gómez-Herrero et al., 2021). Langmuir waveforms have been measured by the Time Domain Sampler TDS (Soucek et al., 2021). As detailed in Section 2.3, whistler waves were also observed by Kretzschmar et al. (2021), Chust et al. (2021), and Berčič et al. (2021). The methods of detection and characterization of whistler waves used in this thesis are detailed in Section 3.3.1.

3.1.1.5 Low Frequency Receiver data

In this thesis, we use data from the Low Frequency Receiver (LFR), which processes data at frequencies between [$\simeq$ 3Hz, 10kHz] for the magnetic and [DC, 10kHz] for the electric fields. LFR produces data in several formats, listed below. There are continuous waveforms (CWFs, 3 magnetic and 2 electric potential components) at 16 Hz, 256 Hz and 4096 Hz (in burst

mode). The 256 Hz measurements are available from a few tens of minutes to several hours per day depending on the telemetry. There are also snapshot waveforms (SWFs, 3 magnetic and 2 electric potential components) which are composed of 2048 points at an acquisition frequency of 256, 4096, and 24 576 Hz every 300 s in mode configuration (this cadence is increased when enough telemetry is available). There are also spectral matrices (ASMs and BP2s) and basic wave parameters (BP1s). For the study presented in Chapter 4, we use CWFs and SWFs at 256 Hz. When available, we use the electron density delivered by RPW as a level 3 data product by measuring the probe-to-spacecraft potential (Khotyaintsev et al., 2021). The BP1s are used in the context of the supervision of Tom Cooper's M1 internship. Some of the results of this internship will be discussed in Chapter 4.

3.1.2 SWA

The SWA experiment includes 3 instruments: an Electron Analyzer System (SWA-EAS), a Proton and Alpha particle Sensor (SWA-PAS), and a Heavy Ion Sensor (SWA-HIS) (Owen et al., 2020). In this thesis, we use SWA-EAS and SWA-PAS. SWA-EAS includes two heads (EAS1 and EAS2) that are electrostatic analyzers mounted at the end of the boom (Figure 3.1). Both heads measure, in their reference frames, elevations between $\pm 45°$ distributed in 16 bins, azimuths between 0 and 360° distributed in 32 bins, and energies between 1 eV and 5 keV distributed in 64 bins. The combined field of view (FOV) of the two heads enables a quasi-complete view of the sky ($\sim 4\pi$sr, but blockages due to the spacecraft, the sensor structure, etc are present). SWA-EAS produces, among others, full 3D VDF with a time resolution up to 10 s and burst mode electron pitch angle (2D) distributions with a time resolution up to 0.125 s. Burst modes use MAG data to select the head (EAS1 or EAS2) and two elevations of the selected head that contain the direction of $\pm\vec{B}_0$. With this method, measurements are taken at two elevations instead of 16 since the distribution function is independent of the azimuth around $\vec{B}_0$. This increases temporal resolution. We use the full 3D VDF measurements for the study presented in Chapter 4. We also use SWA-PAS data to estimate the Solar wind speed and the density.

3.1.3 MAG

The triaxial fluxgate magnetometer (MAG, (Horbury et al., 2020)) measures the background magnetic field $\vec{B}_0$ and its low frequency variations. MAG has two sensors, MAG-IBS and MAG-OBS, which are positioned on the spacecraft boom (Figure 3.1). Fluxgate magnetometers are composed of a magnetically susceptible core wrapped by two coils. One coil has an alternating electric current that drives the core through a cycle of magnetic saturation. The other coil measures the voltage induced by the change of the relative permeability which depends on the external magnetic field (Acuña, 2002). MAG measures the background magnetic field continuously in three directions. In normal mode acquisition frequencies are between 1 and 16 Hz. Bursts are also produced at acquisition frequencies up to 128 Hz about 10% of the time. For the study presented in Chapter 4, we use continuous MAG measurements and burst mode whenever available.

3.2 Parker Solar Probe

Parker Solar Probe (PSP) is a NASA mission launched in August 2018 to collect measurements of plasma parameters and electromagnetic fields in the inner heliosphere. The first solar encounter had its perihelion at 35.7 $R_\odot$ ($\simeq$ 0.17 AU); subsequent perihelia over the seven-year nominal mission will drop closer to the Sun, eventually reaching a heliocentric distance of 10 $R_\odot$ ($\simeq$ 0.05 AU) in mid-2025. This mission offers unique opportunities to study *in situ* the young solar wind in areas where no direct measurements have ever been performed before (Fox et al., 2016; Raouafi et al., 2023). The mission has three main objectives (taken from Fox et al., 2016):

- Trace the flow of energy that heats the solar corona and accelerates the solar wind;
- Determine the structure and dynamics of the plasma and magnetic fields at the sources of the solar wind;
- Explore mechanisms that accelerate and transport energetic particles.

To answer these questions PSP has three *in situ* experiments, SWEAP (Kasper et al., 2016) , FIELDS (Bale et al., 2016), IS⊙IS (McComas et al., 2016) and one remote sensing WISPR (Vourlidas et al., 2016). SWEAP and IS⊙IS measure the particles (IS⊙IS measuring the most energetic particles) while FIELDS measures the electromagnetic fields. WISPR measures the solar corona in white light. The numerous discoveries of Parker Solar Probe have been the subject of a recent review by Raouafi et al. (2023).

In this thesis, we use FIELDS and SWEAP. We present briefly hereafter the main characteristics of these instrument suites (Sections 3.2.1 and 3.2.2).

3.2.1 FIELDS

The FIELDS experiment suite includes four electric antennas (EFI) located in the plane of the spacecraft heat shield. This plane is the $(\vec{X}, \vec{Y})$ plane of the spacecraft (SC) coordinate system, where the $\vec{Z}$ axis is directed toward the Sun as presented in Figure 3.2. These antennas can therefore be used to determine $E\mathrm{w_x}$ and $E\mathrm{w_y}$ using the measurements of $E\mathrm{w}_{1,2} = (V_1 - V_2)/L_{\mathrm{eff}}$ and $E\mathrm{w}_{3,4} = (V_3 - V_4)/L_{\mathrm{eff}}$ (if L_{eff} is known), which we then transfer to the $(\vec{X}, \vec{Y})$ reference frame. These antenna measurements cover frequencies from DC to 1 MHz. A Search-coil Magnetometer (SCM) (Jannet et al., 2021) measures the 3 Hz to 1 MHz fluctuations of up to three of the orthogonal $(\vec{u}, \vec{v}, \vec{w})$ components of the magnetic field. The SCM has three low-frequency (LF) windings, one for each component, that cover frequencies from 3 Hz Hz to 20 kHz, and one medium-frequency (MF) winding on the $\vec{u}$ component that measures from 1 kHz to 1 MHz. The SCM is placed at the end of the boom (Figure 3.2) and its reference frame $(\vec{u}, \vec{v}, \vec{w})$ is different from that of the spacecraft (Malaspina et al., 2016). A description of these various reference frames as well as the rotation matrix for transforming from the SCM frame to the spacecraft frame is presented in Appendix B. The

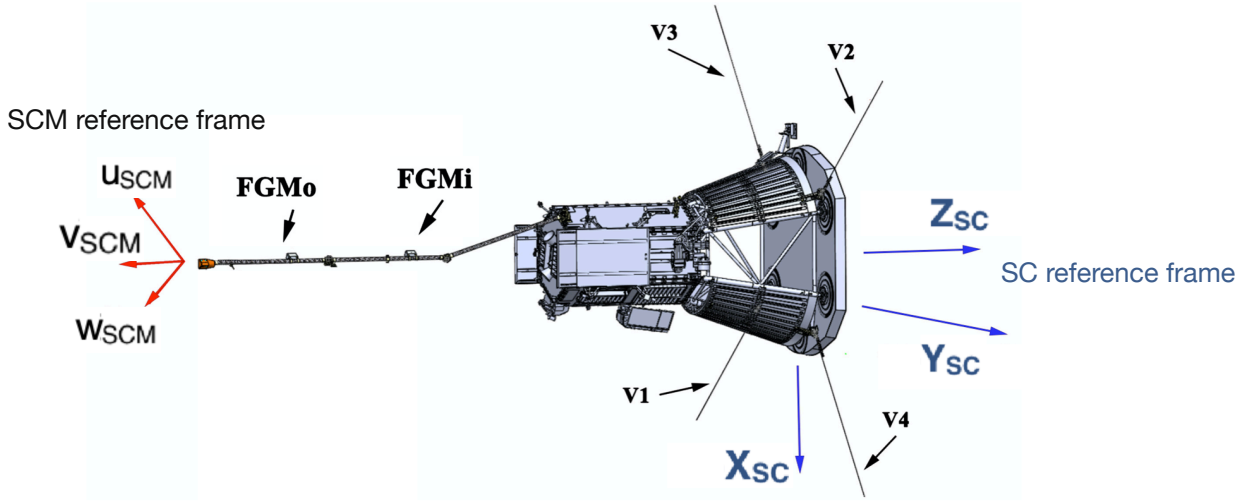

Figure 3.2: Schematic representing Parker Solar Probe and the sensors of the FIELDS experiment. The spacecraft (resp., SCM) reference frames described in the text are represented by blue (resp., red) arrows. Adapted from Malaspina et al. (2016).

SCM has revealed a multitude of different wave phenomena in the solar wind, reviewed by Dudok De Wit et al. (2022). The FIELDS experiment also includes two triaxial fluxgate magnetometers (called MAGs or FGMs) that measure the background magnetic field from DC up to about 100Hz. These magnetometers are shown in Figure 3.2.

The data products from FIELDS include continuous waveforms with sampling rates between 292.97 and 2343.75 Hz in the vicinity of perihelia (146 Hz and 73 Hz at larger distances from the Sun). Waveforms with an acquisition frequency of 2343.75 Hz are only available from Encounter 7 (January 2021). There are also 3.5 s burst waveform intervals with 150 kHz sampling rate (up to a few dozen a day in the vicinity of perihelia). Another product is continuous cross-spectra (every 27.96 s) that enable the polarization properties of whistler waves to be determined over the frequency range of 23 to 4541 Hz in 54 logarithmically spaced frequency channels. Finally, Band-Pass Filtered data (BPF) provide the amplitude of the magnetic field every 0.87 s with a lower frequency resolution. In this thesis we use continuous waveforms at 292.97 Hz, burst waveforms at 150 kHz) and MAG data for the studies presented in Chapters 4 and 5.

3.2.2 SWEAP

The SWEAP experiment is composed of four instruments. There is one Faraday cup: Solar Probe Cup (SPC) (Case et al., 2020). The three other instruments are electrostatic analyzers: the Solar Probe ANalyzer for Ions (SPAN-I, (Livi et al., 2022)) and the Solar Probe ANalyzer for Electrons (SPAN-E), which is composed of two heads (SPAN-A and SPAN-B, (Whittlesey et al., 2020)).
The SPC instrument is always pointing toward the Sun and measures the ions and electrons

of the solar wind whose flow is mainly radial with a FOV $\sim 30°$.
The SPAN-I instrument points toward the $-\vec{X}$ direction and is complementary to SPC for the measurement of ions, especially during the closest encounters. Indeed, during these encounters the measured solar wind will have a strong non-radial component because of the important orbital velocity of PSP $\sim 190\text{kms}^{-1}$. An important part of the ion flux will then enter the FOV of SPAN-I. The latter, measures ions with energies between 2 eV and 30 keV and separate measurements of the 3D VDFs of H^+ and He^{++} ions.
The two heads SPAN-A and SPAN-B have a combined FOV of $\sim 4\pi$ sr (as for the SWA experiment, blockages due to the spacecraft, the sensor structure, etc. are present). These electrostatic analyzers measure the electron distribution functions in their reference frames in 16 azimuths, 8 elevations, and 32 energy bins (between 2 eV to 30 keV). Temporal resolution these full 3D distributions varies between 27.96 s and 0.3 s. In Chapters 4 and 5 we use data from SPC to estimate the background plasma density and the solar wind speed.

3.3 Data analysis and caveats

We now present the work performed and the analysis methods used on the data presented in the previous sections. We emphasize the precautions to be taken in order to exploit at best these data.

3.3.1 Methods of detection and characterization of whistler waves

We begin by describing the methods used to detect and characterize whistler waves. The statistical study of the characteristics of whistler waves in the solar wind was often carried out in the spacecraft frame using spectral products (Tong et al., 2019a; Jagarlamudi et al., 2020; Jagarlamudi et al., 2021; Cattell et al., 2022).

The full characterization of the waves, with their amplitudes, angle of propagations, frequencies, and polarizations in the plasma frame using waveforms necessitates the joint and careful analysis of both the electric and magnetic fluctuations but also of some basic plasma parameters.

3.3.1.1 Detection of whistler waves

Whistler waves are detected in a similar way as in Kretzschmar et al. (2021). In short, this consists of locating the periods of time where the magnetic field fluctuations over at least 2 Hz are at least twice the median fluctuation of the day. If such a bump is detected, we define a wave packet as the part of the band-pass filtered time series with fluctuations larger than the upper quartile. A wave packet must be composed of at least four periods. We choose to detect waves using their amplitudes of fluctuations and not by looking for planarity or polarization close to 1. Indeed, we first wanted to make sure there were no other modes in the frequency range under consideration $\omega \in\sim [0.02, 0.3]\omega_{\text{ce}}$. The threshold considered is quite low, as most of the waves observed have fluctuations of several orders of magnitude

greater than the median fluctuations over about ten hertz. We also tried several thresholds and didn't notice any significant change in the results.

Next, we calculate the propagation angle with respect to the background magnetic field (θ) using both a minimum variance analysis (Sonnerup and Scheible, 1998) on the filtered wave packets and the analysis of the computed spectral matrices (Means, 1972; Santolík, Parrot, and Lefeuvre, 2003; Taubenschuss and Santolík, 2019). The final angle of propagation is the mean value of the angles obtained with the two methods (which give generally very close results). These methods are presented in Appendices C.1 and C.2. We also check, in the plasma frame, that the coherence, planarity, and polarization of the waves (see Appendix C.2) are all greater (using the spectral energy content weighted average) than 0.6 over the considered frequency range.

The methods described in Appendices C.1 and C.2 give the propagation angle with an ambiguity of $\pm 180°$ which is removed by calculating the radial direction of propagation, as explained in the next section. In the next two sections (3.3.1.2, 3.3.1.3), we place ourselves in the Solar Orbiter SRF reference frame, described in Section 3.1. We present methods for determining the direction of propagation of whistler waves and the effective length of electric antennas in the context of the Solar Orbiter mission. The methods described are also applicable to Parker Solar Probe.

3.3.1.2 Radial direction of propagation

As explained in Section 2.3, the radial direction of propagation (sunward or anti-sunward) indicates whether the wave is directed toward the Sun or not. The radial direction of propagation, in the spacecraft frame, is determined by computing the sign of the X component of the Poynting vector $\vec{S}$ (Equation 3.4, (Chust et al., 2021)):

$$S_{\mathrm{X}} = \frac{\left(E^{\mathrm{SC}}{}_{\mathrm{WY}} B^{*}{}_{\mathrm{WZ}}\right)(\omega, t) - \left(E^{\mathrm{SC}}{}_{\mathrm{WZ}} B^{*}{}_{\mathrm{WY}}\right)(\omega, t)}{2\mu_0} \tag{3.4}$$

where (ω, t) stands for the time average Fourier component and * for the complex conjugate. The electric field is measured in the spacecraft frame, which is different from the plasma frame. In the following, quantities with the $^{\mathrm{SC}}$ superscript are in the spacecraft frame while quantities in the plasma frame (i.e., taking into account the Lorentz transformations (Feynman, 1964)) are noted without superscript. For the magnetic field, since the measured solar wind speed (V_{SW}) verifies $V_{\mathrm{SW}} << c$ (where c is the speed of light) these transformations can be neglected and we can safely consider that $\vec{B}^{\mathrm{SC}}\mathrm{w} = \vec{B}\mathrm{w}$. For the electric field, on the other hand, we have:

$$\vec{E}^{\mathrm{SC}}\mathrm{w} = \vec{E}\mathrm{w} - \left(\vec{V}_{\mathrm{SW}} \wedge \vec{B}\mathrm{w}\right) \tag{3.5}$$

We can note that the X component of the Poynting vector is the only one directly available. A positive value of $\Re S_{\mathrm{X}}$ indicates a propagation toward the Sun (where $\Re$ is the real part).

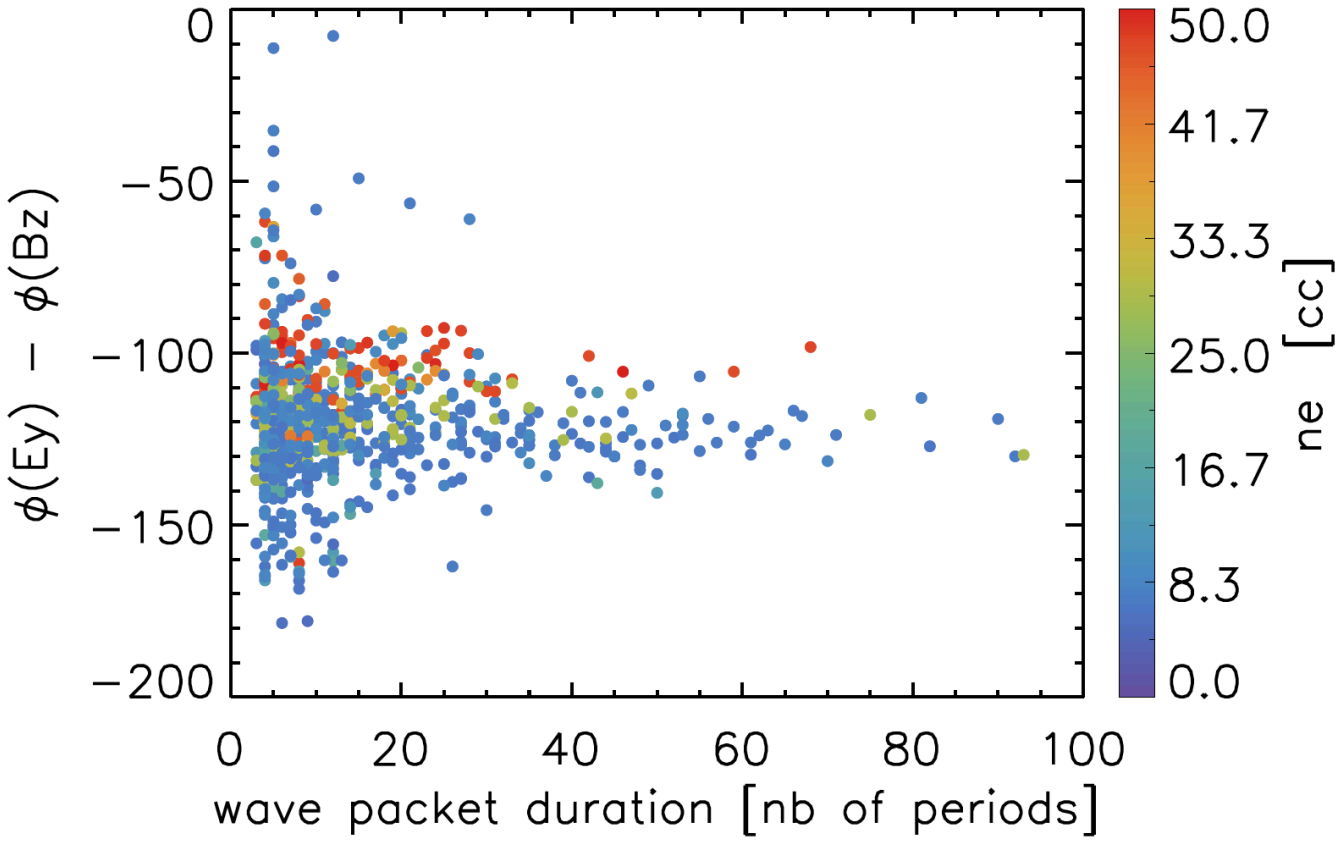

Figure 3.3: Phase shift between $E\mathrm{w_Y}$ and $B\mathrm{w_Z}$ as a function of the wave paquets duration and the density in cm^{-3}. Figure taken from Kretzschmar et al. (2021).

As explained by Kretzschmar et al. (2021), there is an unexpected and nearly constant phase shift between the electric and magnetic field in the Solar Orbiter RPW LFR measurements. In this study, they showed that $E\mathrm{w_Y}$ (resp., $B\mathrm{w_Z}$) should be delayed (resp., advanced) by removing (resp., adding) 50°, which is the weak phase deviation hypothesis. This phase shift has been well established in the case of quasi-aligned whistler waves. A constant 50° phase shift correction would not change the sign of $\Re S_\mathrm{X}$ for a perfect wave having a theoretical phase shift between the magnetic and electric field equal to 0° or 180° (for sunward and anti-sunward propagation, respectively). However, as was shown by Kretzschmar et al. (2021), the phase shift is not perfectly constant (small dependence with density) and there are of course uncertainties in the measurements. The phase shift between $E\mathrm{w_Y}$ and $B\mathrm{w_Z}$ obtained by Kretzschmar et al. (2021) using SWFs from Solar Orbiter during Orbit 1 is shown in Figure 3.3. We can see that if $B\mathrm{w_Z}$ is advanced by 50°, we obtain a phase shift between the magnetic and electric field equal to 180°, coherent with anti-sunward propagating waves.

In this thesis, we therefore pay special attention to the determination of the radial direction of propagation of the waves measured by Solar Orbiter RPW LFR. First, we consider only the cases with $k_\mathrm{X}/|k| \geq 15\%$ and with the coherence between $(E\mathrm{w_Y}, B\mathrm{w_Z})$ and $(E\mathrm{w_Z}, B\mathrm{w_Y})$

greater than 0.6. Then, we look at the phase of S_{X} ($\varphi_{S_{\mathrm{X}}}$). With a constant 50° phase shift, the observed value of $\varphi_{S_{\mathrm{X}}}$ is expected to be $\varphi_{S_X} = 50°$ and $\varphi_{S_X} = -130°$ for sunward and anti-sunward propagation, respectively. Here, we categorise the cases as sunward propagating if $0° \leq \varphi_{S_{\mathrm{X}}} \leq 100°$ and anti-sunward propagating if $-180° \leq \varphi_{S_X} \leq -80°$. These restrictive constraints leave a large number of cases unresolved (hereafter, referred to as "poorly defined") but ensure, when they are verified, that the direction of propagation is correctly characterized.

We finally determine the right or left-handed polarization (in the spacecraft frame) in the following way. For a right-handed polarization, with the magnetic field fluctuations $\vec{B}_{\mathrm{w}}$ expressed in a direct orthogonal Cartesian reference frame where $\vec{Z}$ is along the wave vector $\vec{k}$, we expect a phase shift of $\pm$ 90 ° between the X and Y components (if $\vec{k}$ and $\vec{B}_0$ are aligned and anti-aligned, respectively). This is the case, for anti-sunward waves and for sunward waves with $V_\varphi \geq V_{\mathrm{SW_k}}$ (where V_φ is the phase velocity in the plasma frame and $V_{\mathrm{SW_k}}$ the solar wind speed along the $\vec{k}$ direction). Sunward whistler waves propagating with $V_\varphi < V_{\mathrm{SW_k}}$ have a left-handed polarization in the spacecraft frame.

We can then determine other parameters characterizing these wave packets, such as their durations, amplitudes, and frequencies. For this last parameter, we calculate the frequency in the plasma reference frame (taking into account the Doppler effect) using the following equation:

$$\omega\mathrm{SC} = \omega\mathrm{asun,sun} \pm kV_{\mathrm{SW}}|\cos(\theta_{\vec{k},\vec{V}_{\mathrm{SW}}})| \tag{3.6}$$

where ωSC is the frequency in the spacecraft frame, $\omega\mathrm{asun,sun}$ the frequency in the plasma frame for an anti-sunward (resp., sunward) whistler waves corresponding to the + (resp., −) in Equation 3.6. k is computed with Equation 2.8.

3.3.1.3 Effective length

In this section, we detail the method used to determine the effective length of the antennas. As a first approximation, it is possible to take the tip-to-tip length between the antennas as effective length (Maksimovic et al., 2020; Steinvall et al., 2021; Chust et al., 2021). On the other hand, the observation of whistler waves can be used to determine precisely the effective length by comparing theoretical and measured phase velocities of the waves (Chust et al., 2021; Kretzschmar et al., 2021).
Writing the electric and magnetic fields as plane wave superposition and using the Maxwell-Faraday equation one obtains:

$$\vec{n} \wedge \vec{E}_{1\vec{k}} = \frac{\omega}{k}\vec{B}_{1\vec{k}} \tag{3.7}$$

where $\vec{n} = \vec{k}/k$. By projecting on $\vec{X}$ we arrive at:

$$\frac{\omega}{k} = \frac{n_{\mathrm{Y}}E_{1\vec{k}\mathrm{Z}} - n_{\mathrm{Z}}E_{1\vec{k}\mathrm{Y}}}{B_{1\vec{k}\mathrm{X}}} \tag{3.8}$$

As detailed in Appendix A of Chust et al. (2021) a way to estimate $\frac{\omega}{k}$ with measurements is the following:

$$\frac{\omega}{k} \simeq \frac{n_{\mathrm{Y}}\left(E\mathrm{w}_{\mathrm{Z}}B^{*}\mathrm{w}_{\mathrm{X}}\right)(\omega,t)/\rho_{E\mathrm{w}_{\mathrm{Z}}B\mathrm{w}_{\mathrm{X}}} - n_{\mathrm{Z}}\left(E\mathrm{w}_{\mathrm{Y}}B^{*}\mathrm{w}_{\mathrm{X}}\right)(\omega,t)/\rho_{E\mathrm{w}_{\mathrm{Y}}B\mathrm{w}_{\mathrm{X}}}}{\left(B\mathrm{w}_{\mathrm{X}}B^{*}\mathrm{w}_{\mathrm{X}}\right)(\omega,t)} = v_{\varphi 1}(\omega) \tag{3.9}$$

With the hypothesis of plane waves, $v_{\varphi 1}(\omega)$ is real. However, since we do not exactly measure plane waves, we can estimate, in practice, the phase speed using:

$$v_{\varphi 1}(\omega) = sign(\Re v_{\varphi 1})|v_{\varphi 1}| \tag{3.10}$$

Moreover, if one makes the approximation $\vec{E_{\mathrm{w}}} \cdot \vec{B_0} \simeq 0$ (whose validity is discussed in detail in Section 5.1.3), one can establish another approximation for the phase velocity (see Appendix A of Chust et al. (2021)):

$$\frac{\omega}{k} \simeq \frac{\left(\vec{n}\cdot\vec{B_0}\right)\left(E\mathrm{w}_{\mathrm{Y}}B^{*}\mathrm{w}_{\mathrm{Y}}\right)(\omega,t)/\rho_{E_{\mathrm{Y}}B_{\mathrm{Y}}}}{B_{0X}\left(B\mathrm{w}_{\mathrm{Z}}B^{*}\mathrm{w}_{\mathrm{Y}}\right)(\omega,t)/\rho_{B\mathrm{w}_{\mathrm{Z}}B\mathrm{w}_{\mathrm{Y}}} - B_{0Z}\left(B\mathrm{w}_{\mathrm{X}}B^{*}\mathrm{w}_{\mathrm{Y}}\right)(\omega,t)/\rho_{B\mathrm{w}_{\mathrm{X}}B\mathrm{w}_{\mathrm{Y}}}} = v_{\varphi 2}(\omega) \tag{3.11}$$

Similarly, $v_{\varphi 2}(\omega)$ can be calculated as:

$$v_{\varphi 2}(\omega) = sign(\Re v_{\varphi 2})|v_{\varphi 2}| \tag{3.12}$$

With Equation 3.11 the phase velocity is expressed using only the Y component of the electric field. As explained by Chust et al. (2021) and Kretzschmar et al. (2021), this component is the most reliable at this stage of the mission. This can be explained by the fact that the evaluation of this component requires only the measurement of a single potential difference (see Equation 3.2), unlike the Z component.

Taking into account Lorentz transformations (Equation 3.5), we have:

$$E\mathrm{w}_{\mathrm{Y}} = E\mathrm{w}_{\mathrm{Y}}^{\mathrm{SC}} - V_{\mathrm{SWX}}B\mathrm{w}_{\mathrm{Z}} + V_{\mathrm{SWZ}}B\mathrm{w}_{\mathrm{X}} \tag{3.13}$$

Using Equations 3.2, 3.11 and 3.13 we find:

$$L_{\mathrm{effY}} = \left| \frac{\left(V^{\mathrm{SC}}\mathrm{w}_{\mathrm{Y}}B^{*}\mathrm{w}_{\mathrm{Y}}\right)}{\frac{\omega}{k(\vec{n}\vec{B_0})}\left(B_{0X}\left(B\mathrm{w}_{\mathrm{Z}}B^{*}\mathrm{w}_{\mathrm{Y}}\right) - B_{0Z}\left(B\mathrm{w}_{\mathrm{X}}B^{*}\mathrm{w}_{\mathrm{Y}}\right)\right) + V_{\mathrm{SWX}}B\mathrm{w}_{\mathrm{Z}}B^{*}\mathrm{w}_{\mathrm{Y}} - V_{\mathrm{SWZ}}B\mathrm{w}_{\mathrm{X}}B^{*}\mathrm{w}_{\mathrm{Y}}} \right| \tag{3.14}$$

where we dropped the $(\omega,t)/\rho$ to simplify notations. It is worth noting that we generally have $V_{\mathrm{SWZ}} \ll V_{\mathrm{SWX}}$, so the last term of the denominator can be neglected. Finally, note that

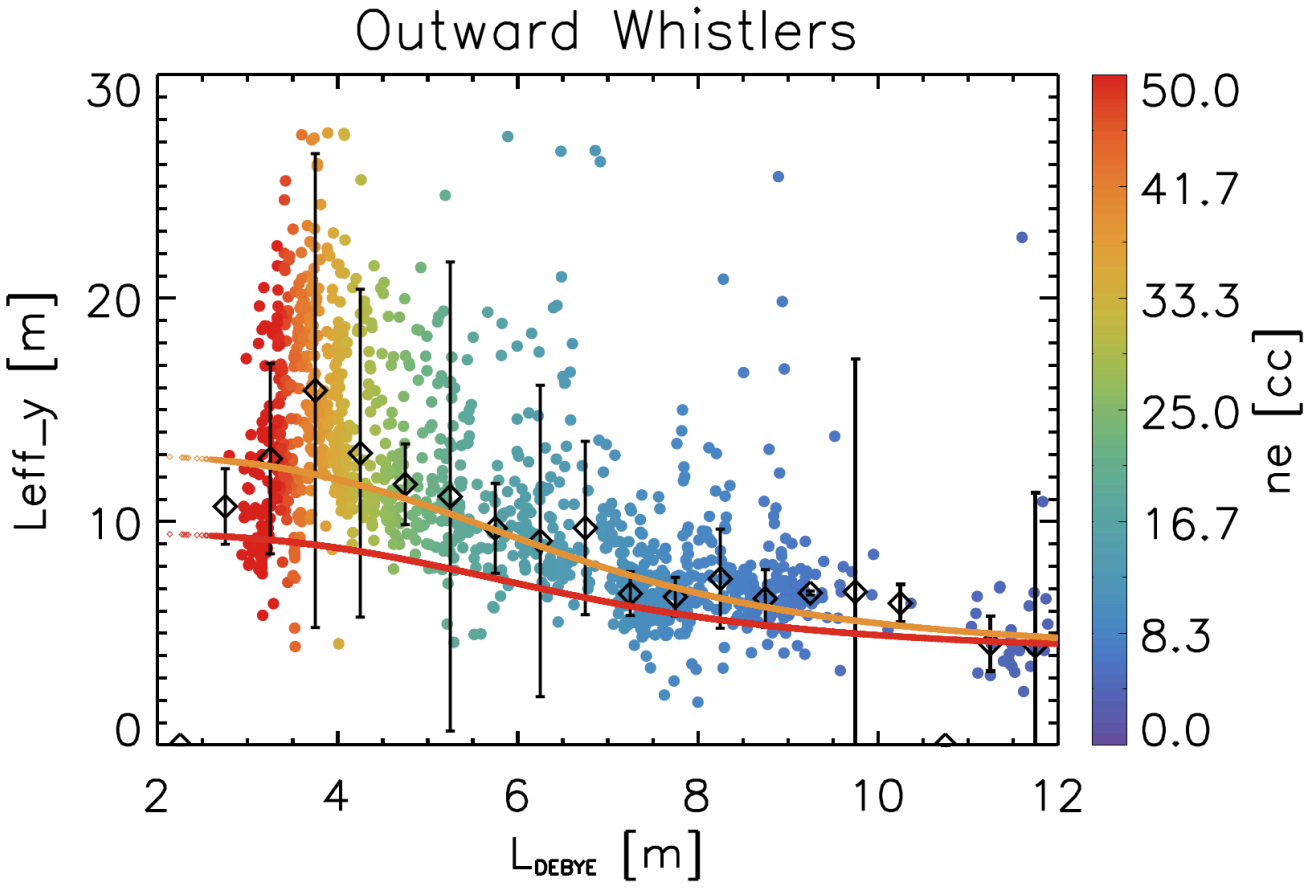

Figure 3.4: Effective length (L_{effY}) as a function of the Debye length and the local electron density for anti-sunward (outward) propagating whistlers in colored dot. The relation derived by Steinvall et al. (2021) is in red and the same relation but using Leff,max=13 m is in orange. Figure taken from Kretzschmar et al. (2021).

since we are in the SRF reference frame, $V_{\text{SWX}} \leq 0$.

Kretzschmar et al. (2021) used Equation 3.14 to calculate L_{effY} and compared it to the relation derived by Steinvall et al. (2021). In the latter study, they compared the solar wind speed measured by SWA/PAS with the values obtained by measurements of the DC electric and magnetic fields expressed in the deHomann-Teller reference frame. The comparison of the results of these two studies is presented in Figure 3.4. There is a global good agreement between the results of Steinvall et al. (2021) (using Leff,max=13 meter) and those of Kretzschmar et al. (2021). On the other hand, there is a large dispersion of effective lengths obtained by Kretzschmar et al. (2021), especially for short Debye lengths. Furthermore, we note large effective lengths (over 25 meters) compared to the length of the electrical antennas (6.5 meters). The origin of these long effective lengths is not fully understood at this time.

3.3.2 Methods for analyzing electron distribution functions

The methods used in this thesis to obtain pitch-angle distributions, fit the VDFs by Maxwellian functions and plot the VDFs in a 2D velocity space $(v_\perp, v_{||})$ in the solar wind reference frame are similar to those detailed in Bercic et al. (2019), Berčič (2020), and Berčič et al. (2021) and are briefly described below.

First, we express the data (measured in the spherical reference frame of the instrument) in the spacecraft reference frame. We then go to the plasma reference frame by subtracting the solar wind and spacecraft speeds from the measured velocities. Finally, we go to a spherical reference frame whose axis $\vec{Z}$ is along $\vec{B}_0$.

To obtain a pitch-angle distribution, energies of interest must be selected. Those energies typically correspond to the suprathermal electrons of the halo and the Strahl. It is then sufficient to sum over all the azimuths. Such plots are shown in Chapter 4 (Figures 4.6 and 4.11).

To realize a fit of the VDF by a Maxwellian distribution, it is necessary to choose the energy range corresponding to the population we want to fit. The fitting method by a bi-Maxwellian distribution is detailed in Berčič et al. (2021). We can note that to fit the core electrons, electrons in the Strahl direction are not to be taken into account, so as not to be contaminated by this population and overestimate the parallel temperature. These fits can then be superposed to the data by selecting the electrons with a pitch angle between $[90° - \alpha_{lim}/2d, 90° + \alpha_{lim}/2d]$, $[0°, \alpha_{lim}]$, $[180° - \alpha_{lim}, 180°]$ for the perpendicular, aligned and anti-aligned components, respectively. Where α_{lim} is taken equal to 15°. An example of such a plot is shown in Figure 3.5. In this figure, we plot the mean values of the velocity distribution functions measured by PSP/SWEAP (SPAN-A and SPAN-B) on 2021/11/20 between 8:50 and 9:10 for different pitch angle ranges. This example has already been studied by Halekas et al. (2022). We only show the core electron fit in the parallel direction for readability. We obtain for this example $T_{c||} = 34$ eV, in agreement with the study of Halekas et al. (2022). As the radial component of the magnetic field is sunward in this example (and we are outside a switchback), the Strahl is anti-parallel to the magnetic field. Indeed, the Strahl is clearly visible for speeds between $\sim [8000, 20000]\text{kms}^{-1}$ and for pitch angles between $[150, 180]°$). Above $20,000\text{kms}^{-1}$ the halo population dominates. We also notice a sunward suprathermal electrons deficit (Sections 1.3.2 and 2.3.1.2).

For 2D plots in the velocity space $(v_\perp, v_{||})$, we first construct a grid in the spherical frame with $\vec{Z}$ along $\vec{B}_0$. The data are then interpolated to this grid. An example of such a plot is shown in Figure 3.6, for the same case as in Figure 3.5. For the scaled distribution function (Figure 3.6b) each energy bin (i.e., each circle centered on (0,0) in the space $(v_\perp, v_{||})$) is scaled to the values between 0 and 1 (Berčič, 2020). For the normalized distribution function (Figure 3.6c) the values of the distribution are normalized by the perpendicular cut of the VDF ($\alpha = 90°$) (Berčič, 2020). Figures 3.6b and 3.6c again show the presence of the Strahl, anti-aligned with the magnetic field. The sunward deficit of suprathermal electrons is also

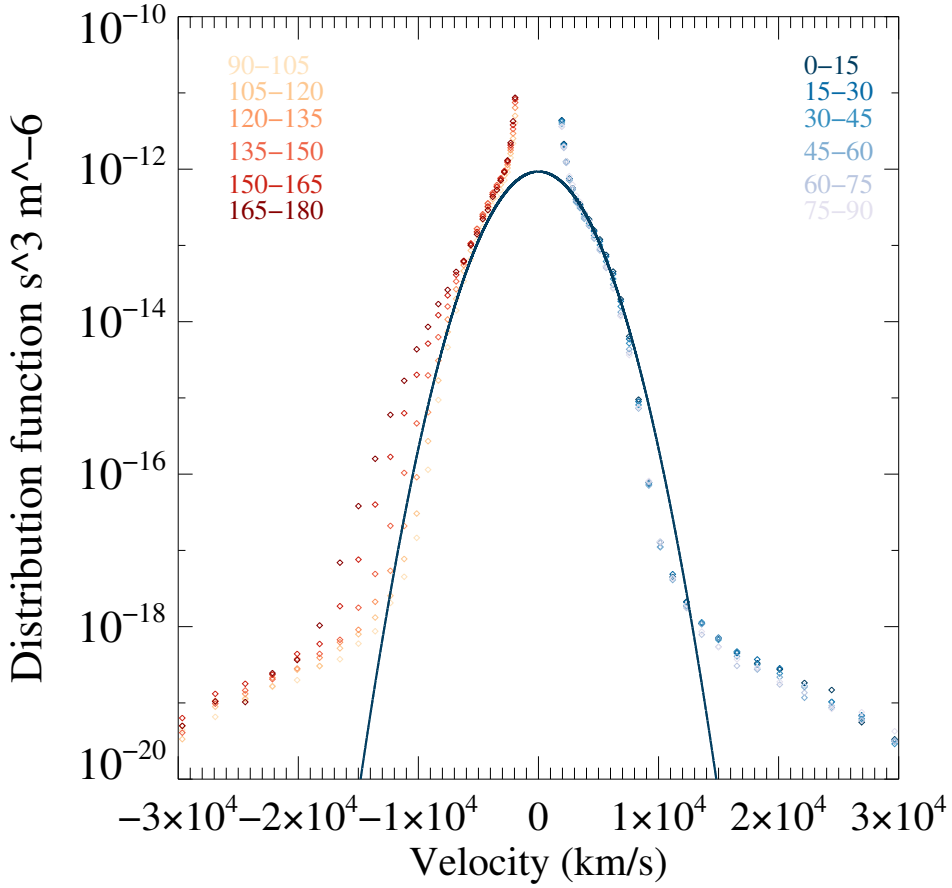

Figure 3.5: Mean values of the velocity distribution functions measured by PSP/SWEAP (SPAN-A and SPAN-B) on 2021/11/20 between 8:50 and 9:10 for different pitch angle ranges, in the proton reference frame. The pitch angle ranges are indicated in red-yellow ($\alpha > 90°$) and grey-blue ($\alpha < 90°$).

visible in Figure 3.6c.

Finally, we can note some caveats in the electron distribution functions measured by Solar Orbiter and Parker Solar Probe electrostatic analyzers. First, low-energy bins are polluted by secondary electrons. Therefore, energy bins below $\sim$ 15 eV ($\sim$ 2300kms^{-1}) for Solar Orbiter (Owen et al., 2020; Berčič et al., 2021) and below $\sim$ 25 eV ($\sim$ 3000kms^{-1}) for Parker Solar Probe measurements (Whittlesey et al., 2020) must not be used. These secondary electrons are visible in Figure 3.5. Thus, to achieve the Maxwellian fit Figure 3.5 we use electrons with energies between $[25, 180]$ eV. Moreover, as mentioned in Section 3.1.2 some areas of the FOV are blocked by the spacecraft, the sensor structure, etc. It is therefore necessary to take these blockages into account in the analysis of the data in order not to misinterpret a lack of electrons in one direction. Specifically, electrons with perfectly radial, anti-sunward velocities will be blocked by the heat shields. Data from these directions are therefore ignored.

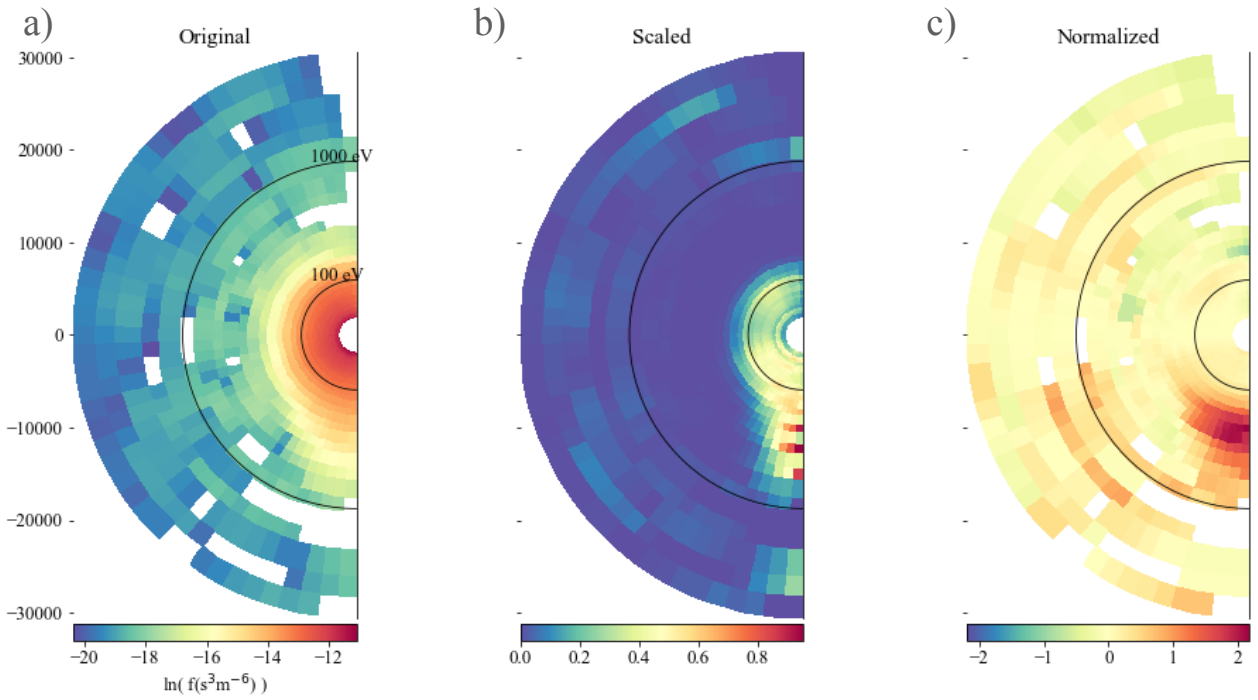

Figure 3.6: Mean values of the velocity distribution functions measured by PSP/SWEAP (SPAN-A and SPAN-B) on 2021/11/20 between 8:50 and 9:10 in the plane $(v_\perp, v_{||})$, in the proton reference frame. *Panel a):* Raw data.*Panel b):* Scaled distribution (see text). *Panel c):* Normalized distribution (see text).

3.3.3 RPW low frequency interferences

Some signals measured by RPW are produced by the satellite or its instruments. These signals are interferences and when they are in the expected frequency range of whistler waves, they must be identified in order to take them into account when identifying the waves. The main known interferences, in the frequency range of whistler waves ($\sim [3 - 100]$ Hz, with Solar Orbiter) are described in the following Sections (3.3.3.1,3.3.3.2).

3.3.3.1 Electric variable interference and magnetic 8 Hz interference

Figure 3.7 represents the daily median power spectrum obtained with the continuous waveforms of the electric (Figure 3.7a) and the magnetic (Figure 3.7b) fields between July 7, 2020, and March 16, 2022. We notice the presence of a signal in the electric field (the thin yellow line between 20 and 40 Hz in the Figure 3.7a) which is most likely an interference. The frequency of this signal seems to be correlated with the heliocentric distance (green line). The 3rd order harmonic is partially visible between 60 and 100 Hz. The intensity of this interference is about two orders of magnitude higher than the background spectrum (this depends on the turbulence level of the day). Moreover, the frequency of the signal is variable and in the typical range of whistler waves at the heliocentric distances considered. We can note that the source of the interference has not been identified at this time. The detection of whistlers using the electric field and automatically detecting this interference was carried out. The results are presented in Chapter 4.
We notice, that this interference is not present in the magnetic field. On the other hand, horizontal lines in the magnetic field daily median power spectrum correspond to interference at 8 Hz and its harmonics (Figure 3.7b). The source of this interference has been identified as the on-board computer clock. This interference is of low intensity compared to the measured waves and about one order of magnitude greater than the background spectrum (this depends again on the turbulence level of the day). The frequency of this interference does not vary with time. The detection method consisting of dividing the spectrum of the magnetic field fluctuations by the median spectrum of the day, as explained in Section 3.3.1.1, is therefore sufficient to solve this issue.

3.3.3.2 1.3 Hz SCM interference

Figure 3.8 represents the median power spectrum obtained using the continuous waveforms of the magnetic field measured on March 15, 2021. We notice a strong signal at 1.3Hz, its harmonics, and the interference at 8 Hz (already discussed in the previous section). The 1.3Hz (and harmonics) signal is continuously present. This interference might be due to the heating of the SCM. Indeed, the SCM being in the umbra of the heat shield it is necessary to heat this instrument periodically. At the time of the heating, a current is created and generates a strong magnetic field. The operating times of the heater are known and taken into account in the quality flag of the SCM. However, this might also create a persistent interference at 1.3 Hz. This interference is of high amplitude and prevents the characterization of whistler

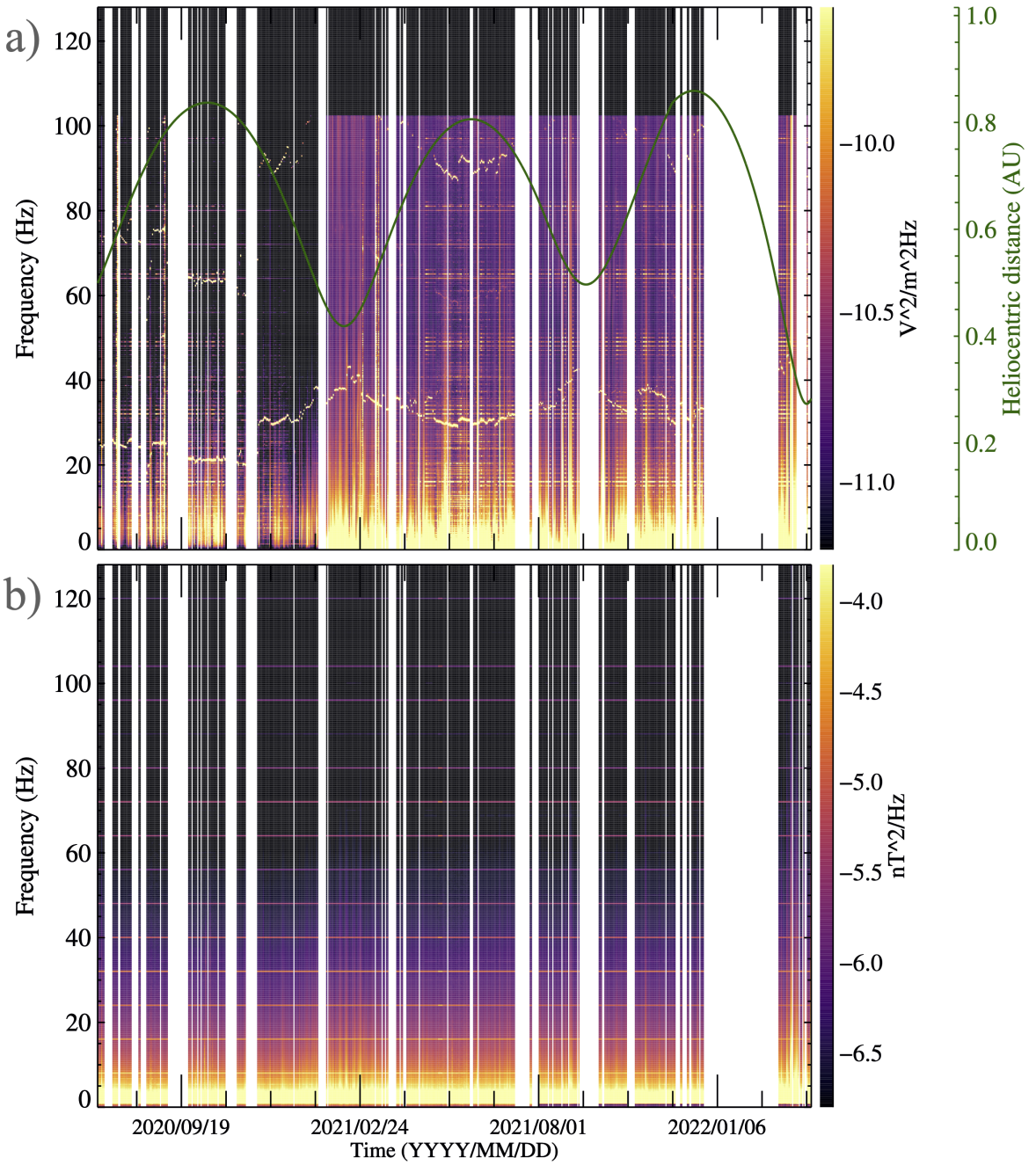

Figure 3.7: *Panel a):* Daily median power spectral density of the electric field using CWFs between 2020/07/07 and 2022/03/16. The heliocentric distance is plotted in green. *Panel b):* Same as the *Panel a):* for the magnetic field.

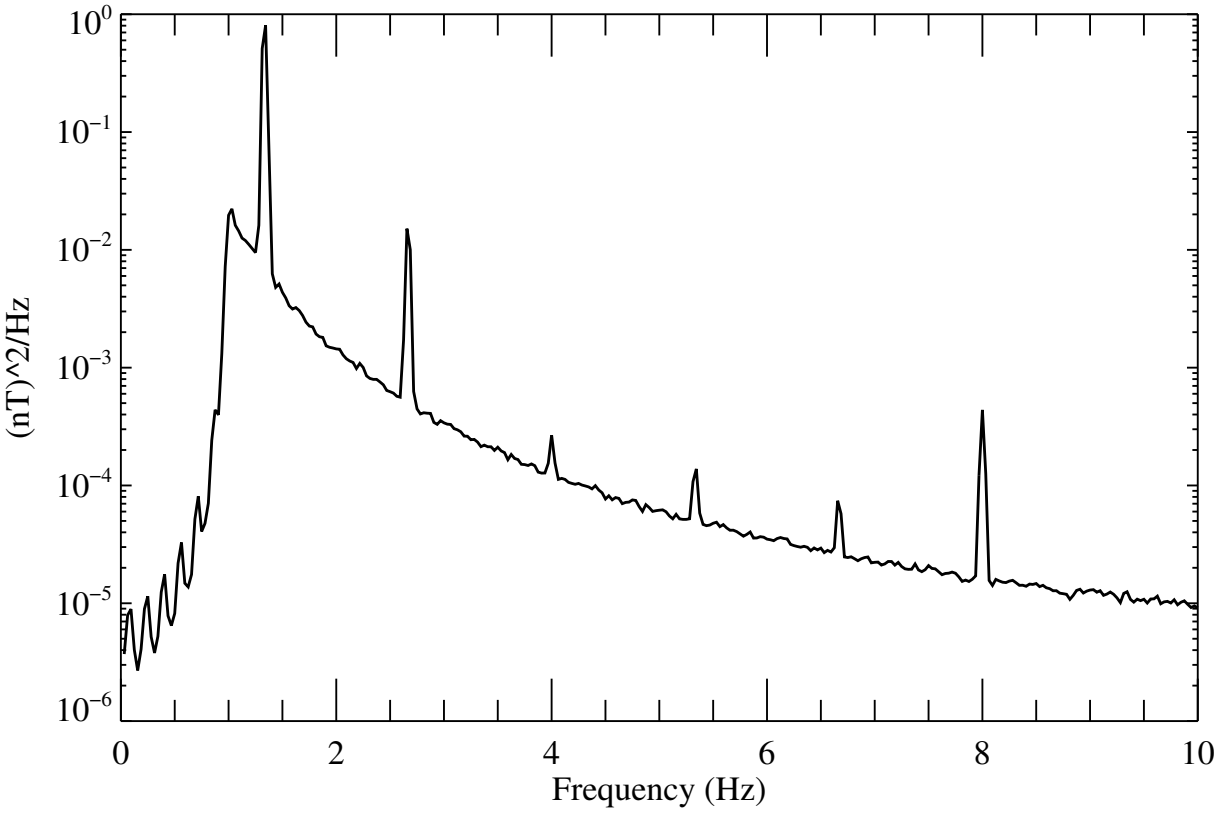

Figure 3.8: Daily median power spectrum of continuous waveforms of the magnetic field observed the 2021/03/15.

waves around 1.3 Hz and 2.6 Hz. These frequencies are however well covered by MAG which is not polluted by this interference.

3.3.4 PSP/FIELDS waveforms caveats

3.3.4.1 SCM burst waveforms V02/V03/V04 data

Burst waveforms of the SCM of Parker Solar Probe are available in several versions, with the latest versions correcting the earlier ones. Version 3 (V03) (dating from October 2020) was intended to correct a sign error in V02. We have noticed some unexpected differences between these two versions, already pointed out by Scott Karbashewski. Therefore, we compared the waveforms of a whistler wave packet measured by the SCM and the MAG of PSP. In Figure 3.9 we show a whistler wave packet observed on 2018/11/03 at 10:30 UT whose major part of the spectral energy content is between 4 and 70 Hz (Figure 3.9e). This wave packet is therefore in the frequency range of SCM and MAG. In Figures 3.9a to 3.9d, all waveforms are bandpass filtered between 4 and 70 Hz (3rd order Butterworth) and we plot the v component (in the SCM frame). We notice that V02 data (taking into account the sign error, Figure 3.9a) are in better agreement with the MAG measurements than V03 data (Figure 3.9b), as

Scott Karbashewski suggested. We note especially a significant phase shift between V02 and V03 (Figure 3.9d). This is surprising given that V03 must simply correct the sign error of V02. We have shown this case to the FIELDS team who have been able to discover an error in the processing of V03 data. For two days of Encounter 1 (2018-11-03 and 2018-11-05), V03 was created with an outdated kernel. The FIELDS team has provided a new version (V04) that corrects this error, which is equal in absolute value to V02, and which we use thereafter.

3.3.4.2 Comparison between continuous and burst waveforms

We finally compare the continuous (at 2343.75 Hz) and burst (at 150 kHz) waveforms to check their agreement. Figure 3.10 presents a whistler wave packet measured on 2021/08/08, whose spectral energy content is between about 200 and 400 Hz (not shown). All waveforms are band pass filtered between 200 and 400 Hz (3rd order Butterworth) and we plot the v component (in the SCM frame). We notice a good agreement between the burst and continuous waveforms of the SCM (Figure 3.10a). On the other hand, there is a phase and amplitude discrepancy between the burst and continuous electric field data (Figure 3.10b). We have reported this information to the FIELDS team and investigations are in progress to understand this discrepancy.

3.4 Conclusions

Overall, plasma and electromagnetic measurements in the solar wind can be complex to apprehend and analyze. Being part of the LPC2E has allowed me to participate in the team meetings of the RPW and FIELDS consortia and to gain a good knowledge of the data and their artifacts. This with the analyses presented above allowed to fully characterize whistler waves observed in the solar wind between 0.2 AU and 1 AU. The results are presented in the next chapter.

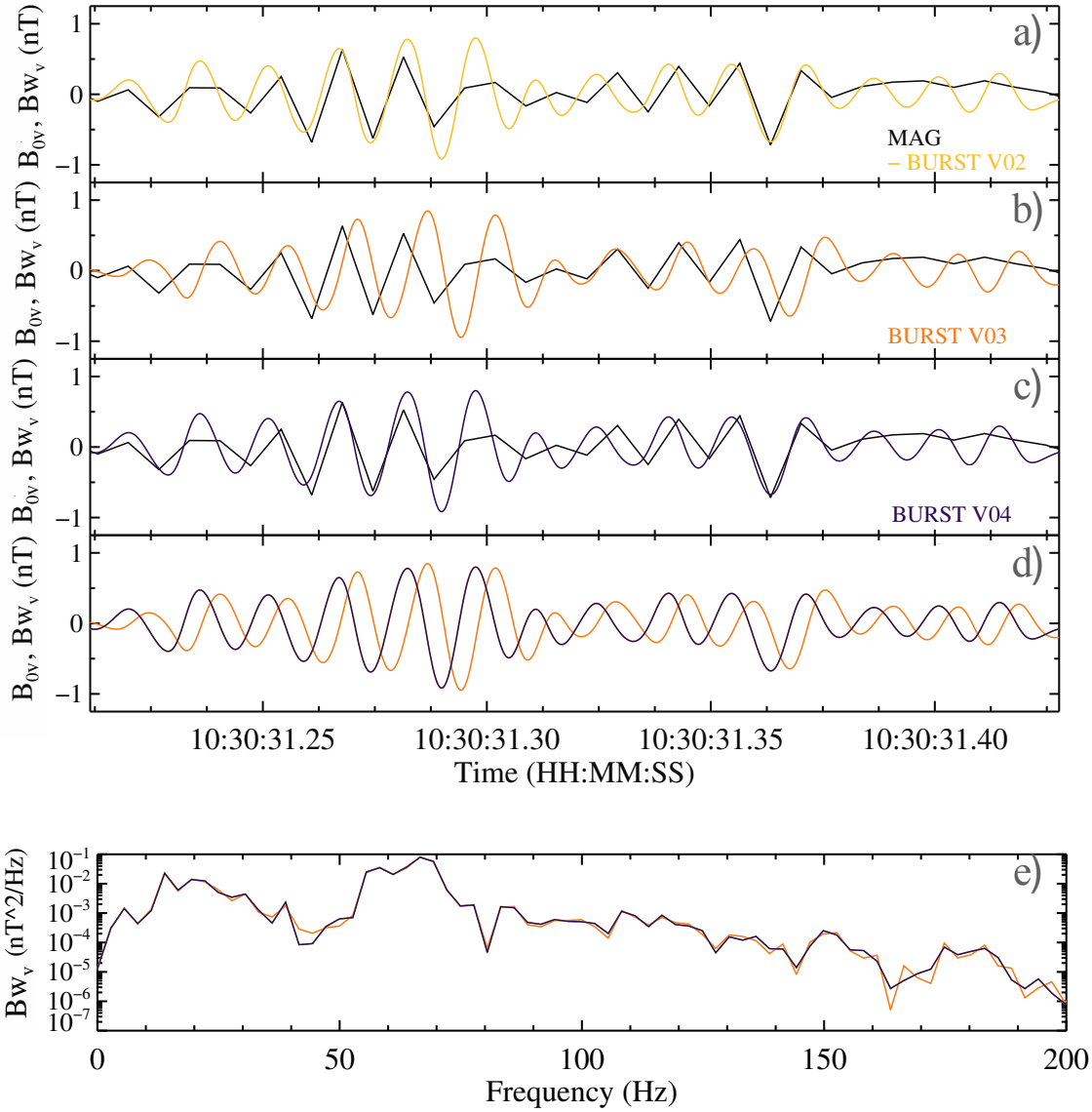

Figure 3.9: Magnetic field waveforms and power spectral density of a whistler wave packet observed by PSP on 2018/11/03 at 10:30 UT. *Panel a):* Magnetic field waveforms of the v component using MAG (B_{0v} in black) and V02 of the SCM burst data (Bw_v in yellow, with the "-" sign correction). *Panel b):* Same as in *panel a)* but using V03 of the SCM burst data (in orange). *Panel c):* Same as in *panels a) and b)* but using V04 of the SCM burst data (in purple). *Panel d):* All SCM burst data for comparison (same color code as in the previous panels, the results for V04 and V02 are identical). *Panel e):* Power spectral density of the wave packet for the different versions of the SCM burst data (same color code as in the previous panels, the results for V04 and V02 are identical).

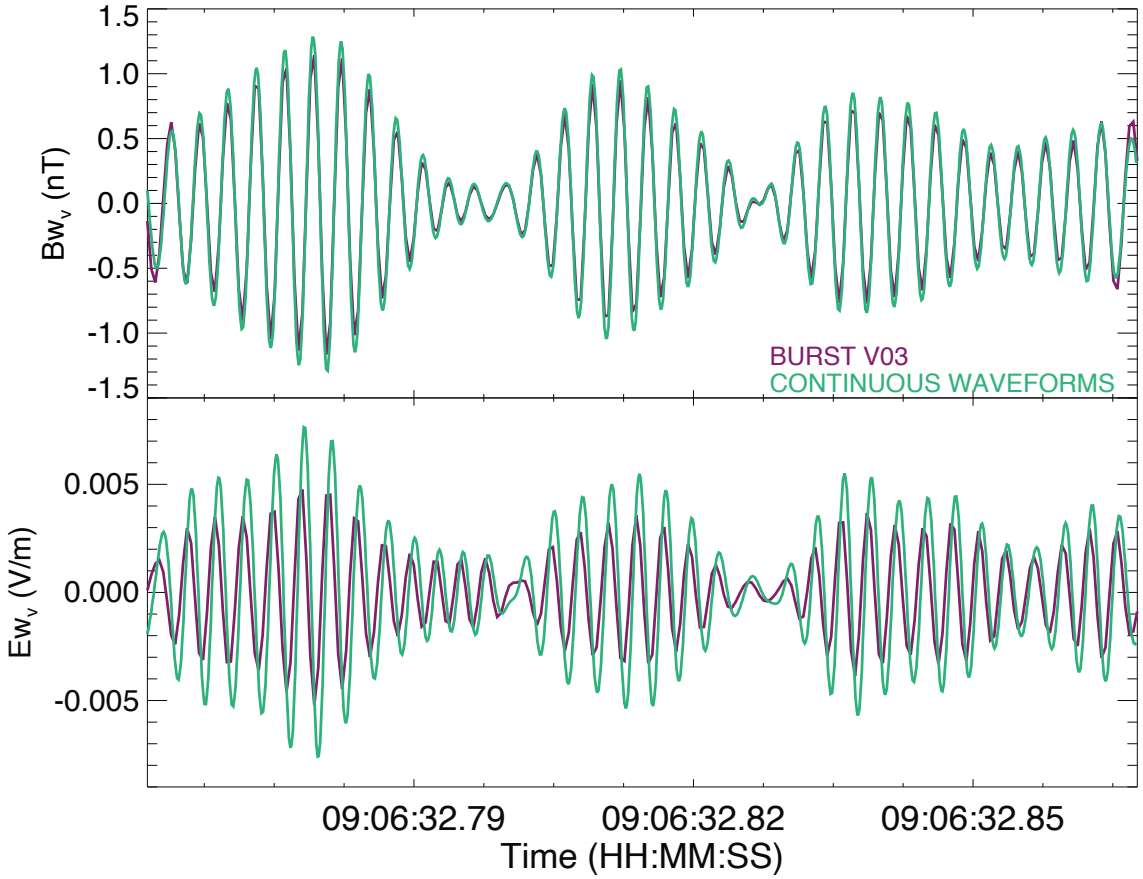

Figure 3.10: Magnetic and electric waveforms of a whistler wave packet observed by PSP on 2021/08/08 at 09:06 UT. *Upper panel:* $B\mathrm{w}_v$ continuous (resp., burst V04) waveforms in green (resp., purple). *Bottom panel:* $E\mathrm{w}_v$ continuous (resp., burst V04) waveforms in green (resp., purple).

3.5 Résumé en français du chapitre 3

Dans ce chapitre, nous présentons tout d'abord brièvement la mission Solar Orbiter. Cette dernière est une mission de l'ESA/NASA lancée en février 2020. Solar Orbiter dispose de 10 expériences, 4 *in situ* et 6 de télédétection. La phase nominale de la mission devrait durer 7 ans avec des périodes orbitales comprises entre 150 et 180 jours et des manœuvres d'assistances gravitationnelles au niveau de la Terre et de Vénus. Le périhélie le plus proche se situe à $0,28$ UA et l'aphélie le plus éloigné à $1,02$ UA. Solar Orbiter atteindra une latitude héliosphérique allant jusqu'à 18° pendant la phase nominale et supérieure à 30° pendant la phase étendue de la mission (3 ans). La combinaison de sa trajectoire et de ses nombreux instruments *in situ* et de télédétection représente une opportunité unique d'améliorer notre compréhension de l'héliosphère. Dans cette thèse, on utilise les données de 3 expériences de Solar Orbiter : RPW (Radio and Plasma Waves), MAG (Magnetometer) et SWA (Solar Wind Analyzer). RPW est un groupe d'instruments comportant un fluxmètre tri-axial (qui a été réalisé au LPC2E), trois antennes électriques et différents analyseurs à basses et hautes fréquences. Le fluxmètre mesure les fluctuations du champ magnétique entre 3 Hz et 50 kHz dans trois directions et jusqu'à 1 MHz dans une direction. Les trois antennes électriques de RPW (monopôle déployable de 6,5 m) mesurent deux composantes du champ électrique entre le continu et 16 MHz dans le plan du bouclier thermique. L'expérience SWA comprend trois instruments, dans cette thèse, nous utilisons SWA/EAS qui comprend deux têtes (EAS1 et EAS2) qui sont deux analyseurs électrostatiques permettant de mesurer la fonction de distribution des électrons. On utilise également les données de SWA/PAS pour déterminer la vitesse et la densité du vent solaire. Enfin, le magnétomètre MAG permet de déterminer le champ magnétique et ses variations.

Parker Solar Probe (PSP) est une mission de la NASA lancée en août 2018 pour mesurer des paramètres du plasma et des champs électromagnétiques dans l'héliosphère interne. La première orbite a eu un périhélie à 35,7 $R_\odot$ ($\simeq$ 0,17 AU) ; les périhélies suivants au cours de la mission nominale de 7 ans se rapprocheront du Soleil pour atteindre une distance héliocentrique de 10 $R_\odot$ ($\simeq$ 0,05 AU) au milieu de l'année 2025. Cette mission offre des opportunités uniques d'étudier *in situ* le jeune vent solaire dans des zones où aucune mesure n'a jamais été effectuée auparavant. PSP dispose de trois expériences *in situ* et une de télédétection. Dans cette thèse, on utilise les données de deux groupes d'instruments mesurant *in situ* FIELDS et SWEAP. L'expérience FIELDS comprend quatre antennes électriques (EFI) situées dans le plan du bouclier thermique du satellite. Ces antennes permettent des mesures à des fréquences allant du continu à 1 MHz. FIELDS comprend également un fluxmètre tri-axial (similaire à celui présenté pour Solar Orbiter) également construit au LPC2E, un magnétomètre et différents analyseurs. L'expérience SWEAP comprend quatre instruments, nous utilisons les données de l'instrument SPC (coupe de Faraday) pour déterminer la vitesse et la densité du vent solaire.

Nous présentons ensuite les méthodes de détection et de caractérisation des ondes de sifflement. Ces ondes sont détectées de la même manière que par Kretzschmar et al. (2021).

La cohérence, la planarité et la polarisation de l'onde sont vérifiées. L'angle de propagation par rapport au champ magnétique est déterminé en utilisant à la fois une analyse en minimum de variance et l'analyse des matrices spectrales. Ces méthodes donnent un angle de propagation avec une ambiguïté de $\pm 180°$ qui est levée en calculant la direction radiale de propagation. Cette direction est déterminée en calculant le signe de la composante radiale du vecteur de Poynting grâce à l'analyse conjointe du champ électrique. Kretzschmar et al. (2021) ont montré la présence d'un déphasage expérimental constant entre le champ magnétique et électrique mesurés par RPW, dans les données basses fréquences. Nous prenons en compte ce déphasage dans le calcul de la direction radiale de propagation en réalisant l'hypothèse de faible déviation de phase présentée dans cette étude. On décrit ensuite comment l'observation des ondes de sifflement permet de déterminer avec précision la longueur effective des antennes en comparant la vitesse de phase théorique des ondes avec la vitesse de phase mesurée. On détaille par la suite les méthodes d'analyses des fonctions de distribution des électrons, qui sont les mêmes que celles présentées dans Bercic et al. (2019, 2020, 2021).

Enfin, on décrit les interférences identifiées dans les données de RPW dans notre gamme de fréquences d'intérêt ainsi que l'identification de versions de données éronnées dans les formes d'ondes produites par PSP/FIELDS.

Chapter 4

Quantifying the diffusion of suprathermal electrons by whistler waves between 0.2 and 1 AU with Solar Orbiter and Parker Solar Probe

As explained at the end of Chapter 2, there are indications suggesting the important role of whistler waves in solar wind electron diffusion. However, a quantification of the effect of these waves on the evolution of suprathermal electron populations is still missing.

In this chapter, we aim to answer the question of whether whistler waves can explain the transfer of electrons from the Strahl to the halo and, if so, what are the characteristics are of the waves responsible for it. To do so, we first analyze Solar Orbiter and Parker Solar Probe data to determine the whistler wave properties between 0.2 and 1 AU. Then, we use the quasi-linear theory to compute the efficiency of these waves in diffusing the electron populations. Section 4.1 presents the identification of the whistler waves and the determination of their properties. In Section 4.2, we compute both the local and integrated effect of the whistler waves on the electron diffusion. In Section 4.3, we discuss our results. This chapter is based on the accpeted article: Colomban et al. (2023a).

4.1 Whistler waves statistics

4.1.1 Data and analysis

4.1.1.1 Solar Orbiter and Parker Solar Probe data

We use data from the Solar Orbiter mission (Mueller et al., 2013; Müller et al., 2020) obtained between July 2020 and March 2022, covering distances between 0.3 AU and 1 AU (four perihelia). We exclude the two Venus flybys. The waves are identified and characterized using the Radio and Plasma Waves (RPW) experiment (see section 3.1.1). We use continuous

(CWF) and snapshot (SWF) waveforms at 256 Hz. Both the consideration of the CWF data products in addition to the SWF and the extension of the considered period is a significant improvement over the analysis of (Kretzschmar et al., 2021). We also utilize data from the magnetometer (MAG) (Horbury et al., 2020) and the Solar Wind analyzer (SWA) (Owen et al., 2020) instruments to retrieve the background magnetic field ($\vec{B_0}$ in the following) and the proton moments (density and velocity) of the solar wind. When available, we use the electron density delivered by RPW as a level 3 data product (Khotyaintsev et al., 2021). We also use 3D normal mode velocity distribution functions of EAS 1 and EAS 2 (Owen et al., 2020).

For Parker Solar Probe (Fox et al., 2016; Raouafi et al., 2023), the whistler waves are characterized using the FIELDS experiment (see section 3.2.1). Specifically, we use continuous waveforms (acquired at 297.97 Hz) and burst waveforms (150 000 Hz) data products from November 1st to 11th, 2018. We limit ourselves to the first perihelion of Parker Solar Probe because of the change in the response in one of the SCM component for the following encounters, making it impossible to compute directly the polarization properties of the waves (Dudok De Wit et al., 2022). A method using the two available components of the magnetic and electric fields to recover the whistlers polarization properties despite this technical issue is proposed in the following chapter. We also use the SWEAP Solar Probe Cup (SPAN-C) L3 data (Kasper et al., 2016; Case et al., 2020) for the density and solar wind speed. In the following, we round the heliocentric distance of Parker Solar Probe during the first encounter ($\in$ [0.16-0.25] AU) to 0.2 AU.

4.1.1.2 Detection and characterization

The wave detection and characterization method is presented in detail in section 3.3.1.

This statistical analysis includes several improvements over previous works. Most other statistical studies used only the power spectrum to detect whistlers without checking the polarization properties (Lacombe et al., 2014; Tong et al., 2019a; Jagarlamudi et al., 2020; Jagarlamudi et al., 2021). In addition, the joint analysis of the magnetic and electric fields makes it possible to determine the direction of propagation, which is the most crucial parameter for understanding the wave interactions with electrons. This also allows us to take into account the Doppler effect and to determine the wave frequency in the plasma frame. This joint statistical analysis of magnetic and electric fields was not performed in most of the previous studies of whistler waves in the solar wind (Lacombe et al., 2014; Tong et al., 2019a; Jagarlamudi et al., 2020; Jagarlamudi et al., 2021; Cattell et al., 2020, 2021b, 2022; Froment et al., 2023). Finally, the analysis of the waveforms allows us to precisely determine the parameters of the wave packets (e.g., amplitude, duration).

Figure 4.1 shows a typical example of whistler wave activity, detected by Solar Orbiter RPW on 2020 July, 22th. The spectral energy content is present between approx. 8 and 21 Hz (Figure 4.1e). In this frequency range, the polarization (Lp), planarity (F), and coherence between the different components are close to 1 (Figures 4.1f and 4.1h). The phase of the

radial component of the Poynting vector, φ_{S_X}, is close to -130 ° (Figure 4.1i). Taking into account the instrumental phase shift correction of -50° (see Section 3.3.1.2), this indicates an anti-sunward propagation that is consistent with the negative sign of the X component of the Poynting vector (Figure 4.1d). Taking into account this anti-sunward propagation, we notice that the propagation angle θ is small ($\leq 20°$, on the frequency range considered), which indicates a quasi-parallel propagation (Figure 4.1f). Since we have an anti-sunward propagation, in the background magnetic field direction, the phase shift of 90° (Figures 4.1g) indicates a right-handed circular polarization in both the spacecraft and plasma frame, as expected.

4.1.2 Results

4.1.2.1 Whistler waves occurence and polarization properties

Figure 4.2 gives an overview of the observations and occurrence of whistler waves. The occurrence is defined as the summed duration of the wave packets divided by the total observation time. Thefore, its absolute value cannot be compared directly with occurrences computed with data of lower temporal resolution (Lacombe et al., 2014; Jagarlamudi et al., 2020; Jagarlamudi et al., 2021; Froment et al., 2023). Figure 4.2a is made using Solar Orbiter data only, between 0.3 and 1 AU and when the solar wind speed data were available. Figures 4.2b and 4.2c are obtained with both Solar Orbiter and Parker Solar Probe observations. The occurrence for Parker Solar Probe is computed using burst waveforms only as the continuous waveforms have an overly low acquisition frequency and miss many whistler waves. Nevertheless, the occurrence calculated with Parker Solar Probe data is biased because burst waveforms are triggered to detect intermittent waves in the electric field (Bale et al., 2016; Malaspina et al., 2016). It is therefore likely that the occurrence of whistler waves is overestimated at 0.2 AU. On the other hand, it allows us to give an estimation of the proportion of sunward and anti-sunward waves.
Figure 4.2a shows that most Solar Orbiter observations were made in a slow wind (90% with $V_{SW} \leq 450$ km/s) and between 0.45 and 0.75 AU. We analyze in total 2673 hours of observations with Solar Orbiter and 68 hours of observations with Parker Solar Probe.
More than 110,000 whistler wave packets are detected and analyzed, which is the largest statistical study of whistler waves in the solar wind to date. Because of the lower statistics with Parker Solar Probe (232 wave packets) and between 0.3 and 0.5 AU with Solar Orbiter (900 wave packets), we concentrate in some figures only on distances between 0.5 and 1 AU. Figure 4.2b shows that the occurrence rate increases from 1 to 0.6 AU and decreases from 0.6 to 0.2 AU, and that anti-sunward whistler waves are largely dominant above 0.3 AU. The increase in the occurrence from 1 to 0.6 AU is in agreement with the observations of Kretzschmar et al. (2021) (using snapshot waveforms of Solar Orbiter first orbit) but in disagreement with the results of Jagarlamudi et al. (2020) (using magnetic spectra from the HELIOS mission). There seems to be a slow increase in the number of sunward whistlers between 1 and 0.3 AU but more statistics are needed to verify this trend. At 0.2 AU the occurrence of sunward whistlers is about the same as that of anti-sunward whistlers, but

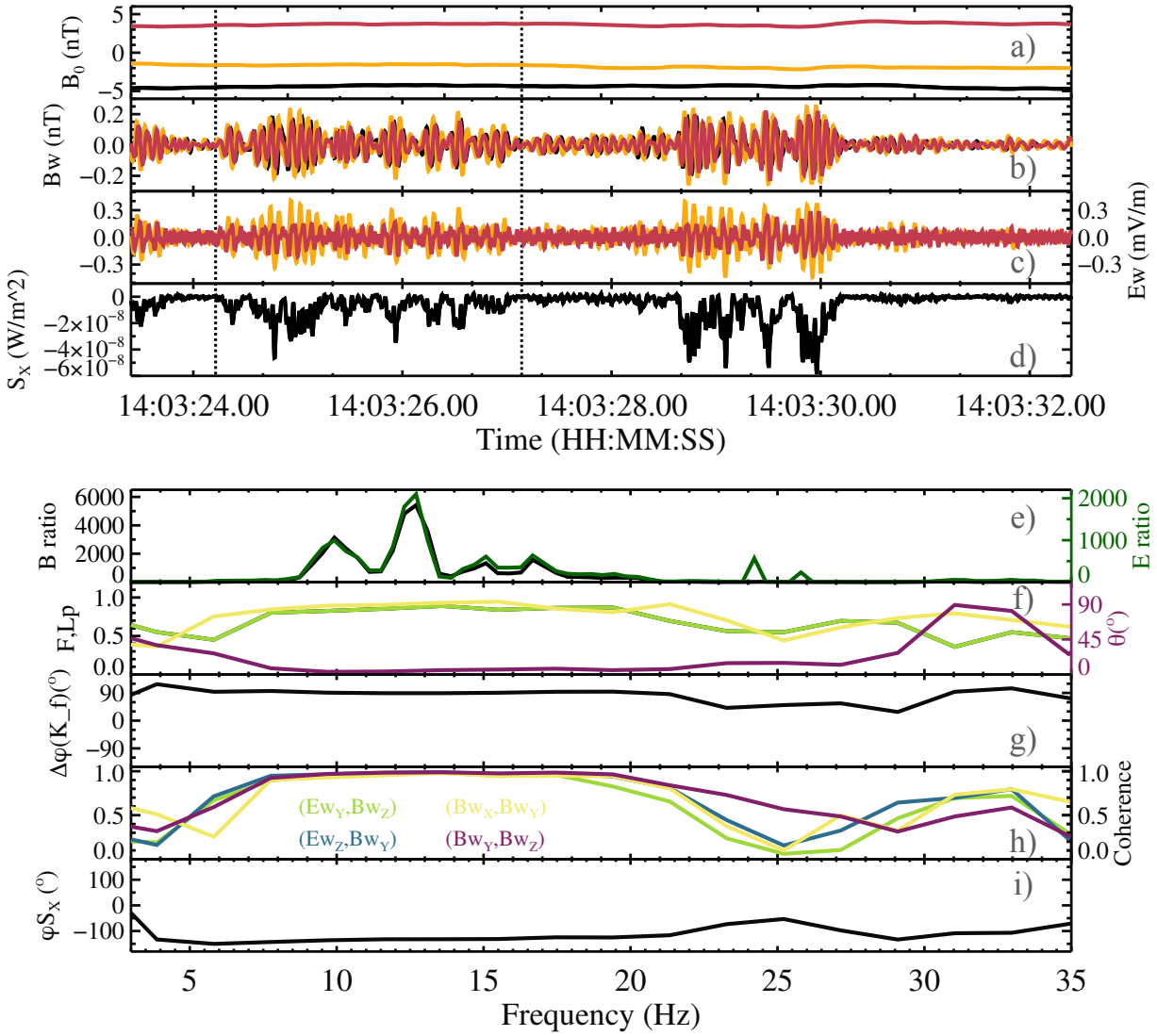

Figure 4.1: Analysis of whistler waves detected by Solar Orbiter RPW on 2020 July, 22nd around 14:03. *Panels a) to d):* The X component is in black, Y in red, and Z in yellow (spacecraft reference frame). *Panel a):* Background magnetic field B_0. *Panels b) and c):* Waveforms of the magnetic Bw and electric Ew fields. *Panel d):* X component of the Poynting vector (S_X). For *Panels c) and d)* we used an effective length of the electric antennas equal to 6 m. *Panels e) to i):* Analysis of the wave packet delimited by vertical dotted lines. *Panel e):* Ratio of the magnetic power spectrum to the median power spectrum of the day (black) and the same for the electric field (green, with the Y and Z components only). *Panel f):* Polarization (Lp in orange), planarity (F in black), and propagation angle (θ in purple). *Panel g):* Phase shift between $B\mathrm{w_x}$ and $B\mathrm{w_y}$ (in the wave reference frame with $\vec{k} = k\vec{z}$, see Section 3.3.1). *Panel h):* Spectral coherence between different components. *Panel i):* Phase of the X component of the Poynting vector φ_{S_X}.

again more statistics are necessary. Kretzschmar et al. (2021) also found a huge majority of anti-sunward whistler waves between 0.5 and 1 AU. The evolution of the occurrence with distance is discussed in more details in Section 4.3.
Finally, there is an important decrease in the occurrence with increasing solar wind speed above 350 km/s (0.02 à 350 km/s and 0.0025 at 650 km/s, Figure 4.2c). We also note a very fast decrease in the occurrence in very slow wind (0.001 at 250 km/s). These results are in good agreement with the study of Tong et al. (2019a), using Artemis data. A decrease in the occurrence with increasing solar wind speed (above 300 km/s) was also found by Jagarlamudi et al. (2020) and Jagarlamudi et al. (2021). Moreover, observations of Cattell et al. (2022) also suggest a decrease in occurrence with the solar wind speed. We note that Kretzschmar et al. (2021) did not study the occurrence as a function of solar wind speed. Jagarlamudi et al. (2020) showed that the lower turbulence level and the lower Doppler effect in the slow solar wind were not sufficient to explain the increase in the occurrence. The temperature anisotropy of the core and of the halo being more important in a slow solar wind, the generation mechanisms for whistler waves (heat flux and temperature anisotropy instabilities) are more favorable. The low occurrence at 250 km/s (representing around 5% of observations) still needs to be explained. It should be noted that SWA/PAS solar wind speed data are less reliable in very slow solar winds ($<$ 300km/s). However, this has no impact on wave detection with SCM.

We can note that Kellogg et al. (1992) using Ulysses and Jagarlamudi et al. (2021) using PSP data, found a correlation between the occurrence of whistler and Langmuir waves. Following these observations, we tried to reproduce these results using Solar Orbiter data. Here, Langmuir waves were detected using the Solar Orbiter RPW TDS survey data (Maksimovic et al., 2020). If a wave is detected at a frequency f that verifies $0.5f_{\mathrm{pe}} \leq f \leq 1.5f_{\mathrm{pe}}$ then it is considered as a Langmuir wave (Graham et al., 2021). We detected 16 hours of Langmuir waves over the 1200 hours during which the detection was possible. We find that the total occurrence of whistler waves between 0.3 and 1 AU is $\sim$ 1.65 % and that the occurrence of whistler waves when a Langmuir wave activity is detected is 2.42 times bigger: $\sim$ 4 %. This is probably due to a link between the generation mechanisms of whistler and Langmuir waves (characteristics of the distribution function that facilitate the instabilities generating both types of waves). This can also be due to plasma conditions favorable to instabilities such as magnetic dips (Boldú et al., 2023).

Figure 4.3 shows the distribution of the wave propagation angle of anti-sunward whistlers measured with Solar Orbiter and its variations with heliocentric distance (Figures 4.3a and 4.3c) and solar wind speed (Figures 4.3b and 4.3d). Most whistler waves are found to be quasi-aligned with the magnetic field. Indeed, for all distances and speeds, the distribution of the propagation angle peaks between 3 and 7°. Moreover, only 7.5 % of the waves have a propagation angle larger than 15° and 0.5 % have an angle of propagation greater than 45°. These results are in good agreement with the studies of Lacombe et al. (2014), Tong et al. (2019a), and Kretzschmar et al. (2021) that also found a majority of quasi-aligned whistlers between 0.5 and 1 AU. Below 15°, the distribution can be explained by considering

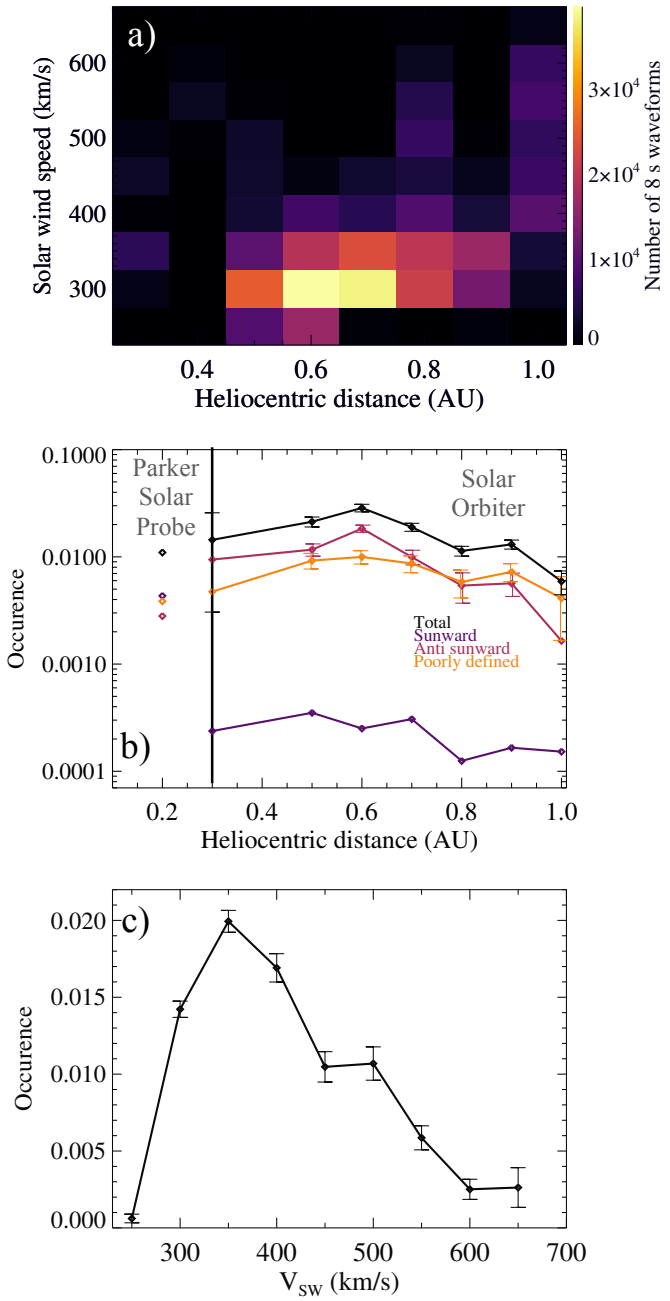

Figure 4.2: Observation and occurrence of whistlers as a function of heliocentric distance and solar wind speed. *Panel a):* Number of analyzed 8s-waveforms with Solar Orbiter as a function of heliocentric distance and solar wind speed. *Panel b):* Whistler wave occurrence as a function of heliocentric distance for sunward, anti-sunward, and poorly defined propagation direction. When, due to low statistics, the 95% confidence intervals (calculated assuming a normal distribution) are of the order of magnitude of values, they are not shown. *Panel c):* Occurrence as a function of the solar wind speed.

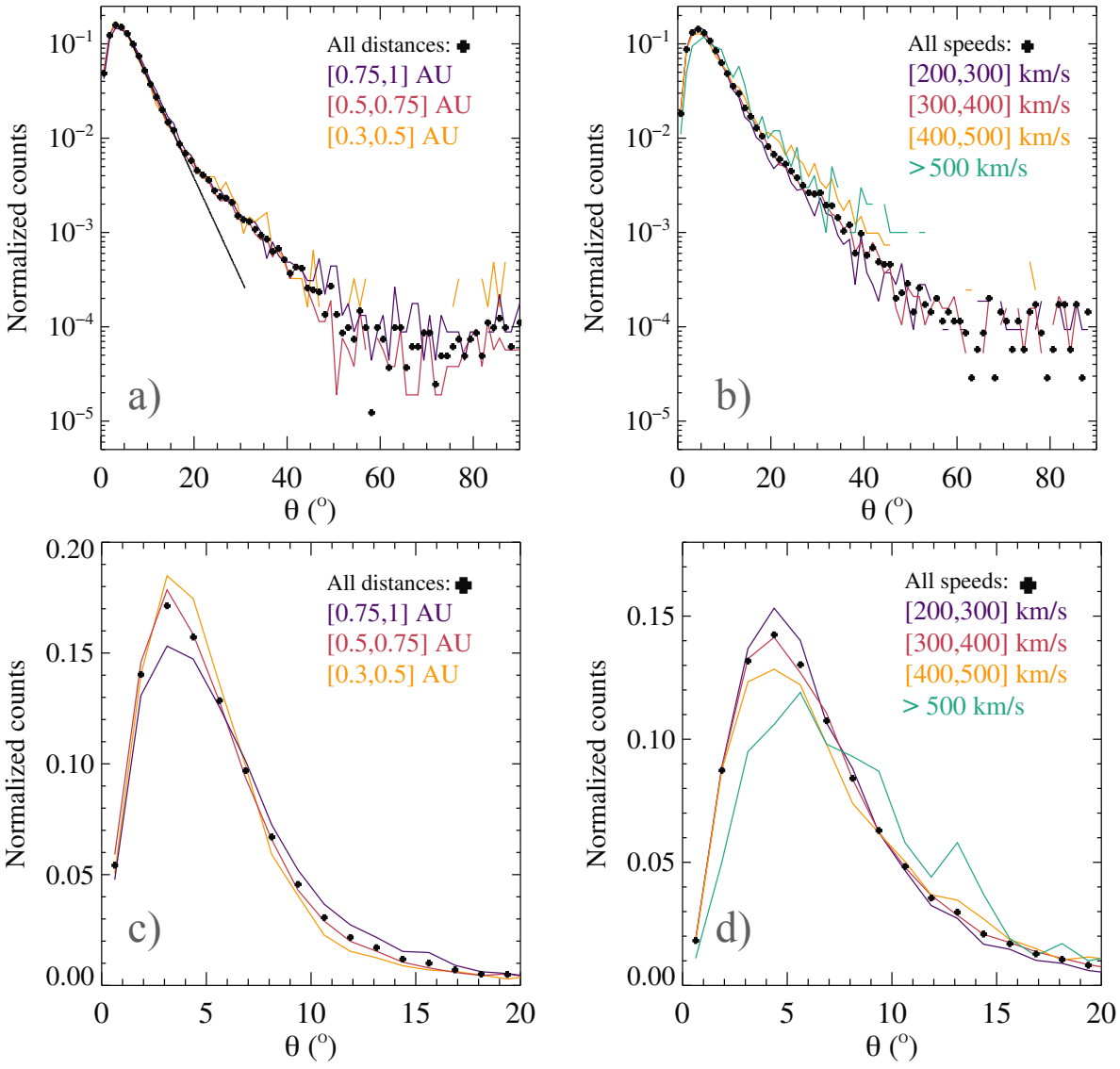

Figure 4.3: Histograms of propagation angle distribution as a function of heliocentric distance and solar wind speed. *Panel a):* Normalized histogram of the number of whistler waves as a function of the propagation angle for different heliocentric distances. *Panel b):* Normalized histogram of the number of whistler waves as a function of the propagation angle for different solar wind speeds. *Panel c):* Same as *panel a)* zoomed between 0 and 20°. *Panel d):* Same as *panel b)* zoomed between 0 and 20°.

an instability that has a maximum growth rate at 0°, which is the case of the WHFI, the TAI, or the sunward suprathermal deficit instability. The departure from 0° can be explained with a geometrical effect due to the curvature of the field lines (Agapitov et al., 2013). This explanation is consistent with the slight increase in propagation angle with the heliocentric distance, already observed by Kretzschmar et al. (2021), and noticeable in Figure 4.3c) and with the solar wind speed (Figure 4.3d). Indeed, the field lines are less curved close to the Sun (considering a simple Parker spiral) and whistlers propagate over greater distances as solar wind speed increases. More measurements within the fast solar wind and closer to the Sun would allow us to confirm this point more rigorously.
Between 15° and up to 45°, we notice a slight change in the slope of the distribution with respect to smaller angles and this is accompanied by other changes that we describe below together with Figure 4.4.
Above 45°, very few waves are detected, and a detailed analysis of these cases (not carried out here) would be needed to determine their physical or non-physical origins.
At 0.2 AU (distribution is not shown because the number of cases is too small), we also find a majority of quasi-aligned whistler waves with, however, a higher percentage of waves propagating obliquely ($\sim 4\%$ with $\theta \geq 45°$). This percentage is comparable with the results of Froment et al. (2023) (3% with $\theta \geq 45°$) using cross spectra of Parker Solar Probe. This higher percentage can be explained by the fact that, at 0.2 AU, whistlers are often associated with structures such as magnetic dips or switchbacks and therefore propagate in a highly inhomogeneous background magnetic field (Agapitov et al., 2020; Froment et al., 2023; Karbashewski et al., 2023).

It should be noted that in this thesis we also performed whistler wave detection on the electric field. Since oblique waves have a larger electrostatic component, such a method makes it easier to detect them. The results of electric-field detection are very similar to those of magnetic-field detection. Specifically, the percentage of oblique waves (propagation angle larger than 45°) remains very low. This confirms their virtual absence in the free solar wind between 0.2 and 1 AU.

Figure 4.4 shows the evolution of the median value of several wave parameters with the angle of propagation. To calculate the theoretical phase velocity, we use the wave vector from the cold plasma dispersion equation (Lyons, 1974b). Below 15°, we note a decrease (or a plateau) among some parameters with the propagation angle. This may be due to the fact that waves with larger propagation angles are generated at greater distances from the spacecraft. These changes would in this case be due to wave propagation. However, we note that these parameters increase slightly (or there is a plateau) from 15° to around 45°. This is clearly visible in Figures 4.4a, 4.4b and 4.4d, even though the error bars are large due to the low number of waves verifying $\theta \geq 15°$. These observations, coupled with the change in slope of the distribution (noted in Figures 4.3a and 4.3b), could be the signature of different conditions (e.g., particularly inhomogeneous magnetic field like in dips and switchbacks) and/or mechanisms (instability having a maximum growth rate between 15° and 45°) generating these waves. Further investigations are needed to determine the origin of these

slightly oblique waves.

Figure 4.5 shows the distribution of various wave parameters with heliocentric distance. It can be seen in Figure 4.5a that the amplitude of the waves decreases with the heliocentric distance. This is expected since the amplitude of the background magnetic field decreases as $\sim r^{-2}$ with distance (at the distances we consider). Nevertheless, there may be a slight increase in the normalized amplitude of the fluctuations with the heliocentric distance (Figure 4.5b). This increase may be caused by the fact that both the temperature anisotropy (Jagarlamudi et al., 2020; Štverák, Trávníček, and Hellinger, 2015) and the plasma, β_{e}, increase with distance. Indeed, Tong et al. (2019a) have shown that these two parameters control the ratio, $\frac{B_{\mathrm{w}}}{B_0}$. Longer wave packet durations are observed far from the Sun (Figure 4.5c). This is probably caused by the decreasing phase velocity at larger heliocentric distances and by the fact that the characteristic spatial scales of the plasma are much larger far from the Sun. The frequency width decreases with the Heliocentric distance (Figure 4.5e). The trends observed in Figures 4.5a, 4.5b and 4.5e confirm what was already observed by Kretzschmar et al. (2021). The ratio f/f_{ce} does not clearly depend on the heliocentric distance (Figure 4.5d) in the plasma frame, while this ratio seems to increase with distance in the spacecraft frame (Kretzschmar et al., 2021). This can be explained by a more important role of the Doppler shift far from the Sun because of the smaller phase velocity. Figure 4.5f shows that f/f_{ce} (in the spacecraft frame) is lower for sunward whistlers than for anti-sunward ones. This is explained by the Doppler effect and gives a good indication that the determination of the propagation direction (sunward or anti-sunward) is correct. The observed amplitudes and frequencies are in agreement with previous observations of small-amplitude quasi-parallel whistler waves in the solar wind (Lacombe et al., 2014; Tong et al., 2019a; Chust et al., 2021; Kretzschmar et al., 2021; Froment et al., 2023), and are consistent with whistler heat flux instability simulations (Kuzichev et al., 2019; López et al., 2019).

4.1.2.2 Exploring whether sunward whistler waves are counter-propagating with respect to Strahl electrons

In Figure 4.2b, we note the interesting fact that the proportion of sunward whistler waves seems to increase when getting closer to the Sun. However, since 1) the number of detected sunward whistler waves is always quite low between 0.3 and 1 AU and 2) there is an instrumental phase shift between the magnetic and electric fields on Solar Orbiter, we pay special attention to these sunward waves in this section. Figure 4.6 shows two examples of sunward whistler waves activity detected with Solar Orbiter. Figures 4.6a to 4.6d and 4.6i to 4.6l are typical of whistler waves observed with Solar Orbiter, with a planarity and an ellipticity close to 1 and a quasi-parallel propagation. Figures 4.6e and 4.6m show the phase of the X component of the Poynting vector ($\varphi_{S_{\mathrm{x}}}$) that is used to determine the radial direction of propagation (sunward or anti-sunward) of the waves. Taking into account the instrumental phase shift, as explained in Section 3.3.1.1, $-180° \leq \varphi_{S_{\mathrm{x}}} \leq -80°$ indicates a wave propagating anti-sunward, while $0° \leq \varphi_{S_{\mathrm{x}}} \leq 100°$ indicates a wave propagating sunward. Two sunward propagating cases are clearly visible between 16:30 and 17:30 on the 2021 August,

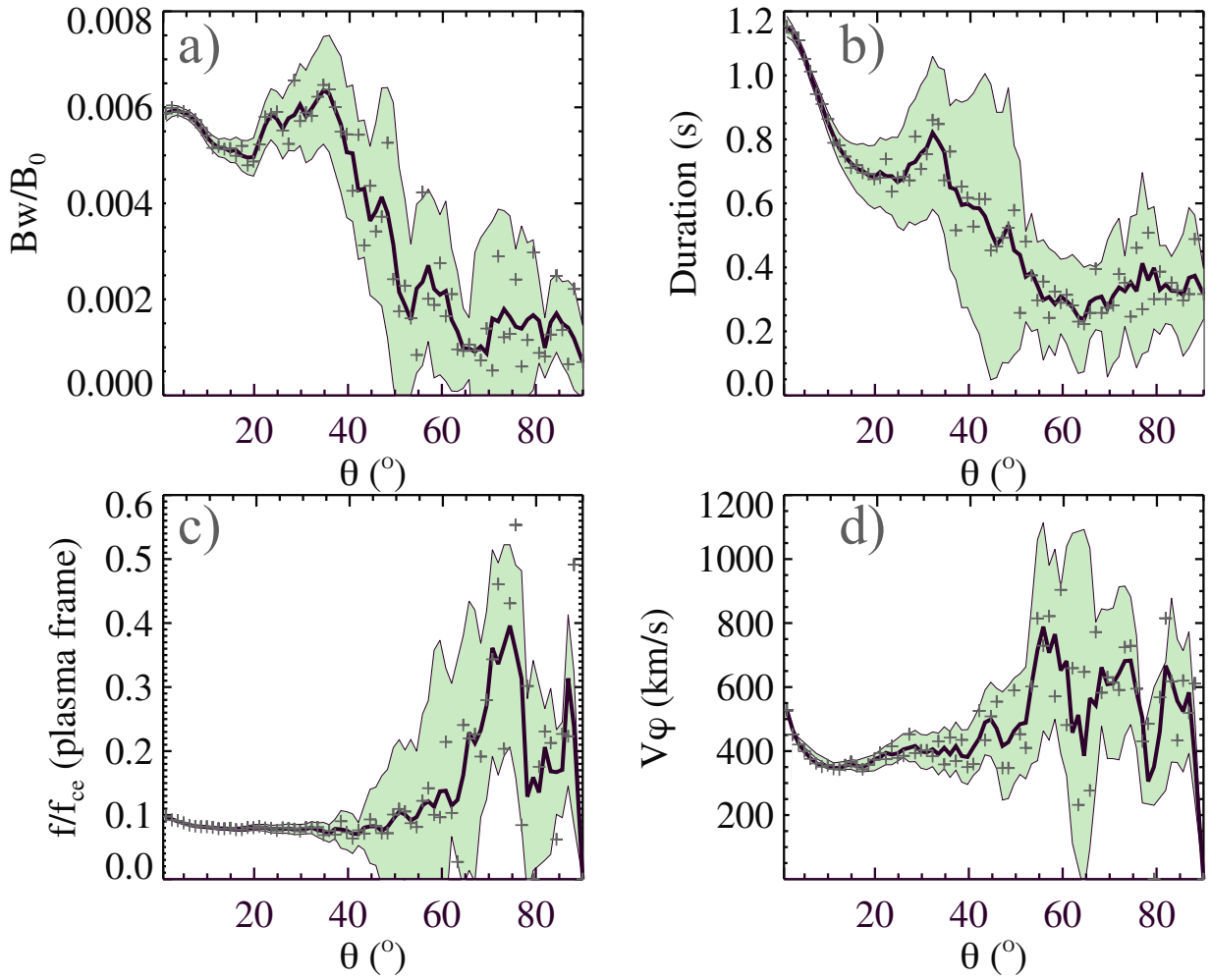

Figure 4.4: Median value (crosses) of several whistler wave parameters as a function of the propagation angle. The black lines show the smoothed values and the smoothed 95% error bars (assuming a normal distribution) are shown in green. *Panel a):* Wave amplitude normalized to the background magnetic field amplitude. *Panel b):* Duration of the wave packets. *Panel c):* Frequency in the plasma frame normalized by the local electron cyclotron frequency. *Panel d):* Theoretical phase velocity (v_φ) in the plasma frame.

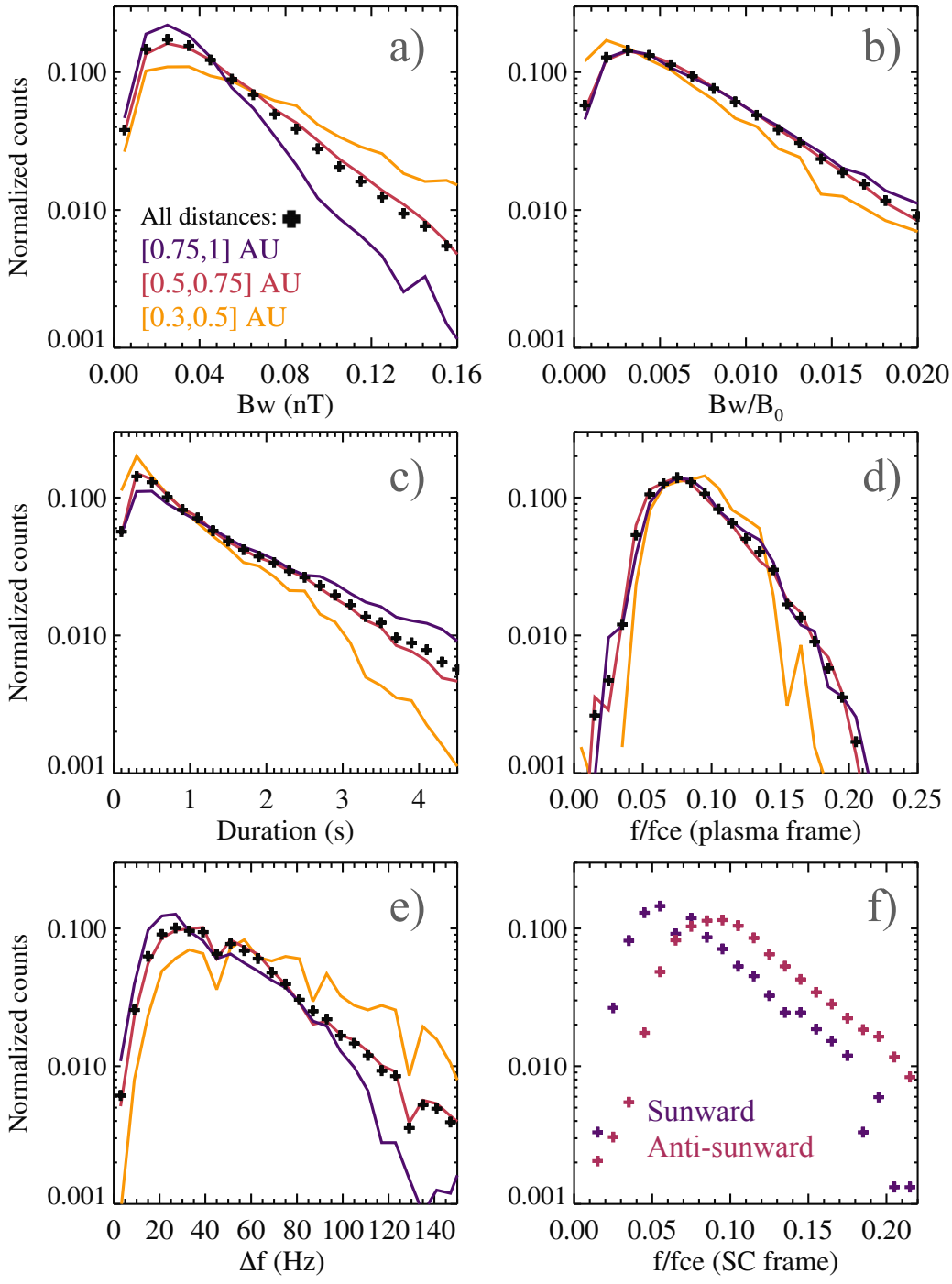

Figure 4.5: *Panels a) to e)*: Normalized histograms for different wave parameters as a function of heliocentric distance. The wave parameters are as follows: *Panel a):* Wave amplitude. *Panel b):* Wave amplitude normalized by the the background magnetic field. *Panel c):* Duration of the wave packets. *Panel d):* Frequency in the plasma frame normalized by the local electron cyclotron frequency. *Panel e):* Frequency width. *Panel f):* Histogram of the frequency in the spacecraft frame normalized by the electron cyclotron frequency for sunward (in purple) and anti-sunward whistler waves (in pink).

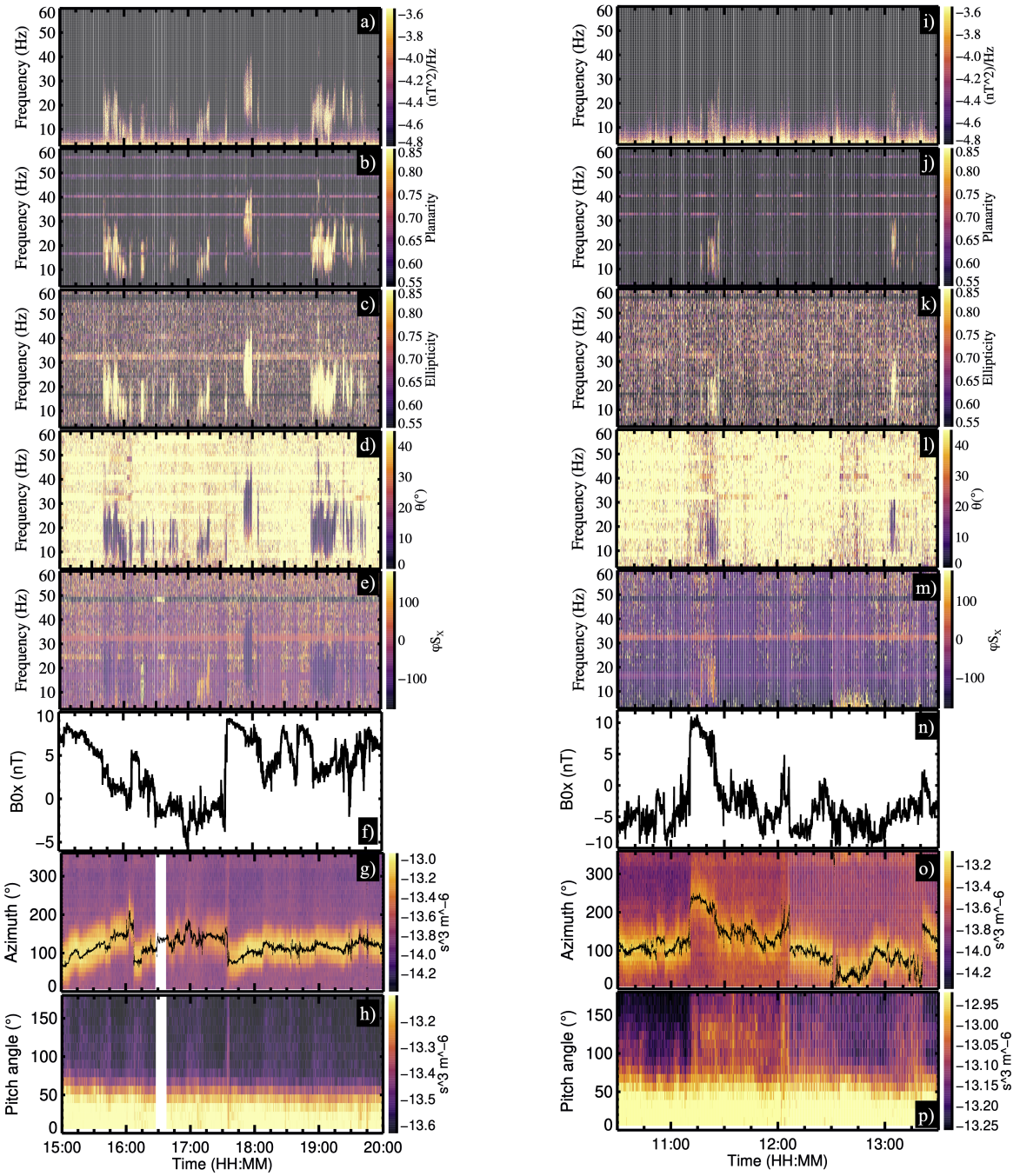

Figure 4.6: Observations of whistler waves activities with Solar Orbiter on 2021/08/15 (left) and 2021/10/08 (right). *Panels a) to e) and i) to m):* Spectrograms of several wave parameters calculated from CWF with: *Panels a) and i):* Power spectral density. *Panels b) and j):* Planarity. *Panels c) and k):* Ellipticity. *Panels d) and l):* Propagation angle. *Panels e) and m):* φS_X. *Panels f) and n):* X components of the background magnetic field. *Panels g) and o):* Velocity distribution functions (summed over energies between 100 and 1000 eV and over all elevations) as a function of time and azimuth angle of EAS 1 with the azimuth of the background magnetic field in black (in the EAS 1 reference frame). *Panels h) and p):* Pitch angle distribution (summed over energies between 100 and 1000 eV) using EAS 1 and EAS 2 data.

15th (Figure 4.6e) and between 11:00 and 11:30 on the 2021 October, 8th (Figure 4.6m). The other observed wave packets are propagating anti-sunward or are poorly defined. The surprising feature is that these sunward propagating waves occur during switchbacks with a change of sign of the radial component of the background magnetic, such that they are still aligned with the Strahl. This can be seen by observing the reversal of the radial component (X in solar Orbiter reference frame) of the background magnetic field at the time of the observed sunward waves (positive to negative in Figure 4.6f, negative to positive in Figure 4.6n), while the Strahl stays aligned with the magnetic field (Figures 4.6g, 4.6o, 4.6h and 4.6p).

We then look to find whether cases similar to those shown in Figure 4.6 represent the majority of sunward cases. Figure 4.7 presents the percentage of cases in which the sign of the radial component during the measurement is not the median sign of this component over a period of 24 hours centered on the measurement. Such a change in the sign of the radial component would suggest the presence of switchbacks, as shown in Figure 4.6. We note that this technique is not perfect since we do not verify that the Strahl changes direction as well; heliospheric current sheets crossing could cause a change of sign of the radial component of the magnetic field as well. We note that the error bars in Figure 4.7 are estimated using the binomial distribution and do not take into account the possible method errors described above. The percentage of cases with a change of sign of the radial component is around 13 times higher for sunward waves ($\simeq 80\%$) than for anti-sunward waves ($\simeq 6\%$). Without whistler waves, this percentage is $\simeq 12\%$. This suggests that in the vast majority of cases, sunward waves are indeed detected within switchbacks. Therefore, these "sunward" waves actually propagate in the same direction as the Strahl and do not interact with electrons as counter-streaming waves. To keep this distinction in mind when discussing the impact of waves on the suprathermal electrons, we use the distinctive terms of Strahl-aligned and counter-streaming whistler waves. The 6% of anti-sunward waves with a sign change of the radial component and the 20% of sunward waves without a sign change are potentially counter-streaming. On the other hand, visual inspection of these cases shows that the vast majority of them are associated with heliospheric current sheets, biasing the detection method. The vast majority of these cases are therefore also Strahl-aligned.
The almost systematic presence of switchbacks with a change of sign of the radial component of the background magnetic field when observing whistler waves propagating sunward above 0.3 AU has been verified by Tom Cooper during his M1 internship (which I supervised). Tom used the basic wave parameters from Solar Orbiter RPW and the 3D electron distribution functions measured by SWA at March 2022 perihelion (~ 0.32) AU to verify this result.
Conversely, we did not observe switchbacks with a change of sign of the radial component of the background magnetic field during sunward whistler wave activity closer to the Sun (i.e., with Parker Solar Probe). These sunward waves are therefore truly counter-streaming and can strongly contribute to the diffusion of Strahl electrons. Finally, we found that they are associated with magnetic dips (greater than 5%) in 80% of the cases (compared to only 30% for the Strahl-aligned waves). The magnetic dips are detected similarly to the method described in Froment et al. (2023). In the present paper, we compute: $(|B_0| - |B_0|_{\text{filt}})/|B_0|_{\text{filt}}$

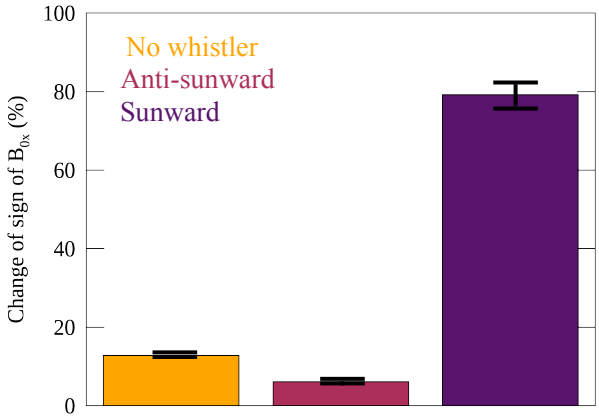

Figure 4.7: Percentage of cases in which the sign of the radial component of the background magnetic field during the measurement is not the median sign of this component over a 24-hour period centered on the measurement. Only Solar Orbiter data were used to construct this figure.

and identify the magnetic dips when this quantity is lower than -0.03. $|B_0|$ is the background magnetic field smoothed (sliding average) over 0.05 s and $|B_0|_{\text{filt}}$ is smoothed over 60 s.

4.1.2.3 Overview of whistler waves detected with Parker Solar Probe and Solar Orbiter between 0.2 and 1 AU

Here, we present a quick overview of the results obtained in the previous sections and a discussion.

Between 0.3 and 1 AU, we detect a majority of quasi-parallel whistler waves. When $\theta \leq 15°$ (i.e., 92.5% of the cases), the following generation mechanisms can produce waves with the observed properties: WHFI, TAI, and the sunward suprathermal deficit (Tong et al., 2019b; Jagarlamudi et al., 2020; Berčič et al., 2021). The existence of waves with propagation angles up to 15° can be explained by a parallel generation associated with the geometric effect of propagation in a curved magnetic field. The 7% of cases with $\theta \in [15, 45]°$ may find their origin in another generation mechanism favoring larger propagation angles; however, we set this point aside for future studies. There are virtually no waves with propagation angles greater than 45° (0.5% of the case). Moreover, the waves almost all propagate in the direction of the Strahl propagation, including within switchbacks, and the waves are therefore Strahl-aligned.

The quasi-absence of counter-streaming whistler waves beyond 0.3 AU is an important finding. Indeed, Vasko et al. (2020) predicted the existence of counter-streaming waves with small frequencies and amplitude and emphasized their potential importance in diffusing the Strahl. These waves might be at too small frequencies and amplitudes to be detected by the Search-Coil Magnetometer of Solar Orbiter. We may note, however, that Khotyaintsev et al. (2021) analyzed the low-frequency magnetic field measured by MAG as well as the electric potential from RPW and found only proton-band electromagnetic ion cyclotron (PB-EMIC)

waves (and no fast-magnetosonic whistler waves). The absence (or even the scarcity) of counter-streaming whistler waves far from the Sun, with respect to observations at 0.2 AU, can probably be explained both by the rarity of magnetic dips larger than 5% beyond 0.3 AU, and by the evolution of the distribution function.
Similarly, the fact that there are very few oblique whistlers at all the covered distances is an important result for the diffusion of electrons. Oblique waves ($\sim 70°$) were predicted to be produced by fan-like instabilities (Vasko et al., 2019; Verscharen et al., 2019; Micera et al., 2020, 2021) and therefore favored by a high Strahl's density and drift. Our observations close to the Sun and up to solar wind speed of 500 km/s should cover conditions where the Strahl is generally strong (Rosenbauer et al., 1977; Pilipp et al., 1987a; Štverák et al., 2009; Maksimovic et al., 2005a; Bercic et al., 2019). However, we find that whistler waves with $\theta \geq 45°$ constitute only 4% at 0.2 AU (consistently with Froment et al. (2023)) and 0.5% beyond 0.3 AU of observed waves. As mentioned in the introduction, the near-absence of oblique waves had been predicted by Schroeder, Boldyrev, and Astfalk (2021) and Jeong et al. (2022).
However, we do find an important number of counter-streaming waves at 0.2 AU. They are mainly associated with dips in the background magnetic field, which indicates that these structures favor the generation of counter-streaming whistler waves, as proposed by Karbashewski et al. (2023). Moreover, we show in Chapter 5, using burst data of Parker Solar Probe, that these counter-streaming waves are detected at higher frequencies (in the plasma reference frame) than the Strahl-aligned waves. This is again in agreement with the mechanism proposed by Karbashewski et al. (2023).

Taking into account the results of this section, we expect wave interactions with the Strahl to be rather slow above 0.3 AU (compared to interaction with oblique or counter-streaming waves). At 0.2 AU, on the other hand, counter-streaming waves interact efficiently. In the next section, we compute the diffusion coefficients to quantify the interactions of observed whistler waves with suprathermal electrons.

4.2 Diffusion of solar wind electrons by whistler waves

Here, we focus on the quantification of the effect of whistler waves on suprathermal electrons along their propagation. The method used to compute the diffusion coefficients is presented in Section 4.2.1, while Sections 4.2.2 and 4.2.3 present the result.

4.2.1 Theory and method

As detailed in Section 2.2 the effect of waves on particles can be calculated in the framework of quasi-linear theory (Vedenov, 1963; Yakimenko, 1963).

One way to estimate the time scale of the electron diffusion in the velocity space is to calculate the diffusion coefficients (Lyons, Thorne, and Kennel, 1971, 1972; Lyons, 1974a). These coefficients are computed from the characteristics of the waves and take into account their polarization properties, their amplitudes, and the resonant conditions of wave-particle interactions.

Three diffusion coefficients, $D_{\alpha\alpha}$, $D_{\alpha,p}$, and D_{pp} can be calculated (α is the pitch angle and p is the electron momentum). Here, we are interested in the interaction of electrons with whistler waves, which are mainly electromagnetic in their reference frame (moving with the wave). Therefore, the perturbations produced by the waves are primarily magnetic. As it is well known, the magnetic field cannot transfer energy to an isolated charge, and therefore the main effect of the waves is angular diffusion. Although energy diffusion is important for the damping/instability of the waves, its effect on the shape of the overall electron VDF is negligible. This angular diffusion is, therefore, the only one we will consider in the following, it is described by the diffusion coefficient, $D_{\alpha\alpha}$.

Lyons (1974b) used the expression of diffusion coefficients derived by Lyons (1974a) (presented in Section 2.2.3) to calculate these coefficients for whistler and ion-cyclotron waves in the context of the Earth's radiation belts. For whistler waves, they used the dispersion relation of equation 2.8 (i.e. using the high density assumption $(\frac{\omega_{\rm pe}}{\omega_{\rm ce}})^2 \gg 1$). Glauert and Horne (2005) developed a code (PADIE) that calculates these coefficients, solving the full electromagnetic dispersion relation. This enables the calculation of the diffusion coefficients for any linear electromagnetic wave mode in the case of a cold plasma, without making the high-density assumption. In this study we use the cold plasma whistler waves dispersion relation (Equation 2.8) and therefore the high density approximation. Indeed, Glauert and Horne (2005) have shown that if $\omega_{pe}/\omega_{ce} \geq 10$ (which is the case for our observations, see Section 2.1.1), the high density approximation is well valid for all energies.

We first use the diffusion coefficients to evaluate the angular diffusion caused by an isolated wave packet. We use $D_{\alpha\alpha}$ to calculate the angular diffusion/widening in angular space of the distribution function ($\Delta\alpha$) for a group of resonant particles, which results from the interaction with a wave packet, using:

$$\Delta\alpha^2 = 2D_{\alpha\alpha}\tau/p^2 \tag{4.1}$$

where τ is the wave packet duration. In the following, $\Delta\alpha/\tau$ is called the local diffusion coefficient and describes the typical angular diffusion that an electron with momentum, p, undergoes in one second. We calculate the local diffusion coefficients using the mean values of the wave parameters derived in the previous sections (see details in Appendix A.2) for different bins of heliocentric distances, propagation angles, and wave amplitudes. This allows us to study which wave parameters are important for the diffusion. We focus on the diffusion of halo and Strahl electrons by whistler waves propagating either mainly along the Strahl (Strahl-aligned) or against it (counter-streaming). For simplicity, we only consider two energies, 300 eV and 700 eV, that are representative of these suprathermal electron populations and at which the Strahl diffusion cannot be explained by collisions (Boldyrev and Horaites, 2019; Berčič, Landi, and Maksimović, 2021). In the following, we use an anti-sunward magnetic field convention, so that the electrons with a pitch angle between 0 and 90 ° (respectively, 90-180°) propagate anti-sunward (respectively, sunward) in the solar wind reference frame.

Then, in order to estimate the global impact of whistler waves on the distribution function along the propagation, we calculate the integrated diffusion coefficients. For each bin presented above, we compute the number of wave packets that an electron encounters on average during its propagation. We assume that the occurrence and characteristics of whistlers encountered by electrons on their journey are identical to those encountered by the satellites. We describe each wave packet encounter by a "kick widening": $(\Delta\alpha^2)_i$, where the index, i, numerates a wave packet. Therefore, the total angular deviation, after multiple encounters with different wave packets for the same group of resonant particles should be evaluated as:

$$(\Delta\alpha^2)_{total} = \sum_i (\Delta\alpha^2)_i = 2\frac{1}{p^2}\sum_i (D_{\alpha\alpha})_i \tau_i \tag{4.2}$$

The total diffusion is achieved when $\sqrt{(\Delta\alpha^2)_{total}} = 180°$. In the following $(\Delta\alpha)_{total}$ is called the integrated diffusion coefficient. Since this approach is based on diffusion the kick caused by each encounter with a wave packet is assumed to be small.

The travel time of the electrons in each bin of heliocentric distance is calculated by dividing the total length of the interplanetary magnetic field, considered to be equal to 1.6 times the radial distance (Graham et al., 2018), by the electron velocity. Electrons velocity is calculated using their energies (the solar wind speed is neglected). Electrons follow the field lines and their rotation around it is considered negligible compared to the total length. We take the example of an electron with an energy of 300 eV that corresponds to a speed of 15675 km/s. Between 0.5 and 0.75, it travels a distance of about $0.25 * 1.6 * 1.496 * 10^8 = 59840004$ km and its travel time is therefore on the order of 1h04.

With the chosen anti-sunward magnetic field convention and at the considered energies, small pitch angles ($\lesssim 55°$, depending on the heliocentric distance) indicate Strahl electrons while larger pitch angles indicate halo electrons.

Below, we first present the local and integrated diffusion coefficients between 0.5 and 1 AU (using Solar Orbiter, Section 4.2.2), and then near 0.2 AU (using Parker Solar Probe, Section 4.2.3).

4.2.2 Electron diffusion between 0.5 and 1 AU

As explained in Section 4.1.2.2, between 0.5 and 1 AU, we almost exclusively detect Strahl-aligned whistler waves. Figure 4.8 shows the local diffusion coefficients and Figure 4.9 the integrated ones, for this direction of propagation. Three different propagation angle ($[0, 15], [15, 30], [30, 45]°$) and two heliocentric distance ($[0.5, 0.75], [0.75, 1]$ AU) bins are considered (we find that modifying these bins do not modify the conclusions). Waves with an angle of propagation greater than 45° occur so infrequently that electrons at 700 eV will encounter only about 0.08 waves of this type as they travel 0.25 AU. We therefore neglect these waves as their overall effect on the Strahl is negligible, but we are mindful that they may sporadically have an effect on Strahl diffusion.

We should start by explaining some general features of Figures 4.8 and 4.9. As we work with averaged parameter values for each bin, there is only a specific range of pitch angles

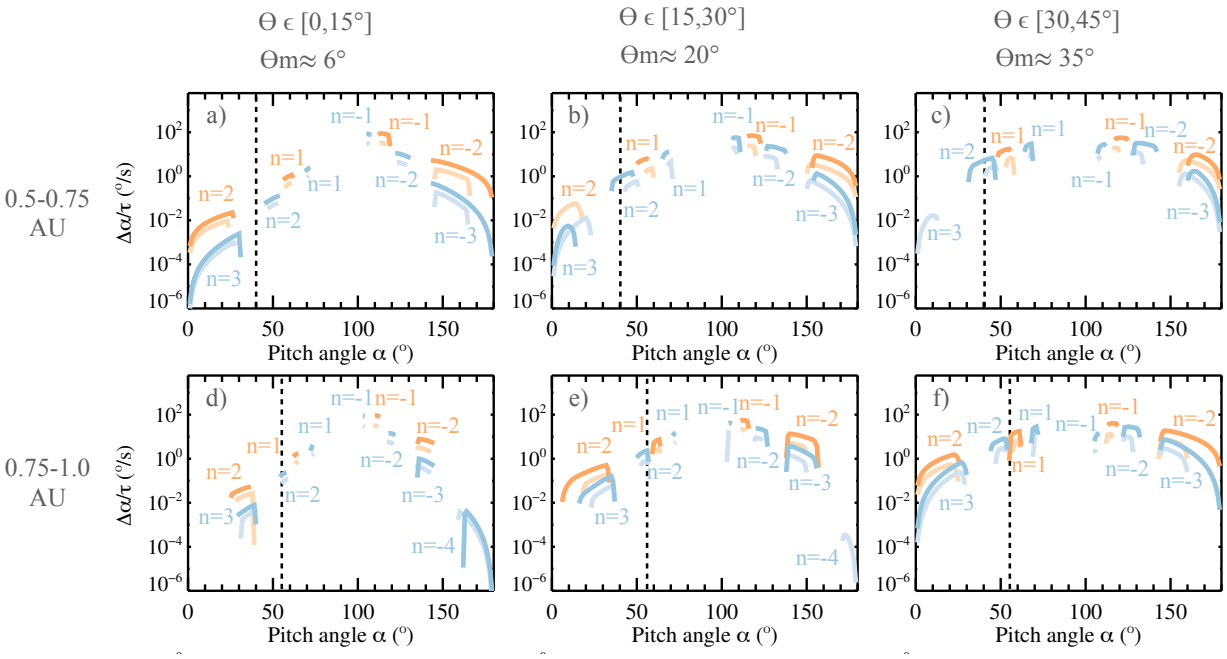

Figure 4.8: Local diffusion coefficients at two different heliocentric distance (rows) and three wave propagation angle θ (columns) bins. θ_m is the approximate mean angle used for the calculation in each propagation angle bin. The orange color (resp., blue) corresponds to an electron energy of 300 eV (resp., 700 eV) in the proton reference frame. The lighter lines show the effect of the 80% least intense waves while the darker ones are for the 20% most intense waves. The observed Strahl PAW (Bercic et al., 2019) for each distance bin is indicated by a black vertical line. The resonance orders are indicated.

that matches the resonance conditions; in reality, the diffusion is caused by the encounter with a multitude of wave packets (with a multitude of parameters) so that electrons at other pitch angles can also be in resonance. To quantify the effect of waves on Strahl electrons we interpolate the diffusion coefficients at the pitch angle corresponding to the Strahl PAW. Strahl PAW values are those obtained by Bercic et al. (2019) using Helios data (using values of the core electron plasma β_{ec} greater than 0.4, coherent with a slow solar wind). Finally, we can note that since whistler activity is intermittent, total diffusion will vary according to the periods of activity encountered.

We must also note that in some cases (described below), the wave-particle interaction is found to be very effective such that we are at the limit or outside the applicability of the quasi-linear theory. For such waves, it would be necessary to apply another approach that would take into account the effect of nonlinear interactions with a monochromatic solitary wave (Karpman, Istomin, and Shklyar, 1975). Nevertheless, as we will see, these cases that concern the diffusion of the halo do not impact the main conclusions of this work.

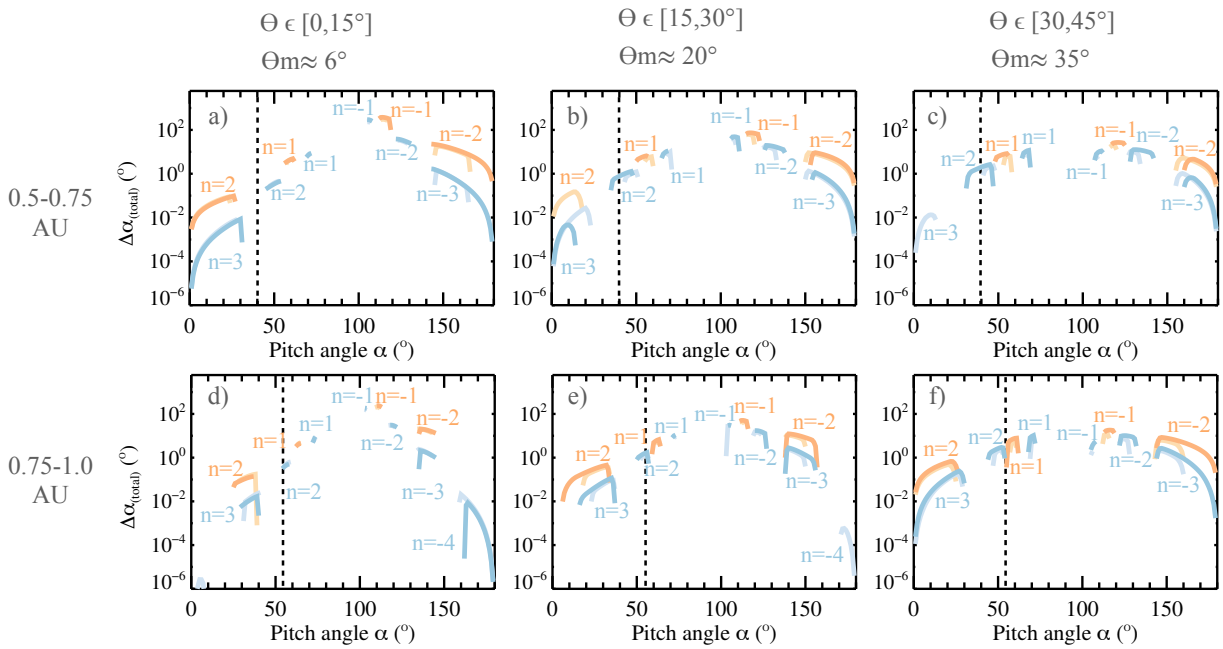

Figure 4.9: Integrated diffusion coefficients at two heliocentric distance and three propagation angle θ bins. Legends and notations are comparable to those in Figure 4.8.

4.2.2.1 Local diffusion between 0.5 and 1 AU

We first discuss the local diffusion coefficients and we begin with the role of whistler waves on 300 eV electrons (in orange) between 0.5 and 0.75 AU (first row of Figure 4.8). It can be seen in Figure 4.8a that the diffusion of Strahl electrons by quasi-aligned whistler waves ($\theta \in [0, 15]^\circ$), due to the $n = 1$ and $n = 2$ resonances, is slow. Indeed, even the 20% most intense whistler waves (darker curve) can diffuse electrons in pitch angle by about only 0.1 °/s at the PAW, which is small considering the typical duration of 1 s of a wave packet. On the other hand, for pitch angles greater than 90°, the diffusion is very efficient: up to 100 °/s for the $n = -1$ resonance and for the most intense waves. This means that in that last case, the timescale of the variation of the distribution function is not much lower than the wave period: $\sim 5^\circ$/wave period (wave period of the order of 0.05 s at these distances). Therefore, we are at the limit of applicability of the quasi-linear theory. Moreover, the approach of diffusion by "kick widening" is also at the limit of applicability since a kick corresponds to a diffusion of the order of 100°. We can generally note that the 20% most intense waves are approximately four times more efficient than the remaining 80% of the waves.
For $\theta \in [15, 30]^\circ$ (Figure 4.8b), the diffusion of the Strahl is again due to the $n = 1$ and $n = 2$ resonances and is between 3 and 10 times (depending on the resonance) more effective than for waves with $\theta \in [0, 15]^\circ$. The $n = -1$ resonance is again at the limit of applicability of our method.
Finally, for $\theta \in [30, 45]$ (Figure 4.8c), the diffusion of the Strahl becomes much more efficient (about a few degrees per second). However, we remain within the range of applicability of

quasi-linear theory: diffusion of $\sim 0.25°$/wave period for n=2. The diffusion of electrons at $n = -1$ is slightly less efficient than for more aligned waves. We recall that the whistler waves with $\theta \in [30, 45]$ represent only 1% of the total number of waves, so the statistics for the right column are smaller than for the others.

Similar conclusions can be drawn for heliocentric distances between 0.75 and 1 AU (2nd row). We note, however, that for quasi-aligned waves (Figures 4.8d and 4.8e), the resonances are slightly closer to 90° with respect to Figures 4.8a and 4.8b. This is due to the fact that the resonance velocity decreases with distance (not shown), which implies that for the same particle energy, the absolute value of $\cos(\alpha)$ must be smaller (Equation 2.13).
When we consider an electron energy of 700 eV (blue lines), we also notice that the pitch angle of resonance approaches 90° (which is again expected from Equation 2.13) and that there are resonances at higher harmonics ($n = -4$ for the second row). Finally, using Equation 2.13, it is possible to understand that the range of resonance pitch angles and the difference in resonance pitch angles between the 2 energies increase with $|n|$.

4.2.2.2 Integrated diffusion between 0.5 and 1 AU

We now focus on the integrated diffusion coefficients and start by discussing the total impact of whistler waves on 300 eV electrons between 0.5 and 0.75 AU (first row of Figure 4.9). At this energy, electrons take about 1h40 to travel a radial distance of 0.25 AU. As the occurrence of the 80% less intense whistler waves with $\theta \in [0, 15]°$ is about 1.25% at these distances, the electrons encounter about 75 wave packets. Using Equation 4.2, we deduce that the total diffusion of Strahl electrons due to these waves is of the order of 0.5°. The role of the 20% most intense waves is similar. Therefore, in spite of the fact that they represent the majority of the observed waves (92.5% of the cases), the most aligned whistlers ($\theta \in [0, 15]°$) cannot explain the Strahl diffusion (at 300 eV) observed between 0.5 and 0.75 AU (of the order of 10° (Bercic et al., 2019)). However, for halo electrons, the $n = -1$ and $n = -2$ resonances provoke highly efficient interactions and contribute effectively to the isotropization of this population.
The total diffusion of 300 eV Strahl electrons by waves with a propagation angle $\theta \in [15, 30]°$ (Figure 4.9b) is more important because (as discussed in Section 4.2.2.1) there are more effective (up to one order of magnitude). The total diffusion of 300 eV Strahl electrons due to these waves is about 4°. This diffusion is due to the encounter with an average of eight wave packets verifying $\theta \in [15, 30]°$. These waves also participate in the isotropization of the halo by the $n < 0$ resonances.
Finally, whistler waves with propagation angle $\theta \in [30, 45]°$ (Figure 4.9c) are also important despite their very low occurrence. Indeed, the total diffusion of 300 eV Strahl electrons is of the order of 8° and is due to the encounter with an average of 1.5 wave packets. Their role in the isotropization of the halo with respect to the more aligned waves is negligible.

We therefore expect a diffusion on the order of 10° of the 300 eV Strahl electrons between 0.5 and 0.75 AU (by integrating the effect of the waves from all the propagation angle bins)

which is consistent with what was observed by Bercic et al. (2019). Our method indicates that whistlers with $\theta \in [15, 45]^\circ$ seem to be responsible for most of the diffusion of the Strahl electrons (at 300 eV), although they represent only 7% of the waves. In the majority of cases the most important diffusion is at n=2 and not n=1 (resonance pitch angle too large in relation to the Strahl PAW). We are at the limit of applicability of the quasi-linear theory for n=-1 resonance, which leads to an overestimation of the diffusion of the halo. However, our results still show that the waves also participate effectively in the isotropization of the halo electrons, most of which is due to waves having $\theta \leq 15^\circ$.

For 700 eV electrons, the conclusions are similar to the case of 300 eV electrons.

The results between 0.75 and 1 AU (fourth row) are close to those obtained between 0.5 and 0.75 AU, with whistler waves with $\theta \in [15, 45]^\circ$ providing a diffusion of the Strahl electrons of the order of 10° at both energies. This is notably facilitated since the PAW is larger at these distances. As we have fewer statistics between 0.3 and 0.5 AU, and in order not to overload the figures, we do not show this distance range in Figures 4.8 and 4.9. However, as discussed in Section 4.1.2.1, the occurrence and properties of these waves are similar to those between 0.5 and 1 AU. We can therefore assume that whistler waves are also involved in Strahl scattering between 0.3 and 0.5 AU.

4.2.3 Electron diffusion around 0.2 AU

Around 0.2 AU, with Parker Solar Probe observations, we have identified both Strahl-aligned and counter-streaming whistler waves (Section 4.1.2.2). We consider these two cases separately in the following. As there are fewer statistics than with Solar Orbiter, we average over all propagation angles and amplitudes to obtain Figure 4.10. This figure shows the local (first row) and integrated (second row) diffusion coefficients for Strahl-aligned (first column) and counter-streaming (second column) whistler waves.

We start by describing the local diffusion of electrons by Strahl-aligned whistler waves (Figure 4.10a). We first note the absence of resonance with $n > 0$ for 300 eV electrons (orange color), which prevents the Strahl from being diffused by these waves. This absence of resonance seems to be due to a lower ω_{pe}/ω_{ce} ratio (and therefore a higher phase speed) for the Strahl-aligned whistlers at these heliocentric distances: $\omega_{pe}/\omega_{ce} \simeq 87$ at 0.2 AU while $\omega_{pe}/\omega_{ce} > 220$ between 0.5 and 1 AU (average values). Nevertheless, since only 30 of these waves were detected, more statistics are necessary to confirm if this is a true effect or if this is caused by low statistics. The resonance at $n = -1$ is close to a pitch angle of 180° but gives a diffusion coefficient of the order of 200°/s. Since the frequency of the waves is more important at this distance (f $\simeq$ 180Hz), the quasi-linear theory is still valid for this resonance diffusion of $\sim 1.1^\circ$/wave period). For 700 eV Strahl electrons, only the resonance n=1 (for $\alpha \leq 90^\circ$) occurs, again due to the low ω_{pe}/ω_{ce}. As the average amplitude of these waves is important (0.33 nT, against 0.05 nT between 0.5 and 1 AU) their efficiency is similar to waves with $\theta > 30^\circ$ between 0.5 and 1 AU in spite of the fact that the average angle of propagation is 12°.

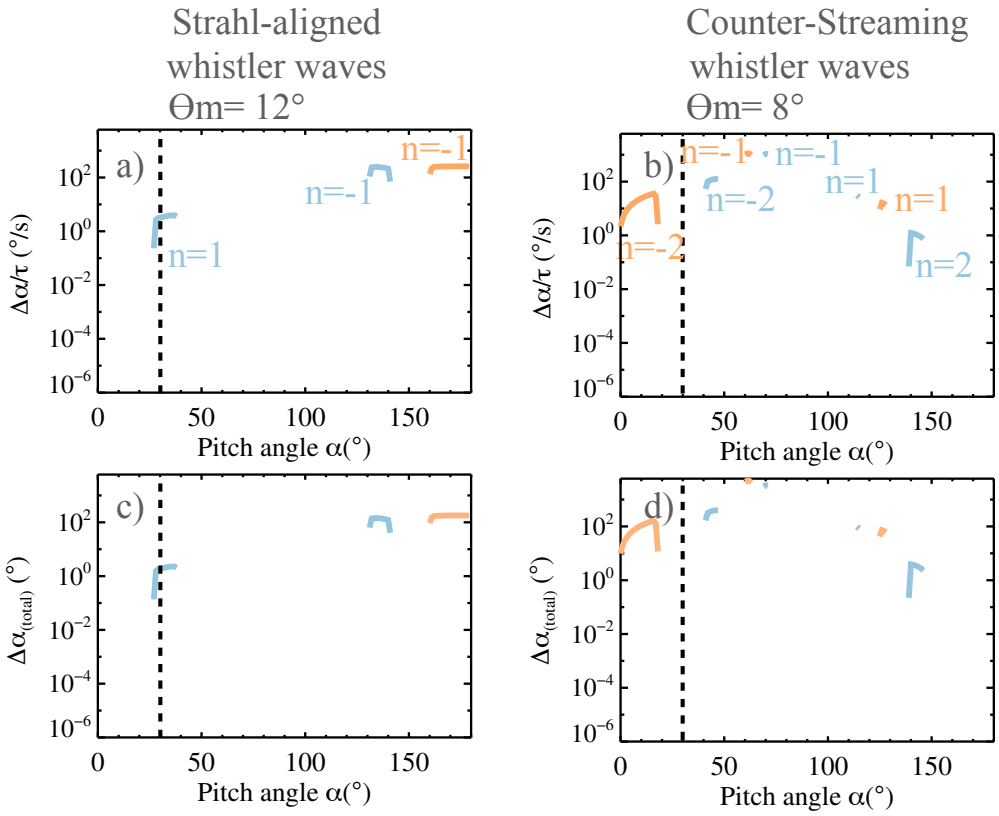

Figure 4.10: Local (first row) and integrated (second row) diffusion coefficients for Strahl-aligned (left column) and counter-streaming whistler waves (right column), at 0.2 AU. The diffusion coefficients are integrated over 0.05 AU only. Legends and notations are comparable to those of Figure 4.8.

We now focus on the counter-streaming whistler waves (right column). We notice that they are very efficient in diffusing the Strahl (interpolation of local diffusion coefficients gives about a hundred degrees per second at the PAW, Figure 4.10b). The Strahl diffusion is mainly due to the $n = -2$ resonance since the PAW is small at 0.2 AU. The $n = -1$ resonance is out of the range of applicability of quasi-linear theory.

As explained in Section 4.1.2.1, the PSP burst mode being triggered, the occurrence of whistler waves is probably overestimated. This therefore induces an overestimation of their global effect (Figures 4.10c and 4.10d). On the other hand, counter-streaming waves are very efficient in diffusing Strahl electrons and account for at least half of all waves. This indicates that they probably play an important role in the Strahl diffusion around 0.2 AU. These waves are probably more important than the oblique waves ($\theta \geq 45°$) in the Strahl scattering since oblique waves account for only 3% of the whistlers measured (Froment et al., 2023).

4.2.4 Signature of Strahl diffusion by whistler waves?

In this section, we discuss evidence of the Strahl diffusion by whistler waves provided by the simultaneous observation of whistler waves and electron distribution functions.

Figure 4.11 shows a period of whistler activity observed by Parker Solar Probe on 2018/11/03 between 9:00 and 11:30, at a heliocentric distance of ~ 0.17 AU. This example has already been studied by Cattell et al. (2021b). In this study, they used band-pass filtered and burst waveforms data (7 measurements of ~ 3.5s during this interval). Consequently, they were unable to determine the precise angle of propagation of the whistler waves during the full duration of this interval. Here, the angle of propagation (Figure 4.11c) is computed using the method presented in Froment et al. (2023). This method consists of the joint analysis of spectral matrices and band-pass filtered data. Band-pass filtered data (with a measurement rate (0.87 s) allows us to determine the precise background magnetic field at the time of the wave packet. This value is then used with the cross spectra data to determine the angle of propagation. As can be seen in Figure 4.11c the majority of the waves are quasi-aligned with the magnetic field. Only 3% of the waves have a propagation angle greater than 45°.
It is noticeable that this whistler activity is associated with a pitch angle diffusion of the Strahl as was shown by Cattell et al. (2021b). Here, we show that these whistlers are not oblique but mostly quasi-aligned. Moreover, our analysis of burst waveforms data shows that a significant proportion (75% of the wave packets in the burst waveforms) propagates counter-streaming. These observations are in agreement with the results of sections 4.2.2 and 4.2.3, which indicate that whistler waves and especially counter-streaming waves can diffuse Strahl electrons very efficiently. On the other hand, one must be cautious when interpreting the observations shown in Figure 4.11. Indeed, we notice in Figure 4.11a the presence of many switchbacks during this interval. Since the acquisition time of the e-VDFs is long during this interval ~ 20s, the observation of Strahl diffusion, may, in some cases, simply be due to significant deflection of the magnetic field during the acquisition.

4.3 Discussion and conclusion

The main findings of the previous sections can be summarised as follows.

First, around 0.2 AU, both Strahl-aligned and counter-streaming whistler waves are present and can play a role in the Strahl diffusion. However, counter-streaming waves are up to two orders of magnitude more efficient than Strahl-aligned ones. The interaction of these waves with Strahl electrons is mainly due to the $n = -2$ resonance. A highly efficient Strahl electron diffusion process is expected around 0.2 AU to explain the observed increase in PAW in spite of the significant focusing at these distances. The integrated effect of the observed waves is difficult to estimate because of the bias in the occurrence rate determined for PSP, due to burst modes being triggered to detect intermittent waves in the electric field (Bale et al., 2016; Malaspina et al., 2016), and because of the low statistics. However, given their very high efficiency, we can assume that counter-streaming waves play an important role in Strahl diffusion around 0.2 AU.

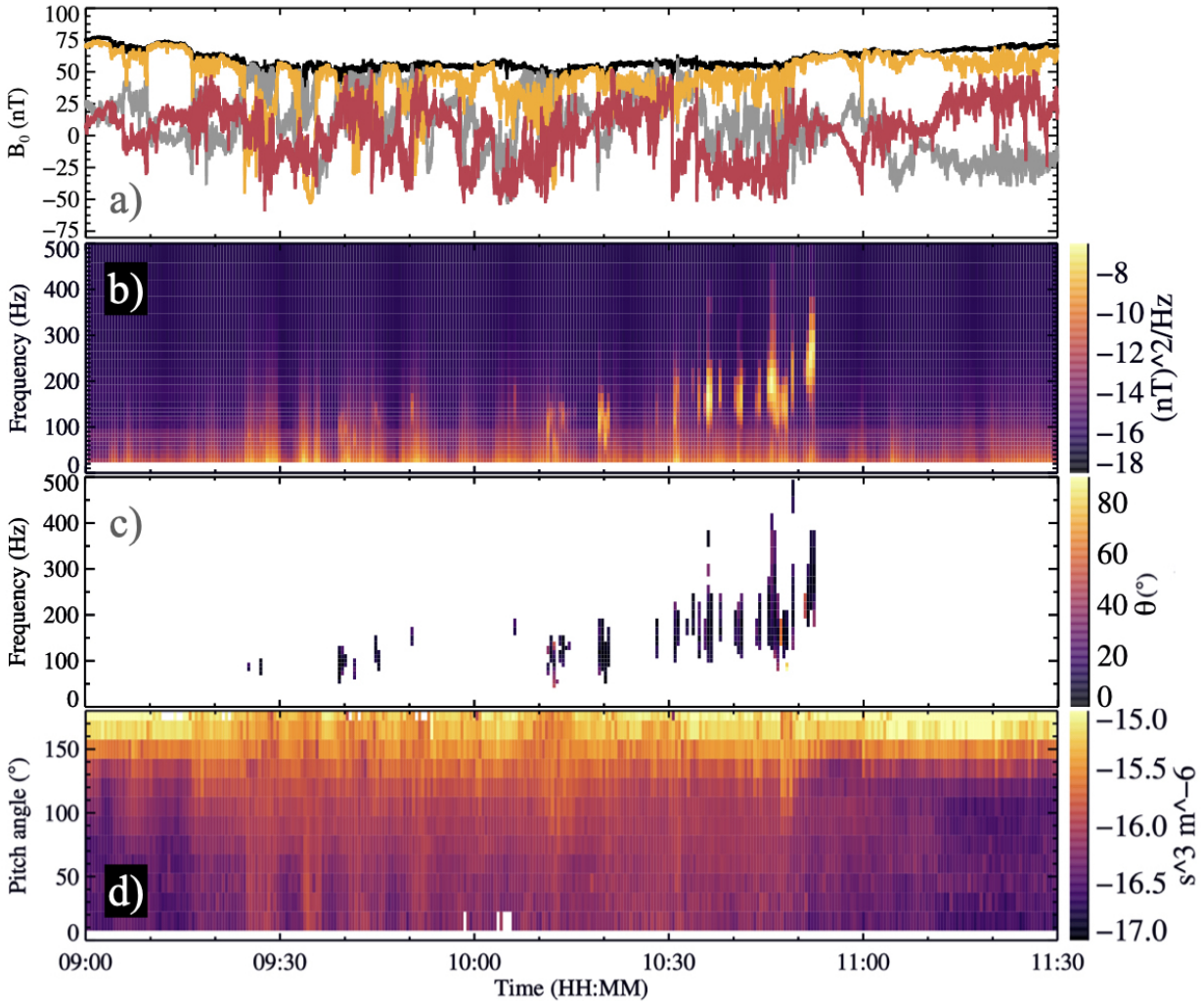

Figure 4.11: Parker Solar Probe observations on 2018/11/03. *Panel a):* Background magnetic field B_0. The X component is in grey, Y is in red, Z is in yellow and the norm is in black (spacecraft reference frame). *Panel b):* Power spectral density of the magnetic fluctuation cross spectra data. *Panel c):* Angle of propagation. *Panel d):* Pitch angle distribution for electrons with an energy between 100 and 1000 eV.

Second, between 0.3 and 1 AU, our method suggests that Strahl-aligned whistler waves can explain the observed diffusion of the Strahl electrons. Indeed, our estimate for the total diffusion of the Strahl is of the order of 10° every 0.25 AU, which is consistent with the observations of Bercic et al. (2019). We found that although whistler waves with $\theta \in [15, 45]^\circ$ represent only 7% of the waves, their efficiency ($\sim 1^\circ/\text{s}$) is large enough to be responsible for the majority of the Strahl diffusion. Specifically, waves with $\theta \geq 30^\circ$ account for the majority of the diffusion. The origin of waves verifying $\theta \in [15, 45]^\circ$ is not clearly established and deserves further study. These waves may be due to another instability generating slightly oblique waves or are associated with particular magnetic configurations (e.g. dips, switchbacks). Waves verifying $\theta \geq 45^\circ$, are too few in number and can only have a sporadic impact on the Strahl electrons. It is therefore important to note that our results suggest that Strahl diffusion is not due to an instability generating oblique whistlers, such as the fan instability ($\theta \sim 70^\circ$), as has been often suggested. It is also interesting to note that, contrary to the results obtained in the radiation belts (Artemyev et al., 2012), that it is not only the most intense waves that are responsible for the diffusion. Indeed, we found that the role of the 80% less intense whistler waves is equivalent to that of the 20% most intense ones. It should be noted that these results are coherent with observations by Kajdič et al. (2016). Indeed, using Cluster data at 1 AU, they showed that the Strahl PAW is between 2° and 12° larger during intervals when whistlers are present than during intervals when they are absent. The whistlers observed were also predominantly quasi-aligned. The diffusion of halo electrons by Strahl-aligned whistler waves is very efficient. Specifically, quasi-aligned whistlers ($\theta \in [0, 15]^\circ$) make a very effective contribution to the isotropization of the halo electrons.

Figure 4.12 shows these results together with schematics of the electron velocity distribution functions (e-VDFs) for different heliocentric distances, with the aim of representing how whistler waves interact with the distribution. The parallel $||$ and perpendicular $\perp$ temperatures of the core electrons observed by Štverák, Trávníček, and Hellinger (2015) are used to represent the anisotropy of this population. The halo is assumed to be isotropic. The energy distribution of the different populations and their velocity drifts in the proton reference frame are taken from Halekas et al. (2020, 2022) for Figures 4.12a and 4.12b, Berčič et al. (2021) for Figure 4.12c, and Tong et al. (2019b) for Figure 4.12d. The phase and resonance velocities are the mean values observed in this study and we can note that they were found to decrease with distance. As explained in Section 4.1.2.1, to calculate the wave vector, we use the cold plasma dispersion equation Lyons (1974b), which allows us to calculate the phase velocity and the resonance velocity (Equation 2.13). The electron diffusion occurs along circles centered on the parallel wave phase velocity (orange dotted lines, called single-wave characteristics), and the net flux of particles is directed towards a less dense area of the phase space. If the electrons gain (resp., lose) energy in the plasma frame, then they damp (resp., amplify) the waves (Kennel and Wong, 1967; Lyons, 1974b; Verscharen et al., 2022).

Each panel of Figure 4.12 illustrates a diffusion process caused by whistler waves that can be described as follows. First, an instability is triggered by the free energy available in the distribution function. Then, the instability creates a wave that interacts with the electrons of

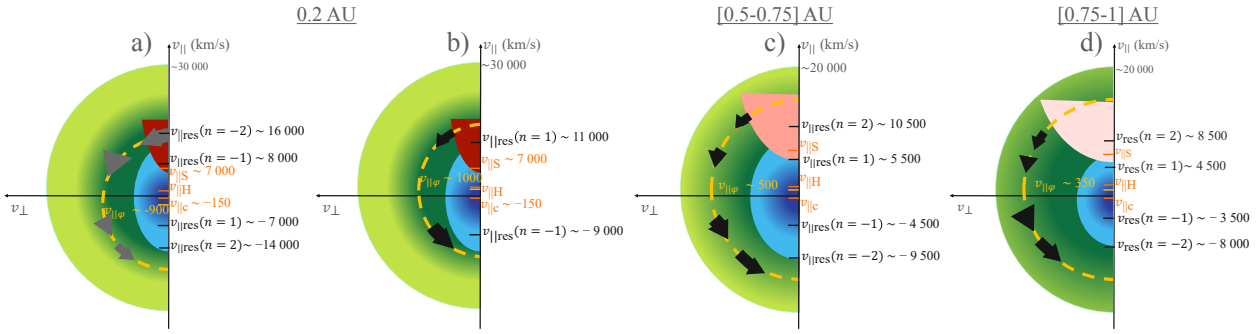

Figure 4.12: Scheme of the evolution of the e-VDF in the ($v_{\perp}$, $v_{||}$) plane and its interaction with whistler waves as a function of heliocentric distance. *Panel a)* represents the effect of counter-streaming whistler waves at 0.2 AU. *Panels b),c),d)* show the effect of Strahl-aligned whistler waves between 0.2 and 1 AU. The blue circles represent the core electrons, the green circles the halo electrons, and the red and pink beams the Strahl electrons. The intensity of the color represents the population's relative density. The resonance velocities ($v_{\mathrm{res}||}$) for $n = \pm 1$ and $n = \pm 2$, the drift velocities of the core, halo, and Strahl (noted $v_{\mathrm{c}||}$,$v_{\mathrm{H}||}$,$v_{\mathrm{S}||}$, respectively), and the parallel phase velocities $v_{\varphi||}$ of the waves are indicated along the $v_{||}$ axis. The resonance velocities with $n = \pm 3$ are not represented for clarity. One of the single-wave characteristics (centered around $v_{\varphi||}$) is represented by an orange dotted line. The path of the diffusing electrons is indicated by the arrows. This diffusion takes place around parallel resonance speeds. The role of the diffusing electrons in the amplification (resp., damping) of the waves is represented by black (resp., grey) arrows.

the distribution function and diffuses them in the phase space. The objective of Figure 4.12 is not to represent the instabilities that can create the waves but to schematically represent the evolution of the distribution function and the role of the whistler waves in this evolution. Nevertheless, at 0.2 AU, for counter-streaming whistlers, the instability can be caused by trapped electrons as proposed by Karbashewski et al. (2023). For Strahl-aligned whistlers, the instabilities can be the WHFI (Gary et al., 1975; Tong et al., 2019b), the temperature anisotropy (Sagdeev and Shafranov, 1960; Kennel and Petschek, 1966; Jagarlamudi et al., 2020; Vasko et al., 2020) or the sunward suprathermal electron deficit (Berčič et al., 2021).

At 0.2 AU we represent the distribution function with a high density ratio between the Strahl and the halo and with a strongly focused Strahl, as is widely known (Maksimovic et al., 2005a; Štverák et al., 2009; Bercic et al., 2019). The diffusion of Strahl electrons by the counter-streaming whistlers is very efficient (Figure 4.12a). However, the diffusion of Strahl electrons by Strahl-aligned whistlers is less efficient (Figure 4.12b). It is likely that these diffusion processes at 0.2 AU explain the increase in the Strahl PAW as well as of the relative proportion of halo electrons, which we schematize in Figure 4.12c).

An increase in relative halo density and Strahl PAW is also represented (Figures 4.12c to 4.12d) (Maksimovic et al., 2005a; Štverák et al., 2009; Bercic et al., 2019). The results of previous sections suggest that whistler waves verifying $\theta \in [15, 45]^\circ$ explain the increase in the Strahl PAW and probably the increase in the relative density of the halo. The observed evolution of the wave occurence (Figure 4.2) can be interpreted as follows. The growth of the relative halo density could explain the increase in the occurrence of the waves in the observations between 0.3 and 0.6 AU. Indeed, Strahl-aligned waves are generated by halo electrons. We can then suppose that the quasi-aligned waves saturate the instabilities (i.e. eliminates the free energy present in the distribution function), which could then explain the decrease in the occurrence between 0.6 and 1 AU. For Figures 4.12b to 4.12d the $n < 0$ resonances are very efficient and participate in the halo istropization whereas $n > 0$ resonances participate slowly to the Strahl diffusion.

Our conclusions are as follows:

- We perform the largest statistical study of whistler waves in the solar wind to date (about 110,000 wave packets). This statistic contains all important whistler parameters between 0.2 and 1 AU to understand the wave-particle interactions. In particular, we characterize whistler wave occurrence, amplitude, propagation angle, and radial direction of propagation.

- Between 0.3 and 1 AU, we observe an overwhelming majority of whistlers propagating in the Strahl direction (Strahl-aligned) and also nearly aligned with the magnetic field. The few whistler waves found to propagate sunward are within switchbacks with a change of sign of the radial component, so that they are still aligned with the Strahl. At 0.2 AU, we observe both Strahl-aligned and counter-streaming (propagating in the opposite direction to the Strahl) whistler waves.

- Between 0.3 and 1 AU, whistlers propagating at an angle verifying $\theta \in [15, 45]^\circ$ (the

origin of which has not yet been fully determined) are sufficiently efficient (of the order of 1 °/s) to explain the observed increase in the Strahl PAW in spite of the fact that they represent only 7% of the cases. These waves also explain the observed transfer from the Strahl to the halo. At 0.2 AU the counter-streaming whistler waves are more efficient in diffusing the Strahl than the Strahl-aligned waves by two orders of magnitude. However, we had to restrict our analysis to the first perihelion of PSP and the statistics is small. We have developed a method to retrieve whistler waves properties for other perihelia (Chapter 5) which will enable us to increase the statistics at 0.2 AU and below and to better characterize whistler occurrences and generation mechanisms in future studies.

4.4 Résumé en français du chapitre 4

Comme expliqué dans le chapitre 1, l'évolution de la fonction de distribution des électrons dans le vent solaire présente différentes caractéristiques qui restent inexpliquées, en particulier la diminution rapide du flux de chaleur et l'augmentation de la largeur angulaire du Strahl. Les interactions ondes-particules entre les électrons et les ondes de sifflement sont souvent proposées pour expliquer ces phénomènes. Dans ce chapitre, nous cherchons à quantifier l'effet des ondes de sifflement sur la fonction de distribution des électrons en fonction de la distance héliocentrique. Spécifiquement, nous voulons quantifier l'augmentation de la largeur angulaire du Strahl causée par l'interaction avec les ondes de sifflement.

Pour cela, nous effectuons d'abord une analyse statistique des ondes de sifflement (occurrence et propriétés) observées par Solar Orbiter et Parker Solar Probe entre 0,2 et 1 UA.
Au-delà de 0,3 UA, nous trouvons une majorité d'ondes de sifflement quasi-parallèles. La fonction de distribution des angles de propagation pique entre 3 et 7° et diminue ensuite rapidement avec l'angle. Seulement 7,5% des ondes ont un angle de propagation supérieur à 15° et 0,5% ont un angle de propagation supérieur à 45°. Ceci est en contraste avec de nombreuses études prédisant le rôle majeur des ondes obliques ($\sim 70°$) dans l'évolution de la fonction de distribution des électrons.
En dessous de 15°, la distribution des angles peut s'expliquer par une instabilité générant des ondes alignées (taux de croissance maximal à 0°) et avec la propagation des ondes dans un champ magnétique courbé. Ces instabilités peuvent être : l'instabilité de flux de chaleur, d'anisotropie de température ou de déficit suprathermique vers le Soleil (Tong et al., 2019b; Jagarlamudi et al., 2020; Berčič et al., 2021). Une étude supplémentaire est nécessaire pour déterminer l'origine des ondes ayant un angle de propagation $\in [15, 45]°$ et pour confirmer l'origine physique des ondes ayant un angle de propagation supérieur à 45°. De plus, les ondes se propagent presque toutes dans la direction de la propagation du Strahl, y compris à l'intérieur de "switchbacks". La quasi-absence d'ondes obliques et d'ondes se propageant vers le Soleil est un résultat important. En effet, ces ondes sont les plus efficaces pour interagir avec le Strahl ; elles ont été souvent proposées pour expliquer l'augmentation de sa largeur angulaire.
Cependant, à 0,2 UA, nous trouvons un nombre important d'ondes "counter-streaming" (se propageant dans le sens opposé au Strahl) . Elles sont en majorité associées à des creux dans le champ magnétique, ce qui indique que ces structures favorisent la génération d'ondes de sifflement counter-streaming, comme proposé par Karbashewski et al. (2023).

Les caractéristiques des ondes sont ensuite utilisées pour calculer les coefficients de diffusion des électrons suprathermiques du vent solaire dans le cadre de la théorie quasi-linéaire. Ces coefficients sont intégrés afin de déduire l'effet global des ondes de sifflement sur les électrons tout au long de leur propagation.
Entre 0,3 et 1 UA, les siffleurs se propageant avec un angle $\in [15, 45]°$ sont suffisamment efficaces (de l'ordre de 1 °/s) pour expliquer l'augmentation observée de la largeur angulaire du Strahl malgré le fait qu'ils ne représentent que 7% des cas. Il est probable que ces ondes

expliquent également le transfert observé du Strahl vers le halo. Les ondes ayant un angle de propagation inférieur à 15° sont trop peu efficaces, et celles ayant un angle supérieur à 45° trop peu nombreuses pour avoir un impact.
À 0,2 UA, les ondes de sifflement counter-streaming sont plus efficaces pour diffuser le Strahl que les ondes alignées avec le Strahl (deux ordres de grandeur). Cependant, nous avons dû restreindre notre analyse au premier périhélie de PSP à cause du problème technique survenu sur une antenne du SCM au début du 2ème périhélie. Les statistiques de cette étude sont donc trop faibles pour conclure sur le rôle total des ondes à cette distance. Une méthode pour augmenter cette statistique et trouver les propriétés de polarisation des ondes de sifflement malgré ce problème technique est présentée dans le prochain chapitre.

Chapter 5

Reconstruction of polarization properties of whistler waves from two magnetic and two electric field components: application to Parker Solar Probe measurements

As described in Section 2.3, several studies have investigated whistler waves using data from PSP. In previous studies, the polarization properties of whistler waves in the young solar wind were inferred from the three SCM components during Encounter 1 (Agapitov et al., 2020; Cattell et al., 2020, 2021b, 2022; Dudok De Wit et al., 2022; Froment et al., 2023; Karbashewski et al., 2023). The statistical study of whistler properties by (Froment et al., 2023) revealed that most of the whistler wave packets recorded during Encounter 1 were quasi-parallel to the background magnetic field: 97% had WNA between 0 and 25°. Whistler waves were observed in the frequency range from the local lower hybrid frequency $f_{\rm lh}$ up to $0.2f_{\rm ce}$. The observed oblique whistlers (with WNA $> 45°$) tend to have lower frequencies than the quasi-parallel whistlers. The sunward propagating whistler waves, both quasi-parallel and oblique waves, were often collocated with short-lived magnetic dips observed at switchback boundaries. This indicates a possible generation of whistlers in these structures due to a trapped electron population (Agapitov et al., 2020; Froment et al., 2023; Karbashewski et al., 2023). These waves tend to be detected at frequencies that are lower than those for waves that are not collocated with magnetic dips (Froment et al., 2023). Another statistical study by (Cattell et al., 2022), on the basis of electric field measurements from the first nine encounters, showed that below the heliocentric distance of 100 $R_\odot$ whistler wave frequencies in the spacecraft frame were below $0.2f_{\rm ce}$ with the tendency to decrease below $0.1f_{\rm ce}$ when approaching the Sun closer than 50 $R_\odot$. To further elucidate the impact of whistler waves on the suprathermal electrons it is necessary to extend the statistics reported by (Froment et al., 2023) for Encounter 1 (the only one available with a full set of SCM magnetic measurements (Dudok De Wit et al., 2022)) to the later encounters and update the statistics of whistler

waves presented by Cattell et al. (2021b) and Cattell et al. (2022) with the wave polarization parameters.

A change in the response in one of the SCM components: $B\mathrm{w_u}$ of the SCM reference frame, $(\vec{u}, \vec{v}, \vec{w})$ (Malaspina et al., 2016), appeared after March 2019. Here and in the following $\vec{B}\mathrm{w}$ and $\vec{E}\mathrm{w}$ represent the wave magnetic and electric perturbations, respectively. This anomaly considerably reduces the amplitude of the $B\mathrm{w_u}$ component in the frequency range of whistler waves (typically, below 400 Hz) and also affects its phase. This makes it impossible to unambiguously determine the polarization properties using the three components of the magnetic field and the two components of the electric field. The inability to determine the whistler wave properties beyond Encounter 1 has motivated us to propose a novel technique for reconstructing the whistler wave polarization parameters. The technique uses the two components of the SCM that are available together with the two electric field components recorded by the EFI. It can be noted that the STEREO spacecraft have electrical antennas that measure 3 components of the electric field but do not have SCMs. Breneman et al. (2010) therefore developed a method based on the whistler wave cold dispersion relation and the ratio of transverse electric field components to determine whistler WNAs. This method is not designed to reconstruct electromagnetic field components and is different from the one proposed here. In addition, in the case of Breneman et al. (2010) the absence of magnetic field fluctuation measurements makes it impossible to determine the direction of propagation.

In the following, we present the data used (Section 5.1.1), our reconstruction method (Section 5.1.2) and its range of applicability (Section 5.1.3). We then detail the reconstruction of three whistler wave packets from Encounter 1 (Sections 5.2.1, 5.2.2, 5.2.3). We finally discuss the applicability of the method to other encounters (Section 5.3.1) and apply the technique to a whistler wave packet from Encounter 2 (Section 5.3.2). This chapter is based on the article accepted in the Journal of Geophysical Research: Colomban et al. (2023b).

5.1 Data and method descriptions

5.1.1 Data

In this study, we use the survey mode waveforms (292.97 Hz) and the burst waveforms (150 kHz) of the magnetic and electric fields from the SCM and EFI. We also use data from the PSP DC fluxgate magnetometer (MAG), that measures three components of the magnetic field in spacecraft coordinates, to estimate the background magnetic field. The background plasma density and the solar wind speed are obtained from the SWEAP Solar Probe Cup, SPAN-C (Kasper et al., 2016; Case et al., 2020).

5.1.2 The reconstruction technique

With three components of the fluctuating magnetic field the ellipticity of the wave can be obtained by the analysis of the spectral matrices (Means, 1972; Santolík, Parrot, and Lefeuvre, 2003; Taubenschuss and Santolík, 2019). The WNA can be determined with these matrices

or by a minimum variance analysis (Sonnerup and Cahill Jr., 1967; Sonnerup and Scheible, 1998; Paschmann and Daly, 1998). These methods give the propagation angle with an ambiguity of $\pm 180°$ which is removed by calculating the radial direction of propagation (sunward or anti-sunward). The latter is determined by calculating the sign of the Z component (S_{Z}, of the spacecraft reference frame) of the Poynting flux. We use these methods in Chapter 4. The three components of the magnetic field and the two components of the electric field can also be used with the equation $\vec{E}\mathrm{w}(\omega,t)\cdot\vec{B}\mathrm{w}(\omega,t)=0$ to find the missing component of the electric field and thus determine the Poynting flux completely.

If one of the three components of magnetic field perturbations is not measured, direct estimation of wave polarization parameters is not possible. However, if two magnetic components and two electric field components are geometrically independent, as in the case of the SCM and EFI, it can be possible to reconstruct the missing third component of the fluctuating magnetic field; this requires knowledge of the wave dispersion and polarization properties over the range of observed perturbation frequencies. Whistler waves, as an electromagnetic plasma mode with a well-defined right-handed polarization in the frequency range from f_{lh} to f_{ce}, are a good candidate for reconstruction.

Using the cold plasma dispersion relation for whistler waves and the low-frequency and high-density limits ($\omega/\omega_{\mathrm{ce}} \ll 1$, $\omega_{\mathrm{pe}}^2 \gg \omega_{\mathrm{ce}}^2$ where ω_{pe} is the local electron plasma frequency, ω the wave frequency in the plasma frame and $\omega_{\mathrm{ce}} = 2\pi f_{\mathrm{ce}}$), one can show that (see details in Appendix D.1):

$$\frac{|E^{\mathrm{SC}}\mathrm{w}_{||}|}{|E\mathrm{w}|} \leq \left(\frac{V_{\mathrm{SW}\perp}}{V_\varphi} + \left(\frac{\omega}{\omega_{\mathrm{ce}}}\right)\tan\theta\right) \tag{5.1}$$

where $|E^{\mathrm{SC}}\mathrm{w}_{||}|$ is the modulus of the electric field component along the background magnetic field $\vec{B}_0$ in the spacecraft frame. In the following, quantities with the $^{\mathrm{SC}}$ superscript are in the spacecraft frame while quantities in the plasma frame (i.e., taking into account the Lorentz transformations (Feynman, 1964)) are noted without superscript. Subscripts are used to give the reference frames, $(\vec{X},\vec{Y},\vec{Z})$ corresponding to the spacecraft, $(\vec{u},\vec{v},\vec{w})$ corresponding to the SCM and $(\|,\perp)$ corresponding to the background magnetic field. $V_{\mathrm{SW}\perp}$ is the measured perpendicular solar wind speed and V_φ is the wave phase speed. We note that $|E^{\mathrm{SC}}\mathrm{w}_{||}|/|\mathrm{Ew}|$ is small if $\omega \ll \omega_{\mathrm{ce}}$, $\tan\theta \leq 1$ and $V_{\mathrm{SW}\perp}/V_\varphi \ll 1$. In this case, we can make the following approximation:

$$E^{\mathrm{SC}}\mathrm{w}_{\mathrm{X}}B_{0\mathrm{X}} + E^{\mathrm{SC}}\mathrm{w}_{\mathrm{Y}}B_{0\mathrm{Y}} + E^{\mathrm{SC}}\mathrm{w}_{\mathrm{Z}}B_{0\mathrm{Z}} = E^{\mathrm{SC}}\mathrm{w}_{||} \simeq 0 \tag{5.2}$$

The validity of this approximation and its effect on reconstruction is discussed in detail in Section 5.1.3. Equation 5.2 enables a reconstruction of the third component ($E^{\mathrm{SCre}}\mathrm{w}_{\mathrm{Z}}$) of the electric field from the measured values $E^{\mathrm{SC}}\mathrm{w}_{\mathrm{X}}$ and $E^{\mathrm{SC}}\mathrm{w}_{\mathrm{Y}}$. Note that there is a division by zero when $B_{0\mathrm{Z}} = 0$, in which case the method cannot work.
The reconstructed electric field $\vec{E}^{\mathrm{SCre}}\mathrm{w}$ (in the spacecraft reference frame) can then be expressed in the SCM reference frame and used to reconstruct the third component of wave magnetic field $B^{\mathrm{SCre}}\mathrm{w}_{\mathrm{u}}$. For this purpose, we use the two measured components of the SCM

($B^{\mathrm{SC}}\mathrm{w_v}$ and $B^{\mathrm{SC}}\mathrm{w_w}$) and the electromagnetic wave equation in which the only unknown is $B^{\mathrm{SCre}}\mathrm{w_u}$:

$$\vec{E}^{\mathrm{SCre}}\mathrm{w}(\omega,t)\cdot\vec{B}^{\mathrm{SC}}\mathrm{w}(\omega,t)\simeq 0 \tag{5.3}$$

The right-hand side of Equation 5.3 is not explicitly zero because of the approximation made in Equation 5.2. (ω,t) represents the time averaged Fourier transform. Equation 5.3 is solved in the Fourier frequency domain to take into account the whistler dispersion relation and the dependence of the estimation error on frequency. The waveform $B^{\mathrm{SCre}}\mathrm{w_u}$ is then obtained from the inverse Fourier transform. As explained in Appendix D.1, because $V_{\mathrm{SW}} \ll c$ (where c is the speed of light) we can safely consider that $\vec{B}^{\mathrm{SC}}\mathrm{w} = \vec{B}\mathrm{w}$.

Since the right-hand side of Equations 5.2 and 5.3 is 0, they do not depend on the amplitude of the electric field. The method presented here is therefore independent of the effective length. In the following, we therefore take an effective length of 3.5 m, even though this length depends on the frequency and on the propagation direction as shown by Karbashewski et al. (2023).

5.1.3 Validity of the approximation

The main approximation of this method is therefore to consider $E^{\mathrm{SC}}\mathrm{w}_{||} = 0$. An upper value of $|E^{\mathrm{SC}}\mathrm{w}_{||}|/|E\mathrm{w}|$ is given by Equation 5.1. We can distinguish two sources of error.
The first source of error comes from the fact that the measured electric field is different from the electric field in the plasma frame. To obtain the electric field in the plasma frame, one needs to carry out the Lorentz transformations (Feynman, 1964), which is not directly possible with only two components of the magnetic field. This error can be expressed as $\frac{V_{\mathrm{SW}\perp}}{V_\varphi}$ and can be significant if the solar wind velocity and background magnetic field are not aligned and if the phase velocity is low.
The second source of error comes from the parallel component of the electric field in the plasma frame, which is not zero if the WNA is not equal to zero. This error can be expressed as $(\frac{\omega}{\omega_{\mathrm{ce}}})\tan\theta$ and can be significant if the wave is oblique or if $\frac{\omega}{\omega_{\mathrm{ce}}}$ is large. These errors are detailed in Appendix D.2.

The propagation of these errors gives an error on the reconstructed magnetic field, whose amplitude can be approximated as follows (see details in Appendix D.2):

$$(|B^{\mathrm{error}}\mathrm{w_u}/B\mathrm{w}|) \lesssim \sqrt{(\frac{V_{\mathrm{SW}\perp}}{V_\varphi}\sin\theta)^2 + ((\frac{\omega}{\omega_{\mathrm{ce}}})\tan\theta\sin\theta)^2}\frac{1}{\sin\theta_{\vec{B}_0,\vec{u}}} \tag{5.4}$$

We note a multiplication by $\sin\theta$ (compared to Equation 5.1), which can be explained by the fact that the error is on the parallel component of the electric field, which is multiplied (Equation 5.3) by the parallel component of the magnetic field. Finally, the term $\sin\theta_{\vec{B}_0,\vec{u}}$ comes from the fact that we can't reconstruct the parallel component of the fields correctly since we are making the assumption $E^{\mathrm{SC}}\mathrm{w}_{||} = 0$. Thus, the error increases as the angle between $\vec{B}_0$ and $\vec{u}$ decreases.

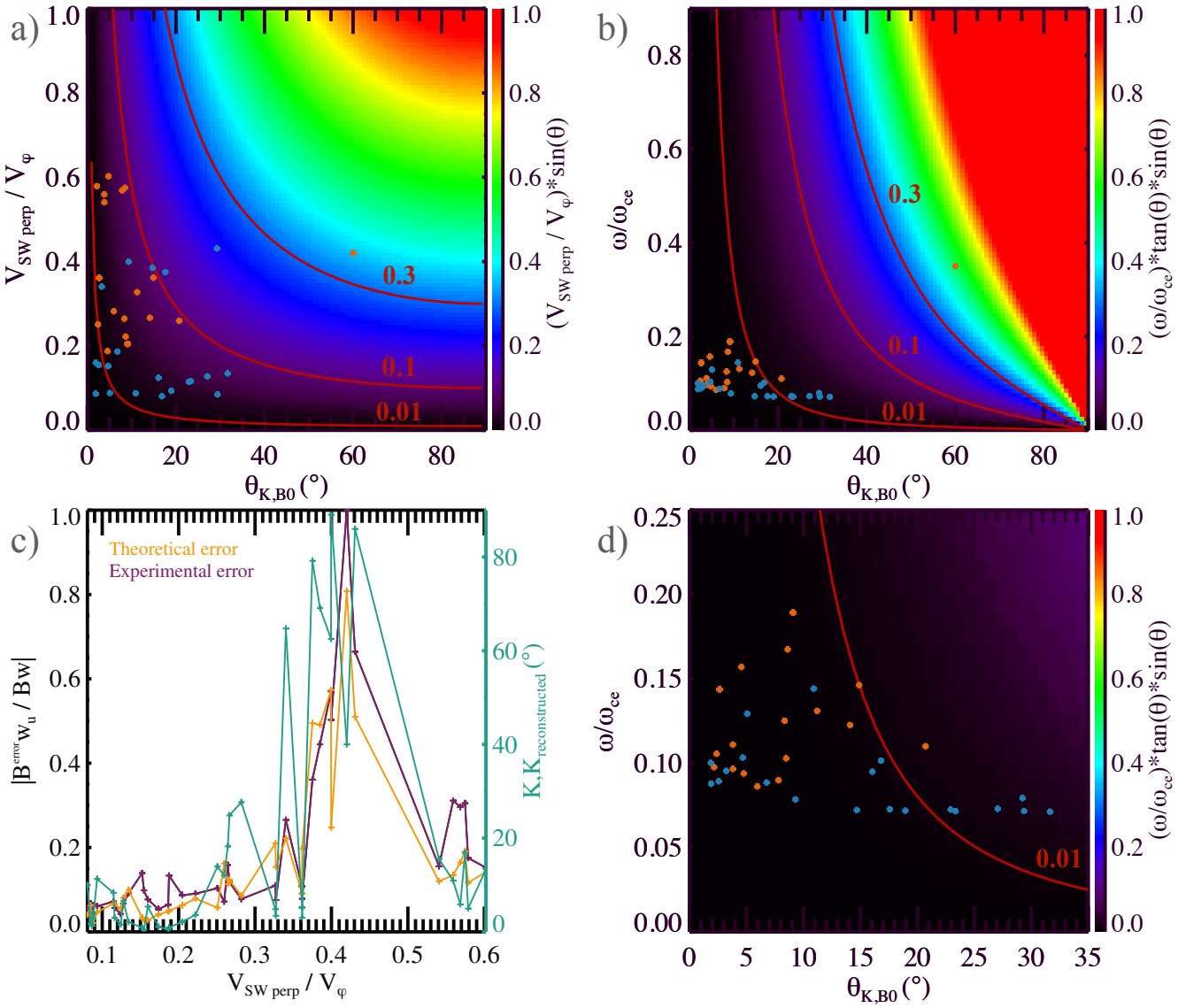

Figure 5.1: *Panel a):* Parameters of whistler waves in the $(\theta, \frac{V_{SW\perp}}{V_\varphi})$ plane observed by PSP during encounter 1 (see text). Anti-sunward (resp., sunward) whistler waves are represented by blue (resp., orange) dots. The error due to the term $\frac{V_{SW\perp}}{V_\varphi}\sin\theta$ is indicated by the background color. *Panel b):* Parameters of whistler waves in the $(\theta, \omega/\omega_{ce})$ plane. The error due to the term $(\frac{\omega}{\omega_{ce}})\tan\theta\sin\theta$ is indicated by the background color. *Panel c):* Theoretical and experimental errors of the reconstruction technique, as well as the angular deviation between the measured and reconstructed wave vector as a function of $\frac{V_{SW\perp}}{V_\varphi}$. *Panel d):* Zoom on the on the lower left side of the *panel b).* In *panels a), c) and d)* ω is the frequency in the plasma frame.

In Figure 5.1a we represent $\frac{V_{\mathrm{SW}\perp}}{V_\varphi}\sin\theta$ in the $(\theta, \frac{V_{\mathrm{SW}\perp}}{V_\varphi})$ plane. The whistler wave packets measured during Parker Solar Probe's first encounter using burst mode are superimposed on this panel (50 wave packets were detected). We also add the characteristics of a wave packet from continuous waveforms at 292.97 Hz (point with $\theta \simeq 60°$). This wave packet is studied in detail in Section 5.2.3. Whistler detection and characterization methods are described in Kretzschmar et al. (2021). We note that the vast majority of points (96%) are below the 10% error line.
In Figure 5.1b we represent $\frac{\omega}{\omega_{\mathrm{ce}}}\tan\theta\sin\theta$ in the $(\theta, \frac{\omega}{\omega_{\mathrm{ce}}})$ plane. The measured whistler characteristics are also superimposed on this panel (see Figure 5.1a). Note that the vast majority (99%) of points are below the 10% error line and 92% of points are below the 0.1% line. We can note that the frequency in the plasma frame of the sunward waves is generally greater than that of the anti-sunward waves (Figure 5.1d). This is a good indication of validity of the generation mechanism proposed by Karbashewski et al. (2023). Note that in this study we are only interested in the clearly sunward or anti-sunward cases, and do not consider the counter-streaming cases (Karbashewski et al., 2023).

The final theoretical error (given by Equation 5.4) is plotted as a function of $\frac{V_{\mathrm{SW}\perp}}{V_\varphi}$ on Figure 5.1c using the characteristics of the measured whistler wave packets. This error is compared with the experimental error defined as $mean(|B^{\mathrm{re}}\mathrm{w_u} - B\mathrm{w_u}|/max(B\mathrm{w_u}))$. There is a good agreement between these two curves which is a good indication that the error is well estimated by Equation 5.4. We note that theoretical and experimental errors tend to increase with $\frac{V_{\mathrm{SW}\perp}}{V_\varphi}$. We also observe a significant error for cases with $0.35 < \frac{V_{\mathrm{SW}\perp}}{V_\varphi} < 0.5$ which is due to the fact that for the majority of these cases $\vec{B_0}$ and $\vec{u}$ were almost aligned. The decrease in error for cases verifying $\frac{V_{\mathrm{SW}\perp}}{V_\varphi} > 0.5$ is due to the fact that their WNAs are close to 0°. In addition, when the theoretical and experimental errors are large, there is a large discrepancy between the measured and reconstructed wave vectors.

For 78% of cases, the theoretical and experimental errors are less than 0.2. For these cases, the error between the measured and reconstructed wave vectors is always less than 30° with an average value of 6°. For 100% of these cases, the reconstructed direction of propagation (sunward or anti-sunward) was found to be correct. Moreover, the averaged reconstructed ellipticity is 0.80, compared with 0.85 for the measured wave packets.
For cases where the error is greater than 0.2, large discrepancies are found between the measured and reconstructed wave vectors (up to 90°), and the sunward or anti-sunward propagation direction is found in only 65% of the cases. For these cases, the averaged reconstructed ellipticity is 0.46.

We can therefore conclude that in about 80% of the burst mode data from the first Parker Solar Probe encounter, the reconstruction method is applicable. When the theoretical error (given by Equation 5.4) is below 0.2, the technique allows to find the direction of propagation (sunward or anti-sunward) in 100% of cases and the error on the WNA is on average 6°. When the theoretical error is bigger than 0.2, the technique is not applicable and this is mainly due to a high $\frac{V_{\mathrm{SW}\perp}}{V_\varphi}$ or a low $\theta_{\vec{B_0},\vec{u}}$. This last source of errors can be easily checked. On the other hand, θ, V_φ and ω are no longer directly accessible after March 2019. The applicability of

this method after this date is therefore discussed in detail Section 5.3.1.

Finally, as mentioned above, Equation 5.1 (and therefore Equation 5.4) is based on the high density hypothesis $\omega_{pe}^2 \gg \omega_{ce}^2$. As explained in Section 2.1.1, extrapolation of helios data (between 0.3 and 1 AU, (Bale et al., 2016)) shows that the expected $\omega_{pe}^2/\omega_{ce}^2$ is around 150 at 10 $R_\odot$. This ratio increases with distance, indicating that this assumption should be valid for all Parker Solar probe encounters.

The results of the reconstruction and its accuracy are illustrated below on three examples from Encounter 1 when all three $(\vec{u}, \vec{v}, \vec{w})$ components of the SCM were available. Two examples demonstrate the regularly observed by PSP whistler wave characteristics: Case 1 and Case 2. Case 3 is atypical because of its frequency, its phase speed, and its WNA and illustrates what happens when one is out of the applicability range of the method. We provide the results of polarization analysis (the radial component of Poynting flux, WNA, ellipticity) and the power spectral density to compare with the values obtained by making use of the reconstructed $B^{\mathrm{re}}\mathrm{w_u}$ magnetic field component. For these 3 examples, we first present the case using the actual measurements (Figures 5.2, 5.4 and 5.6) and then compare them with the results of the reconstruction (Figures 5.3, 5.5 and 5.7).

5.2 Application of the method

5.2.1 Case 1: November 3, 2018, 10:33:31.0-10:33:34.5 UT

Figure 5.2 presents two typical anti-sunward propagating whistler wave packets, recorded at the heliocentric distance of $\sim$ 41 ($R_\odot$) in the FIELDS burst mode (150 kHz) at 10:33:31.0 UTC, November 3, 2018. This figure is adapted from Figure 9 of (Karbashewski et al., 2023). The polarization parameters are directly evaluated using measurements of the three magnetic field components and the missing component of the electric field is estimated from $\vec{E}\mathrm{w}(\omega, t) \cdot \vec{B}\mathrm{w}(\omega, t) = 0$ (Figures 5.2c and 5.2e). This allows us to estimate the Poynting flux vector. The Poynting flux reveals that the whistler waves are propagating from the Sun almost field-aligned, in the opposite direction to the background magnetic field (Figures 5.2e and 5.2f). These wave packets are not associated with any significant perturbation of the background magnetic field (Figure 5.2a), which is regular for anti-sunward propagation (Karbashewski et al., 2023). The observed wave and plasma parameters are typical of the young solar wind: the background magnetic field magnitude is 55 nT; the plasma density is $\sim$ 290 cm^3; $(\omega_{pe}/\omega_{ce})^2 \sim$ 10 000; $\omega/\omega_{ce} \sim 0.1$ (in the plasma frame); the bulk radial plasma velocity is 310 km/s; the wave amplitudes reache 0.5 nT. The observed WNAs of the packets are below 20° (Figure 5.2f). The wave packets propagating anti-sunward have the wave frequency downshifted from the range 130-200 Hz (in the spacecraft frame) to 110-180 Hz (0.08-0.13 f_{ce}) in the plasma frame. The solar wind velocity perpendicular to the magnetic field $V_{SW\perp}$ is about 134 km/s. Finally, the phase velocity is $V_\varphi \sim$ 893km/s and the component to be reconstructed for this test event satisfies the condition of being nearly perpendicular to the magnetic field $\sin(\theta_{\vec{u},\vec{B_0}}) \sim 0.99$.

The results of wave polarization reconstruction on the first wave packet are shown in

Figure 5.3. The orange curves represent the original data, while the black and green curves are obtained using the reconstructed $B^{\mathrm{re}}\mathrm{w_u}$ component. For Figures 5.3a, 5.3b, 5.3h, and 5.3i the thickness of the green and black lines corresponds to the estimation of the theoretical error of the technique (Equation 5.4). This relative error is calculated using the typical frequency (in the plasma frame) and angle of propagation of the wave (black) and a proxy of the propagation angle in green. This proxy is estimated using the theoretical ratio $E_{\mathrm{w}||}/E_{\mathrm{w}}$ in the plasma frame (Equation D.9). For a given value of $\omega/\omega_{\mathrm{ce}}$ the curve $E_{\mathrm{w}||}/E_{\mathrm{w}}$ as a function of θ has a plateau shape. The proxy of the WNA represents the mean value of θ on this plateau. For Figure 5.3c the theoretical errors (associated with each frequency and angle of propagation) are in black and using a proxy of the angle of propagation in green. These theoretical relative errors are shown in Figure 5.3g and are limited to 1. Figures 5.3c to 5.3f the error bars correspond to the statistical errors of the computation of spectral matrices. The case satisfies very well the applicability parameters for the reconstruction: $|B^{\mathrm{error}}\mathrm{w_u}/B\mathrm{w}|$ is in the range 0.02-0.05 for the entire frequency range of the whistler activity (Figure 5.3g). The results obtained from the reconstructed $B^{\mathrm{re}}\mathrm{w_u}$ are in very good agreement with the results based on the measured $B\mathrm{w_u}$. Indeed, we can see in Figures 5.3a, 5.3b, 5.3h, and 5.3i that there is a very good agreement (phase and amplitude) between the waveforms. The initially measured waveforms are very often contained in the error bars. This shows that the error is estimated adequately. Furthermore, we can see in Figures 5.3b, 5.3f, and 5.3i that the Z component of the Poynting vector is very well reconstructed, allowing the propagation direction to be recovered without ambiguity. We can also reconstruct the spectrum (Figure 5.3c) in a satisfactory manner, the whistler spectral bump is clearly identified. The measured and reconstructed ellipticity values are greater than 0.6 over the entire frequency range of the wave. The WNA θ (Figure 5.3f) is also in very good agreement with the measurement and the typical error on the frequency range of the wave is of the order of a degree. Finally, the minimum variance analysis gives less than 2° deviation between the wave vectors using the measured and reconstructed $B\mathrm{w_u}$ (not shown).

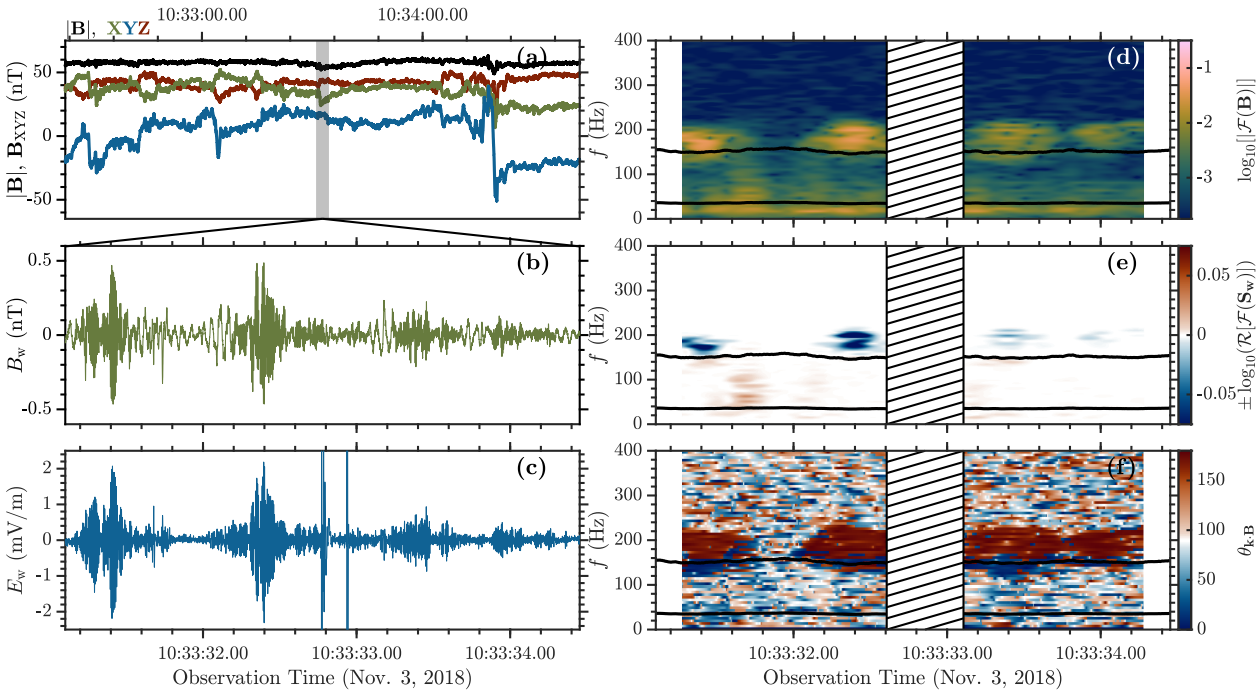

Figure 5.2: Whistler wave packets recorded by PSP on November 3, 2018. *Panel a):* Background magnetic field in the spacecraft coordinates over a short window around the burst. *Panel b):* Burst waveform of the Y magnetic field component, $B\mathrm{w_Y}$. *Panel c):* Burst waveform of the Y electric field component, $E\mathrm{w_Y}$. *Panel d):* Spectrogram of the magnetic field burst waveforms. *Panel e):* Z component of the Poynting flux. *Panel f):* WNA $\theta_{k,\vec{B}}$, ranging from 0° to 180° and indicating parallel (below 90°) and anti-parallel propagation (above 90°), respectively. The lower and upper solid lines in *panels d) to f)* indicate f_{lh} and $0.1f_{\mathrm{ce}}$, respectively. For *panels d) to f)* the frequency is shown in the spacecraft frame.

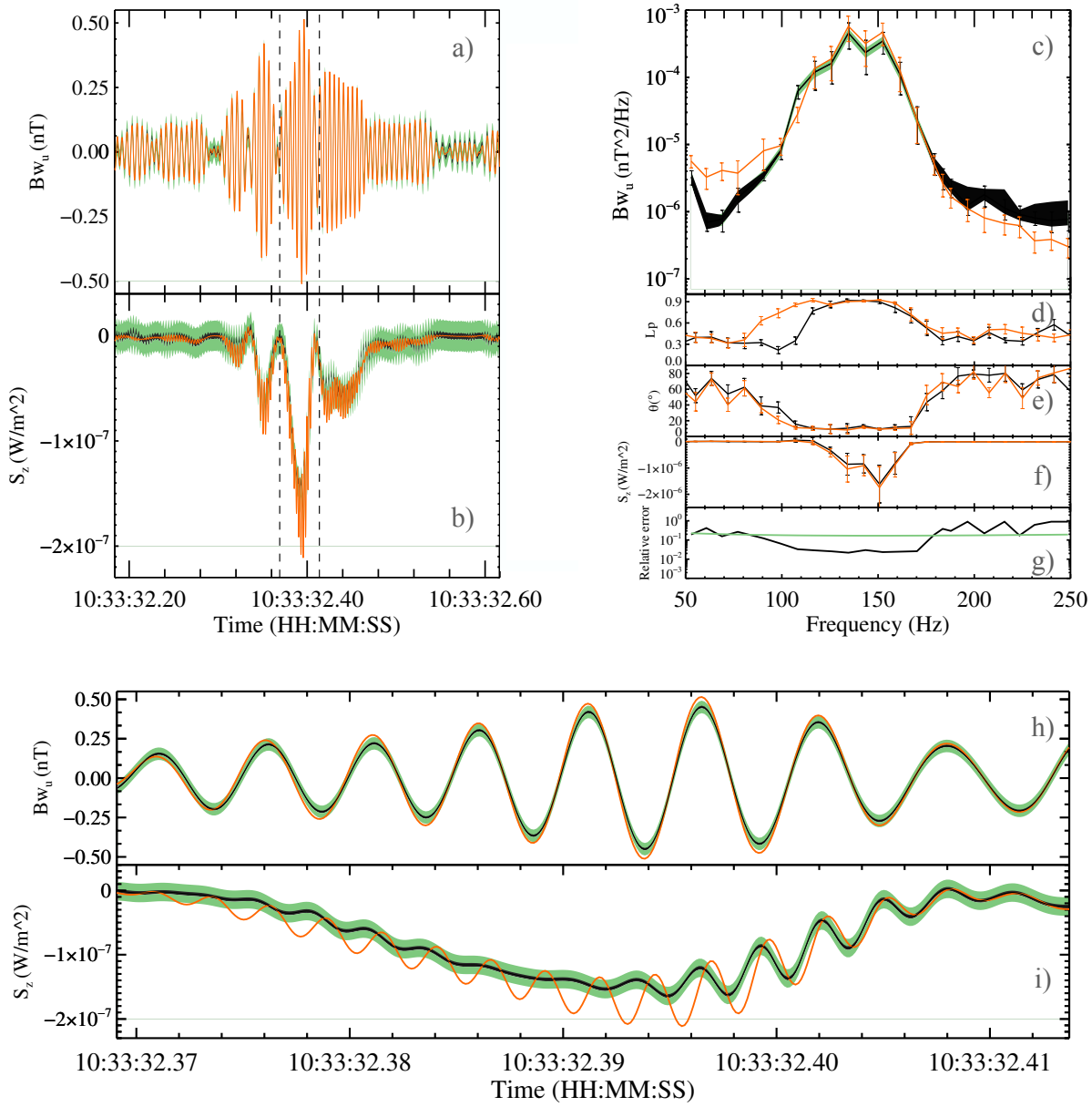

Figure 5.3: Comparison between the whistler wave packet recorded by PSP on November 3, 2018 and its reconstruction. The original data are in orange and the reconstructed ones are in black. The error bars are detailed in the text. *Panel a):* Burst waveform of the u magnetic field component. *Panel b):* Z component of the Poynting flux. The *panels c) to g)* show the frequency in the plasma frame. *Panel c):* Power spectral density of the u component. *Panel d):* Ellipticity. *Panel e):* WNA $\theta_{\vec{k},\vec{B}}$. *Panel f):* Z component of the Poynting flux. *Panel g):* Theoretical relative error in black and using a proxy of the angle of propagation in green. *Panels h) and i)* show a zoom on the period between the vertical dotted lines in *panels a) and b).*

Thus, for this anti-sunward propagating wave packet, which clearly satisfies the applicability parameters for reconstruction, the technique works effectively. Specifically, all important reconstructed parameters are in good agreement with the measurements: amplitude, ellipticity, direction of propagation, and WNA (with an error of less than 2°).

5.2.2 Case 2: November 3, 2018, 10:19:15.6-10:19:19.4 UT

Figure 5.4 presents two typical sunward whistler wave packets, recorded at the heliocentric distance of ~ 41 ($R_\odot$) in the FIELDS burst mode (150 kHz) at 10:19:15.57 UTC, November 3, 2018. This figure is adapted from Figure 6 of (Karbashewski et al., 2023). The polarization parameters and the missing component of the electric field are evaluated as in Section 5.2.1. The Poynting flux shows a sunward propagation, quasi-aligned with the background magnetic field (Figures 5.4e and 5.4f). As we can see in Figure 5.4a, the wave packets are associated with a dip of the background magnetic field of the order of 20%. This is expected for sunward whistler waves (Karbashewski et al., 2023). The background magnetic field magnitude is 48 nT; the plasma density is $\sim$ 410 cm^3; $(\omega_{\rm pe}/\omega_{\rm ce})^2 \sim 28\ 900$; $\omega/\omega_{\rm ce} \sim 0.17$ (in the plasma frame); the bulk radial plasma velocity is 310 km/s; the wave amplitudes reache 2.5 nT. The observed WNAs are below 30° (Figure 5.4f). The wave packets propagating sunward have the wave frequency shifted from the range 60-160 Hz (in the spacecraft frame) to 120-240 Hz (0.11-0.22 $f_{\rm ce}$, in the plasma frame). The solar wind velocity perpendicular to the magnetic field $V_{\rm SW\perp}$ is about 194 km/s. The phase velocity is $V_\varphi \sim 562$ km/s and $\sin(\theta_{\vec{u},\vec{B_0}}) \sim 0.76$.

The results of wave polarization reconstruction of the first whistler wave packet are shown in Figure 5.5. The color code is the same as in Figure 5.3. This case satisfies the applicability parameters for the reconstruction: $|B^{\rm error}{\rm w_u}/B{\rm w}|$ is in the range 0.06-0.2 for the entire frequency range of the whistler activity (Figure 5.5g). Because of a larger $\omega/\omega_{\rm ce}$ and a lower V_φ (which is typical for sunward whistlers, see Figure 5.1) the typical relative errors are about 2 times larger than for Case 1. Once again the results obtained from the reconstructed $B^{\rm re}{\rm w_u}$ are in very good agreement with the results based on the measured $B{\rm w_u}$ and are very similar to those described for Case 1. The reconstructed waveforms are in good agreement with those originally measured (Figures 5.5a, 5.5b, 5.5h and 5.5i). With the reconstructed data we can find without ambiguity the characteristics of a whistler wave packet propagating sunward (Figures 5.5b, 5.5d, 5.5f, and 5.5i). Figure 5.5f shows that the error on the propagation angle is of the order of a few degrees over the frequency range of the wave. The minimum variance analysis gives less than 2° deviation between the wave vectors using the measured and reconstructed $B{\rm w_u}$ (not shown).

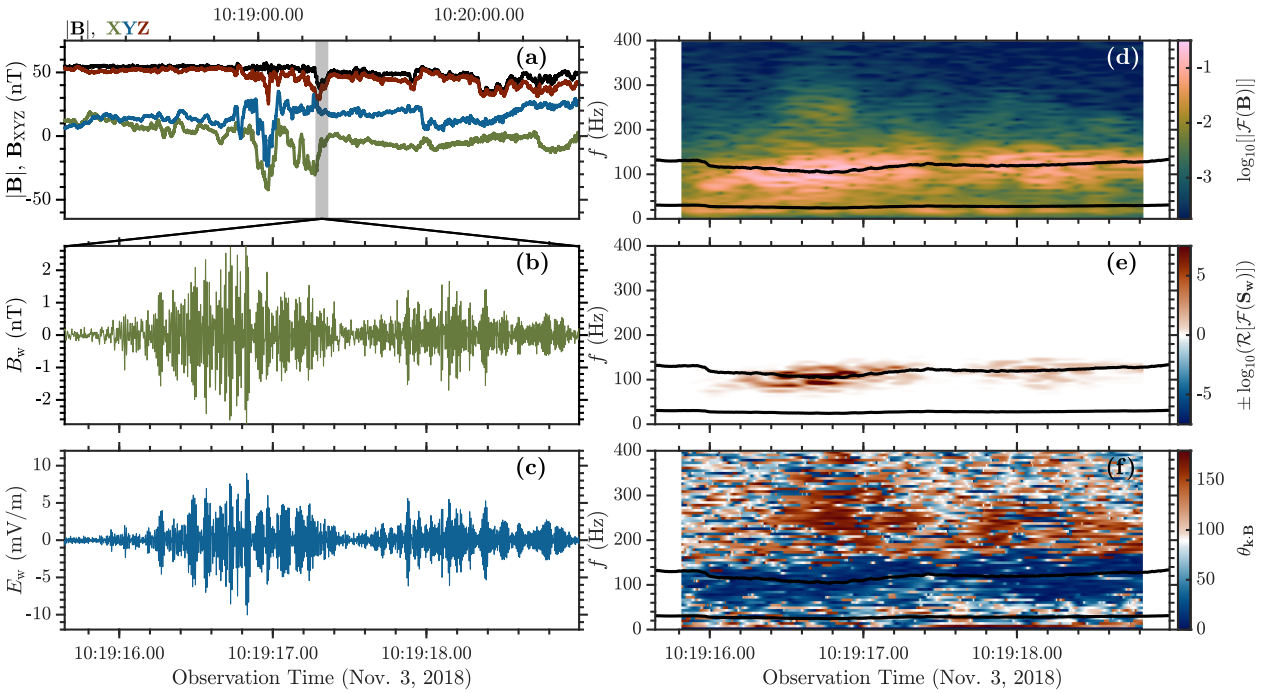

Figure 5.4: Whistler wave packets recorded by PSP on November 3, 2018. *Panel a):* Background magnetic field in the spacecraft coordinates over a short window around the burst. *Panel b):* Burst waveform of the Y magnetic field component, $B\mathrm{w_Y}$. *Panel c):* Burst waveform of the Y electric field component, $E\mathrm{w_Y}$. *Panel d):* Spectrogram of the magnetic field burst waveform. *Panel e):* Z component of the Poynting flux. *Panel f):* WNA $\theta_{\vec{k},\vec{B}}$, ranging from 0° to 180° and indicating parallel (below 90°) and anti-parallel propagation (above 90°), respectively. The lower and upper solid lines in *panels d) to f)* indicate f_{lh} and $0.1f_{\mathrm{ce}}$, respectively. For *panels d) to f)* the frequency is shown in the spacecraft frame.

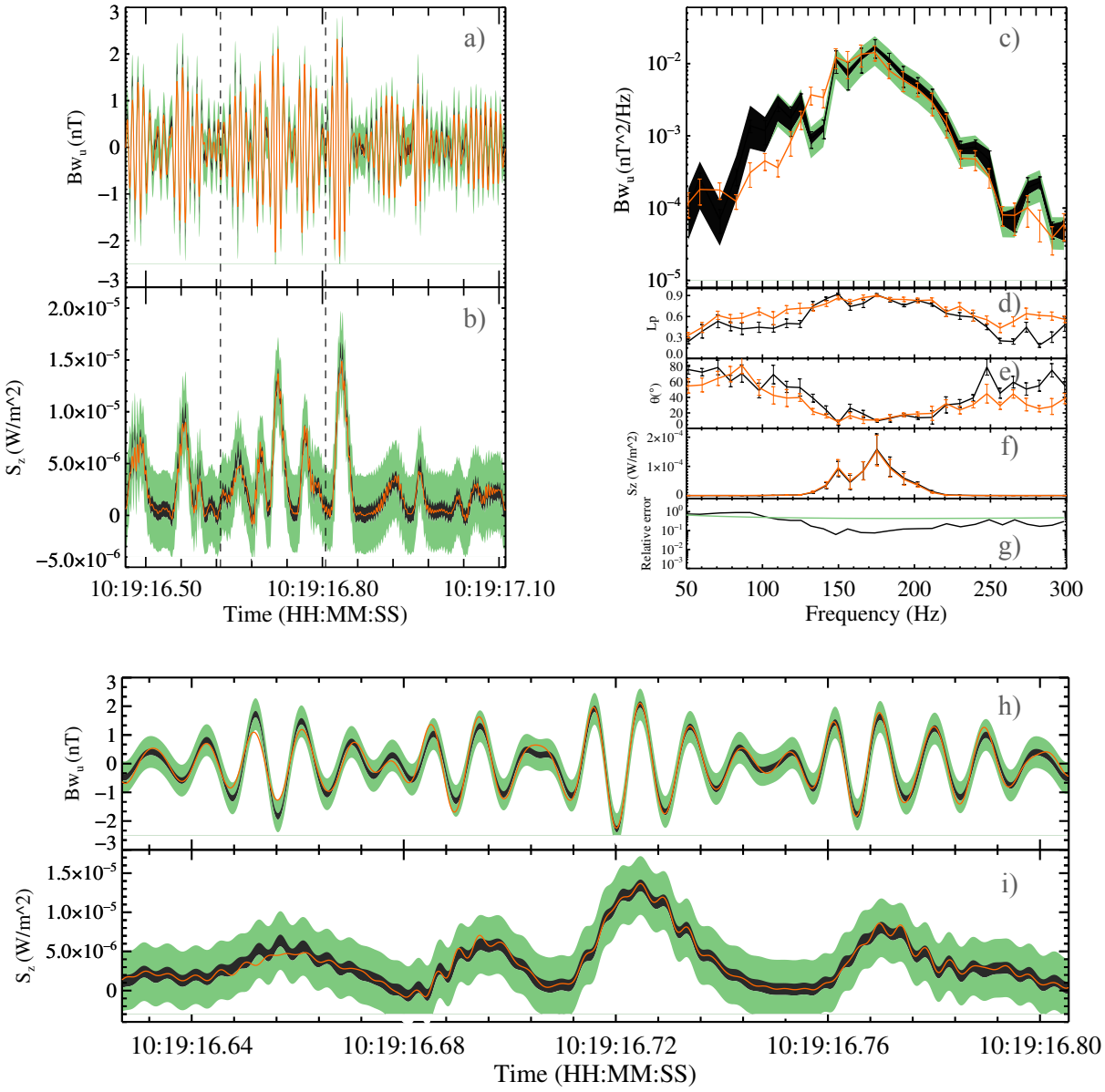

Figure 5.5: Comparison between the whistler wave packet recorded by PSP on November 3, 2018 and its reconstruction. The original data are in orange and the reconstructed ones are in black. The error bars are detailed in Section 5.2.1. *Panel a):* Burst waveform of the u magnetic field component. *Panel b):* Z component of the Poynting flux. The *panels c) to g)* show the frequency in the plasma frame. *Panel c):* Power spectral density of the u component. *Panel d):* Ellipticity. *Panel e):* WNA $\theta_{\vec{k},\vec{B}}$. *Panel f):* Z component of the Poynting flux. *Panel g):* Theoretical relative error in black and using a proxy of the angle of propagation in green. *Panels h) and i)* show a zoom on the period between the vertical dotted lines in *panels a) and b).*

Thus, for this sunward propagating wave packet, in the applicability range of the technique, the reconstruction works effectively. Again, all important reconstructed parameters are in good agreement with the measurements: amplitude, ellipticity, direction of propagation, and WNA (with an error of less than 2°).

5.2.3 Case 3: November 4, 2018, 17:06:47-17:06:51 UT

In Figure 5.6 we show the case presented in detail by (Agapitov et al., 2020), recorded in waveforms with a 292.97 Hz sampling rate at 17:06:48 UTC, November 4, 2018. We can see a sunward propagating whistler with several oblique WNA sub-packets (Figures 5.6e and 5.6f). The packet is co-located with a local minimum of the background magnetic field magnitude located at a switchback boundary. The minimum $|B_0|$ value is $\sim$ 15 nT with the ambient magnetic field magnitude of $\sim$ 70 nT (Figure 5.6a). The corresponding enhancement of $(\omega_{\rm pe}/\omega_{\rm ce})^2$ (up to 250 000 with the background value of $\sim$ 10 000) inside the magnetic dip causes an unusually large Doppler shift. The wave frequency in the plasma frame is between 0.2 and 0.45 of the local $f_{\rm ce}$. The solar wind velocity perpendicular to the magnetic field $V_{\rm SW\perp}$ is about 160 km/s. The phase velocity is $V_\varphi \sim 439$ km/s and $\sin(\theta_{\vec{u},\vec{B_0}}) \sim 0.56$.

The results of wave polarization reconstruction are shown in Figure 5.7. The color code is the same as in Figures 5.3 and 5.5 (explained in Section 5.2.1). This is a difficult case for reconstruction. Indeed, as explained above the wave contains several oblique sub-packets (up to 80°, Figure 5.6f), and the main angle of propagation can be as oblique as 70° (Figure 5.7e). Moreover, we have spectral energy content up to 120 Hz (in the spacecraft frame), therefore close to the Nyquist frequency (Figures 5.6d and 5.6e). Finally, the main issues are that the wave frequency in the plasma frame is about 0.35 $f_{\rm ce}$ and can be up to 0.45 $f_{\rm ce}$, $\frac{V_{\rm SW\perp}}{V_\varphi}$ is about 0.35 and that $\sin(\theta_{\vec{u},\vec{B_0}}) \sim 0.56$. Therefore, taking into account the obliquity of the wave, the theoretical relative error is important: $|B^{\rm error}{\rm w_u}/B{\rm w}|$ is about 0.5 and can be greater than 1 (Figure 5.7g). The results obtained from the reconstructed $B^{\rm re}{\rm w_u}$ are not in good agreement with the results based on the measured $B{\rm w_u}$. As we can see on Figures 5.7a , 5.7b, 5.7h and 5.7i the reconstructed waveforms do not approach the initial waveforms well. Important overestimation of the amplitude (about 3 times) is noted in the reconstructed $B^{\rm re}{\rm w_u}$ component. The Poynting flux is not perfectly recovered but the sunward direction of propagation is still clear (Figures 5.7b, 5.7f, and 5.7i). The reconstructed spectrum is about an order of magnitude larger than the measured one (Figure 5.7c). The reconstructed ellipticity is lower than 0.6 on all frequencies of the waves, which does not allow us to find the classical characteristics of a whistler wave. The propagation angle is wrong by 40° for some frequencies, which can lead to a misinterpretation of the effect of the wave on the electrons.

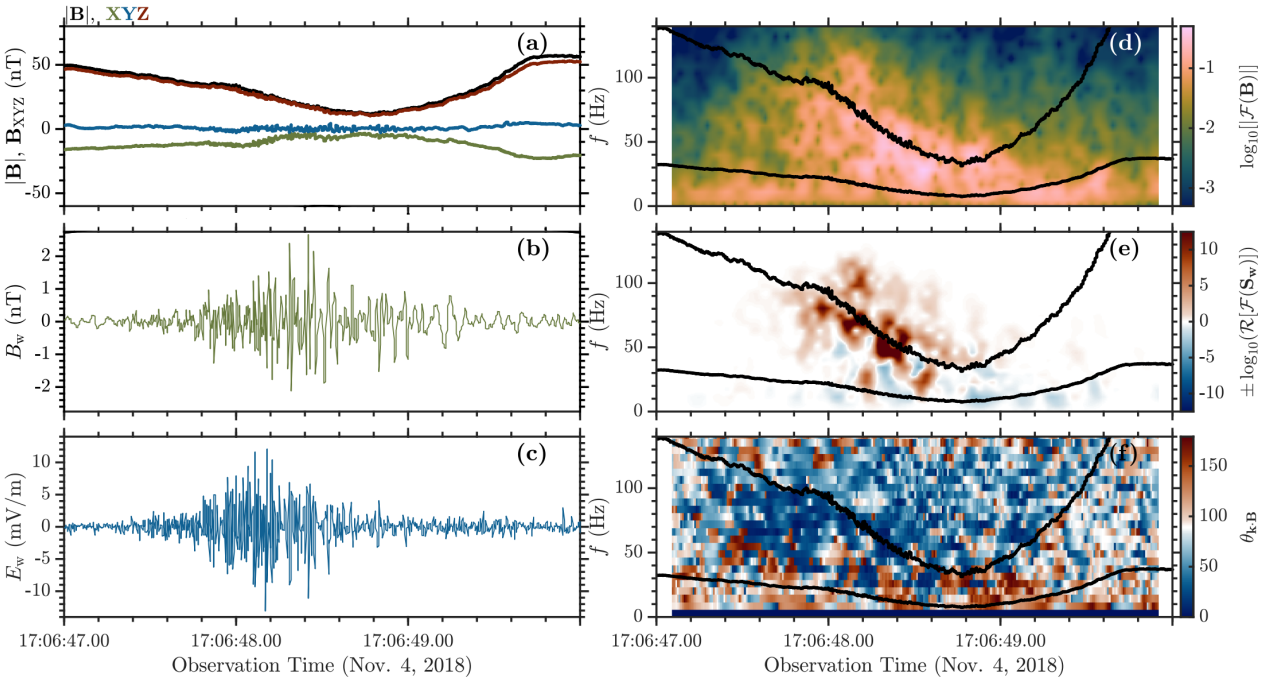

Figure 5.6: Whistler wave packet recorded by PSP on November 4, 2018. *Panel a):* Background magnetic field in spacecraft coordinates. *Panel b):* Burst waveform of the Y magnetic field component, $B\mathrm{w_Y}$. *Panel c):* Burst waveform of the Y electric field component, $E\mathrm{w_Y}$. *Panel d):* Spectrogram of the magnetic field burst waveform. *Panel e):* Z component of the Poynting flux. *Panel f):* WNA $\theta_{k\cdot\vec{B}}$, ranging from 0° to 180° and indicating parallel (below 90°) and anti-parallel propagation (above 90°), respectively. The lower and upper solid lines in *panels d) to f)* indicate f_{lh} and $0.1f_{\mathrm{ce}}$, respectively. For *panels d) to f)* the frequency is shown in the spacecraft frame.

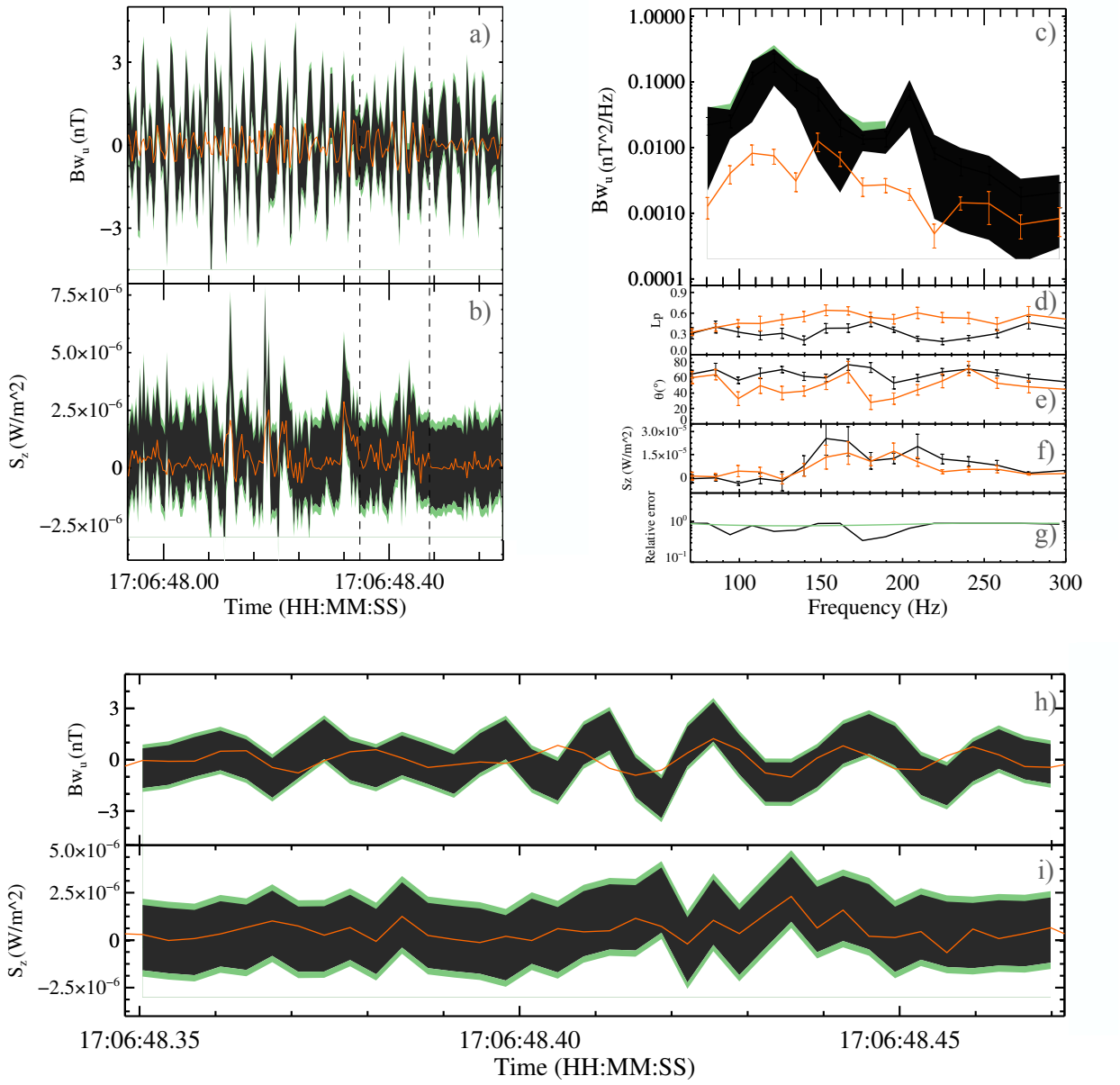

Figure 5.7: Comparison between the whistler wave packet recorded by PSP on November 4, 2018 and its reconstruction. The original data are in orange and the reconstructed ones are in black. The error bars are detailed in Section 5.2.1. *Panel a):* Burst waveform of the u magnetic field component. *Panel b):* Z component of the Poynting flux. The *panels c) to g)* show the frequency in the plasma frame. *Panel c):* Power spectral density of the u component. *Panel d):* Ellipticity. *Panel e):* WNA $\theta_{\vec{k}\cdot\vec{B}}$. *Panel f):* Z component of the Poynting flux. *Panel g):* Theoretical relative error in black and using a proxy of the angle of propagation in green. *Panels h) and i)* show a zoom on the period between the vertical dotted lines in *panels a) and b).*

Thus, for this case out of the applicability range of the technique, the reconstruction doesn't work effectively. Specifically, there is an important overestimation (one order of magnitude) of the amplitude and large errors (tens of degrees) on the WNA. The ellipticity is also not well reconstructed. However, the sunward direction of propagation is clearly found.

These three cases (Case 1, Case 2, Case 3) represent a range of whistler wave parameters that can be observed by PSP during Encounter 1. Two of them (Cases 1 and 2) are within the method applicability limits. In both cases, all important reconstructed parameters are in good agreement with the measurements. Moreover, the theoretical error based on the wave frequency and using a proxy of the propagation angle is lower than the experimental error. Case 3 is an atypical case because of its high values of $f/f_{\mathrm{ce}} \sim 0.2 - 0.45$, its low phase speed and, its obliquity and is out of the applicability range. In this last case, the reconstructed waveform amplitudes and the power spectral density are largely overestimated and the reconstructed WNA differs by several tens of degrees from the actual value. However, the sunward propagation direction was clearly identified.

5.3 Application of the method to the data collected after March 2019

5.3.1 Discussion on the applicability of the method

For Encounter 2 and the following ones, we do not know the typical characteristics of the waves in the plasma frame. It is therefore not certain that the method is applicable in 80% of cases as in the first encounter. On the other hand, here are some arguments that suggest that the method should work in many cases:
Firstly, one of the most important sources of error in the first encounters is the ratio $V_{\mathrm{SW}\perp}/V_{\varphi}$. Phase velocity increases when getting closer to the Sun and should be multiplied by about 3 at 10 $R_{\odot}$ compared to Encounter 1 (Bale et al., 2016), which will greatly reduce the error.
Moreover, a simple Parker spiral model predicts that the background magnetic field is more radial as we get closer to the Sun. Therefore, the perpendicular component of the solar wind speed will tend to decrease. Moreover, the fact that the background magnetic field is more radial should also reduce the number of configurations in which the background magnetic field is aligned with $\vec{u}$.
Another important source of error is the $(\omega/\omega_{\mathrm{ce}})\tan\theta$ term, whose evolution cannot be predicted for the next encounters. However, Encounters 2 and 3 have similar perihelion distances and the following ones will slowly approach 10 $R_{\odot}$. This suggests that for at least some perihelia the waves should have similar characteristics to those observed in the first encounter. Then, as mentioned in Section 5.1, (Cattell et al., 2022) statistics from 9 encounters showed that whistler waves frequency in the spacecraft frame was below 0.2 f_{ce} with the tendency to decrease below 0.1 approaching the Sun. Figure 5.1b shows that in the case where $\omega/\omega_{\mathrm{ce}} \leq 0.1$ this term gives an error of less than 30% with WNAs up to 70°.

In addition, there are several pre- and post-reconstruction methods that give indications of the quality of the reconstruction. These methods are not definitive proofs but can be used

as good indicators of correct reconstruction.
One can use a pre-check based on $\omega/\omega_{\mathrm{ce}}$ in the spacecraft frame (as the phase velocity increases, the measured $\omega/\omega_{\mathrm{ce}}$ becomes closer to the one in the plasma frame). By using a proxy for the propagation angle (based on $\omega/\omega_{\mathrm{ce}}$) and the ratio $\omega_{\mathrm{pe}}/\omega_{\mathrm{ce}}$ it is possible to calculate the phase velocity and derive the theoretical error using Equation 5.4.
Moreover, outside the range of applicability, we do not expect to reconstruct a good circular polarization (see Section 5.1.3). The circular polarization can therefore be used as a post-reconstruction indicator of the method's effectiveness.

5.3.2 Application of the reconstruction technique to whistler waves recorded during Encounter 2 (no $B\mathrm{w_u}$ measurements): 2019/04/03, 05:48:35-05:48:37 UT

Figures 5.8 and 5.9 present a reconstructed whistler wave packet from Encounter 2, recorded at the heliocentric distance of ~ 37 ($R_{\odot}$) in the FIELDS burst mode (150 kHz) at 05:48:35 UTC, April 4, 2019. The background magnetic field magnitude is 73 nT; the plasma density is $\sim 170\ cm^3$; $(\omega_{\mathrm{pe}}/\omega_{\mathrm{ce}})^2 \sim 3250$; the bulk radial plasma velocity is 310 km/s; and $\sin(\theta_{\vec{u},\vec{B_0}}) = 0.98$. The WNA, direction of propagation, and frequency in the plasma reference frame are unknown without reconstruction due to the technical issue on the u component since March 2019. Figure 5.8e and Figures 5.9b, 5.9f and 5.9i show that the reconstructed propagation direction is anti-sunward. The reconstructed WNA is less than 30° (Figure 5.8f and Figure 5.9e) and the reconstructed planarity is bigger than 0.6 over the whole frequency range of the wave (Figure 5.9d). We can therefore deduce that $\frac{V_{\mathrm{SW}\perp}}{V_{\varphi}^{\mathrm{re}}} \sim 0.06$ and $f/f_{\mathrm{ce}} \sim 0.13$ (in the plasma frame). The reconstructed components thus show that we are well within the range of application of the method and $|B^{\mathrm{error}}\mathrm{w_u}/B\mathrm{w}|$ is in the range of $0.03 - 0.1$ (Figure 5.9g). The method proposed in Section 5.3.1 using a proxy for the propagation angle also shows that we're within the range of application (relative error less than 0.1). Moreover, ellipticity close to 1 is a good indication of correct reconstruction.

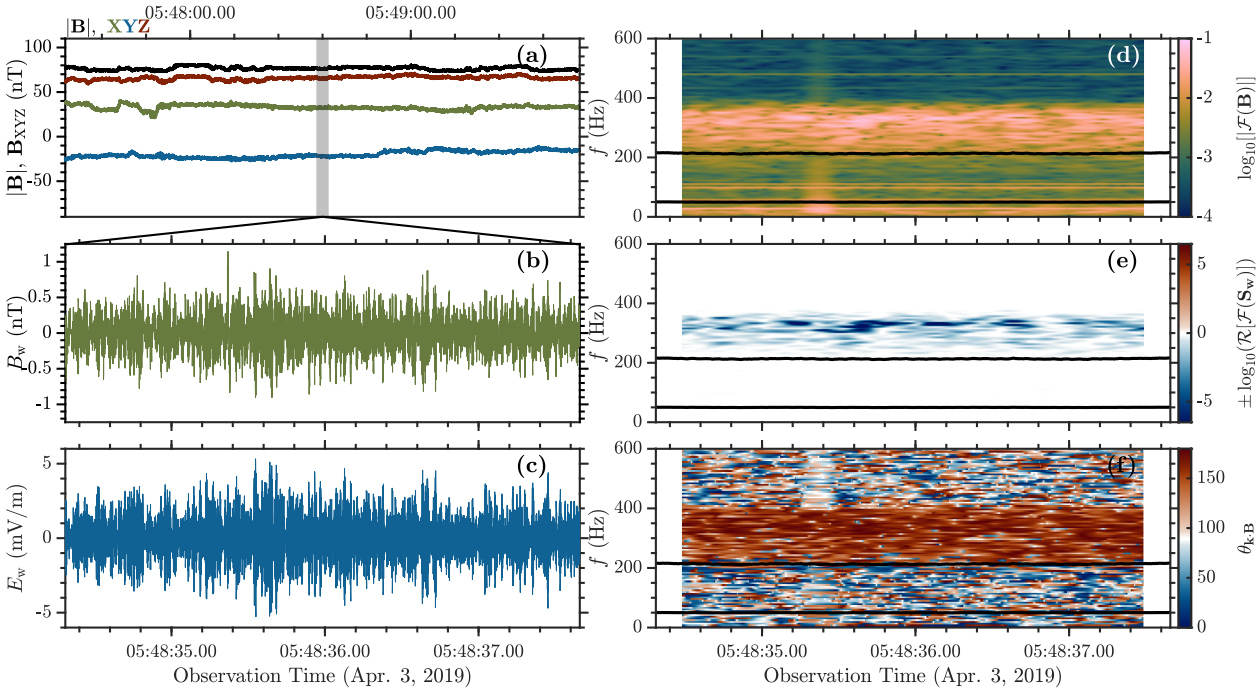

Figure 5.8: Whistler wave packet recorded by PSP on April 3, 2019. *Panel a):* Background magnetic field in spacecraft coordinates over a short window around the burst. *Panel b):* Burst waveform of the Y magnetic field component, $B\mathrm{w_Y}$. *Panel c):* Burst waveform of the Y electric field component, $E\mathrm{w_Y}$. *Panel d):* Spectrogram of the magnetic field burst waveform. *Panel e):* Z component of the Poynting flux. *Panel f):* Reconstructed WNA $\theta_{k\cdot\vec{B}}$, ranging from 0° to 180° and indicating parallel (below 90°) and anti-parallel propagation (above 90°), respectively. The lower and upper solid lines in (d)-(f) indicate f_{lh} and $0.1f_{\mathrm{ce}}$, respectively. For *panels d) to f)* the frequency is shown in the spacecraft frame.

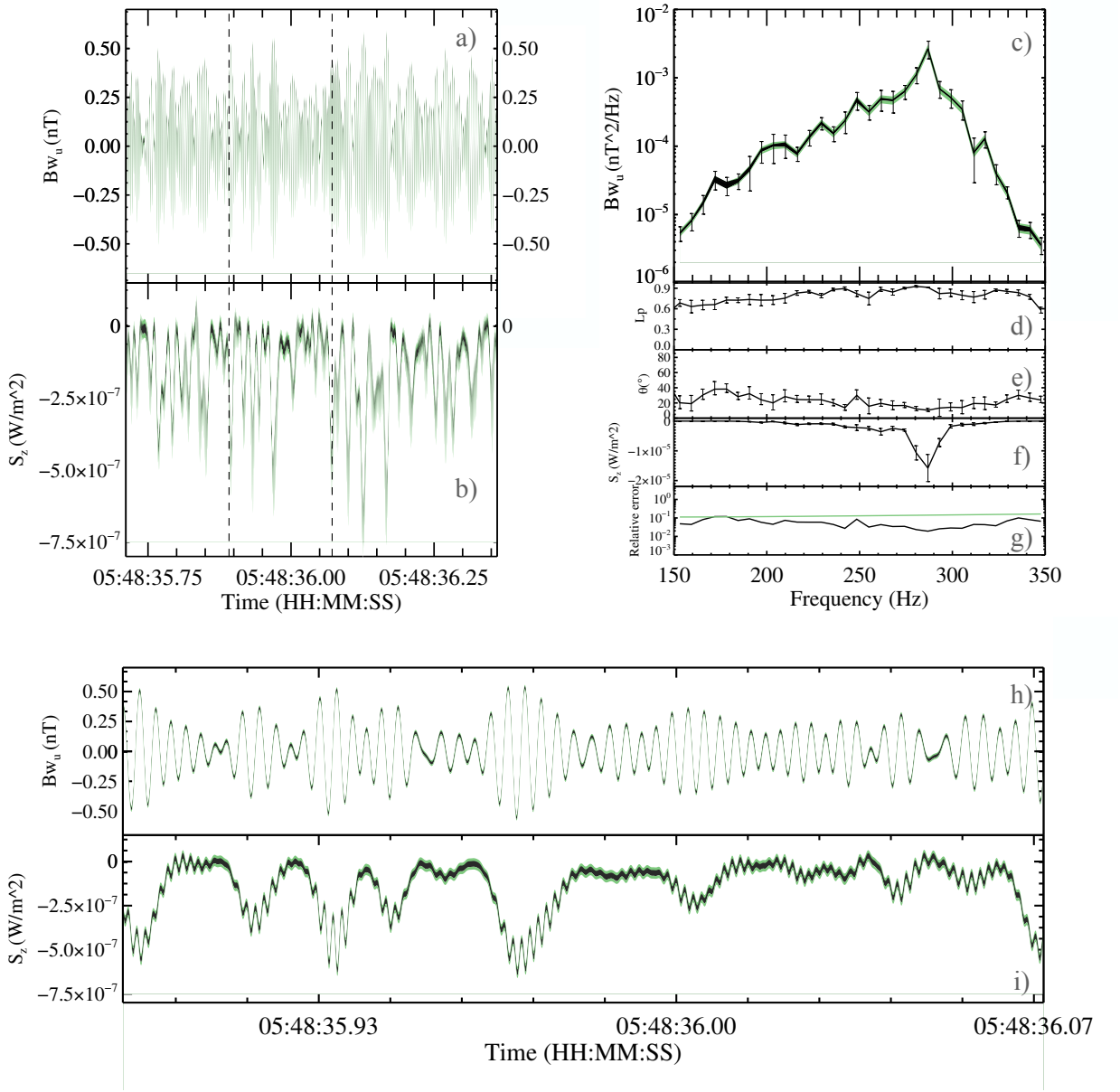

Figure 5.9: Reconstructed whistler wave packet recorded by PSP on April 3, 2019. The error bars are detailed in Section 5.2.1. *Panel a):* Burst waveform of the u magnetic field component. *Panel b):* Z component of the Poynting flux. The *panel c) to g):* show the frequency in the plasma frame. *Panel c):* Power spectral density of the u component. *Panel d):* Ellipticity. *Panel e):* WNA $\theta_{\vec{k},\vec{B}}$. *Panel f):* Z component of the Poynting flux. *Panel g):* Theoretical relative error in black and using a proxy of the angle of propagation in green. *Panels h) and i)* show a zoom on the period between the vertical dotted lines in *panels a) and b).*

5.4 Conclusions

The Parker Solar Probe mission will last until 2025 (nominal part) and 24 perihelia are expected to be completed, approaching down to 10 $R_\odot$ and probing *in situ* regions where no direct measurements have ever been made. One component of the magnetic field measured by the search-coil magnetometer is unavailable at low frequency after Encounter 1 because of a technical issue. We propose a method to determine whistler wave polarization despite the missing component. This makes it possible to evaluate wave-particle interactions effects on the dynamics of solar wind electron populations.

To conclude:

1. We develop a technique to reconstruct the polarization parameters of whistler waves based on only two components of magnetic and electric field measurements (the PSP fields measurement regime after March 2019). We reconstruct the missing components by neglecting the electric field parallel to the background magnetic field.

2. This technique is applicable with the assumptions of (i) low-frequency whistlers in the plasma frame relative to the electron cyclotron frequency; (ii) a small propagation angle with respect to the background magnetic field; and (iii) a large wave phase speed relative to the cross-field solar wind velocity. Critically, the method cannot be applied if the background magnetic field is aligned with the affected SCM coil.

3. When within the range of applicability, all polarization parameters could be found, including propagation direction, WNA, and ellipticity. We propose pre- and post-reconstruction methods to estimate the quality of the reconstruction. One of them is to check that the ellipticity of the reconstructed magnetic field is close to 1.

4. Our method will enable polarization properties of whistler waves in the young Solar to be determined. These polarization properties are necessary for a better understanding of particle-wave interactions.

5.5 Résumé en Français du chapitre 5

Comme expliqué au chapitre 3, la sonde Parker Solar Probe (PSP) comprend un fluxmètre tri-axial (SCM) qui mesure les fluctuations de trois composantes orthogonales du champ magnétique entre 3 Hz et 20 kHz (et une composante jusqu'à 1 MHz). Lors de l'orbite 1, en novembre 2018, le SCM a fonctionné comme prévu ; cependant, en mars 2019, des problèmes techniques avec une bobine du SCM ont limité les rencontres ultérieures à deux composantes pour les fréquences inférieures à 1 kHz. De manière préjudiciable, la plupart des ondes de sifflement sont observées dans la bande de fréquences affectée. Les techniques d'analyse de signaux établies et détaillées au chapitre 3 ne peuvent pas extraire avec précision les propriétés de polarisation des ondes de sifflement avec seulement deux composantes de champ magnétique. Comme expliqué au chapitre 2, ces propriétés sont pourtant primordiales pour quantifier l'interaction ondes particules. Le SCM à bord de PSP est complété par un instrument de mesure du champ électrique (EFI) qui mesure deux composantes du champ électrique et couvre les fréquences affectées du SCM. Nous proposons une technique pour reconstruire la polarisation des ondes de sifflement en utilisant deux composantes du champ magnétique et deux composantes du champ électrique. Cette méthode utilise les champs électromagnétiques disponibles pour reconstruire les composantes manquantes en négligeant le champ électrique parallèle au champ magnétique. Cette technique nous permet de déterminer les propriétés de polarisation des ondes de sifflement après mars 2019, lorsque les données à basses fréquences sont devenues inutilisables.

Cette technique repose sur les hypothèses suivantes : (i) ondes de sifflement à basses fréquences dans le référentiel du plasma par rapport à la fréquence cyclotronique électronique ; (ii) angle de propagation faible ; et (iii) vitesse de phase de l'onde élevée par rapport à la vitesse du vent solaire transversale au champ magnétique. Si le champ magnétique est aligné avec la bobine SCM concernée, la méthode ne peut pas être appliquée, même si les hypothèses préalables sont respectées. Nous avons validé notre nouvelle méthode en utilisant des mesures en mode rafale des trois composantes magnétiques contenant des paquets d'ondes effectuées avant mars 2019. Le résultat montre que les conditions de reconstruction sont satisfaites pour 80% des paquets d'ondes détectés en mode rafale lors de l'orbite 1. Enfin, nous appliquons la méthode pour déterminer la polarisation d'un paquet d'ondes observé après mars 2019 lors de l'orbite 2. La méthode que nous proposons est une étape encourageante vers des analyses statistiques des propriétés des ondes de sifflement au-delà de l'orbite 1, afin d'améliorer notre compréhension des interactions ondes-particules dans le vent solaire.

Chapter 6

Conclusions and perspectives

In Chapter 1, we raised two open questions concerning suprathermal electrons in the solar wind. Indeed, a clear explanation of the increase of the angular width of the Strahl (associated with the relative increase of the halo density) and of the regulation of the heat flux is still missing. It is likely that wave-particle interactions, not taken into account in most current kinetic models, are needed to answer these questions.
In Chapter 2, we presented the quasi-linear theory that is suitable for describing and quantifying wave-particle interactions in the solar wind. We have carried out a state-of-the-art review of experimental, theoretical, and simulation work on whistler waves, which are observed in the solar wind. We explained that these waves are the most promising for answering the two open questions mentioned above. Indeed, some of these waves, in particular when propagating obliquely or in the sunward direction, can interact very effectively with the Strahl. These waves can thus increase the proportion of halo electrons and probably regulate the heat flux. Oblique waves ($\sim 70°$) produced by fan-like instabilities have been extensively studied by theory and simulation, and many studies have suggested their important role in answering these questions. On the other hand, they have been poorly observed in the free solar wind. Sunward waves have been the subject of several case studies close to the Sun (< 0.2 AU), but few cases have been observed at larger heliocentric distances. Therefore, the actual role of these waves on the solar wind electron distribution function is still to be precised.
In Chapter 3, we detailed why the Solar Orbiter and Parker Solar Probe satellites represent a unique opportunity to study in detail the properties of whistler waves and their occurrence in the solar wind between 0.05 and 1 AU. We described the methods used and the necessary work in order to exploit at best these data.

In Chapter 4, using data from these two missions, we presented a statistical study of plasma waves between around 0.02 and $0.3 f_{ce}$ and between 0.2 and 1 AU. We began by noting that whistler waves constitute the vast majority of the observed electromagnetic waves, so we concentrated on their study. We produced the largest statistic of whistler waves in the solar wind to our knowledge (110,000 wave packets), which includes the determination of the wave parameters in the plasma frame. We found that beyond 0.3 AU the proportion of whistler waves in the solar wind remains relatively constant with distance and that

these waves are present between 1 and 2% of the time. The overwhelming majority of these whistler waves propagate in the same direction as the Strahl (Strahl-aligned), including during switchbacks. On the other hand, at 0.2 AU, counter-streaming waves are present and probably account for at least half of all cases. At all distances, the vast majority of waves are quasi-aligned: the propagation angle distribution peak between 3 and 7° and then decrease rapidly with the propagation angle. Only 7.5% of the waves have a propagation angle larger than 15° and 0.5% have an angle of propagation greater than 45°. This is in contradiction with numerous studies predicting the major role of oblique whistlers ($\sim 70°$) in the evolution of the electron distribution function. Below 15°, the observed propagation angle distribution can be explained by considering an instability that preferentially generates aligned waves, that is, that has a maximum growth rate at 0°. This is the case of the WHFI, the TAI, or the sunward suprathermal deficit instability, that have already been identified in the solar wind (Tong et al., 2019b; Jagarlamudi et al., 2020; Berčič et al., 2021). The departure from 0° can be explained by a geometrical effect due to the curvature of the magnetic field lines. Interestingly, however, from 15° to around 45° the characteristics of the waves change: their amplitudes, durations, and phase velocities increase slightly or remain constant, and their numbers decrease less rapidly. This suggests that these waves could be associated with a particularly inhomogeneous background magnetic field (e.g., dips, switchbacks) or could be produced by another instability generating non-perfectly aligned waves (with a maximum growth rate between 15° and 45°).
We then used these statistical results to compute the diffusion coefficients in the framework of quasi-linear theory to quantify for the first time the role of whistler waves on the suprathermal electron diffusion along their propagation. We showed that, beyond 0.3 AU, aligned waves $\theta < 15°$ are not effective in diffusing the Strahl, despite representing 92.5% of observations. On the other hand, slightly oblique waves, with a propagation angle between 15 and 45°, are sufficiently frequent and effective to explain the increase in the angular width of the Strahl. Oblique waves with an angle greater than 45° are not frequent enough to have an impact. Close to the Sun, at 0.2 AU, counter-streaming waves interact more efficiently (by up to two orders of magnitude) than Strahl-aligned waves. Counter-streaming waves are probably generated by electron populations trapped in a magnetic dip moving relative to the solar wind (Karbashewski et al., 2023).

On the other hand, the technical problem with one of the antennas of Parker Solar Probe's SCM in March 2019 prevented us to detect and determine wave properties after this date. This has prevented us from estimating the role of waves on suprathermal electrons below 0.2 AU. Indeed, with only two of the SCM's three antennas, conventional signal processing techniques are unable to recover the wave polarization properties required to calculate diffusion coefficients. In Chapter 5, we thus proposed a method for determining the polarization properties of whistler waves despite this technical problem. The technique is simple to implement and relies on the measurements of two magnetic components and two electric components. This method uses the available electromagnetic fields to reconstruct the missing components by neglecting the electric field parallel to the background magnetic field. This technique is applicable with the assumptions of (i) a small wave frequency in the plasma frame with

respect to the electron cyclotron frequency; (ii) a small propagation angle with respect to the background magnetic field; and (iii) a large wave phase speed relative to the cross-field solar wind velocity. Critically, the method cannot be applied if the background magnetic field is aligned with the affected SCM coil. We have validated our method using burst mode measurements made before March 2019. The reconstruction conditions are satisfied for 80% of the burst mode whistlers detected during Encounter 1. We applied the method to determine the polarization of a whistler wave packet observed after March 2019 during Encounter 2. We found that obtaining a right-hand circular polarization is a good criterion to check the quality of the reconstruction. We also argue that, as we get closer to the Sun, expected wave parameters, for example the larger phase velocity, should make the method applicable in a wider range of cases. This method will reveal the polarization properties of whistler waves down to 10 $R_\odot \sim 0.05$ AU for the first time.

Several possibilities for pursuing and completing this thesis work can be considered. First, the generation mechanism of the whistlers responsible for the Strahl scattering (and therefore for the increase in relative halo density) was not determined. For this, it is necessary to study in detail the characteristics of the background magnetic field and of the electron distribution function for these cases.

The quantification of the impact of whistler waves on heat flux regulation has not been addressed. Our results show that whistler waves provide pitch-angle diffusion of the Strahl, which is the population carrying the largest proportion of heat flux. We also show that the halo (the other component carrying the heat flux) is diffused very effectively in pitch angle, without however quantifying the impact of these waves on heat flux regulation. To achieve this quantification, it is possible to use the diffusion coefficients calculated in Chapter 4. Indeed, one method consists of finding the solutions of the diffusion equation (Equation 2.20) in the form of a Legendre polynomial expansion, then calculating the heat flux transported by the distribution function to the first order. Similar approaches, in the context of weakly ionized gas in an electric field, have already been applied (Landau and Lifshitz, 1981).

Later on, Solar Orbiter's trajectory could be used to perform a study similar to the one carried out in Chapter 4 outside the ecliptic plane, in order to compare wave properties.

The propagation angle distribution for waves with $\theta < 15°$, can be used to estimate typical wave lifetimes.

The method presented in Chapter 4 can also be applied to other plasma modes in the solar wind. In particular, we can think of the ion cyclotron waves regularly detected by Solar Orbiter and Parker Solar Probe (Khotyaintsev et al., 2021; Shi et al., 2021). This would make it possible to quantify the impact of these waves on the proton distribution function.

The quasi-linear theory also has some limitations. For high-amplitude whistler waves, we sometimes reached the limit of applicability of this theory for the first normal resonance. As

explained in Chapter 4, in such cases it is necessary to apply another approach that takes non-linear effects into account. In particular, the problem can be described as the interaction of electrons with a monochromatic solitary wave (Karpman, Istomin, and Shklyar, 1975). It would be interesting to compare the results of this approach with those obtained with quasi-linear theory.

An obvious perspective of the technique presented in Chapter 5 is its application to encounters occurring after March 2019. This will enable us to determine the polarization characteristics of whistler waves down to 10 $R_\odot$ ($\sim$ 0.05 AU), a region that has never been explored *in situ*. In particular, This method will make it possible to obtain much more extensive whistler statistics (e.g. occurrence, angle and direction of propagation, radial distance dependence). Moreover, it will be interesting to verify the observations indicating the quasi-absence of whistler waves below 28 $R_\odot$ ($\sim$ 0.13 AU) (Cattell et al., 2022).

The origin of counter-streaming waves is not clearly established, despite indications in favor of the mechanism proposed by Karbashewski et al. (2023). To verify this mechanism, it is necessary to measure the electron distribution functions within the dips of the background magnetic field. Since the typical duration of these structures is a second, the acquisition duration of the distribution functions measured by SWEAP during the first encounters with Parker Solar Probe (13.98s) made it impossible to detect this instability in the e-VDF measurements. However, e-VDFs with sub-second acquisition times are available for recent encounters and should allow us to test the presence of this mechanism. In addition, some cases measured by Solar Orbiter (above 0.3 AU) are also potentially counter-streaming. Even though they are rare, a detailed study of these cases could help us to identify their generation mechanism.

Finally, it might be interesting to study in more detail the zone where counter-streaming whistlers start to be observed, in order to understand what causes this evolution.

Overall, we believe that this work has shown how whistler waves are distributed in the solar wind and that they have an important role in the evolution of the electron distribution function with heliocentric distance. The free energy and generation mechanism at the origin of these waves have been discussed and can now be explored in more details. We have proposed methods for quantifying particle-wave interactions in the solar wind. These interactions must be taken into account in order to refine kinetic models and improve our description of the solar wind.

6.1 Résumé en français du chapitre 6

Dans le chapitre 1, nous avons soulevé deux questions ouvertes concernant les électrons suprathermiques du vent solaire. En effet, une explication de l'augmentation de la largeur angulaire du Strahl (associée à l'augmentation relative de la densité du halo) et de la régulation du flux de chaleur fait toujours défaut. Il est probable que les interactions ondes-particules, non prises en compte dans la plupart des modèles cinétiques actuels, soient nécessaires pour répondre à ces questions.
Dans le chapitre 2, nous avons présenté la théorie quasi-linéaire qui est adaptée pour décrire et quantifier les interactions ondes-particules dans le vent solaire. Nous avons réalisé un état de l'art des travaux expérimentaux, théoriques et de simulation sur les ondes de sifflement, couramment observées dans le vent solaire. Nous avons expliqué que ces ondes sont les plus prometteuses pour répondre aux deux questions ouvertes mentionnées ci-dessus. En effet, certaines de ces ondes, en particulier lorsqu'elles se propagent de façon oblique ou dans la direction du Soleil, peuvent interagir très efficacement avec le Strahl. Ces ondes peuvent donc augmenter la proportion d'électrons du halo et probablement réguler le flux de chaleur. Les ondes obliques ($\sim 70°$) produites par des instabilités de type éventail ont été largement étudiées par la théorie et la simulation, et de nombreuses études ont suggéré leur rôle important pour répondre à ces questions. D'autre part, elles ont été peu observées dans le vent solaire libre. Les ondes se propageant vers le Soleil ont fait l'objet de plusieurs études de cas à proximité du Soleil ($< 0,2$ AU), mais peu de cas ont été observés à des distances héliocentriques plus grandes. Par conséquent, le rôle réel des ondes de sifflement sur la fonction de distribution des électrons dans le vent solaire reste à préciser.
Dans le chapitre 3, nous avons expliqué pourquoi les satellites Solar Orbiter et Parker Solar Probe représentent une occasion unique d'étudier en détail les propriétés des ondes de sifflement dans le vent solaire entre 0,05 et 1 UA. Nous avons présenté le travail effectué afin d'exploiter au mieux ces données.

Dans le chapitre 4, en utilisant les données de ces deux missions, nous avons présenté une étude statistique des ondes plasma entre environ 0,02 et 0,3 f_{ce} et entre 0,2 et 1 UA. Nous avons commencé par noter que les ondes de sifflement constituent la grande majorité des ondes électromagnétiques observées, et nous nous sommes donc concentrés sur leur étude. Nous avons produit la plus grande statistique d'ondes de sifflement dans le vent solaire à notre connaissance (110 000 paquets d'ondes), qui inclut la détermination des paramètres des ondes dans le référentiel du plasma. Nous avons constaté qu'au-delà de 0,3 UA, la proportion d'ondes de sifflement dans le vent solaire reste relativement constante en fonction de la distance et que ces ondes sont présentes entre 1 et 2% du temps. L'écrasante majorité des ondes de sifflement se propage dans la même direction que le Strahl (alignée sur le Strahl), y compris lors des switchbacks. En revanche, à 0,2 UA, les ondes counter-streaming sont présentes et représentent probablement au moins la moitié des cas. À toutes les distances, la grande majorité des ondes sont quasi-alignées : les distributions de l'angle de propagation atteignent leur maximum entre 3 et 7° et diminuent ensuite rapidement avec l'angle de propagation. Seulement 7,5% des ondes ont un angle de propagation supérieur à 15° et 0,5% ont

un angle de propagation supérieur à 45°. Ceci est en contraste avec de nombreuses études prédisant le rôle majeur des siffleurs obliques ($\sim 70°$) dans l'évolution de la fonction de distribution des électrons. En dessous de 15°, la distribution des angles de propagation observée peut être expliquée en considérant une instabilité qui génère préférentiellement des ondes alignées, c'est-à-dire avec un taux de croissance maximum à 0°. C'est le cas de l'instabilité de flux de chaleur, d'anisotropie de température, ou de déficit suprathermique vers le Soleil, qui ont déjà été identifiées dans le vent solaire. L'écart par rapport à 0° peut être expliqué par un effet géométrique dû à la courbure des lignes de champ magnétique. Cependant, il est intéressant de noter que de 15° à environ 45°, les caractéristiques des ondes changent : leurs amplitudes, durées et vitesses de phase augmentent légèrement ou restent constantes, et leurs nombres diminuent moins rapidement. Ceci suggère que ces ondes pourraient être associées à un champ magnétique particulièrement inhomogène (par exemple, des creux ou des switchbacks) ou pourraient être produites par une autre instabilité générant des ondes non parfaitement alignées (avec un taux de croissance maximal entre 15° et 45°).
Nous avons ensuite utilisé ces résultats statistiques pour calculer les coefficients de diffusion dans le cadre de la théorie quasi-linéaire et pour quantifier pour la première fois le rôle des ondes de sifflement sur la diffusion d'électrons suprathermiques le long de leur propagation. Nous avons montré qu'au-delà de 0,3 UA, les ondes alignées $\theta < 15°$ ne sont pas efficaces pour diffuser le Strahl, bien qu'elles représentent 92,5% des observations. En revanche, les ondes légèrement obliques avec un angle de propagation compris entre 15 et 45°, sont suffisamment fréquentes et efficaces pour expliquer l'augmentation de la largeur angulaire du Strahl. Les ondes obliques avec un angle supérieur à 45° ne sont pas assez fréquentes pour avoir un impact. Près du Soleil, à 0,2 UA, les ondes counter-streaming interagissent plus efficacement (jusqu'à deux ordres de grandeur) que les ondes alignées avec le Strahl. Les ondes counter-streaming sont probablement générées par des populations d'électrons piégées dans un creux magnétique se déplaçant par rapport au vent solaire (Karbashewski et al., 2023).

D'autre part, le problème technique d'une des antennes du SCM de Parker Solar Probe en mars 2019 nous a empêchés de détecter et de déterminer les propriétés des ondes après cette date. Cela nous a empêché d'estimer le rôle des ondes sur les électrons suprathermiques en dessous de 0,2 UA. En effet, avec seulement deux des trois antennes du SCM, les techniques conventionnelles de traitement du signal sont incapables de déterminer les propriétés de polarisation des ondes nécessaires au calcul des coefficients de diffusion. Dans le chapitre 5, nous avons donc proposé une méthode pour déterminer les propriétés de polarisation des ondes de sifflement malgré ce problème technique. Cette technique est simple à mettre en œuvre et repose sur la mesure de deux composantes magnétiques et de deux composantes électriques. Cette méthode utilise les champs électromagnétiques disponibles pour reconstruire les composantes manquantes en négligeant le champ électrique parallèle au champ magnétique. Cette technique est applicable sous les hypothèses suivantes : (i) onde de faible fréquence dans le repère du plasma par rapport à la fréquence cyclotronique électronique ; (ii) un petit angle de propagation par rapport au champ magnétique ; et (iii) une grande vitesse de phase par rapport à la vitesse du vent solaire perpendiculaire au champ magné-

tique. La méthode ne peut pas être appliquée si le champ magnétique est aligné avec la bobine SCM concernée. Nous avons validé notre méthode en utilisant des mesures en mode rafale effectuées avant mars 2019. Les conditions de reconstruction sont satisfaites pour 80% des siffleurs en mode rafale détectés pendant l'orbite 1. Nous avons appliqué la méthode pour déterminer la polarisation d'un paquet d'ondes de sifflement observé après mars 2019 lors de l'orbite 2. Nous avons constaté que l'obtention d'une polarisation circulaire droite est un bon critère pour vérifier la qualité de la reconstruction. Nous argumentons également qu'à mesure que nous nous rapprochons du Soleil, les paramètres d'ondes attendu, par exemple la vitesse de phase plus importante, devraient rendre la méthode applicable dans un plus grand nombre de cas. Cette méthode devrait révéler pour la première fois les propriétés de polarisation des ondes de sifflement jusqu'à 10 $R_\odot \sim 0,05$ UA.

Ce travail de thèse ouvre la voie à de nouvelles études. Tout d'abord, le mécanisme de génération des ondes de sifflement responsable de la diffusion du Strahl (et donc probablement de l'augmentation de la densité relative du halo) n'a pas été déterminé. Pour cela, il est nécessaire d'étudier en détail les caractéristiques du champ magnétique et de la fonction de distribution des électrons pour ces cas.

La quantification de l'impact des ondes de sifflement sur la régulation du flux de chaleur n'a pas été effectuée. Nos résultats montrent que les ondes de sifflement assurent l'augmentation de la largeur angulaire du Strahl, qui est la population transportant la plus grande proportion du flux de chaleur. Nous montrons également que le halo (l'autre composante transportant le flux de chaleur) est diffusé très efficacement en pitch angle, sans toutefois quantifier l'impact de ces ondes sur la régulation du flux de chaleur. Pour réaliser cette quantification, il est possible d'utiliser les coefficients de diffusion calculés au chapitre 4. En effet, une méthode consiste à trouver les solutions de l'équation de diffusion (Equation 2.20) sous la forme d'un développement polynomial de Legendre, puis à calculer le flux de chaleur transporté par la fonction de distribution à l'ordre 1. Des approches similaires, dans le contexte d'un gaz faiblement ionisé dans un champ électrique, ont déjà été appliquées (Landau and Lifshitz, 1981).

Par la suite, la trajectoire de Solar Orbiter pourrait être utilisée pour réaliser une étude similaire à celle effectuée au chapitre 4 en dehors du plan de l'écliptique, afin de comparer les propriétés des ondes.

La distribution des angles de propagation pour les ondes avec $\theta < 15°$, peut être utilisée pour estimer les durées de vie typiques des ondes.

La méthode présentée au chapitre 4 peut également être appliquée à d'autres modes plasma dans le vent solaire. On peut notamment penser aux ondes cyclotroniques ioniques régulièrement détectées par Solar Orbiter et Parker Solar Probe (Khotyaintsev et al., 2021; Shi et al., 2021). Cela permettrait de quantifier l'impact de ces ondes sur la fonction de distribution des protons.

La théorie quasi-linéaire présente également certaines limites. Pour les ondes de sifflement de grande amplitude, nous avons parfois atteint la limite d'applicabilité de cette théorie pour la première résonance normale. Comme expliqué au chapitre 4, dans de tels cas, il est nécessaire d'appliquer une autre approche qui prend en compte les effets non linéaires. En particulier, le problème peut être décrit comme l'interaction des électrons avec une onde monochromatique (Karpman, Istomin, and Shklyar, 1975). Il serait intéressant de comparer les résultats de cette approche avec ceux obtenus avec la théorie quasi-linéaire.

Une perspective évidente de la technique présentée au chapitre 5 est son application aux orbites se produisant après mars 2019. Cela nous permettra de déterminer les caractéristiques de polarisation des ondes de sifflement jusqu'à 10 $R_\odot$ ($\sim 0,05$ UA), une région qui n'a jamais été explorée *in situ* auparavant. En particulier, il sera intéressant de vérifier les observations indiquant la quasi-absence d'ondes de sifflement en dessous de 28 $R_\odot$ ($\sim 0,13$ UA) (Cattell et al., 2022).

L'origine des ondes counter-streaming n'est pas clairement établie, malgré des indications en faveur du mécanisme décrit par Karbashewski et al. (2023). Pour vérifier ce mécanisme, il est nécessaire de mesurer les fonctions de distribution des électrons dans les creux du champ magnétique. La durée typique de ces structures étant d'une seconde, la durée d'acquisition des fonctions de distribution mesurées par SWEAP lors des premières orbites de Parker Solar Probe (13,98s) n'a pas permis de détecter cette instabilité dans les mesures. Cependant, des e-VDFs avec des temps d'acquisition inférieurs à la seconde sont disponibles pour les orbites récentes et devraient nous permettre de tester la présence de ce mécanisme. De plus, certains cas mesurés par Solar Orbiter (au-dessus de 0,3 UA) sont aussi potentiellement counter-streaming. Même s'ils sont rares, une étude détaillée de ces cas pourrait nous aider à identifier leur mécanisme de génération.

Enfin, il serait intéressant d'étudier plus en détail la zone où les ondes de sifflement counter-streaming commencent à être observées, afin de comprendre les causes de cette évolution.

Dans l'ensemble, nous pensons que ce travail a montré comment les ondes de sifflement sont distribuées dans le vent solaire et qu'elles jouent un rôle important dans l'évolution de la fonction de distribution des électrons en fonction de la distance héliocentrique. L'énergie libre et le mécanisme de génération à l'origine de ces ondes ont été discutés et peuvent maintenant être explorés plus en détail. Nous avons proposé des méthodes pour quantifier les interactions ondes-particules dans le vent solaire. Ces interactions doivent être prises en compte afin d'affiner les modèles cinétiques et d'améliorer notre description du vent solaire.

Appendix A

Appendix: Calculation of diffusion coefficients

A.1 Derivation of the analytical expression

In this appendix, we detail the calculations of the diffusion coefficients that lead to Equations 2.26 and 2.27.

Using cold plasma theory and the Stix parameters (R, L, S, D, P, Stix, 1992), the left and right-hand polarized parts of the electric field (present in the expression of $\Theta_{\mathrm{n},\vec{k}}$ in Equation 2.11) can be expressed as a function of the Fourier transform of the magnetic field $|\vec{B}_{1\vec{k}}|$:

$$E_{1\vec{k},\mathrm{L}} = \left(\frac{(N\sin\theta)^2 - P}{N^2\sin\theta\cos\theta}\right)\left(1 - \frac{D}{N^2 - S}\right)\frac{E_{1\vec{k},||}}{\sqrt{2}} \tag{A.1}$$

$$E_{1\vec{k},\mathrm{R}} = \left(\frac{(N\sin\theta)^2 - P}{N^2\sin\theta\cos\theta}\right)\left(1 + \frac{D}{N^2 - S}\right)\frac{E_{1\vec{k},||}}{\sqrt{2}} \tag{A.2}$$

with

$$|E_{1\vec{k},||}|^2 = \left(\frac{c|\vec{B}_{1\vec{k}}|}{N}\right)^2\left[\left(\frac{R-L}{2(N^2-S)}\right)^2\left(\frac{P-(N\sin\theta)^2}{N^2\sin\theta\cos\theta}\right)^2 + \left(\frac{P}{N^2\sin\theta}\right)^2\right]^{-1} \tag{A.3}$$

Therefore $|\Theta_{\mathrm{n},\vec{k}}|$ can be written as $|\Theta_{\mathrm{n},\vec{k}}| = \frac{c^2|\vec{B}_{1\vec{k}}|^2}{N^2}|\Phi_{\mathrm{n},\vec{k}}|^2$ with

$$|\Phi_{\mathrm{n,k}}|^2 = \left[\left(\left(\frac{N^2-L}{N^2-S}\right)J_{\mathrm{n}+1} + \left(\frac{N^2-R}{N^2-S}\right)J_{\mathrm{n}-1}\right)\left(\frac{N^2\sin(\theta)^2 - P}{2N^2}\right) + \coth\alpha\sin\theta\cos\theta J_n\right]^2 \cdot \left[\left(\frac{R-L}{2(N^2-S)}\right)^2\left(\frac{P-N^2\sin\theta^2}{N^2}\right)^2 + \left(\frac{P\cos\theta}{N^2}\right)^2\right]^{-1} \tag{A.4}$$

S and D are defined as:

$$\begin{matrix} S \\ D \end{matrix} = \frac{1}{2}\big(R \pm L\big) \tag{A.5}$$

In the case of whistler waves, R, L, and P are defined as (Lyons, 1974b):

$$\begin{matrix} R \\ L \end{matrix} = \pm\left(\frac{\omega_{\rm pe}}{\omega_{\rm ce}}\right)^2 \frac{\omega_{\rm ce}}{\omega}\left[\frac{1+M}{1-M \mp (\omega/\omega_{\rm ce} - \omega_{\rm ci}/\omega)}\right] \tag{A.6}$$

$$P = -\big(\frac{\omega_{\rm pe}}{\omega}\big)^2\big(1+M\big) \tag{A.7}$$

It is necessary to express $|\vec{B}_{1\vec{k}}|$ using measurable wave intensity (Lyons and Williams, 1984). Therefore, $|\vec{B}_{1\vec{k}}|^2$ can be write as (Lyons, 1974b):

$$|\vec{B}_{1\vec{k}}|^2 = \frac{V}{N_{norm}(\omega)} B{\rm w}^2(\omega) g(\theta) \tag{A.8}$$

where $B{\rm w}^2(\omega)$ is the measured power spectral density, $g(\theta)$ is the distribution of the wave intensity with the angle of propagation and $N_{norm}(\omega)$ is a normalization factor:

$$N_{norm}(\omega) = \frac{1}{2\pi^2}\int_{X_{\rm min}}^{X_{\rm max}} \frac{g(X)k^2}{(1+X^2)^{3/2}} \frac{\partial \mathcal{D}}{\partial \omega}\Big[\frac{\partial \mathcal{D}}{\partial k}\Big]^{-1} X dX \tag{A.9}$$

where $\mathcal{D}$ is the dispersion relation, in this work we use Equation 2.8. $X_{\rm min}, X_{\rm max}$ are defined below.

We assume that the power spectral density of the perturbations is Gaussian (Lyons, 1974b; Horne, 2003; Glauert and Horne, 2005):

$$B{\rm w}^2(\omega) = \begin{cases} A^2 \exp\Big(-\Big(\frac{\omega-\omega_{\rm m}}{\delta\omega}\Big)^2\Big) & \omega_{\rm lc} \le \omega \le \omega_{\rm uc} \\ 0 & \text{otherwise} \end{cases} \tag{A.10}$$

with $\omega_{\rm m}$ the frequency of the maximum, $\omega_{\rm lc}$ the minimum frequency, $\omega_{\rm uc}$ the maximum frequency, $\delta\omega$ the bandwith and A^2 is given by Equation A.11:

$$A^2 = \frac{|B{\rm w}_{\rm amp}|^2}{\delta\omega}\frac{2}{\sqrt{\pi}}\left(\text{erf}\Big(\frac{\omega_{\rm m}-\omega_{\rm lc}}{\delta\omega}\Big) + \text{erf}\Big(\frac{\omega_{\rm uc}-\omega_{\rm m}}{\delta\omega}\Big)\right)^{-1} \tag{A.11}$$

where $B{\rm w}_{\rm amp}$ is the total wave amplitude (T). By choosing $X = \tan(\theta)$, we also have a Gaussian distribution:

$$g(X) = \begin{cases} \exp\Big(-\big(\frac{X-X_{\rm m}}{X_{\rm w}}\big)^2\Big) & X_{\rm min} \le X \le X_{\rm max} \\ 0 & \text{otherwise,} \end{cases} \tag{A.12}$$

where X_{w} is the angular width and X_{m} is the peak.

Finally $D_{\alpha\alpha}$ can be expressed as:

$$D_{\alpha\alpha} = \sum_{\mathrm{n=nl}}^{\mathrm{nh}} \int_{X_{\min}}^{X_{\max}} X\, dX\ D_{\alpha\alpha}^{nX} \tag{A.13}$$

with nh and nl the maximum and minimum resonances taken into account in Equation 2.24 and $D_{\alpha\alpha}^{nX}$ given by Equation A.14:

$$D_{\alpha\alpha}^{nX} = \sum_i \frac{(e\omega_i)^2}{4\pi(1+X^2)N(\omega_i)} \left(\frac{\frac{-n\omega_{\mathrm{ce}}}{\gamma_l \omega_i} - \sin\alpha^2}{\cos\alpha} \right)^2 B\mathrm{w}^2(\omega_i) g(X) \left[\frac{|\Phi_{\mathrm{n},\vec{k}}|^2}{|v_{||} - \frac{\partial\omega}{\partial k_{||}}|} \right]_{(k_{||\mathrm{i}})} \tag{A.14}$$

where the sum is done on the resonant frequencies ω_i of Equation 2.24.

A.2 Derivation of the needed wave parameters using measurements

To calculate the diffusion coefficients we need: $B\mathrm{w}$, ω_{m}, δ_ω, ω_{lc}, ω_{uc}, X_{m}, $X\mathrm{w}$, $X_{\min}$ and $X_{\max}$, defined in Glauert and Horne, 2005. These parameters are estimated using the statistic on whistler waves:

- $B\mathrm{w}_{\mathrm{amp}}$ is the total wave amplitude;
- ω_{m} is the frequency at which the signal is maximum;
- ω_{lc} is the lowest frequency at which planarity and ellipticity are greater than 0.6;
- ω_{uc} is the highest frequency at which planarity and ellipticity are greater than 0.6;
- $\delta_\omega = (w_{\mathrm{uc}} - w_{\mathrm{lc}})/4$;
- X_{m} is calculated with minimum variance analysis and the spectral matrices (mean value);
- $X\mathrm{w} = tan(3°)$;
- $X_{\min} = X_{\mathrm{m}} - tan(5°)$;
- $X_{\max} = X_{\mathrm{m}} + tan(5°)$;

The values used for ($X\mathrm{w}$,$X_{\min}$,$X_{\max}$), namely, 3 and 5° were obtained using typical repartition of the propagation angle with frequency using spectral matrices and power spectral densities. They mainly modify the range of pitch angles that are in resonances and since we use interpolation at the Strahl PAW, this does not greatly impact our results.

Appendix B

Appendix: Coordinate transforms between the Search-Coil Magnetometer and the SpaceCraft reference frames of PSP

In this appendix we detail the coordinate transforms between the SCM (Search-Coil Magnetometer) and SC (SpaceCraft) reference frames of PSP.

Figure B.1 represents the relationship between the SCM and the spacecraft reference frame. The rotation matrix between these two frames is the following:

$$R_{\mathrm{SCM}\rightarrow\mathrm{SC_{ij}}} = \begin{pmatrix} 0.81654 & -0.40827 & -0.40827 \\ 0 & -0.70715 & 0.70715 \\ -0.57729 & -0.57729 & -0.57729 \end{pmatrix} \tag{B.1}$$

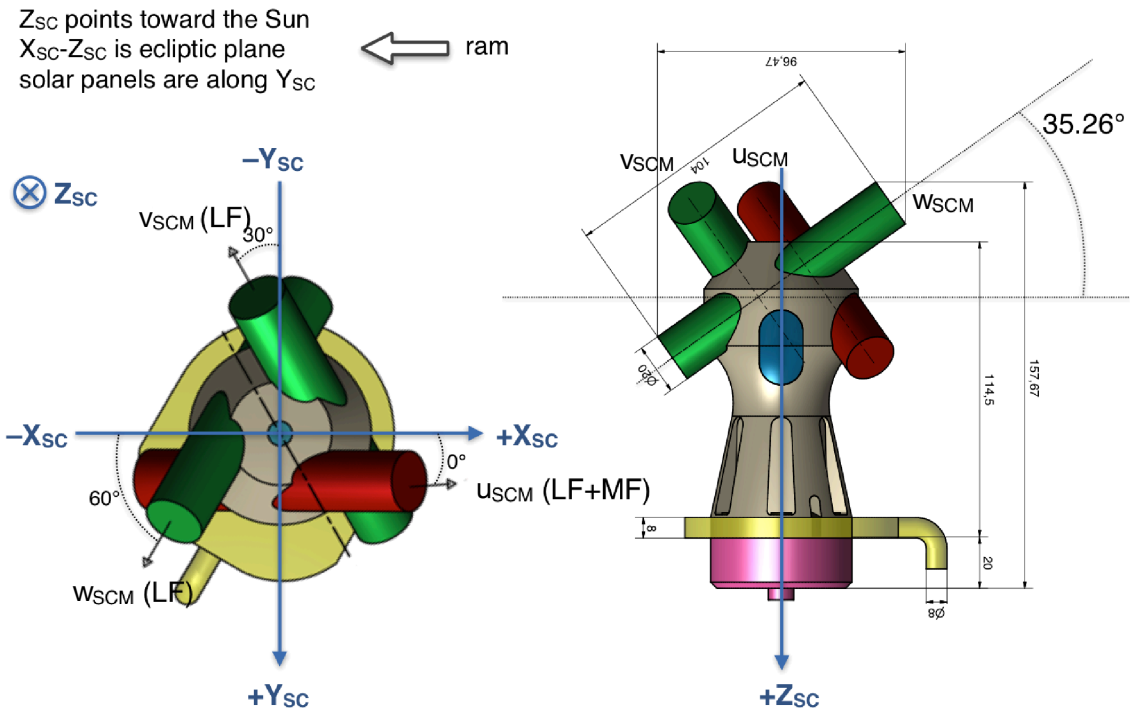

Figure B.1: Schematics of the SCM and of the relation between its reference frame $(\vec{u}, \vec{v}, \vec{w})$ and the one of the spacecraft $(\vec{X}, \vec{Y}, \vec{Z})$.

Appendix C

Appendix: Determination of the propagation angle

In this appendix, we present the two methods used to determine the angle of propagation of whistler waves.

C.1 Minimum variance analysis

The minimum variance analysis (Sonnerup and Cahill Jr., 1967; Sonnerup and Scheible, 1998; Paschmann and Daly, 1998) allows one to estimate the normal vector to a wavefront, a transition layer or, a one dimentinal current layer. This technique is based on the minimization of the following quantity:

$$\sigma^2 = \frac{1}{M}\sum_{m=1}^{M} |(\vec{B}\mathrm{w}^m - < \vec{B}\mathrm{w} >) \cdot \vec{n}|^2 \tag{C.1}$$

where M is the number of data points, $\vec{B}\mathrm{w}^m$ is one data point and

$$< \vec{B}\mathrm{w} >= \frac{1}{M}\sum_{m=1}^{M} \vec{B}\mathrm{w}^m \tag{C.2}$$

We are looking for the normalized vector $\vec{n}$ which minimizes the variance of $\vec{B}\mathrm{w}^m \cdot \vec{n}$, $(m = 1, 2, 3....M)$. This problem can be reduced to the diagonalization of the magnetic variance matrix:

$$M^{\mathrm{B}}_{\mu,\nu} =< B\mathrm{w}_\mu B\mathrm{w}_\nu > - < B\mathrm{w}_\mu >< B\mathrm{w}_\nu > \tag{C.3}$$

Since $M^{\mathrm{B}}_{\mu,\nu}$ is symmetric its eigenvalues are real. The eigenvectors $\vec{x_1}, \vec{x_2}, \vec{x_3}$ associated to the eigenvalues $\lambda_1, \lambda_2, \lambda_3$ (ordered in descending order) correspond to the directions of maximum, intermediate and minimum variance ($\vec{x_3} = \vec{n}$), respectively (Paschmann and Daly,

1998). We then take the wave vector $\vec{k}$ parallel to the direction of the minimum variance $\vec{n}$.

The statistical error on the determination of the eigenvectors can be estimated as follows:

$$|\delta\varphi_{ij}| = |\delta\varphi_{ji}| = \sqrt{\frac{\lambda_3}{(M-1)}\frac{\lambda_i + \lambda_j - \lambda_3}{(\lambda_i - \lambda_j)^2}}, i \neq j \tag{C.4}$$

where $|\delta\varphi_{ij}|$ represents the angular uncertainty (in radian) expected for a rotation of $\vec{x_i}$ around $\vec{x_j}$. The estimation of the direction of $\vec{n}$ is therefore accurate when M is large (assuming that the wave characteristics are the same on all the measurement points) and if the eigenvalues verify: $\lambda_1 \simeq \lambda_2 \gg \lambda_3$ (Paschmann and Daly, 1998).

C.2 Singular Value Decomposition of the magnetic spectral matrix

The polarization properties of an electromagnetic wave can also be determined using the Singular Value Decomposition of the magnetic spectral matrix (Means, 1972; Santolík, Parrot, and Lefeuvre, 2003; Taubenschuss and Santolík, 2019).

By expressing the electromagnetic fields as a superposition of plane waves, Maxwell's equations (Faraday or divergence of B) give directly:

$$\vec{B}_{1\vec{k}} \cdot \vec{n} = 0 \tag{C.5}$$

where $\vec{n}$ is again the normalized vector that we are trying to determine, parallel to the wave vector $\vec{k}$. This is equivalent to solving:

$$S \cdot \vec{n} = 0 \tag{C.6}$$

where S is the spectral matrix:

$$S_{i,j} = \left(B\mathrm{w}_i B\mathrm{w}_j^* \right)(\omega, t) \tag{C.7}$$

where (ω, t) stands for the time average Fourier component and * for the complex conjugate. We then apply the Singular Value Decomposition (SVD) to the real matrix A (composed of the elements of S):

$$A = \begin{pmatrix} \Re S_{11} & \Re S_{12} & \Re S_{13} \\ \Re S_{12} & \Re S_{22} & \Re S_{23} \\ \Re S_{13} & \Re S_{23} & \Re S_{33} \\ 0 & -\Im S_{12} & -\Im S_{13} \\ \Im S_{12} & 0 & -\Im S_{23} \\ \Im S_{13} & \Im S_{23} & 0 \end{pmatrix} \tag{C.8}$$

where $\Re$ and $\Im$ represent the real and imaginary parts, respectively. The SVD consists of expressing A as:

$$A = UWV^T \tag{C.9}$$

where V^T has orthonormal rows and is a $3*3$ matrix, W is a 3*3 diagonal matrix of non-negative real singular values and U has orthonormal columns and is a $6*3$ matrix. The least squares estimate of $\vec{n}$ is directly deduced from the rows of V^T. Indeed, the rows of V^T are the vectors $\vec{x_1}, \vec{x_2}, \vec{x_3}$ associated with the singular values $\lambda_1, \lambda_2, \lambda_3$ (ordered in descending order) corresponding to the directions of maximum, intermediate and minimum variance (Santolík, Parrot, and Lefeuvre, 2003), respectively.

The planarity (F) and the polarization (L_p) are directly estimated from the singular values:

$$F = 1 - \sqrt{\frac{\lambda_1}{\lambda_3}}$$
$$L_p = \frac{\lambda_2}{\lambda_3}$$

and the coherence between two components can be expressed as (Paschmann and Daly, 1998):

$$\rho_{B\mathrm{w_i}B\mathrm{w_i}} = \frac{\sqrt{\Im S_{i,j}{}^2 + \Re S_{i,j}{}^2}}{\sqrt{S_{i,i}S_{j,j}}}$$

Appendix D

Appendix: Estimating the error of the reconstruction technique

D.1 Estimation of the parallel electric field component in the spacecraft frame

In this section, we derive Equation 5.1.

Let us make calculations in the reference frame where $\vec{B}_0$ is directed along the $\vec{z}$ axis, and the $\vec{k}$-vector is in the plane ($\vec{x}$, $\vec{y}$). Therefore, we have: $\vec{k} = k(\sin\theta\cos\varphi, \sin\theta\sin\varphi, \cos\theta)$, with φ the angle between $\vec{x}$ and $\vec{k}$. To begin with, we shall treat the waves at frequencies much larger than the lower hybrid frequency (well verified for whistler waves in the solar wind) and using the cold plasma approximation. In our reference frame the dielectric tensor $\varepsilon_{\rm ij}$ reads:

$$\varepsilon_{\rm ij} = \begin{pmatrix} \varepsilon_1 & i\varepsilon_2 & 0 \\ -i\varepsilon_2 & \varepsilon_1 & 0 \\ 0 & 0 & \varepsilon_3 \end{pmatrix} \tag{D.1}$$

where using the typical conditions of observations $\omega_{\rm pe}^2 >> \omega_{\rm ce}^2 > \omega^2$:
$\varepsilon_1 = -\frac{\omega_{\rm pe}^2}{\omega^2-\omega_{\rm ce}^2}; \varepsilon_2 = \frac{\omega_{\rm pe}^2\omega_{\rm ce}}{\omega(\omega^2-\omega_{\rm ce}^2)}; \varepsilon_3 = -\frac{\omega_{\rm pe}^2}{\omega^2}$
One can find for whistler waves:

$$N^2 = \frac{\omega_{\rm pe}^2}{\omega(\omega_{\rm ce} \mid \cos\theta \mid -\omega)}$$

$$\omega = \omega_{\rm ce} \mid \cos\theta \mid \frac{\frac{k^2c^2}{\omega_{\rm pe}^2}}{(1+\frac{k^2c^2}{\omega_{\rm pe}^2})}$$

The next step is to determine the polarization properties. In the following, we use $E{\rm w}(\omega,t)$ and $B{\rm w}(\omega,t)$ ((ω,t) representing the time averaged Fourier components) to approximate

the theoretical fields of the general dispersion relation. We drop the (ω, t) to simplify the notations.

$$\begin{pmatrix} \varepsilon_1 - N_{\rm y}^2 - N_{\rm z}^2 & i\varepsilon_2 + N_{\rm x}N_{\rm y} & N_{\rm x}N_{\rm z} \\ -i\varepsilon_2 + N_{\rm x}N_{\rm y} & \varepsilon_1 - N_{\rm x}^2 - N_{\rm z}^2 & N_{\rm y}N_{\rm z} \\ N_{\rm x}N_{\rm z} & N_{\rm y}N_{\rm z} & \varepsilon_3 - N_{\rm x}^2 - N_{\rm y}^2 \end{pmatrix} \begin{matrix} E{\rm w_x} \\ E{\rm w_y} \\ E{\rm w_z} \end{matrix} = 0 \tag{D.2}$$

$$\begin{pmatrix} \varepsilon_1 - N^2(\cos^2\theta + \sin^2\theta\sin^2\varphi) & i\varepsilon_2 + N^2\sin^2\theta\sin\varphi\cos\varphi & N^2\cos\theta\sin\theta\cos\varphi \\ -i\varepsilon_2 + N^2\sin^2\theta\sin\varphi\cos\varphi & \varepsilon_1 - N^2(\cos^2\theta + \sin^2\theta\cos^2\varphi) & N^2\cos\theta\sin\theta\sin\varphi \\ N^2\cos\theta\sin\theta\cos\varphi & N^2\cos\theta\sin\theta\sin\varphi & \varepsilon_3 - N^2\sin^2\theta \end{pmatrix} \begin{matrix} E{\rm w_x} \\ E{\rm w_y} \\ E{\rm w_z} \end{matrix} = 0 \tag{D.3}$$

$$\begin{pmatrix} -\frac{\omega_{\rm pe}^2}{\omega^2-\omega_{\rm ce}^2} - N^2(\cos^2\theta + \sin^2\theta\sin^2\varphi) & i\frac{\omega_{\rm pe}^2\omega_{\rm ce}}{\omega(\omega^2-\omega_{\rm ce}^2)} + N^2\sin^2\theta\sin\varphi\cos\varphi & N^2\cos\theta\sin\theta\cos\varphi \\ -i\frac{\omega_{\rm pe}^2\omega_{\rm ce}}{\omega(\omega^2-\omega_{\rm ce}^2)} + N^2\sin^2\theta\sin\varphi\cos\varphi & -\frac{\omega_{\rm pe}^2}{\omega^2-\omega_{\rm ce}^2} - N^2(\cos^2\theta + \sin^2\theta\cos^2\varphi) & N^2\cos\theta\sin\theta\sin\varphi \\ N^2\cos\theta\sin\theta\cos\varphi & N^2\cos\theta\sin\theta\sin\varphi & -\frac{\omega_{\rm pe}^2}{\omega^2} - N^2\sin^2\theta \end{pmatrix} \begin{matrix} E{\rm w_x} \\ E{\rm w_y} \\ E{\rm w_z} \end{matrix} = 0 \tag{D.4}$$

Polarization vectors can be expressed in the reference frame determined at the beginning as:

$$\vec{E}{\rm w} = a \begin{pmatrix} \frac{\omega}{(\omega^2-\omega_{\rm ce}^2)}(i\omega_{\rm ce}\sin\varphi + \omega\cos\varphi) + \frac{k^2c^2}{\omega_{\rm pe}^2}\cos\varphi \\ \frac{\omega}{\omega^2-\omega_{\rm ce}^2}(\omega\sin\varphi - i\omega_{\rm ce}\cos\varphi) + \frac{k^2c^2}{\omega_{\rm pe}^2}\sin\varphi \\ \frac{\frac{k^2c^2}{\omega_{\rm pe}^2}\cos\theta\sin\theta}{(1+\frac{k^2c^2}{\omega_{\rm pe}^2}\sin^2\theta)}\left(\frac{\omega^2}{(\omega^2-\omega_{\rm ce}^2)} + \frac{k^2c^2}{\omega_{\rm pe}^2}\right) \end{pmatrix} \tag{D.5}$$

$$\vec{B}{\rm w} = a\frac{k}{\omega} \begin{pmatrix} -\frac{\cos\theta\sin\varphi}{(1+\frac{k^2c^2}{\omega_{\rm pe}^2}\sin^2\theta)}\left(\frac{\omega^2}{(\omega^2-\omega_{\rm ce}^2)} + \frac{k^2c^2}{\omega_{\rm pe}^2}\right) + i\frac{\omega_{\rm ce}\omega\cos\theta\cos\varphi}{\omega^2-\omega_{\rm ce}^2} \\ \frac{i\omega_{\rm ce}\omega\cos\theta\sin\varphi}{(\omega^2-\omega_e^2)} + \left(\frac{\omega^2}{(\omega^2-\omega_{\rm ce}^2)} + \frac{k^2c^2}{\omega_{\rm pe}^2}\right)\frac{\cos\theta\cos\varphi}{(1+\frac{k^2c^2}{\omega_{\rm pe}^2}\sin^2\theta)} \\ -i\frac{\omega_{\rm ce}\omega\sin\theta}{\omega^2-\omega_{\rm ce}^2} \end{pmatrix} \tag{D.6}$$

Where a is a constant. Using the refractive index magnitude, one can re-write wave polarization dependence upon characteristic frequencies as follows:

$$\vec{E}{\rm w} = a \begin{pmatrix} \frac{\omega}{(\omega^2-\omega_{\rm ce}^2)}(i\omega_{\rm ce}\sin\varphi + \omega\cos\varphi) + \frac{\omega}{\omega_{\rm ce}\cos\theta-\omega}\cos\varphi \\ \frac{\omega}{\omega^2-\omega_{\rm ce}^2}(\omega\sin\varphi - i\omega_{\rm ce}\cos\varphi) + \frac{\omega}{\omega_{\rm ce}\cos\theta-\omega}\sin\varphi \\ \frac{\omega\sin\theta}{(\omega_{\rm ce}-\omega\cos\theta)}\left(\frac{\omega^2}{(\omega^2-\omega_{\rm ce}^2)} + \frac{\omega}{\omega_{\rm ce}\cos\theta-\omega}\right) \end{pmatrix} \tag{D.7}$$

$$\vec{B}{\rm w} = a\frac{k}{\omega} \begin{pmatrix} -\frac{(\omega_{\rm ce}\cos\theta-\omega)\sin\varphi}{(\omega_{\rm ce}-\omega\cos\theta)}\left(\frac{\omega^2}{(\omega^2-\omega_{\rm ce}^2)} + \frac{\omega}{\omega_{\rm ce}\cos\theta-\omega}\right) + i\frac{\omega_{\rm ce}\omega\cos\theta\cos\varphi}{\omega^2-\omega_{\rm ce}^2} \\ \frac{i\omega_{\rm ce}\omega\cos\theta\sin\varphi}{(\omega^2-\omega_e^2)} + \left(\frac{\omega^2}{(\omega^2-\omega_{\rm ce}^2)} + \frac{\omega}{\omega_{\rm ce}\cos\theta-\omega}\right)\frac{(\omega_{\rm ce}\cos\theta-\omega)\cos\varphi}{(\omega_{\rm ce}-\omega\cos\theta)} \\ -i\frac{\omega_{\rm ce}\omega\sin\theta}{\omega^2-\omega_{\rm ce}^2} \end{pmatrix} \tag{D.8}$$

Now one can come to simplifications. We have already noted that the overwhelming majority of observed waves satisfy the condition $\omega << \omega_{\rm ce}$, that is, the parameter $\frac{\omega}{\omega_{\rm ce}} = \epsilon$ is

small. This allows one to use it as the small parameter constructing solutions as power series over this parameter. The first order approximation on ϵ results in:

$$\vec{E}\mathrm{w} = a \begin{pmatrix} \frac{\omega}{\omega_{\mathrm{ce}}}(-i\sin\varphi + \frac{\cos\varphi}{\cos\theta}) \\ \frac{\omega}{\omega_{\mathrm{ce}}}(i\cos\varphi + \frac{\sin\varphi}{\cos\theta}) \\ \frac{\omega^2 \sin\theta}{\omega_{\mathrm{ce}}^2 \cos\theta} \end{pmatrix} \tag{D.9}$$

$$\vec{B}\mathrm{w} = a\frac{k}{\omega} \begin{pmatrix} -\frac{\omega}{\omega_{\mathrm{ce}}}(\sin\varphi + i\cos\theta\cos\varphi) \\ \frac{\omega}{\omega_{\mathrm{ce}}}(-i\cos\theta\sin\varphi + \cos\varphi) \\ i\frac{\omega}{\omega_{\mathrm{ce}}}\sin\theta \end{pmatrix} \tag{D.10}$$

The electric field is measured in the spacecraft frame, which is different from the plasma frame. It is therefore necessary to take Lorentz transformations into account. For the magnetic field, since the measured solar wind speed (V_{SW}) verifies $V_{\mathrm{SW}} << c$ (where c is the speed of light) these transformations can be neglected and we can safely consider that $\vec{B}^{\mathrm{SC}}\mathrm{w} = \vec{B}\mathrm{w}$. For the electric field, on the other hand, we have:

$$\vec{E}^{\mathrm{SC}}\mathrm{w} = \vec{E}\mathrm{w} - \left(\vec{V}_{\mathrm{SW}} \times \vec{B}\mathrm{w}\right) \tag{D.11}$$

where $\vec{V}_{\mathrm{SW}}$ is expressed as:

$$\vec{V}_{\mathrm{SW}} = \begin{matrix} V_{\mathrm{SWx}} \\ V_{\mathrm{SWy}} \\ V_{\mathrm{SWz}} \end{matrix} \tag{D.12}$$

$$\left(\vec{V}_{\mathrm{SW}} \times \vec{B}\mathrm{w}\right) = a\frac{k}{\omega} \begin{pmatrix} \frac{\omega}{\omega_{\mathrm{ce}}}(i\sin\theta V_{\mathrm{SWy}} - V_{\mathrm{SWz}}(-i\cos\theta\sin\varphi + \cos\varphi)) \\ \frac{\omega}{\omega_{\mathrm{ce}}}(-V_{\mathrm{SWz}}(\sin\varphi + i\cos\theta\cos\varphi) - i\sin\theta V_{\mathrm{SWx}}) \\ \frac{\omega}{\omega_{\mathrm{ce}}}(V_{\mathrm{SWx}}(-i\cos\theta\sin\varphi + cos\varphi) + V_{\mathrm{SWy}}(\sin\varphi + i\cos\theta\cos\varphi)) \end{pmatrix} \tag{D.13}$$

Therefore,

$$|\left(\vec{V}_{\mathrm{SW}} \times \vec{B}\mathrm{w}\right)_{\mathrm{z}}| = a\frac{k}{\omega}\frac{\omega}{\omega_{\mathrm{ce}}}\left((V_{\mathrm{SWx}}\cos\varphi + V_{\mathrm{SWy}}\sin\varphi)^2 + \cos^2\theta(V_{\mathrm{SWy}}\cos\varphi - V_{\mathrm{SWx}}\sin\varphi)^2\right)^{1/2} \tag{D.14}$$

By choosing, $\varphi = 0$, then

$$|\left(\vec{V}_{\mathrm{SW}} \times \vec{B}\mathrm{w}\right)_{\mathrm{z}}| = a\frac{k}{\omega}\frac{\omega}{\omega_{\mathrm{ce}}}\left(V_{\mathrm{SWx}}^2 + V_{\mathrm{SWy}}^2\cos^2\theta\right)^{1/2} \tag{D.15}$$

Thus,

$$|E^{\mathrm{SC}}\mathrm{w}_{||}| \leq |\mathrm{Ew}|(\frac{\mathrm{V}_{\mathrm{SW}\perp}}{\mathrm{V}_{\varphi}} + (\frac{\omega}{\omega_{\mathrm{ce}}})\tan\theta) \tag{D.16}$$

D.2 Propagation of the error

The electromagnetic wave equation is expressed as:

$$\vec{E}\mathrm{w} \cdot \vec{B}\mathrm{w} = 0 \tag{D.17}$$

and is also valid in the spacecraft frame:

$$\vec{E}^{\mathrm{SC}}\mathrm{w} \cdot \vec{B}^{\mathrm{SC}}\mathrm{w} = 0 \tag{D.18}$$

Therefore,

$$\vec{E}^{\mathrm{SC}}\mathrm{w}|| \cdot \vec{B}^{\mathrm{SC}}\mathrm{w}|| + \vec{E}^{\mathrm{SC}}\mathrm{w} \perp \cdot \vec{B}^{\mathrm{SC}}\mathrm{w} \perp = 0 \tag{D.19}$$

In our approximation we neglect $\vec{E}^{\mathrm{SC}}\mathrm{w}||$, therefore using results from the previous section we find

$$|\vec{E}^{\mathrm{SCre}}\mathrm{w} \cdot \vec{B}^{\mathrm{SC}}\mathrm{w}| \leq |E\mathrm{w}|(\frac{V_{\mathrm{SW}\perp}}{V_\varphi} + (\frac{\omega}{\omega_{\mathrm{ce}}})\tan\theta)\sin\theta \tag{D.20}$$

One way of approximating the error on the reconstructed component, considering these two errors as independent and following a normal distribution, is as follows:

$$(|B^{\mathrm{error}}\mathrm{w_u}/B\mathrm{w}|) \lesssim \sqrt{(\frac{V_{\mathrm{SW}\perp}}{V_\varphi})^2 + ((\frac{\omega}{\omega_{\mathrm{ce}}})\tan\theta)^2}\frac{\sin\theta}{\sin\theta_{\vec{B_0},\vec{u}}} \tag{D.21}$$

Bibliography

Abramowitz, M and I. A Stegun (1972). *Handbook of Mathematical Functions*.

Acuña, Mario H. (Oct. 2002). "Space-based magnetometers". In: *Review of Scientific Instruments* 73.11, pp. 3717–3736. ISSN: 0034-6748. DOI: 10.1063/1.1510570. URL: https://doi.org/10.1063/1.1510570 (visited on 08/19/2023).

Agapitov, O. V. et al. (Mar. 2020). "Sunward-propagating Whistler Waves Collocated with Localized Magnetic Field Holes in the Solar Wind: *Parker Solar Probe* Observations at 35.7 $R_\odot$ Radii". en. In: *The Astrophysical Journal* 891.1, p. L20. ISSN: 2041-8213. DOI: 10.3847/2041-8213/ab799c. URL: https://iopscience.iop.org/article/10.3847/2041-8213/ab799c (visited on 05/30/2022).

Agapitov, O. V. et al. (Feb. 2022). "Flux Rope Merging and the Structure of Switchbacks in the Solar Wind". en. In: *The Astrophysical Journal* 925.2, p. 213. ISSN: 0004-637X, 1538-4357. DOI: 10.3847/1538-4357/ac4016. URL: https://iopscience.iop.org/article/10.3847/1538-4357/ac4016 (visited on 01/30/2023).

Agapitov, Oleksiy et al. (June 2013). "Statistics of whistler mode waves in the outer radiation belt: Cluster STAFF-SA measurements". en. In: *Journal of Geophysical Research: Space Physics* 118.6, pp. 3407–3420. ISSN: 2169-9380, 2169-9402. DOI: 10.1002/jgra.50312. URL: https://onlinelibrary.wiley.com/doi/abs/10.1002/jgra.50312 (visited on 05/02/2023).

Akhiezer, A. I. et al. (Jan. 1975). "CHAPTER 5 - Oscillations of a Plasma in a Magnetic Field". en. In: *Plasma Electrodynamics*. Ed. by A. I. Akhiezer et al. Vol. 68. International Series in Natural Philosophy. Pergamon, pp. 211–287. DOI: 10.1016/B978-0-08-017783-0.50009-9. URL: https://www.sciencedirect.com/science/article/pii/B9780080177830500099 (visited on 08/11/2023).

Alexandrova, O. et al. (Oct. 2013). "Solar Wind Turbulence and the Role of Ion Instabilities". en. In: *Space Science Reviews* 178.2-4, pp. 101–139. ISSN: 0038-6308, 1572-9672. DOI: 10.1007/s11214-013-0004-8. URL: http://link.springer.com/10.1007/s11214-013-0004-8 (visited on 02/14/2023).

Antonucci, Ester et al. (Oct. 2020). "Metis: the Solar Orbiter visible light and ultraviolet coronal imager". en. In: *Astronomy & Astrophysics* 642, A10. ISSN: 0004-6361, 1432-0746. DOI: 10.1051/0004-6361/201935338. URL: https://www.aanda.org/10.1051/0004-6361/201935338 (visited on 02/14/2023).

Artemyev, A. et al. (Aug. 2012). "Statistical model of electron pitch angle diffusion in the outer radiation belt". en. In: *Journal of Geophysical Research: Space Physics* 117.A8.

ISSN: 01480227. DOI: 10.1029/2012JA017826. URL: http://doi.wiley.com/10.1029/2012JA017826 (visited on 08/17/2022).

Artemyev, Anton et al. (Apr. 2016). "Oblique Whistler-Mode Waves in the Earth's Inner Magnetosphere: Energy Distribution, Origins, and Role in Radiation Belt Dynamics". en. In: *Space Science Reviews* 200.1-4, pp. 261–355. ISSN: 0038-6308, 1572-9672. DOI: 10.1007/s11214-016-0252-5. URL: http://link.springer.com/10.1007/s11214-016-0252-5 (visited on 08/11/2023).

Bale, S. D. et al. (May 2013). "Electron heat conduction in the solar wind: transition from Spitzer-H\"{a}rm to the collisionless limit". en. In: *The Astrophysical Journal* 769.2. arXiv:1303.0932 [astro-ph, physics:physics], p. L22. ISSN: 2041-8205, 2041-8213. DOI: 10.1088/2041-8205/769/2/L22. URL: http://arxiv.org/abs/1303.0932 (visited on 08/16/2022).

Bale, S. D. et al. (Dec. 2016). "The FIELDS Instrument Suite for Solar Probe Plus: Measuring the Coronal Plasma and Magnetic Field, Plasma Waves and Turbulence, and Radio Signatures of Solar Transients". en. In: *Space Science Reviews* 204.1-4, pp. 49–82. ISSN: 0038-6308, 1572-9672. DOI: 10.1007/s11214-016-0244-5. URL: http://link.springer.com/10.1007/s11214-016-0244-5 (visited on 08/16/2022).

Bale, S. D. et al. (Dec. 2019). "Highly structured slow solar wind emerging from an equatorial coronal hole". en. In: *Nature* 576.7786. Number: 7786 Publisher: Nature Publishing Group, pp. 237–242. ISSN: 1476-4687. DOI: 10.1038/s41586-019-1818-7. URL: https://www.nature.com/articles/s41586-019-1818-7 (visited on 12/05/2022).

Bercic, L. et al. (July 2019). "Scattering of Strahl Electrons in the Solar Wind between 0.3 and 1 au: Helios Observations". en. In: *Monthly Notices of the Royal Astronomical Society* 486.3. arXiv:1904.08272 [astro-ph, physics:physics], pp. 3404–3414. ISSN: 0035-8711, 1365-2966. DOI: 10.1093/mnras/stz1007. URL: http://arxiv.org/abs/1904.08272 (visited on 08/16/2022).

Berčič, L., S. Landi, and M. Maksimović (Feb. 2021). "The Interplay Between Ambipolar Electric Field and Coulomb Collisions in the Solar Wind Acceleration Region". en. In: *Journal of Geophysical Research: Space Physics* 126.3, e2020JA028864. ISSN: 2169-9402. DOI: 10.1029/2020JA028864. URL: https://onlinelibrary.wiley.com/doi/abs/10.1029/2020JA028864 (visited on 01/10/2023).

Berčič, Laura (Sept. 2020). "Radial evolution of the solar wind electrons : simulations and preparation of the Solar orbiter and Parker solar probe observations". These de doctorat. Université Paris sciences et lettres. URL: https://www.theses.fr/2020UPSLO003 (visited on 05/09/2023).

Berčič, Laura et al. (Apr. 2020). "Coronal Electron Temperature Inferred from the Strahl Electrons in the Inner Heliosphere: *Parker Solar Probe* and *Helios* Observations". en. In: *The Astrophysical Journal* 892.2, p. 88. ISSN: 1538-4357. DOI: 10.3847/1538-4357/ab7b7a. URL: https://iopscience.iop.org/article/10.3847/1538-4357/ab7b7a (visited on 08/16/2022).

Berčič, Laura et al. (Dec. 2021). "Whistler instability driven by the sunward electron deficit in the solar wind". en. In: *Astronomy & Astrophysics* 656. arXiv:2107.10645 [astro-ph,

physics:physics], A31. ISSN: 0004-6361, 1432-0746. DOI: 10.1051/0004-6361/202140970. URL: http://arxiv.org/abs/2107.10645 (visited on 08/17/2022).

Biermann, L. (Jan. 1951). "Kometenschweife und solare Korpuskularstrahlung". In: *Zeitschrift fur Astrophysik* 29. ADS Bibcode: 1951ZA.....29..274B, p. 274. ISSN: 0372-8331. URL: https://ui.adsabs.harvard.edu/abs/1951ZA.....29..274B (visited on 03/27/2023).

Boldyrev, Stanislav, Cary Forest, and Jan Egedal (Apr. 2020). "Electron temperature of the solar wind". en. In: *Proceedings of the National Academy of Sciences* 117.17, pp. 9232–9240. ISSN: 0027-8424, 1091-6490. DOI: 10.1073/pnas.1917905117. URL: https://pnas.org/doi/full/10.1073/pnas.1917905117 (visited on 05/27/2023).

Boldyrev, Stanislav and Konstantinos Horaites (Nov. 2019). "Kinetic theory of the electron strahl in the solar wind". en. In: *Monthly Notices of the Royal Astronomical Society* 489.3, pp. 3412–3419. ISSN: 0035-8711, 1365-2966. DOI: 10.1093/mnras/stz2378. URL: https://academic.oup.com/mnras/article/489/3/3412/5565056 (visited on 05/18/2023).

Boldú, J. J. et al. (June 2023). "Langmuir waves associated with magnetic holes in the solar wind". en. In: *Astronomy & Astrophysics* 674, A220. ISSN: 0004-6361, 1432-0746. DOI: 10.1051/0004-6361/202346100. URL: https://www.aanda.org/10.1051/0004-6361/202346100 (visited on 08/17/2023).

Breneman, A. et al. (Aug. 2010). "Observations of large-amplitude, narrowband whistlers at stream interaction regions". en. In: *Journal of Geophysical Research: Space Physics* 115.A8, n/a–n/a. ISSN: 01480227. DOI: 10.1029/2009JA014920. URL: http://doi.wiley.com/10.1029/2009JA014920 (visited on 04/03/2023).

Case, A. W. et al. (Feb. 2020). "The Solar Probe Cup on the Parker Solar Probe". en. In: *The Astrophysical Journal Supplement Series* 246.2, p. 43. ISSN: 0067-0049, 1538-4365. DOI: 10.3847/1538-4365/ab5a7b. URL: https://iopscience.iop.org/article/10.3847/1538-4365/ab5a7b (visited on 08/17/2022).

Cattell, C. et al. (July 2020). "Narrowband Large Amplitude Whistler-mode Waves in the Solar Wind and Their Association with Electrons: STEREO Waveform Capture Observations". en. In: *The Astrophysical Journal* 897.2, p. 126. ISSN: 0004-637X, 1538-4357. DOI: 10.3847/1538-4357/ab961f. URL: https://iopscience.iop.org/article/10.3847/1538-4357/ab961f (visited on 05/26/2022).

Cattell, C. et al. (June 2021a). "Narrowband oblique whistler-mode waves: comparing properties observed by Parker Solar Probe at <0.3 AU and STEREO at 1 AU". en. In: *Astronomy & Astrophysics* 650, A8. ISSN: 0004-6361, 1432-0746. DOI: 10.1051/0004-6361/202039550. URL: https://www.aanda.org/10.1051/0004-6361/202039550 (visited on 12/21/2022).

Cattell, C. et al. (Apr. 2021b). "Parker Solar Probe Evidence for Scattering of Electrons in the Young Solar Wind by Narrowband Whistler-mode Waves". en. In: *The Astrophysical Journal Letters* 911.2, p. L29. ISSN: 2041-8205, 2041-8213. DOI: 10.3847/2041-8213/abefdd. URL: https://iopscience.iop.org/article/10.3847/2041-8213/abefdd (visited on 08/16/2022).

Cattell, C. et al. (Jan. 2022). "Parker Solar Probe Evidence for the Absence of Whistlers Close to the Sun to Scatter Strahl and to Regulate Heat Flux". en. In: *The Astrophysical Journal Letters* 924.2. Publisher: The American Astronomical Society, p. L33. ISSN: 2041-

8205. DOI: 10.3847/2041-8213/ac4015. URL: https://dx.doi.org/10.3847/2041-8213/ac4015 (visited on 10/27/2022).

Cattell, Cynthia and Tien Vo (June 2021). "Modeling Interactions of Narrowband Large Amplitude Whistler-mode Waves with Electrons in the Solar Wind inside 0.3 au and at 1 au Using a Particle Tracing Code". en. In: *The Astrophysical Journal Letters* 914.2, p. L33. ISSN: 2041-8205, 2041-8213. DOI: 10.3847/2041-8213/ac08a1. URL: https://iopscience.iop.org/article/10.3847/2041-8213/ac08a1 (visited on 12/21/2022).

Chamberlain, Joseph W. (Jan. 1960). "Interplanetary Gas.II. Expansion of a Model Solar Corona." In: *The Astrophysical Journal* 131. ADS Bibcode: 1960ApJ...131...47C, p. 47. ISSN: 0004-637X. DOI: 10.1086/146805. URL: https://ui.adsabs.harvard.edu/abs/1960ApJ...131...47C (visited on 04/14/2023).

Chapman, Sydney and Harold Zirin (1957). "Notes on the solar corona and the terrestrial ionosphere". en_US. In: Accepted: 2008-12-29T16:01:29Z. ISSN: 0081-0231. URL: http://repository.si.edu/xmlui/handle/10088/6598 (visited on 03/27/2023).

Chust, T. et al. (Dec. 2021). "Observations of whistler mode waves by Solar Orbiter's RPW Low Frequency Receiver (LFR): In-flight performance and first results". en. In: *Astronomy & Astrophysics* 656, A17. ISSN: 0004-6361, 1432-0746. DOI: 10.1051/0004-6361/202140932. URL: https://www.aanda.org/10.1051/0004-6361/202140932 (visited on 08/17/2022).

Colomban, L. et al. (2023a). "Quantifying the diffusion of suprathermal electrons by whistler waves between 0.2 and 1 AU with Solar Orbiter and Parker Solar Probe". In: *Astronomy & Astrophysics*. Submitted.

Colomban, L et al. (2023b). "Reconstruction of polarization properties of whistler waves from two magnetic and two electric field components: application to Parker Solar Probe measurements". In: *Journal of Geophysical Research: Space Physics*. Accepted.

Cowie, L. L. and C. F. McKee (Jan. 1977). "The evaporation of spherical clouds in a hot gas. I. Classical and saturated mass loss rates." In: *The Astrophysical Journal* 211. ADS Bibcode: 1977ApJ...211..135C, pp. 135–146. ISSN: 0004-637X. DOI: 10.1086/154911. URL: https://ui.adsabs.harvard.edu/abs/1977ApJ...211..135C (visited on 05/30/2023).

Dudok De Wit, T. et al. (Feb. 2020). "Switchbacks in the Near-Sun Magnetic Field: Long Memory and Impact on the Turbulence Cascade". en. In: *The Astrophysical Journal Supplement Series* 246.2, p. 39. ISSN: 1538-4365. DOI: 10.3847/1538-4365/ab5853. URL: https://iopscience.iop.org/article/10.3847/1538-4365/ab5853 (visited on 09/04/2023).

Dudok De Wit, T. et al. (2022). "First Results From the SCM Search-Coil Magnetometer on Parker Solar Probe". en. In: *Journal of Geophysical Research: Space Physics* 127.4, e2021JA030018. ISSN: 2169-9402. DOI: 10.1029/2021JA030018. URL: https://onlinelibrary.wiley.com/doi/abs/10.1029/2021JA030018 (visited on 09/04/2023).

Echim, Marius, Joseph Lemaire, and Oystein Lie-Svendsen (Jan. 2011). "A review on solar wind modeling: kinetic and fluid aspects". en. In: *Surveys in Geophysics* 32.1. arXiv:1306.0704 [astro-ph, physics:physics], pp. 1–70. ISSN: 0169-3298, 1573-0956. DOI: 10.1007/s10712-010-9106-y. URL: http://arxiv.org/abs/1306.0704 (visited on 02/24/2023).

Feldman, W. C. et al. (Nov. 1975). "Solar wind electrons". en. In: *Journal of Geophysical Research* 80.31, pp. 4181–4196. ISSN: 01480227. DOI: 10.1029/JA080i031p04181. URL: http://doi.wiley.com/10.1029/JA080i031p04181 (visited on 08/16/2022).

Feldman, W. C. et al. (1978). "Characteristic electron variations across simple high-speed solar wind streams". en. In: *Journal of Geophysical Research: Space Physics* 83.A11, pp. 5285–5295. ISSN: 2156-2202. DOI: 10.1029/JA083iA11p05285. URL: https://onlinelibrary.wiley.com/doi/abs/10.1029/JA083iA11p05285 (visited on 02/24/2023).

Feynman, Richard P. (1964). *The Feynman Lectures on Physics, Vol. II: The New Millennium Edition: Mainly Electromagnetism and Matter*. en. Basic Books. ISBN: 978-0-465-02494-0.

Fitzenreiter, R. J. et al. (1998). "Observations of electron velocity distribution functions in the solar wind by the WIND Spacecraft: High angular resolution Strahl measurements". en. In: *Geophysical Research Letters* 25.3, pp. 249–252. ISSN: 1944-8007. DOI: 10.1029/97GL03703. URL: https://onlinelibrary.wiley.com/doi/abs/10.1029/97GL03703 (visited on 05/30/2023).

Fox, N. J. et al. (Dec. 2016). "The Solar Probe Plus Mission: Humanity's First Visit to Our Star". en. In: *Space Science Reviews* 204.1-4, pp. 7–48. ISSN: 0038-6308, 1572-9672. DOI: 10.1007/s11214-015-0211-6. URL: http://link.springer.com/10.1007/s11214-015-0211-6 (visited on 08/19/2022).

Fried, Burton D. and Roy W. Gould (Jan. 1961). "Longitudinal Ion Oscillations in a Hot Plasma". en. In: *The Physics of Fluids* 4.1, pp. 139–147. ISSN: 0031-9171. DOI: 10.1063/1.1706174. URL: https://pubs.aip.org/pfl/article/4/1/139/403032/Longitudinal-Ion-Oscillations-in-a-Hot-Plasma (visited on 08/16/2023).

Froment, C. et al. (Apr. 2023). "Whistler waves generated inside magnetic dips in the young solar wind: Observations of the search-coil magnetometer on board Parker Solar Probe". en. In: *Astronomy & Astrophysics* 672, A135. ISSN: 0004-6361, 1432-0746. DOI: 10.1051/0004-6361/202245140. URL: https://www.aanda.org/10.1051/0004-6361/202245140 (visited on 07/12/2023).

Gary, S. Peter (1993). *Theory of Space Plasma Microinstabilities*. Cambridge Atmospheric and Space Science Series. Cambridge: Cambridge University Press. ISBN: 978-0-521-43748-6. DOI: 10.1017/CBO9780511551512. URL: https://www.cambridge.org/core/books/theory-of-space-plasma-microinstabilities/11F0E1BEEFCC3A1597230DAF2DD664F7 (visited on 06/14/2023).

Gary, S. Peter and W. C. Feldman (Mar. 1977). "Solar wind heat flux regulation by the whistler instability". en. In: *Journal of Geophysical Research* 82.7, pp. 1087–1094. ISSN: 01480227. DOI: 10.1029/JA082i007p01087. URL: http://doi.wiley.com/10.1029/JA082i007p01087 (visited on 08/16/2022).

Gary, S. Peter, Ruth M. Skoug, and William Daughton (June 1999). "Electron heat flux constraints in the solar wind". en. In: *Physics of Plasmas* 6.6, pp. 2607–2612. ISSN: 1070-664X, 1089-7674. DOI: 10.1063/1.873532. URL: http://aip.scitation.org/doi/10.1063/1.873532 (visited on 08/16/2022).

Gary, S. Peter et al. (Mar. 1975). "Electron heat flux instabilities in the solar wind". en. In: *Geophysical Research Letters* 2.3, pp. 79–82. ISSN: 00948276. DOI: 10.1029/GL002i003p00079. URL: http://doi.wiley.com/10.1029/GL002i003p00079 (visited on 08/16/2022).

Glauert, Sarah A. and Richard B. Horne (Apr. 2005). "Calculation of pitch angle and energy diffusion coefficients with the PADIE code". en. In: *Journal of Geophysical Research: Space Physics* 110.A4. ISSN: 01480227. DOI: 10.1029/2004JA010851. URL: http://doi.wiley.com/10.1029/2004JA010851 (visited on 08/16/2022).

Graham, D. B. et al. (Dec. 2021). "Kinetic Electrostatic Waves and their Association with Current Structures in the Solar Wind". en. In: *Astronomy & Astrophysics* 656. arXiv:2104.01705 [astro-ph, physics:physics], A23. ISSN: 0004-6361, 1432-0746. DOI: 10.1051/0004-6361/202140943. URL: http://arxiv.org/abs/2104.01705 (visited on 05/28/2023).

Graham, G. A. et al. (Apr. 2017). "The evolution of solar wind strahl with heliospheric distance". en. In: *Journal of Geophysical Research: Space Physics* 122.4, pp. 3858–3874. ISSN: 21699380. DOI: 10.1002/2016JA023656. URL: http://doi.wiley.com/10.1002/2016JA023656 (visited on 08/16/2022).

Graham, G. A. et al. (Mar. 2018). "Investigating the Effect of IMF Path Length on Pitch-angle Scattering of Strahl within 1 au". en. In: *The Astrophysical Journal* 855.1, p. 40. ISSN: 1538-4357. DOI: 10.3847/1538-4357/aaaf1b. URL: https://iopscience.iop.org/article/10.3847/1538-4357/aaaf1b (visited on 02/02/2023).

Gurgiolo, Chris and Melvyn L. Goldstein (Jan. 2017). "Absence of the strahl during times of slow wind". English. In: *Annales Geophysicae* 35.1. Publisher: Copernicus GmbH, pp. 71–85. ISSN: 0992-7689. DOI: 10.5194/angeo-35-71-2017. URL: https://angeo.copernicus.org/articles/35/71/2017/ (visited on 05/30/2023).

Gurnett, Donald A. and Roger R. Anderson (1977). "Plasma wave electric fields in the solar wind: Initial results from Helios 1". en. In: *Journal of Geophysical Research (1896-1977)* 82.4. _eprint: https://onlinelibrary.wiley.com/doi/pdf/10.1029/JA082i004p00632, pp. 632–650. ISSN: 2156-2202. DOI: 10.1029/JA082i004p00632. URL: https://onlinelibrary.wiley.com/doi/abs/10.1029/JA082i004p00632 (visited on 05/28/2023).

Gómez-Herrero, R. et al. (Dec. 2021). "First near-relativistic solar electron events observed by EPD onboard Solar Orbiter". en. In: *Astronomy & Astrophysics* 656, p. L3. ISSN: 0004-6361, 1432-0746. DOI: 10.1051/0004-6361/202039883. URL: https://www.aanda.org/10.1051/0004-6361/202039883 (visited on 02/16/2023).

Halekas, J. S. et al. (Feb. 2020). "Electrons in the Young Solar Wind: First Results from the *Parker Solar Probe*". en. In: *The Astrophysical Journal Supplement Series* 246.2, p. 22. ISSN: 1538-4365. DOI: 10.3847/1538-4365/ab4cec. URL: https://iopscience.iop.org/article/10.3847/1538-4365/ab4cec (visited on 04/28/2021).

Halekas, J. S. et al. (June 2021a). "Electron heat flux in the near-Sun environment". en. In: *Astronomy & Astrophysics* 650. arXiv:2010.10302 [astro-ph, physics:physics], A15. ISSN: 0004-6361, 1432-0746. DOI: 10.1051/0004-6361/202039256. URL: http://arxiv.org/abs/2010.10302 (visited on 08/16/2022).

Halekas, J. S. et al. (July 2021b). "The Sunward Electron Deficit: A Telltale Sign of the Sun's Electric Potential". en. In: *The Astrophysical Journal* 916.1, p. 16. ISSN: 0004-637X, 1538-4357. DOI: 10.3847/1538-4357/ac096e. URL: https://iopscience.iop.org/article/10.3847/1538-4357/ac096e (visited on 05/24/2023).

Halekas, J. S. et al. (Sept. 2022). "The Radial Evolution of the Solar Wind as Organized by Electron Distribution Parameters". en. In: *The Astrophysical Journal* 936.1, p. 53. ISSN:

0004-637X, 1538-4357. DOI: 10.3847/1538-4357/ac85b8. URL: https://iopscience.iop.org/article/10.3847/1538-4357/ac85b8 (visited on 02/24/2023).

Hammond, C. M. et al. (Dec. 1996). "Variation of electron-strahl width in the high-speed solar wind: ULYSSES observations." en. In: *Astronomy and Astrophysics* 316, pp. 350–354. ISSN: 0004-6361. URL: https://ui.adsabs.harvard.edu/abs/1996A&A...316..350H/abstract (visited on 01/20/2023).

Horbury, T. S. et al. (Oct. 2020). "The Solar Orbiter magnetometer". en. In: *Astronomy & Astrophysics* 642, A9. ISSN: 0004-6361, 1432-0746. DOI: 10.1051/0004-6361/201937257. URL: https://www.aanda.org/10.1051/0004-6361/201937257 (visited on 02/14/2023).

Horne, R. B. (2003). "Resonant diffusion of radiation belt electrons by whistler-mode chorus". en. In: *Geophysical Research Letters* 30.9, p. 1493. ISSN: 0094-8276. DOI: 10.1029/2003GL016963. URL: http://doi.wiley.com/10.1029/2003GL016963 (visited on 08/17/2022).

Howard, R. A. et al. (Oct. 2020). "The Solar Orbiter Heliospheric Imager (SoloHI)". en. In: *Astronomy & Astrophysics* 642, A13. ISSN: 0004-6361, 1432-0746. DOI: 10.1051/0004-6361/201935202. URL: https://www.aanda.org/10.1051/0004-6361/201935202 (visited on 02/14/2023).

Jagarlamudi, V. K. et al. (June 2021). "Whistler wave occurrence and the interaction with strahl electrons during the first encounter of Parker Solar Probe". en. In: *Astronomy & Astrophysics* 650, A9. ISSN: 0004-6361, 1432-0746. DOI: 10.1051/0004-6361/202039808. URL: https://www.aanda.org/10.1051/0004-6361/202039808 (visited on 05/26/2022).

Jagarlamudi, Vamsee Krishna et al. (July 2020). "Whistler Waves and Electron Properties in the Inner Heliosphere: Helios Observations". en. In: *The Astrophysical Journal* 897.2. arXiv: 2008.02334, p. 118. ISSN: 1538-4357. DOI: 10.3847/1538-4357/ab94a1. URL: http://arxiv.org/abs/2008.02334 (visited on 05/26/2022).

Jannet, G. et al. (Feb. 2021). "Measurement of Magnetic Field Fluctuations in the Parker Solar Probe and Solar Orbiter Missions". en. In: *Journal of Geophysical Research: Space Physics* 126.2. ISSN: 2169-9380, 2169-9402. DOI: 10.1029/2020JA028543. URL: https://onlinelibrary.wiley.com/doi/10.1029/2020JA028543 (visited on 08/17/2022).

Jeong, Seong-Yeop et al. (Oct. 2020). "A Quasi-linear Diffusion Model for Resonant Wave–Particle Instability in Homogeneous Plasma". en. In: *The Astrophysical Journal* 902.2, p. 128. ISSN: 1538-4357. DOI: 10.3847/1538-4357/abb099. URL: https://iopscience.iop.org/article/10.3847/1538-4357/abb099 (visited on 09/22/2023).

Jeong, Seong-Yeop et al. (Feb. 2022). "The Stability of the Electron Strahl against the Oblique Fast-magnetosonic/Whistler Instability in the Inner Heliosphere". en. In: *The Astrophysical Journal Letters* 926.2, p. L26. ISSN: 2041-8205, 2041-8213. DOI: 10.3847/2041-8213/ac4dff. URL: https://iopscience.iop.org/article/10.3847/2041-8213/ac4dff (visited on 08/13/2023).

Kajdič, P. et al. (Dec. 2016). "Suprathermal electron Strahl widths in the presence of narrowband whistler waves in the solar wind". en. In: *The Astrophysical Journal* 833.2, p. 172. ISSN: 1538-4357. DOI: 10.3847/1538-4357/833/2/172. URL: https://iopscience.iop.org/article/10.3847/1538-4357/833/2/172 (visited on 08/16/2022).

Karbashewski, Scott et al. (Apr. 2023). "Whistler Wave Observations by Parker Solar Probe During Encounter 1: Counter-propagating Whistlers Collocated with Magnetic Field Inhomogeneities and their Application to Electric Field Measurement Calibration". In: *The Astrophysical Journal* 947, p. 73. DOI: 10.3847/1538-4357/acc527.

Karpman, V I, J N Istomin, and D R Shklyar (May 1975). "Effects of Nonlinear Interaction of Monochromatic Waves with Resonant Particles in the Inhomogeneous Plasma". In: *Physica Scripta* 11.5, pp. 278–284. ISSN: 0031-8949, 1402-4896. DOI: 10.1088/0031-8949/11/5/008. URL: https://iopscience.iop.org/article/10.1088/0031-8949/11/5/008 (visited on 05/19/2023).

Kasper, J. C. et al. (Dec. 2019). "Alfvénic velocity spikes and rotational flows in the near-Sun solar wind". en. In: *Nature* 576.7786, pp. 228–231. ISSN: 0028-0836, 1476-4687. DOI: 10.1038/s41586-019-1813-z. URL: http://www.nature.com/articles/s41586-019-1813-z (visited on 08/19/2022).

Kasper, Justin C. et al. (Dec. 2016). "Solar Wind Electrons Alphas and Protons (SWEAP) Investigation: Design of the Solar Wind and Coronal Plasma Instrument Suite for Solar Probe Plus". en. In: *Space Science Reviews* 204.1, pp. 131–186. ISSN: 1572-9672. DOI: 10.1007/s11214-015-0206-3. URL: https://doi.org/10.1007/s11214-015-0206-3 (visited on 01/05/2023).

Kellogg, Paul J. et al. (June 1992). "Low frequency magnetic signals associated with Langmuir waves". en. In: *Geophysical Research Letters* 19.12, pp. 1299–1302. ISSN: 00948276. DOI: 10.1029/92GL01033. URL: http://doi.wiley.com/10.1029/92GL01033 (visited on 08/17/2022).

Kennel, C. F. and F. Engelmann (Dec. 1966). "Velocity Space Diffusion from Weak Plasma Turbulence in a Magnetic Field". en. In: *The Physics of Fluids* 9.12. Publisher: American Institute of PhysicsAIP, p. 2377. ISSN: 0031-9171. DOI: 10.1063/1.1761629. URL: https://aip.scitation.org/doi/abs/10.1063/1.1761629 (visited on 08/17/2022).

Kennel, C. F. and H. E. Petschek (1966). "Limit on stably trapped particle fluxes". en. In: *Journal of Geophysical Research (1896-1977)* 71.1, pp. 1–28. ISSN: 2156-2202. DOI: 10.1029/JZ071i001p00001. URL: https://onlinelibrary.wiley.com/doi/abs/10.1029/JZ071i001p00001 (visited on 11/15/2022).

Kennel, C. F. and H. V. Wong (Feb. 1967). "Resonant particle instabilities in a uniform magnetic field". en. In: *Journal of Plasma Physics* 1.1, pp. 75–80. ISSN: 0022-3778, 1469-7807. DOI: 10.1017/S002237780000310X. URL: https://www.cambridge.org/core/product/identifier/S002237780000310X/type/journal_article (visited on 08/16/2022).

Khotyaintsev, Yu. V. et al. (Dec. 2021). "Density fluctuations associated with turbulence and waves: First observations by Solar Orbiter". en. In: *Astronomy & Astrophysics* 656, A19. ISSN: 0004-6361, 1432-0746. DOI: 10.1051/0004-6361/202140936. URL: https://www.aanda.org/10.1051/0004-6361/202140936 (visited on 01/02/2023).

Komarov, S. et al. (June 2018). "Self-inhibiting thermal conduction in a high-, whistler-unstable plasma". en. In: *Journal of Plasma Physics* 84.3, p. 905840305. ISSN: 0022-3778, 1469-7807. DOI: 10.1017/S0022377818000399. URL: https://www.cambridge.org/core/product/identifier/S0022377818000399/type/journal_article (visited on 04/30/2023).

Kontar, E. P. et al. (Nov. 2017). "Imaging spectroscopy of solar radio burst fine structures". In: *Nature Communications* 8. ADS Bibcode: 2017NatCo...8.1515K, p. 1515. ISSN: 2041-1723. DOI: 10.1038/s41467-017-01307-8. URL: https://ui.adsabs.harvard.edu/abs/2017NatCo...8.1515K (visited on 05/06/2023).

Krafft, C. and P. Savoini (Jan. 2022). "Fundamental Electromagnetic Emissions by a Weak Electron Beam in Solar Wind Plasmas with Density Fluctuations". en. In: *The Astrophysical Journal Letters* 924.2, p. L24. ISSN: 2041-8205, 2041-8213. DOI: 10.3847/2041-8213/ac46a7. URL: https://iopscience.iop.org/article/10.3847/2041-8213/ac46a7 (visited on 02/14/2023).

Krasnoselskikh, V. et al. (Apr. 2020). "Localized Magnetic-field Structures and Their Boundaries in the Near-Sun Solar Wind from Parker Solar Probe Measurements". en. In: *The Astrophysical Journal* 893.2, p. 93. ISSN: 1538-4357. DOI: 10.3847/1538-4357/ab7f2d. URL: https://iopscience.iop.org/article/10.3847/1538-4357/ab7f2d (visited on 10/27/2022).

Kretzschmar, M. et al. (Dec. 2021). "Whistler waves observed by Solar Orbiter/RPW between 0.5 AU and 1 AU". en. In: *Astronomy & Astrophysics* 656, A24. ISSN: 0004-6361, 1432-0746. DOI: 10.1051/0004-6361/202140945. URL: https://www.aanda.org/10.1051/0004-6361/202140945 (visited on 05/31/2022).

Krucker, Säm et al. (Oct. 2020). "The Spectrometer/Telescope for Imaging X-rays (STIX)". en. In: *Astronomy & Astrophysics* 642, A15. ISSN: 0004-6361, 1432-0746. DOI: 10.1051/0004-6361/201937362. URL: https://www.aanda.org/10.1051/0004-6361/201937362 (visited on 02/14/2023).

Kuzichev, Ilya V. et al. (Sept. 2019). "Nonlinear evolution of the whistler heat flux instability". en. In: *The Astrophysical Journal* 882.2. arXiv:1907.04878 [physics], p. 81. ISSN: 1538-4357. DOI: 10.3847/1538-4357/ab3290. URL: http://arxiv.org/abs/1907.04878 (visited on 08/17/2022).

Lacombe, C. et al. (Oct. 2014). "Whistler mode waves and the electron heat flux in the solar wind: Cluster observations". en. In: *The Astrophysical Journal* 796.1, p. 5. ISSN: 1538-4357. DOI: 10.1088/0004-637X/796/1/5. URL: https://iopscience.iop.org/article/10.1088/0004-637X/796/1/5 (visited on 05/31/2022).

Landau and Lifshitz (1981). *10 Physical Kinetics Landau Lifshitz*. eng. URL: http://archive.org/details/10PhysicalKineticsLandauLifshitz (visited on 08/01/2023).

Landi, S., L. Matteini, and F. Pantellini (July 2014). "Electron heat flux in the solar wind: are we observing the collisional limit in the 1 AU data?" en. In: *The Astrophysical Journal Letters* 790.1. Publisher: The American Astronomical Society, p. L12. ISSN: 2041-8205. DOI: 10.1088/2041-8205/790/1/L12. URL: https://dx.doi.org/10.1088/2041-8205/790/1/L12 (visited on 08/17/2023).

Lazar, M., S. Poedts, and H. Fichtner (Oct. 2015). "Destabilizing effects of the suprathermal populations in the solar wind". en. In: *Astronomy & Astrophysics* 582. Publisher: EDP Sciences, A124. ISSN: 0004-6361, 1432-0746. DOI: 10.1051/0004-6361/201526509. URL: https://www.aanda.org/articles/aa/abs/2015/10/aa26509-15/aa26509-15.html (visited on 09/20/2023).

Lazar, M., S. Poedts, and M. J. Michno (June 2013). "Electromagnetic electron whistler-cyclotron instability in bi-Kappa distributed plasmas". en. In: *Astronomy & Astrophysics* 554, A64. ISSN: 0004-6361, 1432-0746. DOI: 10.1051/0004-6361/201220550. URL: http://www.aanda.org/10.1051/0004-6361/201220550 (visited on 07/10/2023).

Lazar, M., S. Poedts, and R. Schlickeiser (Jan. 2011). "Instability of the parallel electromagnetic modes in Kappa distributed plasmas - I. Electron whistler-cyclotron modes: Stability of Kappa distributed plasmas - I". en. In: *Monthly Notices of the Royal Astronomical Society* 410.1, pp. 663–670. ISSN: 00358711. DOI: 10.1111/j.1365-2966.2010.17472.x. URL: https://academic.oup.com/mnras/article-lookup/doi/10.1111/j.1365-2966.2010.17472.x (visited on 07/10/2023).

— (Dec. 2014). "The interplay of Kappa and core populations in the solar wind: Electromagnetic electron cyclotron instability". en. In: *Journal of Geophysical Research: Space Physics* 119.12, pp. 9395–9406. ISSN: 2169-9380, 2169-9402. DOI: 10.1002/2014JA020668. URL: https://onlinelibrary.wiley.com/doi/abs/10.1002/2014JA020668 (visited on 07/10/2023).

Lazar, M. et al. (Jan. 2015). "Towards realistic parametrization of the kinetic anisotropy and the resulting instabilities in space plasmas. Electromagnetic electron–cyclotron instability in the solar wind". en. In: *Monthly Notices of the Royal Astronomical Society* 446.3, pp. 3022–3033. ISSN: 1365-2966, 0035-8711. DOI: 10.1093/mnras/stu2312. URL: http://academic.oup.com/mnras/article/446/3/3022/2893012/Towards-realistic-parametrization-of-the-kinetic (visited on 07/10/2023).

Lazar, M. et al. (Jan. 2018). "Electromagnetic Electron Cyclotron Instability in the Solar Wind". en. In: *Journal of Geophysical Research: Space Physics* 123.1, pp. 6–19. ISSN: 2169-9380, 2169-9402. DOI: 10.1002/2017JA024759. URL: https://onlinelibrary.wiley.com/doi/10.1002/2017JA024759 (visited on 07/10/2023).

Lazar, M. et al. (Oct. 2019). "Whistler instability stimulated by the suprathermal electrons present in space plasmas". en. In: *Astrophysics and Space Science* 364.10, p. 171. ISSN: 0004-640X, 1572-946X. DOI: 10.1007/s10509-019-3661-6. URL: http://arxiv.org/abs/1910.01506 (visited on 07/10/2023).

Lazar, M. et al. (Oct. 2020). "Characteristics of solar wind suprathermal halo electrons". en. In: *Astronomy & Astrophysics* 642, A130. ISSN: 0004-6361, 1432-0746. DOI: 10.1051/0004-6361/202038830. URL: https://www.aanda.org/10.1051/0004-6361/202038830 (visited on 07/10/2023).

Lazar, M. et al. (Feb. 2023). "The aperiodic firehose instability of counter-beaming electrons in space plasmas". en. In: *Astronomy & Astrophysics* 670, A85. ISSN: 0004-6361, 1432-0746. DOI: 10.1051/0004-6361/202245163. URL: http://arxiv.org/abs/2212.07304 (visited on 08/17/2023).

Lazar, Marian et al. (Jan. 2022). "Temperature Anisotropy Instabilities Stimulated by the Solar Wind Suprathermal Populations". en. In: *Frontiers in Astronomy and Space Sciences* 8, p. 777559. ISSN: 2296-987X. DOI: 10.3389/fspas.2021.777559. URL: https://www.frontiersin.org/articles/10.3389/fspas.2021.777559/full (visited on 08/17/2023).

Lemaire, J. and M. Scherer (1970). "Model of the polar ion-exosphere". en. In: *Planetary and Space Science* 18.1, pp. 103–120. ISSN: 0032-0633. DOI: 10.1016/0032-0633(70)90070-X. URL: https://www.sciencedirect.com/science/article/pii/003206337090070X (visited on 02/24/2023).

— (1971). "Kinetic models of the solar wind". en. In: *Journal of Geophysical Research (1896-1977)* 76.31. _eprint: https://onlinelibrary.wiley.com/doi/pdf/10.1029/JA076i031p07479, pp. 7479–7490. ISSN: 2156-2202. DOI: 10.1029/JA076i031p07479. URL: https://onlinelibrary.wiley.com/doi/abs/10.1029/JA076i031p07479 (visited on 02/24/2023).

Lemaire, Joseph and Viviane Pierrard (June 2001). "Kinetic Models of Solar and Polar Winds". en. In: *Astrophysics and Space Science* 277.1, pp. 169–180. ISSN: 1572-946X. DOI: 10.1023/A:1012245909542. URL: https://doi.org/10.1023/A:1012245909542 (visited on 09/21/2023).

Lie-Svendsen, Øystein, Viggo H. Hansteen, and Egil Leer (1997). "Kinetic electrons in high-speed solar wind streams: Formation of high-energy tails". en. In: *Journal of Geophysical Research: Space Physics* 102.A3, pp. 4701–4718. ISSN: 2156-2202. DOI: 10.1029/96JA03632. URL: https://onlinelibrary.wiley.com/doi/abs/10.1029/96JA03632 (visited on 09/19/2023).

Livi, Roberto et al. (Oct. 2022). "The Solar Probe ANalyzer—Ions on the Parker Solar Probe". en. In: *The Astrophysical Journal* 938.2, p. 138. ISSN: 0004-637X, 1538-4357. DOI: 10.3847/1538-4357/ac93f5. URL: https://iopscience.iop.org/article/10.3847/1538-4357/ac93f5 (visited on 05/15/2023).

Lyons, L. R. and D. J. Williams (1984). *Quantitative Aspects of Magnetospheric Physics*. en. Dordrecht: Springer Netherlands. ISBN: 978-90-481-8391-3 978-94-017-2819-5. DOI: 10.1007/978-94-017-2819-5. URL: http://link.springer.com/10.1007/978-94-017-2819-5 (visited on 04/18/2023).

Lyons, Lawrence R. (Oct. 1973). "Comments on pitch angle diffusion in the radiation belts". en. In: *Journal of Geophysical Research* 78.28, pp. 6793–6797. ISSN: 01480227. DOI: 10.1029/JA078i028p06793. URL: http://doi.wiley.com/10.1029/JA078i028p06793 (visited on 08/17/2022).

— (Aug. 1974a). "General relations for resonant particle diffusion in pitch angle and energy". en. In: *Journal of Plasma Physics* 12.1, pp. 45–49. ISSN: 0022-3778, 1469-7807. DOI: 10.1017/S0022377800024910. URL: https://www.cambridge.org/core/product/identifier/S0022377800024910/type/journal_article (visited on 08/17/2022).

— (Dec. 1974b). "Pitch angle and energy diffusion coefficients from resonant interactions with ion–cyclotron and whistler waves". en. In: *Journal of Plasma Physics* 12.3, pp. 417–432. ISSN: 0022-3778, 1469-7807. DOI: 10.1017/S002237780002537X. URL: https://www.cambridge.org/core/product/identifier/S002237780002537X/type/journal_article (visited on 08/17/2022).

Lyons, Lawrence R., R. M. Thorne, and C. F. Kennel (Dec. 1971). "Electron pitch-angle diffusion driven by oblique whistler-mode turbulence". en. In: *Journal of Plasma Physics* 6.3, pp. 589–606. ISSN: 0022-3778, 1469-7807. DOI: 10.1017/S0022377800006310. URL: https://www.cambridge.org/core/product/identifier/S0022377800006310/type/journal_article (visited on 08/17/2022).

Lyons, Lawrence R., R. M. Thorne, and C. F. Kennel (July 1972). "Pitch-angle diffusion of radiation belt electrons within the plasmasphere". en. In: *Journal of Geophysical Research* 77.19, pp. 3455–3474. ISSN: 01480227. DOI: 10.1029/JA077i019p03455. URL: http://doi.wiley.com/10.1029/JA077i019p03455 (visited on 08/17/2022).

López, R. A. et al. (Sept. 2019). "Particle-in-cell Simulations of the Whistler Heat-flux Instability in Solar Wind Conditions". en. In: *The Astrophysical Journal* 882.1, p. L8. ISSN: 2041-8213. DOI: 10.3847/2041-8213/ab398b. URL: https://iopscience.iop.org/article/10.3847/2041-8213/ab398b (visited on 08/17/2022).

López, R. A. et al. (Apr. 2020a). "A firehose-like aperiodic instability of the counter-beaming electron plasmas". en. In: *Plasma Physics and Controlled Fusion*. arXiv:2003.08245 [physics]. ISSN: 0741-3335, 1361-6587. DOI: 10.1088/1361-6587/ab8bb5. URL: http://arxiv.org/abs/2003.08245 (visited on 08/17/2023).

— (Sept. 2020b). "Alternative high plasma beta regimes of electron heat-flux instabilities in the solar wind". en. In: *The Astrophysical Journal* 900.2. arXiv:2006.04263 [astro-ph, physics:physics], p. L25. ISSN: 2041-8213. DOI: 10.3847/2041-8213/abaf56. URL: http://arxiv.org/abs/2006.04263 (visited on 08/17/2022).

Ma, Chun-yu and Danny Summers (Apr. 1999). "Correction to "Formation of power-law energy spectra in space plasmas by stochastic acceleration due to whistler-mode waves"". en. In: *Geophysical Research Letters* 26.8, pp. 1121–1124. ISSN: 00948276. DOI: 10.1029/1999GL900152. URL: http://doi.wiley.com/10.1029/1999GL900152 (visited on 09/22/2023).

Macneil, Allan R. et al. (Feb. 2020). "Radial Evolution of Sunward Strahl Electrons in the Inner Heliosphere". en. In: *Solar Physics* 295.2, p. 16. ISSN: 0038-0938, 1573-093X. DOI: 10.1007/s11207-019-1579-3. URL: http://link.springer.com/10.1007/s11207-019-1579-3 (visited on 11/17/2022).

Maksimovic, M., V. Pierrard, and J. F. Lemaire (Aug. 1997). "A kinetic model of the solar wind with Kappa distribution functions in the corona." In: *Astronomy and Astrophysics* 324. ADS Bibcode: 1997A&A...324..725M, pp. 725–734. ISSN: 0004-6361. URL: https://ui.adsabs.harvard.edu/abs/1997A&A...324..725M (visited on 05/06/2023).

Maksimovic, M. et al. (1995). "Solar wind electron parameters from quasi-thermal noise spectroscopy and comparison with other measurements on Ulysses". en. In: *Journal of Geophysical Research: Space Physics* 100.A10, pp. 19881–19891. ISSN: 2156-2202. DOI: 10.1029/95JA01550. URL: https://onlinelibrary.wiley.com/doi/abs/10.1029/95JA01550 (visited on 05/06/2023).

Maksimovic, M. et al. (1998). "Solar wind density intercomparisons on the WIND spacecraft using WAVES and SWE experiments". en. In: *Geophysical Research Letters* 25.8, pp. 1265–1268. ISSN: 1944-8007. DOI: 10.1029/98GL00843. URL: https://onlinelibrary.wiley.com/doi/abs/10.1029/98GL00843 (visited on 05/06/2023).

Maksimovic, M. et al. (Sept. 2005a). "Radial evolution of the electron distribution functions in the fast solar wind between 0.3 and 1.5 AU". en. In: *Journal of Geophysical Research: Space Physics* 110.A9. ISSN: 01480227. DOI: 10.1029/2005JA011119. URL: http://doi.wiley.com/10.1029/2005JA011119 (visited on 08/16/2022).

Maksimovic, M. et al. (Jan. 2005b). "Solar wind electron temperature and density measurements on the Solar Orbiter with thermal noise spectroscopy". en. In: *Advances in Space Research*. Solar Encounter, Solar-B and STEREO 36.8, pp. 1471–1473. ISSN: 0273-1177. DOI: 10.1016/j.asr.2005.01.088. URL: https://www.sciencedirect.com/science/article/pii/S0273117705000906 (visited on 05/06/2023).

Maksimovic, M. et al. (Oct. 2020). "The Solar Orbiter Radio and Plasma Waves (RPW) instrument". en. In: *Astronomy & Astrophysics* 642, A12. ISSN: 0004-6361, 1432-0746. DOI: 10.1051/0004-6361/201936214. URL: https://www.aanda.org/10.1051/0004-6361/201936214 (visited on 04/28/2021).

Maksimovic, M. et al. (Dec. 2021). "First observations and performance of the RPW instrument on board the Solar Orbiter mission". en. In: *Astronomy & Astrophysics* 656, A41. ISSN: 0004-6361, 1432-0746. DOI: 10.1051/0004-6361/202141271. URL: https://www.aanda.org/10.1051/0004-6361/202141271 (visited on 02/16/2023).

Maksimovic, Milan, S. Peter Gary, and Ruth M. Skoug (Aug. 2000). "Solar wind electron suprathermal strength and temperature gradients: Ulysses observations". en. In: *Journal of Geophysical Research: Space Physics* 105.A8, pp. 18337–18350. ISSN: 0148-0227. DOI: 10.1029/2000JA900039. URL: https://agupubs.onlinelibrary.wiley.com/doi/10.1029/2000JA900039 (visited on 09/20/2023).

Malaspina, David M. et al. (June 2016). "The Digital Fields Board for the FIELDS instrument suite on the Solar Probe Plus mission: Analog and digital signal processing". en. In: *Journal of Geophysical Research: Space Physics* 121.6, pp. 5088–5096. ISSN: 2169-9380, 2169-9402. DOI: 10.1002/2016JA022344. URL: https://onlinelibrary.wiley.com/doi/10.1002/2016JA022344 (visited on 08/17/2022).

Marsch, Eckart (2006). "Kinetic Physics of the Solar Corona and Solar Wind". en. In: *Living Reviews in Solar Physics* 3. ISSN: 1614-4961. DOI: 10.12942/lrsp-2006-1. URL: http://link.springer.com/10.12942/lrsp-2006-1 (visited on 01/17/2023).

McComas, D. J. et al. (Sept. 2008). "Weaker solar wind from the polar coronal holes and the whole Sun". en. In: *Geophysical Research Letters* 35.18, p. L18103. ISSN: 0094-8276. DOI: 10.1029/2008GL034896. URL: http://doi.wiley.com/10.1029/2008GL034896 (visited on 01/17/2023).

McComas, D. J. et al. (Nov. 2013). "WEAKEST SOLAR WIND OF THE SPACE AGE AND THE CURRENT "MINI" SOLAR MAXIMUM". en. In: *The Astrophysical Journal* 779.1, p. 2. ISSN: 0004-637X, 1538-4357. DOI: 10.1088/0004-637X/779/1/2. URL: https://iopscience.iop.org/article/10.1088/0004-637X/779/1/2 (visited on 03/27/2023).

McComas, D. J. et al. (Dec. 2016). "Integrated Science Investigation of the Sun (ISIS): Design of the Energetic Particle Investigation". en. In: *Space Science Reviews* 204.1, pp. 187–256. ISSN: 1572-9672. DOI: 10.1007/s11214-014-0059-1. URL: https://doi.org/10.1007/s11214-014-0059-1 (visited on 03/15/2023).

Means, Joseph D. (1972). "Use of the three-dimensional covariance matrix in analyzing the polarization properties of plane waves". en. In: *Journal of Geophysical Research (1896-1977)* 77.28. _eprint: https://onlinelibrary.wiley.com/doi/pdf/10.1029/JA077i028p05551, pp. 5551–

5559. ISSN: 2156-2202. DOI: 10.1029/JA077i028p05551. URL: https://onlinelibrary.wiley.com/doi/abs/10.1029/JA077i028p05551 (visited on 11/15/2022).

Melrose, D. B. (July 1982). "Fundamental Emission for Type-Iii Bursts in the Interplanetary Medium - the Role of Ion-Sound Turbulence". In: *Solar Physics* 79. ADS Bibcode: 1982SoPh...79..173M, pp. 173–185. ISSN: 0038-0938. DOI: 10.1007/BF00146981. URL: https://ui.adsabs.harvard.edu/abs/1982SoPh...79..173M (visited on 02/14/2023).

Mendis, D. A. (2006). "The Role of Comet Tails in the Discovery of the Solar Wind and Its Spatial and Temporal Variations". en. In: *Recurrent Magnetic Storms: Corotating Solar Wind Streams*. _eprint: https://onlinelibrary.wiley.com/doi/pdf/10.1029/167GM05. American Geophysical Union (AGU), pp. 31–44. ISBN: 978-1-118-66645-6. DOI: 10.1029/167GM05. URL: https://onlinelibrary.wiley.com/doi/abs/10.1029/167GM05 (visited on 03/27/2023).

Meyer-Vernet, N., K. Issautier, and M. Moncuquet (Aug. 2017). "Quasi-thermal noise spectroscopy: The art and the practice". en. In: *Journal of Geophysical Research: Space Physics* 122.8, pp. 7925–7945. ISSN: 21699380. DOI: 10.1002/2017JA024449. URL: http://doi.wiley.com/10.1002/2017JA024449 (visited on 05/06/2023).

Meyer-Vernet, Nicole (2007). *Basics of the solar wind*. en. Cambridge atmospheric and space science series. OCLC: ocm71808112. Cambridge ; New York: Cambridge University Press. ISBN: 978-0-521-81420-1.

Micera, A. et al. (Nov. 2020). "Particle-In-Cell simulation of whistler heat flux instabilities in the solar wind: heat flux regulation and electron halo formation". en. In: *The Astrophysical Journal Letters* 903.1. arXiv:2010.10832 [astro-ph], p. L23. ISSN: 2041-8205, 2041-8213. DOI: 10.3847/2041-8213/abc0e8. URL: http://arxiv.org/abs/2010.10832 (visited on 08/17/2022).

Micera, A. et al. (Sept. 2021). "On the role of solar wind expansion as a source of whistler waves: scattering of suprathermal electrons and heat flux regulation in the inner heliosphere". en. In: *The Astrophysical Journal* 919.1. arXiv:2106.15975 [astro-ph, physics:physics], p. 42. ISSN: 0004-637X, 1538-4357. DOI: 10.3847/1538-4357/ac1067. URL: http://arxiv.org/abs/2106.15975 (visited on 08/17/2022).

Mozer, F. S., I. Y. Vasko, and J. L. Verniero (Sept. 2021). "Triggered Ion-acoustic Waves in the Solar Wind". en. In: *The Astrophysical Journal Letters* 919.1, p. L2. ISSN: 2041-8205, 2041-8213. DOI: 10.3847/2041-8213/ac2259. URL: https://iopscience.iop.org/article/10.3847/2041-8213/ac2259 (visited on 05/28/2023).

Mozer, F. S. et al. (Oct. 2020). "Large-amplitude, Wideband, Doppler-shifted, Ion Acoustic Waves Observed on the Parker Solar Probe". en. In: *The Astrophysical Journal* 901.2, p. 107. ISSN: 0004-637X, 1538-4357. DOI: 10.3847/1538-4357/abafb4. URL: https://iopscience.iop.org/article/10.3847/1538-4357/abafb4 (visited on 05/28/2023).

Mozer, F. S. et al. (Apr. 2021). "Nonlinear Ion-acoustic Waves, Ion Holes, and Electron Holes in the Near-Sun Solar Wind". en. In: *The Astrophysical Journal* 911.2, p. 89. ISSN: 0004-637X, 1538-4357. DOI: 10.3847/1538-4357/abed52. URL: https://iopscience.iop.org/article/10.3847/1538-4357/abed52 (visited on 05/28/2023).

Mueller, D. et al. (July 2013). "Solar Orbiter: Exploring the Sun-heliosphere connection". en. In: *Solar Physics* 285.1-2. arXiv:1207.4579 [astro-ph, physics:physics], pp. 25–70. ISSN:

0038-0938, 1573-093X. DOI: 10.1007/s11207-012-0085-7. URL: http://arxiv.org/abs/1207.4579 (visited on 02/14/2023).

Musset, S. et al. (Dec. 2021). "Simulations of radio-wave anisotropic scattering to interpret type III radio bursts measurements by Solar Orbiter, Parker Solar Probe, STEREO and Wind". en. In: *Astronomy & Astrophysics* 656. arXiv:2109.13713 [astro-ph, physics:physics], A34. ISSN: 0004-6361, 1432-0746. DOI: 10.1051/0004-6361/202140998. URL: http://arxiv.org/abs/2109.13713 (visited on 02/16/2023).

Müller, D. et al. (Oct. 2020). "The Solar Orbiter mission: Science overview". en. In: *Astronomy & Astrophysics* 642, A1. ISSN: 0004-6361, 1432-0746. DOI: 10.1051/0004-6361/202038467. URL: https://www.aanda.org/10.1051/0004-6361/202038467 (visited on 02/14/2023).

Neubauer, F. M., G. Musmann, and G. Dehmel (1977). "Fast magnetic fluctuations in the solar wind: Helios 1". en. In: *Journal of Geophysical Research (1896-1977)* 82.22, pp. 3201–3212. ISSN: 2156-2202. DOI: 10.1029/JA082i022p03201. URL: https://onlinelibrary.wiley.com/doi/abs/10.1029/JA082i022p03201 (visited on 04/01/2023).

Owen, C. J. et al. (Oct. 2020). "The Solar Orbiter Solar Wind Analyser (SWA) suite". en. In: *Astronomy & Astrophysics* 642, A16. ISSN: 0004-6361, 1432-0746. DOI: 10.1051/0004-6361/201937259. URL: https://www.aanda.org/10.1051/0004-6361/201937259 (visited on 11/11/2022).

Pagel, Christina et al. (2007). "Scattering of suprathermal electrons in the solar wind: ACE observations". en. In: *Journal of Geophysical Research: Space Physics* 112.A4. ISSN: 2156-2202. DOI: 10.1029/2006JA011967. URL: https://onlinelibrary.wiley.com/doi/abs/10.1029/2006JA011967 (visited on 02/24/2023).

Pannekoek, A (July 1922). "Ionization in stellar atmospheres (Errata: 2". In: *Bulletin Astronomical Institute of the Netherlands*.

Parker, E. N. (Nov. 1958). "Dynamics of the Interplanetary Gas and Magnetic Fields." In: *The Astrophysical Journal* 128. ADS Bibcode: 1958ApJ...128..664P, p. 664. ISSN: 0004-637X. DOI: 10.1086/146579. URL: https://ui.adsabs.harvard.edu/abs/1958ApJ...128..664P (visited on 03/27/2023).

— (May 1965). "Dynamical Properties of Stellar Coronas and Stellar Winds, IV. The Separate Existence of Subsonic and Supersonic Solutions." In: *The Astrophysical Journal* 141. ADS Bibcode: 1965ApJ...141.1463P, p. 1463. ISSN: 0004-637X. DOI: 10.1086/148235. URL: https://ui.adsabs.harvard.edu/abs/1965ApJ...141.1463P (visited on 02/24/2023).

Paschmann, Götz and Patrick W. Daly (Jan. 1998). "Analysis Methods for Multi-Spacecraft Data. ISSI Scientific Reports Series SR-001, ESA/ISSI, Vol. 1. ISBN 1608-280X, 1998". In: *ISSI Scientific Reports Series* 1. ADS Bibcode: 1998ISSIR...1.....P. URL: https://ui.adsabs.harvard.edu/abs/1998ISSIR...1.....P (visited on 03/20/2023).

Pavan, J. et al. (May 2013). "Solar wind Strahl broadening by self generated plasma waves". en. In: *The Astrophysical Journal* 769.2, p. L30. ISSN: 2041-8205, 2041-8213. DOI: 10.1088/2041-8205/769/2/L30. URL: https://iopscience.iop.org/article/10.1088/2041-8205/769/2/L30 (visited on 08/17/2023).

Phillips, J. L. et al. (1989). "Anisotropic thermal electron distributions in the solar wind". en. In: *Journal of Geophysical Research: Space Physics* 94.A6, pp. 6563–6579. ISSN: 2156-2202. DOI: 10.1029/JA094iA06p06563. URL: https://onlinelibrary.wiley.com/doi/abs/10.1029/JA094iA06p06563 (visited on 09/21/2023).

Pierrard, V. and M. Lazar (Nov. 2010). "Kappa Distributions: Theory and Applications in Space Plasmas". en. In: *Solar Physics* 267.1, pp. 153–174. ISSN: 0038-0938, 1573-093X. DOI: 10.1007/s11207-010-9640-2. URL: http://link.springer.com/10.1007/s11207-010-9640-2 (visited on 09/20/2023).

Pierrard, V., M. Lazar, and R. Schlickeiser (Apr. 2011). "Evolution of the Electron Distribution Function in the Whistler Wave Turbulence of the Solar Wind". en. In: *Solar Physics* 269.2, pp. 421–438. ISSN: 0038-0938, 1573-093X. DOI: 10.1007/s11207-010-9700-7. URL: http://link.springer.com/10.1007/s11207-010-9700-7 (visited on 08/16/2022).

Pierrard, V. and J. Lemaire (1996). "Lorentzian ion exosphere model". en. In: *Journal of Geophysical Research: Space Physics* 101.A4. _eprint: https://onlinelibrary.wiley.com/doi/pdf/10.1029/95JA0 pp. 7923–7934. ISSN: 2156-2202. DOI: 10.1029/95JA03802. URL: https://onlinelibrary.wiley.com/doi/abs/10.1029/95JA03802 (visited on 02/24/2023).

Pierrard, V., M. Maksimovic, and J. Lemaire (1999). "Electron velocity distribution functions from the solar wind to the corona". en. In: *Journal of Geophysical Research: Space Physics* 104.A8. _eprint: https://onlinelibrary.wiley.com/doi/pdf/10.1029/1999JA900169, pp. 17021–17032. ISSN: 2156-2202. DOI: 10.1029/1999JA900169. URL: https://onlinelibrary.wiley.com/doi/abs/10.1029/1999JA900169 (visited on 02/24/2023).

Pierrard, Viviane (2011). "Solar Wind Electron Transport: Interplanetary Electric Field and Heat Conduction". en. In: *Space Science Reviews* 172.1-4, pp. 315–324. ISSN: 0038-6308, 1572-9672. DOI: 10.1007/s11214-011-9743-6. URL: http://link.springer.com/10.1007/s11214-011-9743-6 (visited on 09/21/2023).

Pierrard, Viviane, Marian Lazar, and Stepan Stverak (June 2022). "Implications of Kappa Suprathermal Halo of the Solar Wind Electrons". en. In: *Frontiers in Astronomy and Space Sciences* 9, p. 892236. ISSN: 2296-987X. DOI: 10.3389/fspas.2022.892236. URL: https://www.frontiersin.org/articles/10.3389/fspas.2022.892236/full (visited on 08/16/2022).

Pierrard, Viviane and Joseph Lemaire (June 1998). "A collisional kinetic model of the polar wind". In: *jgr* 103, pp. 11701–11710. DOI: 10.1029/98JA00628.

Pierrard, Viviane, Milan Maksimovic, and Joseph Lemaire (2001). "Core, Halo and Strahl Electrons in the Solar Wind". en. In: *Physics of Space: Growth Points and Problems*. Ed. by Nicole Meyer-Vernet, Michel Moncuquet, and Filippo Pantellini. Dordrecht: Springer Netherlands, pp. 195–200. ISBN: 978-94-010-3813-3 978-94-010-0904-1. DOI: 10.1007/978-94-010-0904-1_25. URL: http://link.springer.com/10.1007/978-94-010-0904-1_25 (visited on 07/18/2023).

Pilipp, W. G. et al. (Feb. 1987a). "Characteristics of electron velocity distribution functions in the solar wind derived from the helios plasma experiment". In: *Journal of Geophysical Research* 92, pp. 1075–1092. ISSN: 0148-0227. DOI: 10.1029/JA092iA02p01075. URL: https://ui.adsabs.harvard.edu/abs/1987JGR....92.1075P (visited on 11/18/2022).

Pilipp, W. G. et al. (1987b). "Variations of electron distribution functions in the solar wind". en. In: *Journal of Geophysical Research: Space Physics* 92.A2, pp. 1103–1118. ISSN: 2156-2202. DOI: 10.1029/JA092iA02p01103. URL: https://onlinelibrary.wiley.com/doi/abs/10.1029/JA092iA02p01103 (visited on 02/24/2023).

Pistinner, S. L. and D. Eichler (Nov. 1998). "Self-inhibiting heat flux". en. In: *Monthly Notices of the Royal Astronomical Society* 301.1, pp. 49–58. ISSN: 0035-8711, 1365-2966. DOI: 10.1046/j.1365-8711.1998.01770.x. URL: https://academic.oup.com/mnras/article/301/1/49/1058254 (visited on 04/30/2023).

Pulupa, M. and S. D. Bale (Apr. 2008). "Structure on Interplanetary Shock Fronts: Type II Radio Burst Source Regions". en. In: *The Astrophysical Journal* 676.2, p. 1330. ISSN: 0004-637X. DOI: 10.1086/526405. URL: https://dx.doi.org/10.1086/526405 (visited on 08/17/2023).

Píša, D. et al. (Dec. 2021). "First-year ion-acoustic wave observations in the solar wind by the RPW/TDS instrument onboard Solar Orbiter". en. In: *Astronomy & Astrophysics* 656. arXiv:2104.03082 [astro-ph, physics:physics], A14. ISSN: 0004-6361, 1432-0746. DOI: 10.1051/0004-6361/202140928. URL: http://arxiv.org/abs/2104.03082 (visited on 09/08/2023).

Raouafi, N. E. et al. (Jan. 2023). *Parker Solar Probe: Four Years of Discoveries at Solar Cycle Minimum*. arXiv:2301.02727 [astro-ph, physics:physics]. DOI: 10.48550/arXiv.2301.02727. URL: http://arxiv.org/abs/2301.02727 (visited on 01/30/2023).

Roberg-Clark, G. T. et al. (Jan. 2018). "Suppression of electron thermal conduction by whistler turbulence in a sustained thermal gradient". en. In: *Physical Review Letters* 120.3. arXiv:1709.00057 [astro-ph, physics:physics], p. 035101. ISSN: 0031-9007, 1079-7114. DOI: 10.1103/PhysRevLett.120.035101. URL: http://arxiv.org/abs/1709.00057 (visited on 08/17/2022).

Roberg-Clark, G. T. et al. (Dec. 2019). "Scattering of Energetic Electrons by Heat-flux-driven Whistlers in Flares". en. In: *The Astrophysical Journal* 887.2, p. 190. ISSN: 1538-4357. DOI: 10.3847/1538-4357/ab5114. URL: https://iopscience.iop.org/article/10.3847/1538-4357/ab5114 (visited on 08/17/2022).

Rochus, P. et al. (Oct. 2020). "The Solar Orbiter EUI instrument: The Extreme Ultraviolet Imager". en. In: *Astronomy & Astrophysics* 642, A8. ISSN: 0004-6361, 1432-0746. DOI: 10.1051/0004-6361/201936663. URL: https://www.aanda.org/10.1051/0004-6361/201936663 (visited on 02/14/2023).

Rodríguez-Pacheco, J. et al. (Oct. 2020). "The Energetic Particle Detector: Energetic particle instrument suite for the Solar Orbiter mission". en. In: *Astronomy & Astrophysics* 642, A7. ISSN: 0004-6361, 1432-0746. DOI: 10.1051/0004-6361/201935287. URL: https://www.aanda.org/10.1051/0004-6361/201935287 (visited on 02/14/2023).

Rosenbauer, H. et al. (1976). "Preliminary Results of the Helios Plasma Measurements". en. In: *Physics of Solar Planetary Environments: Proceedings of the International Symposium on Solar—Terrestrial Physics, June 7–18,1976 Boulder, Colorado, Volume I*. American Geophysical Union (AGU), pp. 319–331. ISBN: 978-1-118-66904-4. URL: https://onlinelibrary.wiley.com/doi/abs/10.1029/SP007p0319 (visited on 06/01/2023).

Rosenbauer, H. et al. (Jan. 1977). "A survey on initial results of the HELIOS plasma experiment". In: *Journal of Geophysics Zeitschrift Geophysik* 42, pp. 561–580. URL: https://ui.adsabs.harvard.edu/abs/1977JGZG...42..561R (visited on 05/29/2023).

Rosseland, S. (July 1924). "Electrical State of a Star". In: *Monthly Notices of the Royal Astronomical Society* 84.9, pp. 720–729. ISSN: 0035-8711. DOI: 10.1093/mnras/84.9.720. URL: https://doi.org/10.1093/mnras/84.9.720 (visited on 05/29/2023).

Sagdeev, R. Z. and V. D. Shafranov (July 1960). "On the instability of a plasma with an anisotropic distribution of velocities in a magnetic field". Russian. In: *Zhur. Eksptl'. i Teoret. Fiz.* Vol: 39. URL: https://www.osti.gov/biblio/4135931 (visited on 11/15/2022).

Saito, Shinji and S. Peter Gary (Jan. 2007). "All whistlers are not created equally: Scattering of strahl electrons in the solar wind via particle-in-cell simulations". en. In: *Geophysical Research Letters* 34.1, p. L01102. ISSN: 0094-8276. DOI: 10.1029/2006GL028173. URL: http://doi.wiley.com/10.1029/2006GL028173 (visited on 08/17/2022).

Salem, C. et al. (Mar. 2003). "Electron Properties and Coulomb Collisions in the Solar Wind at 1 AU: *Wind* Observations". en. In: *The Astrophysical Journal* 585.2, pp. 1147–1157. ISSN: 0004-637X, 1538-4357. DOI: 10.1086/346185. URL: https://iopscience.iop.org/article/10.1086/346185 (visited on 09/06/2023).

Salem, Chadi S. et al. (July 2021). *Precision Electron Measurements in the Solar Wind at 1 au from NASA's Wind Spacecraft.* en. arXiv:2107.08125 [astro-ph, physics:physics]. URL: http://arxiv.org/abs/2107.08125 (visited on 02/24/2023).

Santolík, O., M. Parrot, and F. Lefeuvre (Feb. 2003). "Singular value decomposition methods for wave propagation analysis". en. In: *Radio Science* 38.1, n/a–n/a. ISSN: 00486604. DOI: 10.1029/2000RS002523. URL: http://doi.wiley.com/10.1029/2000RS002523 (visited on 05/26/2022).

Sarfraz, M. and P. H. Yoon (Jan. 2020). "Combined Whistler Heat Flux and Anisotropy Instabilities in Solar Wind". en. In: *Journal of Geophysical Research: Space Physics* 125.1. ISSN: 2169-9380, 2169-9402. DOI: 10.1029/2019JA027380. URL: https://onlinelibrary.wiley.com/doi/10.1029/2019JA027380 (visited on 08/17/2022).

Schlickeiser, R. (1999). "Mean free path of solar electrons and nucleons". In: *Astronomy & Astrophysics* 351, pp. 382–384. URL: http://cdsarc.u-strasbg.fr/ftp/vizier/aa/papers/9351001/2300382/small.htm.

Schroeder, J M, S Boldyrev, and P Astfalk (Aug. 2021). "Stability of superthermal strahl electrons in the solar wind". en. In: *Monthly Notices of the Royal Astronomical Society* 507.1, pp. 1329–1336. ISSN: 0035-8711, 1365-2966. DOI: 10.1093/mnras/stab2228. URL: https://academic.oup.com/mnras/article/507/1/1329/6335496 (visited on 08/16/2023).

Schwenn, Rainer and Eckart Marsch (Jan. 1990). *Physics of the Inner Heliosphere I. Large-Scale Phenomena.* Publication Title: Physics of the Inner Heliosphere I ADS Bibcode: 1990pihl.book.....S. DOI: 10.1007/978-3-642-75361-9. URL: https://ui.adsabs.harvard.edu/abs/1990pihl.book.....S (visited on 07/18/2023).

Scime, Earl E. et al. (1994). "Regulation of the solar wind electron heat flux from 1 to 5 AU: Ulysses observations". en. In: *Journal of Geophysical Research* 99.A12, p. 23401. ISSN:

0148-0227. DOI: 10.1029/94JA02068. URL: http://doi.wiley.com/10.1029/94JA02068 (visited on 08/16/2022).

Scudder, J. D. and H. Karimabadi (May 2013). "Ubiquitous non-thermals in astrophysical plasmas: restating the difficulty of maintaining Maxwellians". en. In: *The Astrophysical Journal* 770.1. Publisher: The American Astronomical Society, p. 26. ISSN: 0004-637X. DOI: 10.1088/0004-637X/770/1/26. URL: https://dx.doi.org/10.1088/0004-637X/770/1/26 (visited on 08/17/2023).

Scudder, Jack D. (Oct. 1992a). "On the Causes of Temperature Change in Inhomogeneous Low-Density Astrophysical Plasmas". In: *The Astrophysical Journal* 398. ADS Bibcode: 1992ApJ...398..299S, p. 299. ISSN: 0004-637X. DOI: 10.1086/171858. URL: https://ui.adsabs.harvard.edu/abs/1992ApJ...398..299S (visited on 06/01/2023).

— (Oct. 1992b). "Why All Stars Should Possess Circumstellar Temperature Inversions". In: *The Astrophysical Journal* 398. ADS Bibcode: 1992ApJ...398..319S, p. 319. ISSN: 0004-637X. DOI: 10.1086/171859. URL: https://ui.adsabs.harvard.edu/abs/1992ApJ...398..319S (visited on 06/01/2023).

Shaaban, S M, M Lazar, and S Poedts (Oct. 2018). "Clarifying the solar wind heat flux instabilities". en. In: *Monthly Notices of the Royal Astronomical Society* 480.1, pp. 310–319. ISSN: 0035-8711, 1365-2966. DOI: 10.1093/mnras/sty1567. URL: https://academic.oup.com/mnras/article/480/1/310/5043237 (visited on 08/17/2022).

Shaaban, S M et al. (July 2019). "Quasi-linear approach of the whistler heat-flux instability in the solar wind". en. In: *Monthly Notices of the Royal Astronomical Society* 486.4, pp. 4498–4507. ISSN: 0035-8711, 1365-2966. DOI: 10.1093/mnras/stz830. URL: https://academic.oup.com/mnras/article/486/4/4498/5426828 (visited on 08/17/2022).

Shi, Chen et al. (Feb. 2021). "Parker Solar Probe Observations of Alfvénic Waves and Ion-cyclotron Waves in a Small-scale Flux Rope". en. In: *The Astrophysical Journal Letters* 908.1. Publisher: The American Astronomical Society, p. L19. ISSN: 2041-8205. DOI: 10.3847/2041-8213/abdd28. URL: https://dx.doi.org/10.3847/2041-8213/abdd28 (visited on 09/25/2023).

Shklyar, David and Hiroshi Matsumoto (Apr. 2009). "Oblique Whistler-Mode Waves in the Inhomogeneous Magnetospheric Plasma: Resonant Interactions with Energetic Charged Particles". en. In: *Surveys in Geophysics* 30.2, pp. 55–104. ISSN: 0169-3298, 1573-0956. DOI: 10.1007/s10712-009-9061-7. URL: http://link.springer.com/10.1007/s10712-009-9061-7 (visited on 08/11/2023).

Shoub, E. C. (Mar. 1983). "Invalidity of local thermodynamic equilibrium for electrons in the solar transition region. I - Fokker-Planck results". In: *The Astrophysical Journal* 266, pp. 339–369. ISSN: 0004-637X. DOI: 10.1086/160783. URL: https://ui.adsabs.harvard.edu/abs/1983ApJ...266..339S (visited on 08/17/2023).

Shprits, Yuri Y. et al. (Nov. 2008). "Review of modeling of losses and sources of relativistic electrons in the outer radiation belt I: Radial transport". en. In: *Journal of Atmospheric and Solar-Terrestrial Physics* 70.14, pp. 1679–1693. ISSN: 13646826. DOI: 10.1016/j.jastp.2008.06.008. URL: https://linkinghub.elsevier.com/retrieve/pii/S1364682608001648 (visited on 08/11/2023).

Solanki, S. K. et al. (Oct. 2020). "The Polarimetric and Helioseismic Imager on Solar Orbiter". en. In: *Astronomy & Astrophysics* 642, A11. ISSN: 0004-6361, 1432-0746. DOI: 10.1051/0004-6361/201935325. URL: https://www.aanda.org/10.1051/0004-6361/201935325 (visited on 02/14/2023).

Sonnerup, B. U. Ö and L. J. Cahill Jr. (1967). "Magnetopause structure and attitude from Explorer 12 observations". en. In: *Journal of Geophysical Research (1896-1977)* 72.1, pp. 171–183. ISSN: 2156-2202. DOI: 10.1029/JZ072i001p00171. URL: https://onlinelibrary.wiley.com/doi/abs/10.1029/JZ072i001p00171 (visited on 07/22/2023).

Sonnerup, Bengt U. Ö. and Maureen Scheible (Jan. 1998). "Minimum and Maximum Variance Analysis". In: *ISSI Scientific Reports Series* 1, pp. 185–220. URL: https://ui.adsabs.harvard.edu/abs/1998ISSIR...1..185S (visited on 08/17/2022).

Soucek, J. et al. (Dec. 2021). "Solar Orbiter Radio and Plasma Waves – Time Domain Sampler: In-flight performance and first results". en. In: *Astronomy & Astrophysics* 656, A26. ISSN: 0004-6361, 1432-0746. DOI: 10.1051/0004-6361/202140948. URL: https://www.aanda.org/10.1051/0004-6361/202140948 (visited on 02/16/2023).

SPICE Consortium et al. (Oct. 2020). "The Solar Orbiter SPICE instrument: An extreme UV imaging spectrometer". en. In: *Astronomy & Astrophysics* 642, A14. ISSN: 0004-6361, 1432-0746. DOI: 10.1051/0004-6361/201935574. URL: https://www.aanda.org/10.1051/0004-6361/201935574 (visited on 02/14/2023).

Spitzer, Lyman and Richard Härm (Mar. 1953). "Transport Phenomena in a Completely Ionized Gas". en. In: *Physical Review* 89.5, pp. 977–981. ISSN: 0031-899X. DOI: 10.1103/PhysRev.89.977. URL: https://link.aps.org/doi/10.1103/PhysRev.89.977 (visited on 04/28/2021).

Steinvall, K. et al. (Dec. 2021). "Solar wind current sheets and deHoffmann-Teller analysis: First results of DC electric field measurements by Solar Orbiter". en. In: *Astronomy & Astrophysics* 656. arXiv:2104.03553 [astro-ph, physics:physics], A9. ISSN: 0004-6361, 1432-0746. DOI: 10.1051/0004-6361/202140855. URL: http://arxiv.org/abs/2104.03553 (visited on 09/29/2022).

Stix, Thomas Howard (Jan. 1992). *Waves in plasmas*. Publication Title: Waves in plasmas ADS Bibcode: 1992wapl.book.....S. URL: https://ui.adsabs.harvard.edu/abs/1992wapl.book.....S (visited on 03/07/2023).

Taubenschuss, Ulrich and Ondřej Santolík (Jan. 2019). "Wave Polarization Analyzed by Singular Value Decomposition of the Spectral Matrix in the Presence of Noise". en. In: *Surveys in Geophysics* 40.1, pp. 39–69. ISSN: 0169-3298, 1573-0956. DOI: 10.1007/s10712-018-9496-9. URL: http://link.springer.com/10.1007/s10712-018-9496-9 (visited on 08/16/2022).

Thejappa, G. and R. J. MacDowall (Apr. 2008). "Effects of Scattering on Radio Emission from the Quiet Sun at Low Frequencies". In: *The Astrophysical Journal* 676. ADS Bibcode: 2008ApJ...676.1338T, pp. 1338–1345. ISSN: 0004-637X. DOI: 10.1086/528835. URL: https://ui.adsabs.harvard.edu/abs/2008ApJ...676.1338T (visited on 05/06/2023).

Tong, Yuguang et al. (June 2019a). "Statistical Study of Whistler Waves in the Solar Wind at 1 au". In: *The Astrophysical Journal* 878, p. 41. DOI: 10.3847/1538-4357/ab1f05.

Tong, Yuguang et al. (Jan. 2019b). "Whistler Wave Generation by Halo Electrons in the Solar Wind". In: *The Astrophysical Journal* 870. ADS Bibcode: 2019ApJ...870L...6T, p. L6. ISSN: 0004-637X. DOI: 10.3847/2041-8213/aaf734. URL: https://ui.adsabs.harvard.edu/abs/2019ApJ...870L...6T (visited on 07/27/2023).

Tsallis, Constantino (July 1988). "Possible generalization of Boltzmann-Gibbs statistics". en. In: *Journal of Statistical Physics* 52.1, pp. 479–487. ISSN: 1572-9613. DOI: 10.1007/BF01016429. URL: https://doi.org/10.1007/BF01016429 (visited on 05/29/2023).

Vainio, R. (Dec. 2000). "Charged-Particle Resonance Conditions and Transport Coefficients in Slab-Mode Waves". en. In: *The Astrophysical Journal Supplement Series* 131.2, pp. 519–529. ISSN: 0067-0049, 1538-4365. DOI: 10.1086/317372. URL: https://iopscience.iop.org/article/10.1086/317372 (visited on 09/22/2023).

Vasko, I. Y. et al. (Jan. 2019). "Whistler Fan Instability Driven by Strahl Electrons in the Solar Wind". en. In: *The Astrophysical Journal* 871.2, p. L29. ISSN: 2041-8213. DOI: 10.3847/2041-8213/ab01bd. URL: https://iopscience.iop.org/article/10.3847/2041-8213/ab01bd (visited on 08/16/2022).

Vasko, I. Y. et al. (Aug. 2020). "On quasi-parallel whistler waves in the solar wind". en. In: *Physics of Plasmas* 27.8, p. 082902. ISSN: 1070-664X, 1089-7674. DOI: 10.1063/5.0003401. URL: http://aip.scitation.org/doi/10.1063/5.0003401 (visited on 08/17/2022).

Vedenov, A. A. (Jan. 1963). "Quasi-linear plasma theory (theory of a weakly turbulent plasma)". en. In: *Journal of Nuclear Energy. Part C, Plasma Physics, Accelerators, Thermonuclear Research* 5.3, p. 169. ISSN: 0368-3281. DOI: 10.1088/0368-3281/5/3/305. URL: https://dx.doi.org/10.1088/0368-3281/5/3/305 (visited on 02/25/2023).

Verscharen, Daniel et al. (Nov. 2019). "Self-induced Scattering of Strahl Electrons in the Solar Wind". en. In: *The Astrophysical Journal* 886.2, p. 136. ISSN: 1538-4357. DOI: 10.3847/1538-4357/ab4c30. URL: https://iopscience.iop.org/article/10.3847/1538-4357/ab4c30 (visited on 04/28/2021).

Verscharen, Daniel et al. (Aug. 2022). "Electron-Driven Instabilities in the Solar Wind". en. In: *Frontiers in Astronomy and Space Sciences* 9, p. 951628. ISSN: 2296-987X. DOI: 10.3389/fspas.2022.951628. URL: https://www.frontiersin.org/articles/10.3389/fspas.2022.951628/full (visited on 04/19/2023).

Vocks, C. and G. Mann (Aug. 2003). "Generation of Suprathermal Electrons by Resonant Wave-Particle Interaction in the Solar Corona and Wind". en. In: *The Astrophysical Journal* 593.2, pp. 1134–1145. ISSN: 0004-637X, 1538-4357. DOI: 10.1086/376682. URL: https://iopscience.iop.org/article/10.1086/376682 (visited on 08/25/2022).

Vocks, C. et al. (July 2005). "Electron Halo and Strahl Formation in the Solar Wind by Resonant Interaction with Whistler Waves". en. In: *The Astrophysical Journal* 627.1, pp. 540–549. ISSN: 0004-637X, 1538-4357. DOI: 10.1086/430119. URL: https://iopscience.iop.org/article/10.1086/430119 (visited on 08/17/2022).

Vourlidas, Angelos et al. (Dec. 2016). "The Wide-Field Imager for Solar Probe Plus (WISPR)". en. In: *Space Science Reviews* 204.1, pp. 83–130. ISSN: 1572-9672. DOI: 10.1007/s11214-014-0114-y. URL: https://doi.org/10.1007/s11214-014-0114-y (visited on 02/15/2023).

Whittlesey, Phyllis L. et al. (Feb. 2020). "The Solar Probe ANalyzers—Electrons on the Parker Solar Probe". en. In: *The Astrophysical Journal Supplement Series* 246.2, p. 74. ISSN: 0067-0049, 1538-4365. DOI: 10.3847/1538-4365/ab7370. URL: https://iopscience.iop.org/article/10.3847/1538-4365/ab7370 (visited on 01/20/2023).

Wimmer-Schweingruber, Robert F. (Jan. 2002). "The composition of the solar wind". en. In: *Advances in Space Research* 30.1, pp. 23–32. ISSN: 0273-1177. DOI: 10.1016/S0273-1177(02)00262-4. URL: https://www.sciencedirect.com/science/article/pii/S0273117702002624 (visited on 07/18/2023).

Yakimenko, V L (1963). "ABSORPTION OF WAVES IN A PLASMA (QUASILINEAR APPROXIMATION)". en. In: *Journal of Experimental and Theoretical Physics* 17.

Štverák, Štěpán, Pavel M. Trávníček, and Petr Hellinger (Oct. 2015). "Electron energetics in the expanding solar wind via Helios observations". en. In: *Journal of Geophysical Research: Space Physics* 120.10, pp. 8177–8193. ISSN: 21699380. DOI: 10.1002/2015JA021368. URL: http://doi.wiley.com/10.1002/2015JA021368 (visited on 08/16/2022).

Štverák, Štěpán et al. (Mar. 2008). "Electron temperature anisotropy constraints in the solar wind". en. In: *Journal of Geophysical Research: Space Physics* 113.A3. ISSN: 01480227. DOI: 10.1029/2007JA012733. URL: http://doi.wiley.com/10.1029/2007JA012733 (visited on 08/16/2022).

Štverák, Štěpán et al. (May 2009). "Radial evolution of nonthermal electron populations in the low-latitude solar wind: Helios, Cluster, and Ulysses Observations". en. In: *Journal of Geophysical Research: Space Physics* 114.A5, n/a–n/a. ISSN: 01480227. DOI: 10.1029/2008JA013883. URL: http://doi.wiley.com/10.1029/2008JA013883 (visited on 08/16/2022).

Lucas COLOMBAN

Interactions entre les ondes de sifflement et les électrons suprathermiques du vent solaire : observations de Solar Orbiter et de Parker Solar Probe

L'évolution de la fonction de distribution des électrons du vent solaire avec la distance héliocentrique présente des caractéristiques encore inexpliquées. Nous pouvons citer l'augmentation de la largeur angulaire du faisceau d'électrons suprathermiques aligné avec le champ magnétique (Strahl). Cette augmentation est associée à une augmentation de la densité relative des électrons suprathermiques plus isotrope du halo et à la diminution rapide du flux de chaleur. Dans cette thèse, nous cherchons à préciser le rôle des interactions ondes-particules dans cette dynamique et en particulier à savoir si les ondes de sifflement peuvent expliquer l'augmentation observée de la largeur angulaire du Strahl. Pour ce faire, nous effectuons d'abord une analyse statistique de ces ondes avec Solar Orbiter et Parker Solar Probe (PSP), entre 0,2 et 1 UA. 110 000 paquets d'ondes sont détectés et caractérisés dans le référentiel du plasma. L'écrasante majorité des ondes ont un angle de propagation (θ) quasi-aligné avec le champ magnétique. Au-delà de 0,3 UA, les ondes sont alignées avec le Strahl (y compris lors des "switchbacks"), et il n'y a pratiquement pas d'ondes obliques ($\theta \sim 70°$). Ces dernières ont pourtant été prédites par de nombreuses études et sont théoriquement très efficaces pour diffuser les électrons du Strahl. À 0,2 UA, environ la moitié des ondes sont "counter-streaming" et la proportion d'ondes obliques reste très faible. Les caractéristiques des ondes sont ensuite utilisées pour calculer les coefficients de diffusion dans le cadre de la théorie quasi-linéaire. Ces coefficients sont intégrés, en utilisant l'occurrence des ondes, afin de déduire l'effet global des siffleurs sur les électrons suprathermiques. Au-delà de 0,3 UA, les ondes de sifflement peuvent expliquer l'augmentation observée de la largeur angulaire du Strahl et sont efficaces pour isotropiser le halo. Nous montrons que la diffusion du Strahl est due à des ondes légèrement obliques, $\theta \in [15, 45]°$. Près de 0,2 UA, les ondes counter-streaming diffusent les électrons de Strahl plus efficacement que les ondes alignées avec le Strahl de deux ordres de grandeur. Par ailleurs, un problème technique avec une bobine du fluxmètre tri-axial (SCM) de PSP à la fin de l'orbite 1 nous a empêché de déduire directement les propriétés de polarisation des ondes de sifflement pour les orbites suivantes. Nous proposons une technique utilisant les champs électromagnétiques disponibles pour reconstruire les composantes manquantes (et donc les propriétés de polarisation des ondes) en négligeant le champ électrique parallèle au champ magnétique. Cette technique est applicable avec les hypothèses suivantes : (i) la fréquence de l'onde dans le repère du plasma est petite par rapport à la fréquence cyclotronique électronique ; (ii) un petit angle de propagation par rapport au champ magnétique ; et (iii) une grande vitesse de phase par rapport à la vitesse du vent solaire perpendiculaire au champ magnétique. La méthode ne peut pas être appliquée si le champ magnétique est aligné avec la bobine du SCM concernée. Nous validons notre méthode en utilisant les mesures en mode rafale effectuées lors de l'orbite 1. Les conditions de reconstruction sont satisfaites pour 80% des siffleurs détectés. Cette méthode devrait permettre de révéler pour la première fois les propriétés de polarisation des ondes sifflantes jusqu'à 10 rayons solaires ($\simeq$ 0,05 UA). Ce travail est une étape importante pour la prise en compte des interactions ondes-particules dans les modèles cinétiques et pour améliorer notre description du vent solaire. Mots clés : Vent solaire, ondes de siffements, Strahl et halo, Solar Orbiter, Parker Solar Probe, diffusion en pitch angle, théorie quasi-linéaire, technique de reconstruction

Interactions between whistler waves and solar wind suprathermal electrons: Solar Orbiter and Parker Solar Probe observations

The evolution of the solar wind electron distribution function with heliocentric distance exhibits features that are still unexplained. We can mention the increase in the angular width of the beam of suprathermal electrons aligned with the magnetic field (Strahl). This increase is associated with an increase in the relative density of the more isotropic halo electrons and the rapid decrease of the heat flux. In this thesis, we investigate the role of wave-particle interactions in these dynamics, and in particular whether whistler waves can explain the observed increase in the Strahl angular width. To achieve this, we first perform a statistical analysis of these waves with Solar Orbiter and Parker Solar Probe (PSP), between 0.2 and 1 AU. 110,000 wave packets are detected and characterized in the plasma frame. The overwhelming majority of waves have an angle of propagation (θ) quasi-aligned with the magnetic field. Beyond 0.3 AU, the waves are aligned with the Strahl (including during switchbacks), and there are virtually no oblique ($\theta \sim 70°$) waves. The latter were predicated by many studies and are theoretically very efficient in diffusing Strahl electrons. At 0.2 AU, about half of the waves are counter-streaming, and the proportion of oblique waves remains very low. The wave characteristics are then used to compute the diffusion coefficients in the framework of quasi-linear theory. These coefficients are integrated, using the occurrence of the waves, in order to deduce the overall effect of whistlers on suprathermal electrons. Beyond 0.3 AU, whistler waves can explain the observed increase in Strahl angular width and are effective in isotropizing the halo. Strahl diffusion is due to slightly oblique ($\theta \in [15, 45]°$) waves. Near 0.2 AU, counter-streaming waves diffuse Strahl electrons more efficiently than Strahl-aligned waves by two orders of magnitude. However, a technical issue with one coil of the Search-Coil Magnetometer (SCM) of PSP at the end of Encounter 1 prevented us from directly deducing the polarization properties of whistler waves for the subsequent encounters. We propose a technique using the available electromagnetic fields to reconstruct the missing components (and therefore the polarization properties of the waves) by neglecting the electric field parallel to the background magnetic field. This technique is applicable with the assumptions of (i) a small wave frequency in the plasma frame with respect to the electron cyclotron frequency; (ii) a small propagation angle with respect to the background magnetic field; and (iii) a large wave phase speed relative to the cross-field solar wind velocity. Critically, the method cannot be applied if the background magnetic field is aligned with the affected SCM coil. We validate our method using burst mode measurements made during Encounter 1. The reconstruction conditions are satisfied for 80% of the whistlers detected. This method should reveal the polarization properties of whistler waves down to 10 solar radii ($\simeq$ 0.05 AU) for the first time. This work is an important step in order to include wave-particle interactions in kinetic models and to improve our description of the solar wind. Keywords : Solar wind, Whistler waves, Strahl and halo, Solar Orbiter, Parker Solar Probe, Pitch angle diffusion, Quasi-linear theory, Reconstruction technique